Technische Universität München
TUM School of Natural Sciences

Two-Dimensional Group IV Nanomaterials:

Preparation, Modification, and Degradation of Hydride-Terminated Silicon and Germanium Nanosheets

Amelie Mareike Mühlbach

Vollständiger Abdruck der von der TUM School of Natural Sciences

der Technischen Universität München zur Erlangung einer

Doktorin der Naturwissenschaften (Dr. rer. nat.)

genehmigten Dissertation.

Vorsitz: Prof. Dr. Tom Nilges

Prüfende der Dissertation:

1. Prof. Dr. Dr. h.c. Bernhard Rieger
2. Prof. Dr. Jonathan Veinot

Die Dissertation wurde am 07.06.2024 bei der Technischen Universität München eingereicht

und durch die TUM School of Natural Sciences am 25.06.2024 angenommen.

Für meine Familie

Acknowledgments

First, I express my gratitude to Prof. Dr. Bernhard Rieger for giving me the opportunity to pursue my doctorate within his group. Thank you for allowing me the freedom to explore and grow in my research.

I extend my gratitude to Prof. Dr. Jonathan Veinot for hosting me at the University of Alberta during my research stay. I appreciated our discussions and your ideas that reflected a scientific approach from a different point of view.

I thank Dr. Carsten Troll for taking care of the organization of our group and for being available to help or fix broken instruments. Thank you, Dr. Sergei Vagin and Leah Veinot, for all ATUMS-related organizational matters. Thanks to Annette Bauer for her support in all administrative matters. Katia Rodewald is thanked for ordering materials and maintaining the SEM instruments.

Many results would not have been possible without people who helped me by providing materials or performing material characterization. I thank Sabine Zeitz for preparing Zintl phases; Katia Rodewald, Dr. Carsten Troll, Dr. Sergei Vagin, Philipp Weingarten, and Dr. Cheng Sun for SEM and/or TEM measurements; Sabrina Artmeier for AFM measurements; Tim Kratky for XPS measurements and data evaluation; Dominik Dankert for providing Zintl phases, XRD measurements, and sharing knowledge about DRS.

Special gratitude goes to Prof. Dr. Stelios Couris and Dr. Michalis Stavrou. I really appreciated and enjoyed our productive collaboration. Thank you for patiently explaining the theory of nonlinear optics and for all the discussions.

Thanks to the students I was allowed to supervise during my doctoral studies: Svenja Knösch, Jiale Zhang, and Tobias Käter. I appreciated their help in performing experiments.

I am thankful to the Veinot group at the University of Alberta for welcoming me. I thank Dr. Martin (Chuyi) Ni for his help in the laboratory and Dr. I Teng (Emily) Cheong for our free time activities in Germany and Canada. I would also like to thank Sabrina Artmeier for the time in Edmonton.

My thanks are also extended to all current and former members of the WACKER-Chair, especially to those of the Makro Süd lab. Their cordiality and mutual support created a friendly atmosphere in which I enjoyed working. We have had many valuable discussions, and you made the lab hours more fun. Special thanks go to my former lab partner, Dr. Elisabeth Groß, for our fruitful scientific discussions, collaboration, and time spent together in Canada. I thank Marina Wittig for our discussions and SET breaks. Further, I thank Dr. Paula Großmann for all the conversations and her advice.

I especially thank you, Tim, for your support and motivation over the past few years.

Finally, I am very grateful to my family. Thank you, Adrian, and especially thank you, Mama and Papa, for your unconditional support, encouragement, trust, patience, and advice.

Abstract

This thesis presents a series of research projects that share a common focus: the investigation of two-dimensional nanosheets of group IV elements. These studies include hydrogenated silicon and germanium analogs of graphene, namely hydride-terminated silicon nanosheets (SiNS-H), hydride-terminated germanium nanosheets (GeNS-H), and hydride-terminated mixed nanosheets containing both germanium and silicon (Ge/SiNS-H). Fundamental questions related to the preparation, degradation, surface functionalization, and properties of these nanomaterials are addressed.

At the outset of the investigations, SiNS-H were the material of interest. The state-of-the-art method for preparing SiNS-H involves the topotactic reaction of the Zintl phase calcium disilicide with concentrated aqueous hydrochloric acid at low temperatures. As-prepared SiNS-H are already partially oxidized, as shown by infrared spectroscopy. To address this challenge, the objective of this project was to develop a novel preparation method that should result in the formation of oxygen-free SiNS-H. The solvent water was identified as the oxidation source in the state-of-the-art preparation method. Consequently, the transformation of calcium disilicide to SiNS-H under the exclusion of moisture was investigated. A set of organic solvents with high dipole moments combined with chelating agents with the potential to solvate the calcium cation was tested. However, no conversion of the starting material occurred. As it was demonstrated that water is essential for the successful synthesis of SiNS-H, partial oxidation of the material is inevitable.

SiNS-H are photosensitive and undergo degradation when exposed to 365 nm ultraviolet (UV) irradiation. The degradation process was systematically investigated by irradiating SiNS-H in argon, air, and oxygen atmospheres. The detailed characterization of the irradiated nanosheets revealed their structural decomposition, which was found to be based on a radical process. UV irradiation in an argon atmosphere leads to the amorphization of SiNS-H, while photooxidation occurs in air and oxygen atmospheres.

Mixed Ge/SiNS-H nanosheets were functionalized by the literature-known hydrometalation of 1-dodecene, induced either radically or thermally. The mixed nanosheets exhibited intermediate surface coverages compared to functionalized pure SiNS and GeNS. A follow-up study aimed to establish an advanced modification concept involving the selective functionalization of silicon or germanium atoms in Ge/SiNS-H. Several modification procedures on pure SiNS-H and GeNS-H were tested, but none of these approaches demonstrated selectivity towards either silicon or germanium functionalization.

Pure GeNS-H can be functionalized with butyl groups by the reaction with *n*-butyllithium. In an attempt to apply this reaction to SiNS-H, these nanosheets decomposed. It was determined that the decomposition was not caused by *n*-butyllithium, but by lithium methoxide, which was formed during the workup with methanol. Consequently, the behavior of SiNS-H, GeNS-H, and Ge/SiNS-H towards lithium methoxide was investigated. In the presence of lithium methoxide, SiNS-H decomposed, while GeNS-H remained intact. This allowed the selective removal of silicon atoms from Ge/SiNS-H, which was successfully accomplished.

Finally, SiNS-H were functionalized by the hydrosilylation of styrene and *tert*-butyl methacrylate. The products were characterized in terms of their composition, structure, and morphology. The investigation of their third-order nonlinear optical responses demonstrated that they exhibit exceptional properties, rendering them excellent materials for optoelectronic and photonic applications.

Zusammenfassung

Diese Arbeit beinhaltet eine Reihe von Forschungsprojekten, die die Untersuchung von zweidimensionalen Nanoschichten aus Elementen der 4. Hauptgruppe als Schwerpunkt haben. Die Untersuchungen umfassen hydrierte Silicium- und Germanium-Analoga von Graphen, genauer gesagt Hydrid-terminierte Silicium- (SiNS-H) und Germanium-Nanoschichten (GeNS-H) sowie Hydrid-terminierte gemischte Nanoschichten, die gleichzeitig Germanium und Silicium enthalten (Ge/SiNS-H). Die Forschung befasst sich mit grundlegenden Fragen bezüglich der Herstellung, des Abbaus, der Oberflächenfunktionalisierung und der Eigenschaften dieser Nanomaterialien.

Zu Beginn der Untersuchungen standen SiNS-H im Fokus. Derzeit werden SiNS-H durch die topotaktische Reaktion der Zintl-Phase Calciumdisilicid mit konzentrierter wässriger Salzsäure bei niedrigen Temperaturen hergestellt. Infrarotspektroskopische Untersuchngen zeigen, dass SiNS-H, die entsprechend dieser Vorschrift hergestellt wurden, teilweise oxidiert sind. Ziel dieses Projekts war es, ein neuartiges Syntheseverfahren zu entwickeln, das die Bildung von sauerstofffreien SiNS-H ermöglicht. Als Ursache für die Oxidation konnte Wasser identifiziert werden, welches in der Herstellungsmethode nach Literaturvorschrift als Lösungsmittel verwendet wird. Daher wurde die Umsetzung von Calciumdisilicid zu SiNS-H unter Ausschluss von Feuchtigkeit untersucht. Eine Reihe organischer Lösungsmittel mit hohem Dipolmoment wurde in Kombination mit Chelatbildnern getestet, die das Potenzial haben, das Calciumkation zu solvatisieren. Dabei war keine Umsetzung des Ausgangsmaterials festzustellen. Es konnte gezeigt werden, dass Wasser für die erfolgreiche Synthese von SiNS-H erforderlich ist und somit eine teilweise Oxidation des Materials unvermeidbar ist.

SiNS-H sind lichtempfindlich und werden bei Bestrahlung mit ultraviolettem Licht mit einer Wellenlängen von 365 nm abgebaut. Der Abbauprozess wurde systematisch untersucht, indem SiNS-H in Argon-, Luft- und Sauerstoffatmosphäre bestrahlt wurden. Die detaillierte Charakterisierung der bestrahlten Nanoschichten belegt deren strukturelle Zersetzung, die auf einem radikalischen Prozess beruht.

Unter UV-Bestrahlung in einer Argon-Atmosphäre werden SiNS-H amorph, während in Luft- und Sauerstoffatmosphären eine Photooxidation stattfindet.

Gemischte Ge/SiNS-H wurden mittels der literaturbekannten Hydrometallierung von 1-Dodecen funktionalisiert. Die Reaktion wurde sowohl radikalisch als auch thermisch induziert durchgeführt. Im Vergleich zu funktionalisierten reinen SiNS und GeNS, weisen die funktionalisierten gemischten Nanoschichten mittlere Oberflächenbedeckung auf. In folgenden Untersuchungen sollte ein neues Konzept der Oberflächenmodifizierung entwickelt werden, bei welchem die Silicium- bzw. Germaniumatome in den Ge/SiNS-H selektiv unterschiedlich funktionalisiert werden. Mehrere Funktionalisierungsmethoden an reinen SiNS-H und GeNS-H wurden dafür getestet. Jedoch zeigte keiner der Ansätze eine Selektivität bezüglich der Funktionalisierung von Silicium oder Germanium.

Reine GeNS-H können durch die Reaktion mit *n*-Butyllithium mit Butylgruppen funktionalisiert werden. Bei dem Versuch, diese Reaktion auf SiNS-H zu übertragen, kam es zur Zersetzung der Nanoschichten. Es konnte festgestellt werden, dass diese Reaktion nicht durch *n*-Butyllithium verursacht wurde, sondern durch Lithiummethanolat, das sich bei der Aufarbeitung mit Methanol gebildet hatte. Daher wurde das Verhalten von SiNS-H, GeNS-H und Ge/SiNS-H gegenüber Lithiummethoxid untersucht. Es konnte gezeigt werden, dass sich SiNS-H in Anwesenheit von Lithiummethanolat zersetzten, wohingegen GeNS-H intakt blieben. Dies ermöglichte die selektive Entfernung von Siliciumatomen aus Ge/SiNS-H, was experimentell nachgewiesen wurde.

Schließlich wurden SiNS-H durch die Hydrosilylierung mit Styrol und *tert*-Butylmethacrylat funktionalisiert. Die modifizierten Produkte wurden hinsichtlich ihrer Zusammensetzung, Struktur und Morphologie charakterisiert. Die Untersuchung ihrer nichtlinearen optischen Eigenschaften dritter Ordnung zeigte, dass sie hervorragende Eigenschaften besitzen, die sie für optoelektronische und photonische Anwendungen geeignet machen.

Contents

Abbreviations

0D	zero-dimensional
15C5	15-crown-5
18C6	18-crown-6
1D	one-dimensional
1PA	one-photon absorption
2D	two-dimensional
2PA	two-photon absorption
ABCN	1,1'-azobis(cyclohexanecarbonitrile)
ACF	tris(pentafluorophenyl)alane
AFM	atomic force microscopy
AIBN	azobisisobutyronitrile
BAPTA	1,2-bis(*o*-aminophenoxy)ethane-*N,N,N',N'*-tetraacetic acid
BCF	tris(pentafluorophenyl)borane
BIP	bis(4-*tert*-butylphenyl)iodonium hexafluorophosphate
CA	closed-aperture
DMPU	*N,N'*-dimethylpropyleneurea
EDTA	ethylenediaminetetraacetic acid
EDX	energy dispersive X-ray
EMIM OTf	1-ethyl-3-methylimidazolium triflate
FTIR	Fourier-transform infrared spectroscopy
GC	gas chromatography
Ge/SiNS-H	hydride-terminated mixed germanium/silicon nanosheets, $[Ge_3Si_3H_6]_n$
GeNS-H	hydride-terminated germanium nanosheets, $[Ge_6H_6]_n$
GPC	gel permeation chromatography
HEA	high-entropy alloys
IR	infrared
m	multiplet
ML	mass loss
MMA	methyl methacrylate

MsOH	methanesulfonic acid
Mxenes	tranistion metal carbides and nitrides
NIR	near infrared
NLO	nonlinear optics / nonlinear optical
NMR	nuclear magnetic resonance
OA	open-aperture
OL	optical limiting
P3HT	poly(3-hexylthiophene-2,5-diyl)
PL	photoluminescence
PMMA	poly(methyl methacrylate)
RSA	reverse saturable absorption
RT	room temperature
s	singlet
SA	saturable absorption
SC	surface coverage
SEM	scanning electron microscopy
SiNS-H	hydride-terminated silicon nanosheets, $[Si_6H_6]_n$
t	triplet
TBAC	tetrabutylammonium chloride
*t*BuMA	*tert*-butyl methacrylate
TEM	transmission electron microscopy
TFA	trifluoroacetic acid
TfOH	triflic acid
TGA	thermogravimetric analysis
UV	ultraviolet
vis	visible
XPS	X-ray photoelectron spectroscopy
XRD	X-ray diffraction

1 Introduction

Nanoscience and nanotechnology are important research areas in physics, chemistry, engineering, material science, and biology. The term nanotechnology describes numerous technologies, which are at the nanometre scale. The concepts on which this technology was later based, have been first presented by Feynman in his lecture "There's Plenty of Room at the Bottom: An Invitation to Enter a New Field of Physics" in 1959.[1]

Developments in nanotechnology, such as nanoelectronics, which are nowadays implemented into many devices, are changing our lives. It is said that the impact of nanotechnology on our society and economy in the 21^{th} century is compared to that of semiconductor technology, information technology, or cellular and molecular biology in the 20^{th} century.[2] The current importance of nanotechnology was recently demonstrated by the awarding of the Nobel Prize in Chemistry 2023 to Bawendi, Brus and Yekimov "for the discovery and synthesis of quantum dots."[3] The most important property of quantum dots is there size-dependent color. For example, they are applied in monitors and screens based on quantum dot light-emitting diode technology.

In general, nanotechnology deals with so-called nanomaterials. They are characterized by at least one dimension scaled to the range of 1 to 100 nm, which distinguishes them from bulk materials. Based on the number of restricted dimensions, three types of nanomaterials are classified: Two-dimensional (2D) materials, or

single-atom-thick materials, have one confined dimension, one-dimensional (1D) materials are limited to the nanometre scale in two dimensions, and when all three dimensions are in the nanoscale range, zero-dimensional (0D) materials are obtained. Prominent examples of these classes are e.g. graphene (2D), carbon nanotubes (1D), or fullerenes (0D). Of course, there are many other structures besides these carbon representatives. The size reduction to nanostructured materials results in different properties compared to those of bulk materials, where all three dimensions exceed the nanoscale. The reasons for this significant change in properties are a high surface area to volume ratio and thus a high fraction of atoms on the surface, as well as quantum confinement effects.

In the last decades, 2D nanomaterials in particular have gained research interest. Although 2D nanomaterials were studied before the successful exfoliation of graphene from graphite,[4] this finding in 2004 triggered material research. Since then, many types of 2D nanomaterials have been investigated, such as transition metal carbides and nitrides (MXenes),[5] transition metal dichalcogenides,[6] or hexagonal boron nitride.[7]

Among all 2D nanomaterials, silicon nanomaterials are of special interest because they can be integrated into the current silicon-based semiconductor industry. General potential applications of 2D silicon nanomaterials are in the fields of (opto)electronics, catalysis, as well as energy storage and conversion. Silicon is non-toxic and the second most abundant element in the earth's crust,[8] making it readily available and cheap.
The group of 2D silicon nanosheets comprises silicene, silicane, and siloxene, which differ with respect to their composition, structure, and properties. Silicene is analogous to graphene, but in contrast to its carbon counterpart exhibits a puckered layer structure due to mixed sp^2/sp^3 hybridization. The formal hydrogenation of this material, which is only stable on substrates, results in hydride-terminated silicane. The material of interest within this thesis is silicane.
Silicane was first prepared in the 1990s, but research interest continues today. In recent years numerous theoretical and experimental studies have been published on the preparation, functionalization, properties, and applications of silicane. However, there are still unanswered questions, such as the preparation of non-oxidized silicane, its degradation under UV light, as well as tuning the optical properties through surface functionalization. Exchanging a fraction of the silicon atoms in silicane with germanium atoms results in mixed siligane nanosheets,

which were recently discovered. An open research task on this material is its surface functionalization.

2

Theoretical Background

Several types of 2D silicon materials have been reported in experimental and theoretical studies, including silicene, silicane, and siloxene. These nanomaterials, which differ in their structures and properties, are described in this chapter, while the focus is on silicane, which is the material of main interest in this thesis. As this thesis is not solely concerned with silicane but also encompasses the germanium analog and a mixed version of both, a basic overview of germanane and the mixed material is provided.

2.1 Siloxene

The term *siloxene* is used to describe compounds that have the same ideal molecular formula $[Si_6H_6O_3]_n$ but different structures. These layered silicon materials are Wöhler siloxene and Kautsky siloxene. The reason why both modifications are referred to as siloxene is historical. For a long time both substances were believed to have the same structure only differing in their purity.

2.1.1 Discovery, Preparation, and Structure of Siloxene

In 1863, Wöhler discovered siloxene by reacting gray calcium disilicide ($CaSi_2$) with cold fuming hydrochloric acid.[9] Under the evolution of hydrogen, yellow flakes were formed, which he called *Silicon* (in the German language). Later it was

named *Wöhler siloxene*. According to his initial analyses, the material contained silicon, hydrogen, and oxygen. He postulated an empirical chemical formula of either $Si_8H_4O_6$ or $Si_6H_3O_4$. 46 years later, Hönigschmid repeated the experiments of Wöhler and determined the chemical structure of the obtained compound to be $Si_3H_3O_2$.[10]

Several years later, Kautsky restated studying the transformation of $CaSi_2$ in hydrochloric acid and found that the material described by Wöhler is no pure compound but a mixture of different silicon, hydrogen, and oxygen containing compounds. He varied the synthesis protocol by performing the reaction in the dark and using diluted cold alcoholic hydrochloric acid. These milder reaction conditions yield a white to greenish solid with the composition of Si_2H_2O.[11] Detailed investigations of this material by Kautsky and coworkers followed. His postulation of a precise structure of siloxene is Kautsky's most significant contribution. The structure is described by Si_6H_6-rings, which are interconnected *via* Si-O-Si bonds (Scheme 2.1). Hence, the idealized chemical formula is $[Si_6O_3H_6]_n$.[12–14] The suggested structure was based on elemental analysis and observations on the reactivity against several reactants such as bromine. The correct nomenclature of this material is 2D-poly[cyclohexasiltrioxane],[15] but for simplicity, Kautsky introduced the name *siloxene* in 1924.[12] Nowadays, it is referred to as *Kautsky siloxene*.

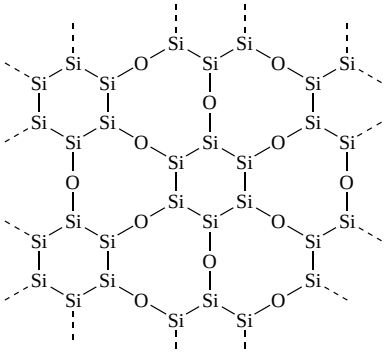

Scheme 2.1: Structural model of siloxene, as proposed by Kautsky, depicted in a top view. Note that the Si_6-rings are bonded to hydrogen atoms either above or below the plane, which are not shown here for clarity.

Later, modern characterization methods were applied to elucidate the structures of siloxenes. Weiss *et al.* reported on the characterization of siloxene prepared analogously to the procedure by Kautsky.[15] However, the description of the experimental conditions (concentrated hydrochloric acid) shows that it corresponds

to that of Wöhler. They performed X-ray diffraction (XRD) experiments, which revealed that siloxene layers are turbostratically stacked. The stacking is explained by van der Waals forces between adjacent layers. More interestingly, they found that the corrugated silicon layers from the starting material $CaSi_2$ (for details on $CaSi_2$ see Section 2.2.2) remains intact after the reaction with hydrochloric acid. Accordingly, the transformation of $CaSi_2$ into Wöhler siloxene is of topochemical character as shown in Scheme 2.2. Further, no oxygen is inserted into the Si-Si bonds in Wöhler siloxene, which is contrary to the assumed structure of Kautsky. Similar results were also obtained in an XRD study of Dahn *et al.*[16] Thus, Wöhler siloxene consists of planes of interconnected Si_6-rings in the chair conformation. The silicon atoms are alternately bonded with hydrogen or hydroxyl groups (see Scheme 2.2). The ideal chemical formula is $[Si_6H_3(OH)_3]_n$ and the nomenclature of this material is 2D-poly[1,3,5-trihydroxocyclohexasilane].[17]
In contrast, no exact structure of Kautsky siloxene has been reported yet as it is an X-ray amorphous compound, which is difficult to analyze.[18] Kurmaev and coworkers analyzed Kautsky siloxene using X-ray emission and infrared spectroscopies. According to their study, Kautsky siloxene is assumed to be a mixture of the ideal structure proposed by Kautsky and other modifications.

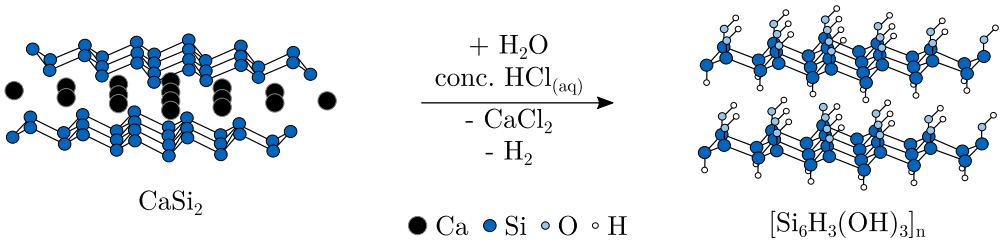

Scheme 2.2: Schematic illustration of the structure transition of $CaSi_2$ to the ideal structure of Wöhler siloxene $[Si_6H_3(OH)_3]_n$.

Further studies on structural analyses of siloxene by vibrational spectroscopy (IR and Raman spectroscopy) or ^{29}Si solid-state nuclear magnetic resonance (NMR) followed.[17,19–25]

2.1.2 Properties of Siloxene

Reactivity

Wöhler siloxene is described as being insoluble in water, organic solvents, and acids, including hydrochloric and sulfuric acid.[9] It is oxidized by water to

form $Si_6H_{3-x}(OH)_{3+x}$, which subsequently undergoes condensation to a three-dimensional interlinked system.[15] In the presence of bases, it either forms hydrogen and silicic acid (e.g., with ammonia) or completely dissolves (with alkali solutions).[9,10] In addition, Wöhler siloxene is a reducing agent, as metal precipitates in aqueous solutions of the corresponding metal salts of copper, mercury, silver, gold, or platinum.[9,10]

Kautsky siloxene is known to hydrolyze with water.[11] Further several oxidation reactions of this material have been observed. It is capable of reducing aldehydes and ketones to alcohols.[26] With halogens (iodine, bromine, chlorine), organo halides (carbon tetrachloride, chloroform, and ethyl iodide), or hydrogen halides (hydrogen iodide, hydrogen bromide, hydrogen chloride), a light-induced transformation towards halogen-containing siloxene derivatives occurs through the substitution of hydrogen atoms with halogen atoms.[11,12,27] Moreover the literature describes the synthesis of alkoxy-derivatives of Kautsky siloxene, in which hydrogen atoms are replaced with alkoxy groups.[14]

Photoluminescence

Siloxene and its derivatives exhibit an outstanding property: strong, visible room temperature luminescence. This property was already reported by Kautsky in the 1920s.[12,28] Following the discovery of the photoluminescence (PL) of porous silicon,[29] research interest in the PL of siloxene and its origin was reinvigorated in the 1990s. Several researchers have drawn parallels between porous silicon and siloxene, stating that the entity responsible for luminescence in porous silicon is the same as in siloxene.[19–21,30,31] This assumption was based on the comparison of optical and structural properties of both materials, which were found to be similar. The Si_6-rings were defined as the structure characteristic for the PL in siloxene.[20] With semi-empirical quantum chemical calculations, Deák *et al.* proposed that the incorporation of oxygen into the 2D silicon network results in chemical quantum confinement, which is responsible for the PL behavior of siloxene.[32] Further experiments were performed to investigate the PL properties in more detail. According to PL excitation spectroscopy experiments, a green luminescence at 2.4 eV was observed, which was most effectively excited for photon energies slightly above the band gap energy (2.6 eV), indicating a direct band gap.[30,33] The PL originates in the electronic structure of siloxene: Optically detected magnetic resonance showed that excitonic processes are involved in the

luminescence mechanism of siloxene.[17,30,31,33–35] Upon recombination of a photogenerated exciton, light emission occurs. As evidenced by several studies, thermal annealing of siloxene samples results in a shift of the PL peak to lower energies and the complete disappearance of PL above temperatures of 400 °C.[17,30,36] According to Brandt *et al.*, the nonresonantly excited PL peaks at 1.8 eV (2.4 eV before annealing), indicating that the band gap is indirect after heating.[30] This phenomenon can be attributed to the structural deterioration that occurs at elevated temperatures.[17,30,36]

2.2 Silicane

The focus of this thesis is on *silicane*, which is described in this section. The nomenclature employed in the literature is not uniform, resulting in numerous terms that refer to the same material. Besides silicane, the terms layered polysilane, (hydride-terminated) silicon nanosheets, hydrogenated silicene, and silicon sheet polymers are used. The following overview provides an introduction to the structure, preparation, properties, and potential applications of this material. Before describing silicane, this section starts with two brief introductions to silicene and $CaSi_2$.

2.2.1 Excursus: Silicene

Graphene is the most prominent two-dimensional nanomaterial. It has been extensively investigated and is of great importance in material research.[37] The formal substitution of carbon in graphene by the heavier homolog silicon results in the so-called *silicene*. Graphene and silicene are members of the group of *Xenes*, which also include the germanium and tin analogs, namely *germanene* and *stanene*. The electronic properties of silicene are similar to graphene, which is why researchers are interested in this material as it promising for applications in modern nano-electronics. Numerous theoretical predictions have been made regarding the exceptional electronic properties of this silicon version of graphene. In the following, the structure and the preparation of silicene are briefly described.
Monolayer graphene can be mechanically exfoliated from graphite and consists of a planar layer of sp^2 hybridized carbon atoms arranged in a honeycomb network.[4] No such silicon analog exists in nature. The first theoretical study of hypothetical infinite 2D silicon layers in the aromatic state was reported by Takeda and Shiraishi in 1994.[38] The theoretical geometrical stability of this material was cal-

culated for two different symmetries: the flat graphene-like conformation, and the corrugated stage similar to the Si(111) plane. According to these calculations, the aromatic stages are more stable in a regularly corrugated structure. Ab initio calculations later confirmed that the slightly buckled honeycomb structure has the lowest energy.[39] This deformation compared to the graphene structure, indicates that the hybridization of silicon differs from the sp^2 hybridization of carbon in graphene. This is in agreement with scanning tunneling microscopy experiments confirming a mixed sp^2/sp^3 hybridization of silicene on an Ag(111) substrate.[40] In contrast to carbon, silicon double bonds are not favorable because of the less effective overlap of the 3p orbitals, which corresponds to the larger atomic radius of silicon. The difference between the planar graphene and the buckled silicene structure is shown in Figure 2.1.

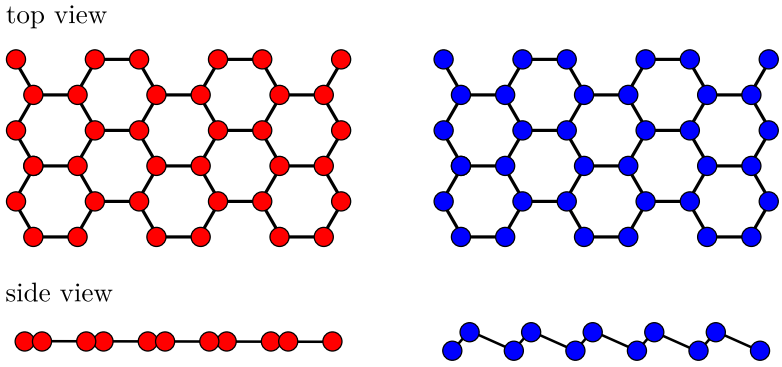

Figure 2.1: Comparison of graphene (red) and silicene (blue) structures.

Silicene structures are not naturally abundant and thus, silicene is prepared in bottom-up approaches on substrates. Bottom-up manufacturing means that single atoms are assembled to form the nanostructure. In the case of silicene, this is done by epitaxial growth on a substrate under ultra-high vacuum. Silicon epitaxy growth is mainly achieved by the thermal evaporation and deposition through condensation on the substrate. Numerous metal surfaces such as Ag(111), Ag(110), Ir(111), Au(110), and Ru(0001) as well as non-metallic substrates like MoS_2, ZrC, ZrB_2, and graphite, are used as substrates. Details on the preparation methods can be found in the review articles in References 41, 42, and 43.
Silicene tends to degrade upon oxidation under ambient conditions.[44] Thus, characterization is hindered and applications in electronic devices are limited. To protect silicene against oxidation, attempts were made, in which silicene is encapsulated by a protective layer (graphene, hexagonal boron nitride, aluminium oxide).[45–47]

2.2.2 Excursus: Calcium Disilicide

$CaSi_2$ is the precursor of siloxene (see Chapter 2.1.1) and silicane (see Chapter 2.2.3), and thus a brief introduction to this material is provided here.

$CaSi_2$ belongs to the group of Zintl phases. These phases are intermetallic compounds in which alkali or alkaline earth metals with low electronegativity are combined with metals of the groups III to VI, which have an intermediate electronegativity. These compounds are characterized by a heteropolar binding character. The valence electrons of the less electronegative element are formally transferred to the element with the higher electronegativity, thus yielding compounds with formal charges. The (8–N) rule determines the structure of the Zintl anions, which are (8–N)-fold coordinated. N represents the number of the valence electrons of the Zintl anions.[48]

$CaSi_2$ was first reported by Wöhler.[9] It is a gray lustrous solid with hexagonal crystals. Böhm and Hassel investigated the structure of this Zintl phase and identified a rhombohedral crystal structure.[49] The silicon atoms form buckled layers of interconnected Si_6-rings, while the layers are intercalated with calcium atoms. According to the Zintl concept described above, silicon is reduced to Si^- and is thus isoelectronic to gray arsenic, which consists of a corrugated layered structure. Thus, silicon is present as a polyanion with covalent Si-Si bonding. Two polymorphs of $CaSi_2$, which are stable in air and ambient pressure, are known (Figure 2.2): 6R-$CaSi_2$ and 3R-$CaSi_2$.[50,51] They differ in the stacking sequence. 6R-$CaSi_2$ has a unit cell of six layers (AABBCC calcium stacking sequence), while 3R-$CaSi_2$ has a unit cell of three layers (ABC calcium stacking sequence).

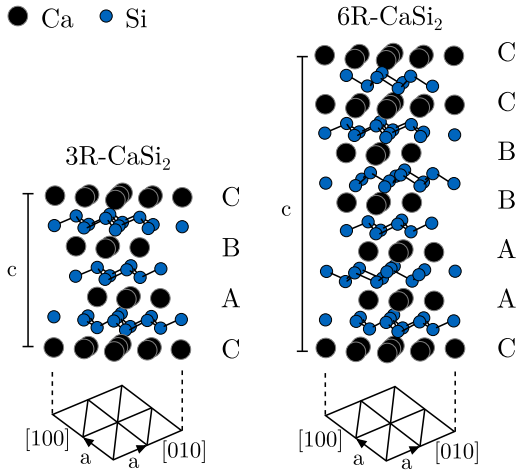

Figure 2.2: Crystal structure of the two trigonal rhombohedral modifications 3R-$CaSi_2$ and 6R-$CaSi_2$. Adapted from Reference 52.

$CaSi_2$ is usually prepared from the corresponding elements in an arc furnace, which results in 6R-$CaSi_2$.[53] 3R-$CaSi_2$ might arise as a side product in this reaction.[50] 6R-$CaSi_2$ can be quantitatively transformed into 3R-$CaSi_2$ by sintering in a hydrogen atmosphere at 30 bar and 200 to 700 °C.[54] Mixtures of both polymorphs were observed in epitaxial $CaSi_2$ films grown on Si(111) and Si(100) planes.[52]

2.2.3 Discovery, Preparation, and Structure of Silicane

Silicane corresponds to the formally hydrogenated version of silicene. The nomenclature is analogous to the hydrogenation of alkenes to alkanes. Through formal hydrogenation, the hybridization of silicon changes from the mixed sp^2/sp^3 in silicene to sp^3 in silicane.[55] As this is the the favored hybridization for silicon, the preparation of silicane is thus easier than that of silicene.[56]
In contrast to silicene, which is prepared in a bottom-up approach, silicane is prepared in a top-down approach. The term top-down refers to the breakdown of a bulk material into nanoscale structures. This procedure is almost identical to the formation of siloxene through the topotactic deintercalation of calcium from the precursor $CaSi_2$ (see Section 2.1.1). In the 1990s, Dahn and Yamanaka modified the siloxene synthesis protocol by applying low temperatures of 0 and −30 °C while treating $CaSi_2$ with concentrated hydrochloric acid (Scheme 2.3).[16,57] Contrary to the formation of siloxene, no hydrogen gas evolves in this low-temperature reactions. The product consists of yellow silicon nanosheets with a reduced oxygen content. The silicon atoms were described to be hydrogen-terminated above and below the layers, leading to the hypothesis that the chemical formula of the material was $[Si_6H_6]_n$.

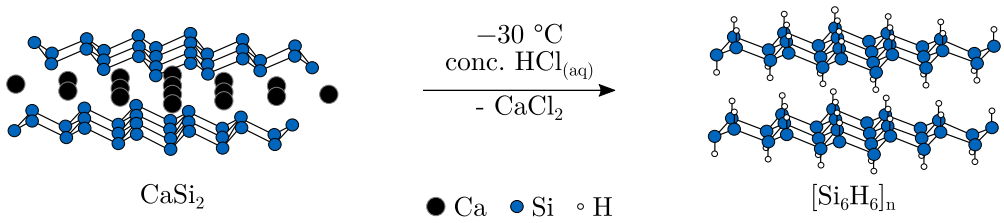

Scheme 2.3: Schematic illustration of the structure transition of $CaSi_2$ to the ideal structure of silicane $[Si_6H_6]_n$.

According to XRD data, silicane consists of turbostratically stacked buckled hexagonal layers with a similar in-plane lattice constant as $CaSi_2$, which confirms that the silicide structure of $CaSi_2$ is preserved and the reaction is topotactic.[16,57,58] However, the observed reaction is not optimal, as not only the $[Si_6H_6]_n$ phase was

identified. It was postulated that the formation of silicane is the primary reaction in the conversion of $CaSi_2$ with aqueous hydrochloric acid. However, impurities of SiO_x were also observed in many reports, which can be removed by hydrofluoric acid.[16,57,59] The occurrence of this oxidized by-product is attributed to the hydrolysis of silicane towards $Si(OH)_x$ features, which subsequently condensate towards SiO_x.[59] In addition, chemical analysis revealed the presence of chlorine impurities in a Cl/Si ratio of 1:6, which was attributed to the incorporation of HCl between the silicon layers.[57] Recently, the group of Panthani performed detailed structure analyses of silicane using XRD, spectroscopic (Raman, IR, and solid-state NMR spectroscopies), thermal, and microscopic techniques.[58,60] This study confirmed the presence of chlorine but proved that chlorine is covalently bond to silicon. The termination of the silicon atoms in the layers was quantified as 70 % Si_3Si-H, 20 % Si-Cl, and 10 % Si-OH.[60]

2.2.4 Excursus: Unconventional Deintercalation Reactions

The existing literature contains several other methods for the transformation of $CaSi_2$ towards silicane and siloxene derivatives, which differ from the standard method with concentrated hydrochloric acid described in Reference 57. In general, these reactions describe the oxidation of the silicide phase and removal of calcium from $CaSi_2$. A concise overview of these preparations is provided below.

Modified Calcium Disilicide Precursors

Nakano *et al.* prepared magnesium-doped $CaSi_2$, namely $CaSi_{1.85}Mg_{0.15}$, by melting calcium silicide (CaSi) with metallic silicon and magnesium followed by slow cooling to room temperature.[61] The magnesium-doping was applied in order to facilitate the deintercalation of calcium by weakening the interaction between the Zintl anion and calcium. The deintercalation of calcium was achieved after ten days in an aqueous solution of propylamine hydrochloride at room temperature under the evolution of hydrogen. Besides an insoluble black metallic solid, magnesium-doped oxygen-capped silicon nanosheets were obtained in this reaction.

Tchalala and coworkers developed the transformation of the amalgam $K_{2x}Ca_{1-x}Si_{2-x}$ with ethanolic propylamine hydrochloride, which they termed redox assisted chemical exfoliation of $CaSi_2$.[62] The amalgam was obtained by heating $CaSi_2$ with metallic potassium in vacuum to 160 °C. The characterization

of the green-brown deintercalation product did not include a comprehensive investigation of its composition. The authors only describe that the nanosheets almost exclusively contain silicon, as determined by X-ray photoelectron spectroscopy (XPS), and that they consist of stacked hexagonal layers.

Halogen-Terminated Silicon Nanosheets

Halogenated silicane represents a promising avenue for surface functionalization through the exchange of a halogen with an organic group, as known from organosilicon chemistry. Only publications from the 1950s and 1960s exist on the subject of chlorinated and brominated structures.
According to Schott, silicon nanosheets with bromine and hydrogen termination were prepared from $CaSi_2$ with hydrogen bromide in molten aluminium bromide.[63]
Later, Bonitz reported on the formation of chlorine-terminated silicon nanosheets by treating $CaSi_2$ with gaseous chlorine or phosphorus pentachloride in carbon tetrachloride.[64] In the initial stage of the reaction, he postulated the generation of active silicon, which subsequently underwent a reaction to yield chlorine-terminated nanosheets. Hengge also obtained chlorine-terminated nanosheets in the reaction between iodine monochloride and $CaSi_2$.[65] This product was formed in both the melt and carbon tetrachloride. Separation of the product from the calcium salt was not achieved, as the salt was not soluble in solvents that did not react with the chlorinated silicon nanosheets.

Reactions in Alcoholic Solutions

Although numerous publications propose that water is necessary for the deintercalation of calcium, some reports on water-free reactions exist.
Schott reported on the successful conversion of $CaSi_2$ with ethanolic hydrogen chloride in 1957.[66] He investigated the reaction at several temperatures in the range of 0 to 75 °C. At temperatures below 20 °C, under exclusion of moisture, air, and in the dark, siloxene derivatives were formed, which are terminated with hydrogen, chlorine, or ethoxy groups with an averaged chemical formula of $Si_6H_3Cl_2(OC_2H_5)$. Similarly, Weiss *et al.* prepared alkoxy-derivatives of siloxene ($Si_6H_3(OCH_3)_3$ and $Si_6H_3(OC_2H_5)_3$) in 1979.[15] Further alkoxy-modified structures of the formula $[Si_6H_5(OR)]_n$ were demonstrated by Sugiyama with 1-butanol, 1-dodecanol, benzyl alcohol, and methyl glycolate.[67]

In 2023 Liu and coworkers reported the successful preparation of silicon nanosheets from $CaSi_2$ with hydrogen chloride in anhydrous ethanol at 30 °C.[68] The obtained material was described as "silicene due to the expected minimal oxidation". There is some confusion regarding the term silicene in this publication. According to a reaction equation presented in the study, the authors refer to Si_6H_6 when using "silicene", which is actually hydride-terminated silicane. Nevertheless, the degree of oxidation, which was described as low, was not substantiated by structural analysis; rather, it was estimated from smooth surfaces in scanning electron microscopy (SEM) images.

Organically Modified Silicon Nanosheets

The most common route towards surface modified silicane is the surface functionalization of the hydride-terminated nanosheets (see Section 2.2.5). More recently, silicane derivatives with organic surface groups were directly prepared from $CaSi_2$ through nucleophilic substitutions in anhydrous systems.[69–71]
The group of Nakano described a simple synthesis of benzyl-functionalized silicane.[69] The topotactic reaction with benzyl bromide was performed without any solvent at high temperatures (150 °C) in a closed system. Nayad *et al.* slightly modified this procedure and also used *p*-fluorobenzyl bromide as substrate.[71] In another study, the authors utilized *p*-toluenesulfonyl chloride for the direct deintercalation of $CaSi_2$, which yielded in the formation of tosyl-modified silicane.[70]

2.2.5 Surface Functionalization of Silicane

The introduction of organic surface ligands into silicane facilitates the exfoliation of stacked sheets,[72] enhances the dispersibility in organic solvents,[73,74] and stabilizes the nanosheets against oxidation, hydrolysis,[75] and photodegradation.[76] In addition to that, the (opto)electronic properties of the nanomaterial might be affected.[69,75] These parameters are of relevance when considering the implementation of nanomaterials in applications. The Si-H bond is polarized as $Si^{\delta+}$-$H^{\delta-}$ due to the greater electronegativity of hydrogen compared to silicon. Consequently, nucleophilic attacks occur at the silicon atoms in silicane. Currently, surface modifications of silicane can be achieved by the formation of either Si-C or Si-N bonds. In the last 15 years, several functionalization methods have been developed, with our group contributing significantly to. Scheme 2.4 graphically summarizes the state-of-the-art silicane functionalization approaches.

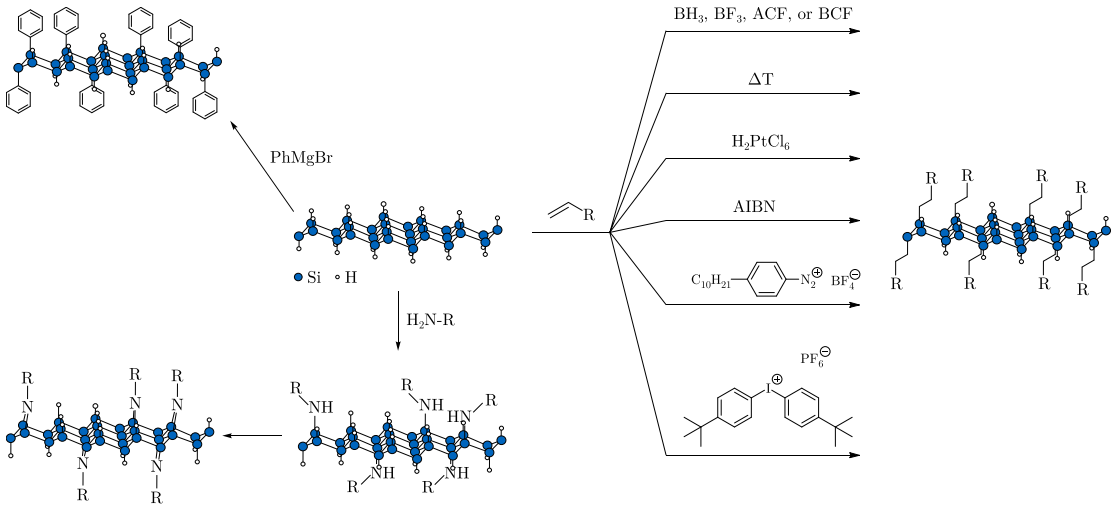

Scheme 2.4: Schematic overview of the state-of-the-art silicane functionalization reactions.

Functionalization via Si-C Bond Formation

The conversion of Si-H to Si-C bonds in silicane can occur in two different ways: reaction with a Grignard reagent or a hydrosilylation reaction. Sugiyama and coworkers used the reaction of silicane with phenylmagnesium bromide (PhMgBr) to synthesize phenyl-functionalized silicane.[75] This reaction is somewhat unexpected, as crystalline Si(111) surfaces are unable to directly react with Grignard reagents but must be chlorinated prior.[77] The success of the direct conversion with silicane demonstrated that Si-H surface in silicane is more reactive than in bulk Si(111). The obtained colorless $Si_6H_4Ph_2$ exhibited good solubility in a variety of organic solvents and showed stability towards oxidation and hydrolysis in an air atmosphere.[75] This is the only report of a Grignard-modification of silicane in the literature. All other reports on the functionalization through Si-H bond formation involve hydrosilylation reactions.

Hydrosilylation, in general, describes the addition of Si-H bonds across unsaturated bonds, e.g. C=C or C≡C bonds. On silicon surfaces, the reaction can be conducted catalytically with transition metal complexes, induced thermally, or initiated radically.[78] The first hydrosilylation with silicane was published by Nakano *et al.*[79] The platinum-catalyzed hydrosilylation of 1-hexene resulted in hexyl-modified silicane which showed minimal oxidation. Chloroplatinic acid hexahydrate was used as the catalyst in this study.
The utilization of transition metal complexes is disadvantageous, as the remaining metal enhances surface oxidation.[80] Furthermore, the presence of transition

metal impurities in the functionalized silicane may result in the quenching of the PL of the material.[81] Thus, other types of hydrosilylation reactions have been developed by our group in recent years. Helbich *et al.* showed that a number of induction principles are effective for the reaction between unsaturated compounds and silicane.

Thermal-induced hydrosilylations of different unsaturated compounds (1-dodecene, 1-dodecyne, undeceneoic acid, and 9-decen-1-ol) were achieved by heating silicene/alkene (or alkyne) mixtures to 130 °C.[73] In the same study, the diazonium salt 4-decylbenzene diazonium tetrafluoroborate was found to radically initiate the reaction with the same substrates as well as *tert*-butyl methacrylate (*t*BuMA), demonstrating its applicability towards a variety of unsaturated compounds. The comparison of the surface coverages obtained from the thermal and the diazonium salt-initiated reactions revealed that the thermal reactions resulted in a higher degree of functionalization with almost all substrates.

Later, Lyuleeva and Holzmüller performed a novel fast thermal hydrosilylation experiment.[82] Reactions between silicane and 1-dodecene, 2-ethinyl-3-hexylthiophene, or phenylacetylene were conducted at 180 °C in a microwave reactor. The reactions were complete after 2 h compared to overnight in the other thermal hydrosilylation.

A Lewis acid catalyzed hydrosilylation of silicane with various unsaturated compounds (1-decyne, trimethylvinylsilane, *t*BuMA, and ethyl-10-undecenoate) was achieved with borane, boron trifluoride, tris(pentafluorophenyl)borane (BCF), and tris(pentafluorophenyl)alane (ACF).[83]

Other investigations focused on the radical initiator azobisisobutyronitrile (AIBN).[76] Several unsaturated compounds, including 1-dodecene, 1-dodecyne, and the radically polymerizable monomers styrene, methyl methacrylate, and acrylic acid, were tested as substrates. Besides surface functionalization, the radical polymerization of the monomers took place. Thus, a nanocomposite of functionalized silicane embedded in a polymeric matrix was formed. This enabled the combination of the properties of both materials. The polymer matrix was found to stabilize silicane against decomposition due to basic conditions or irradiation. Optionally, the polymer was removed from the composite by washing it with a polymer-dissolving solvent, yielding the neat functionalized silicane.

Later, the radical initiators, which enable the hydrosilylation of silicane, were expanded by the group of diaryliodonium salts. Helbich *et al.* therefore employed

bis(4-*tert*-butylphenyl)iodonium hexafluorophosphate (BIP) as initiator.[84] The initiator was found to be effective in modifying silicane with 1-dodecene, 10-undecenoic acid, methyl 10-undecenoate, trimethylvinylsilane and 1-octyne. In addition to the surface functionalization, the authors discovered that the combination of BIP and hydride-terminated silicane initiates the ring opening polymerization of tetrahydrofuran. Consequently, a new nanocomposite was formed, namely silicane embedded in poly(tetrahydrofuran). Diaryliodonium salts previously been employed in polymerizations.[85,86] The UV-induced formation of a cationic aryliodonium radical, initiates cationic and radical polymerizations of various monomers. However, the investigation by Helbich *et al.* demonstrated that the decomposition of the diaryliodonium salt also occurs *via* a single electron transfer from silicane to the iodonium salt, thus enabling polymerization.[84] The investigation of silicane as a coinitiator in diaryliodonium salt-initiated radical and cationic polymerizations was subsequently continued and transferred to other monomers.[87]

Functionalization via Si-N Bond Formation

The modification of silicane with amines through the formation of Si-N bonds is another intensively investigated approach towards functionalized silicanes.[74,88,89] The first direct reaction between silicane and primary organoamines was performed with *n*-decylamine.[88] Under hydrogen evolution, a product was formed containing both single Si-NH-R and Si-NR-Si bonds. In further studies, the authors expanded the surface amination towards other aliphatic and aromatic amines (*n*-alkylamines, α,ω-diaminoalkanes, and ω-aminocarboxylic acids, as well as benzylamine and its derivatives).[74,89] α,ω-Diaminoalkanes were found to bind to two silicon nanosheets.

2.2.6 Properties of Silicane

Theoretically Predicted Properties

Many theoretical studies deal with silicanes with regard to their structural, electronic, and optical properties. In those studies, usually hydrogen is the default surface ligand, as it is experimentally obtained by the transformation of $CaSi_2$ with hydrogen chloride.

Regarding the structure, the three conformations, namely boat, chair, and zigzag,

are discussed. The chair conformation of Si_6H_6, resulting in alternating hydrogen-termination above and below the silicon plane, was calculated to be the energetically favored structure for silicane.[90] This structure corresponds to sp^3 bonding. Hydride-terminated silicane in the chair conformation is predicted to be an indirect semiconductor with a band gap,[91–93] that can be tuned by physical strain.[91,94,95] The band gap energy, depending on the applied computational method, is in the range of 2.2 to 4.0 eV.[90,92,93] The band gap decreases and becomes direct, when tensile strain is applied.[95–97] Furthermore, the size and stacking of silicane affect the properties:[98] An increase in the band gap energy was found when the layer thickness of silicane is reduced, which also leads to a blue shift of the optical absorption edge. Stacking of silicane sheets is favored in the ABC stacking sequence, which at the same time has the largest band gap due to strong interactions between adjacent layers. Changing this structure to the AA stacking sequence red shifts the optical absorption peaks.

It was predicted that the organic modification of silicane would have only a minor effect on the optical properties.[94,99] The attachment of organic groups has no significant influence on the Si-Si bonding orbitals, of which the band edges are comprised. Contrary, exchanging the hydrogen-termination with halogens results in a decrease of the band gap energy.[91,100] This is explained by the further withdrawal of electrons from the silicon network by the electronegative halides. Thus, the Si-Si bonding orbitals are modified and in consequence the band gap becomes smaller.

Photoluminescence and Optical Properties

Hydride-terminated silicane, their derivatives with organic surface groups as well as silicane/polymer composites all exhibit room temperature PL near 500 nm (2.5 eV).[58,73,76,83,84,87] The PL peak center is near the absorption onset, which is characteristic of a direct band gap behavior.[58] A PL quantum yield of 9 % was determined for hydride-terminated silicane.[58]

UV-visible (UV-vis) diffuse reflectance spectroscopy of hydride-terminated silicane provides information on the band gap energy. From the Tauc analysis of the Kubelka-Munk transformed diffuse reflectance spectrum a direct band gap of 2.53 eV was estimated.[58]

Nonlinear Optical Properties

The optical properties of a material system are modified by the presence of intense laser light. The resulting phenomena are studied in the field of nonlinear optics (NLO).[101] The term *nonlinear* refers to the response of the material to an optical field, where the response depends nonlinearly on the strength of the applied field. The polarization ($\vec{P}$) of a material system in an applied optical field is described as a power series expansion of the strength ($\vec{E}$) of the applied field:[101]

$$\vec{P} = \varepsilon_0 \chi^{(1)} \vec{E} + \varepsilon_0 \chi^{(2)} \vec{E}^2 + \varepsilon_0 \chi^{(3)} \vec{E}^3 + ... \tag{2.1}$$

where ε_0 is the permittivity of free space, $\chi^{(1)}$ is the linear susceptibility, and $\chi^{(2)}$ and $\chi^{(3)}$ are the second- and third-order nonlinear optical (NLO) susceptibilities, respectively. The presence of $\chi^{(n)}$ refers to as an n^{th}-order nonlinearity. In the literature on the NLO properties of silicane, the third-order nonlinear responses are of particular interest (see below). The real and imaginary parts of $\chi^{(3)}$ depend on the NLO parameters β (nonlinear absorption coefficient) and γ' (nonlinear refractive index parameter) which can be determined by Z-scan experiments.[102] In this technique, the normalized transmittance of a sample is monitored. The sample moves along the z-axis (propagation direction) of a focused laser beam, thereby undergoing varying laser intensities at different positions. Two different experimental configurations, the so-called open-aperture (OA) and closed-aperture (CA) Z-scans, can be employed. The nonlinear absorption coefficient can be determined from the OA measurement results, whereas the nonlinear refractive index parameter is determined by CA measurements. Processes that can be observed with Z-scan measurements include saturable/reverse saturable absorption (SA or RSA) and self-focusing/defocusing.[101] The phenomenon of SA describes the decrease in laser absorption with increasing light intensity. The opposite case, where the absorption increases with the excitation energy, is called RSA. Self-focusing and defocusing are the result of an intensity-dependent refractive index. The effect, in which the refractive index increases with the intensity of the electric field, is called self-focusing; in this case, the material acts as a positive lens when a beam of light propagates through the material. The reverse phenomenon is self-defocusing.

In recent years, hydride-terminated silicane and silicane with dodecyl surface groups have been subjected to extensive investigation with respect to their third-order NLO properties.[103–105] The group of Couris therefore used Z-scan

techniques at different laser excitation wavelengths and laser pulses (femtosecond, picosecond, and nanosecond regimes).

In the picosecond regime, the functionalized silicane exhibited SA under 532 nm and 1064 nm laser excitation.[103] In contrast, the NLO absorptive response of non-functionalized silicane was negligible. The NLO refractive response was found to be self-focusing for both materials. In comparison to the hydride-terminated material, the nonlinear refractive index parameter of the dodecyl-modified nanosheets exhibited a significantly increased value under both excitation wavelengths. This study provided the first evidence for the significant impact of surface functionalization on the third-order NLO properties of silicane. The authors postulated that surface functionalization represents a valuable approach for the tailoring of NLO responses in silicanes. Moreover, silicanes were found to exhibit comparable or even higher NLO responses than graphene, rendering them a promising candidate for applications in 2D-material-based optoelectronics and photonics.

A second study was conducted to investigate the ultrafast NLO response of these two silicanes under 800 nm excitation in the femtosecond regime.[104] Under these conditions, the hydride-terminated silicon nanosheets again exhibited a negligible absorption, whereas the dodecyl-modified material exhibited SA. Additionally, the NLO refraction was described as self-focusing for both silicanes. As in the previous study, the value of the nonlinear refractive index parameter of the dodecyl-modified silicane was found to be higher than that of the non-functionalized material, thereby confirming the importance of the surface functionalization of silicane on the NLO response. Additionally, the results demonstrated the superior NLO performance of silicanes when compared to a range of other 2D nanomaterials, including graphene, molybdenum chalcogenide nanosheets, and niobium disulfide nanosheets.

The third study on the transient NLO properties of hydride- and dodecyl-terminated silicane was performed under 532 nm and 1064 nm laser excitations, respectively, with laser pulses in the nanosecond regime.[105] Analogous observations were made regarding the nonlinear absorptions and refractions, as had been observed in the two preceding studies.

In all of these studies, the enhanced NLO absorption of silicane upon functionalization was attributed to the presence of point defects, which were presumed to be present in the functionalized silicane. According to this hypothesis, these point defects act as electron trap within the conduction band. Consequently,

the relaxation time of photoexcited electrons trapped in the conduction band is prolonged, preventing the absorption of incident photons due to the Pauli exclusion principle. This would explain the higher probability of absorption bleaching in the alkyl-modified silicane compared to the hydride-terminated one.

Thermal Stability

Hydride-terminated silicane, prepared analogously to the procedure by Dahn,[16] was reported to be thermally stable in an inert nitrogen atmosphere below 100 °C.[59] The thermal behavior of silicane washed with hydrofluoric acid was investigated by thermogravimetric analysis (TGA) coupled with mass spectrometry. Between temperatures of 100 to 160 °C dehydrogenation was observed, which derived from the dehydrocoupling of adjacent silicon sheets leading to cross-linkages. From 200 to 300 °C monosilane and low amounts of fluorosilane were detected besides hydrogen gas. This indicated the fragmentation of the silicane structure which transforms to amorphous hydrogenated silicon. From 300 to 450 °C further hydrogen and monosilane evaporated. In this temperature region, the Si-H bond is homolytically cleaved, which results in the formation of silicon dangling bonds. At temperatures above 450 °C crystalline silicon forms. Because of the structural change upon annealing, a red shift of the PL peak energy was observed at higher temperatures. This was explained by the growth of the silicon network by cross-linking and the formation of silicon dangling bonds, which provide non-radiative recombination pathways.

2.2.7 Applications of Silicanes

Numerous potential applications of silicanes have been described in the literature, including many theoretical studies. Some experimental studies have been realized which demonstrate proof of concept or prototype applications.
Kloberg *et al.* used silicane as a masking substrate for the preparation of surface anisotropic Janus silicon quantum dots.[106] Hydride-terminated silicon quantum dots were deposited on silicane by dehydrogenative coupling. Subsequent hydrosilylation with an alkene resulted in the functionalization of the exposed Si-H bonds of the silicon quantum dots and the silicane. Liberation and simultaneous functionalization of the quantum dots with a second alkene was achieved by UV irradiation. This technique was successfully employed to prepare amphiphilic Janus silicon quantum dots.

In addition to the already described role of silicane as coinitiator in the diaryliodonium salt induced polymerization (see Section 2.2.5), other catalytic applications have been established. Palladium nanoparticle-decorated silicane were shown to enable the reverse water–gas shift reaction in a catalytic cycle.[107]
The application of silicane in the formation of therapeutic hydrogen gas was tested by You *et al.*[108] In vitro and in vivo experiments were conducted to investigate the potential of hydride-terminated silicane in the hydrogen production from water. The results demonstrated that this approach was effective. Biosafe silicon oxide was formed as byproduct in these experiments.
In the field of optoelectronics, Li *et al.* demonstrated the implementation of silicane into a light-emitting diode with deep blue emission.[109] To date, no reports on other proof-of-concept electroluminescence devices based on silicane have been published in the literature.
A functional solution gated field-effect transistor with a film of dodecyl-functionalized silicane blended with poly(3-hexylthiophene-2,5-diyl) (P3HT) was fabricated by Helbich and coworkers.[83] The device showed an enhanced sensitivity and an increased transconductance in comparison to the device with neat P3HT. Another electrolyte-gated field-effect-transistor was presented by Lyuleeva and Holzmüller.[82] A blend film of hexylthiophene modified silicane with P3HT was used for the device fabrication. It was found that the organic surface groups enhanced the interaction between the functionalized silicon nanosheets and the polymer, leading to an overall increase in the transistor performance.
A growing interest is the use of silicane as anode material in lithium ion batteries. Silicanes with hydride- and hydroxyl-termination have been demonstrated to exhibit high capacity and stability when compared to pure silicon anodes, thus leading to good battery performance.[110,111] In the initial steps, silicane is converted to a suboxide-like amorphous structure, which allows for the efficient lithiation and delithiation during the discharge and charge processes. Further, silicane was used as a precursor in the preparation of a silicon-carbon composite anode.[112]

2.3 Photosensitivity of Hydride-Terminated Silicane and Siloxene

Siloxene and silicane were found to be photosensitive. Already in the first publication on siloxene by Wöhler,[9] he described that light induced a bleaching of the yellow color of siloxene. It turned white in water under the evolution of hy-

drogen when exposed to sunlight. Similarly, for silicane, the formation of a white product has been observed under UV irradiation, after which the material lost its characteristic PL.[76]

Parallels can be drawn with other silicon materials where similar phenomena have been observed. A prominent example is the so-called Staebler-Wronski effect in amorphous silicon:[113] Prolonged irradiation with light significantly decreases the photoconductivity and the dark conductivity of amorphous silicon, which is reversible by annealing. The exact mechanism of this phenomenon has not been elucidated yet, but many theories presume the generation of dangling bonds being responsible for this effect.[113–115] Also in porous silicon and in silicon quantum dots, exposure to light affects their properties, as photobleaching occurs during UV irradiation.[116–120] Many reports explain the faded PL in silicon materials by the formation of surface defects and/or dangling bonds created by UV irradiation,[117,118,120] which is often reported to be accompanied with hydrogen loss.[119,121] The presence of dangling bonds was experimentally confirmed by electron paramagnetic resonance spectroscopy.[114,121] These defects are assumed to act as nonradiative recombination centers, thus reducing the PL efficiency.[121] The formation of the dangling bonds must come from Si-Si or Si-H bond cleavage. For hydrogenated amorphous silicon, it has been proposed that the Si-Si bond is cleaved by UV light and subsequently hydrogen from a neighboring Si-H diffuses to the broken Si-Si bond and saturates it, forming a dangling bond at the former position of the hydrogen.[114] Some publications demonstrate that the PL is recovered by annealing, e.g., for porous silicon.[122] In dependence on the atmosphere in which silicon materials are illuminated, oxidation can takes place, which also quenches the PL.[119,123] The photooxidation of porous silicon was described by the oxidation of Si-Si bonds.[124,125] The mechanism was proposed to be induced by an energy transfer from excitons confined in silicon nanocrystallites to molecular oxygen.[126] Thus, highly chemically reactive singlet oxygen molecules are generated, which by the interaction with the hydrogenated silicon surface results in the photooxidation and the creation of nonradiative defects.

For siloxene, the PL fatigue under UV light was observed by several researchers.[127,128] As for other silicon materials (see above), dangling bond formation was assumed to cause the decreased PL efficiency.[20,21,127,129,130] This is similar to what was found during thermal annealing of siloxene. High temperatures lead to the creation of coordination defects that act as nonradiative

recombination centers quenching the PL.[20,31] Intense illumination and temperatures above 300 °C, lead to hydrogen effusion and an irreversible oxidation of siloxene by the insertion of oxygen atoms (from the hydroxyl groups) into the silicon planes as shown in Scheme 2.5.[20,21,129,130] The described studies further show that the siloxene photodegradation occurs with and without oxygen.

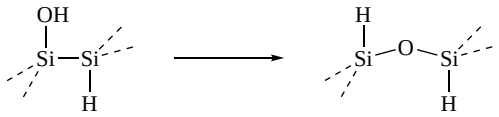

Scheme 2.5: Incorporation of the oxygen atom into the Si-Si bond.

Reports on the photodegradation of silicanes are scarce. The decrease in PL intensity was already observed in 1998.[59] More details on the degradation under UV light were provided by our group in 2016. Helbich *et al.* described the degradation of the yellow silicane to a white product.[76] The degradation mechanism was expected to occur *via* UV-induced homolytic Si-Si and Si-H bond cleavage, comparable to the photodegradation of molecular silanes. Embedding silicanes in a polymer matrix was shown to stabilize them from the photo-induced degradation to the white product. In addition to the study of our own group, no systematic investigation of the photodegradation of silicane is found in the literature.

2.4 Germanane and Mixed Hydride-Terminated Germanium/Silicon Nanosheets

Besides silicanes, their germanium analog and a mixed version of both are interesting nanomaterials. Both exhibit an isomorphic structure to silicane and are prepared by the topochemical reaction between concentrated hydrochloric acid and the layered Zintl phases calcium digermanide ($CaGe_2$) and the mixed phase $CaGe_{2-x}Si_x$, respectively, at low temperatures.

2.4.1 Germanane

The germanium analog of hydride-terminated silicane was first prepared in 2000 from epitaxially grown $CaGe_2$ films on crystalline Ge(111) substrates by the treatment with hydrochloric acid.[131] The structure of the slight reddish as-prepared *polygermyne* was determined to be isomorphic with hydride-terminated silicane. The novel nanomaterial was found to exhibit an intense PL in the near infrared

(NIR) region. 13 years later, the group of Goldberger reported on the low-temperature preparation of *germanane* with bulk $CaGe_2$ as precursor.[132] Germanane was described as gray crystals, which are relatively stable in air. It is thermally stable up to 75 °C and amorphization and dehydrogenation occur at higher temperatures. The experimentally determined band gap is 1.59 eV, which according to theoretical predictions is expected to be a direct band gap. XRD data confirmed the topochemical reaction, and electron microscopy showed sheet structures. Additional spectroscopic analysis confirmed the hydrogen-termination of germanane.

Besides the top-down approach with hydrogen chloride towards hydride-terminated germanane, some topotactic reactions towards organically modified germananes are reported in the literature. By the direct conversion of $CaGe_2$ with organohalides,[133–135] in water or water/acetonitrile mixtures methyl-, propenyl-, and methoxymethyl-terminated germanane were prepared. Changing the organic surface group resulted in a modified band gap energy. The found general trend was: Ligands that are more electron withdrawing and have greater steric hindrance tend to lower the band gap.[135] This approach towards functionalized germananes was further expanded by the reaction of $CaGe_2$ with aryl halides.[136] In a different study,[137] iodine-terminated germanane was prepared in the first step by reacting $CaGe_2$ with iodine monochloride. In the next step, a nucleophilic substitution with 4-fluorophenylmagnesium bromide reagent yielded blue fluorescent aryl-functionalized germanane.

Germanane can be functionalized through Ge-H bond activation in hydrogermylation reactions similar to the hydrosilylation of silicane. Yu *et al.* demonstrated the successful dodecyl-functionalization of germanane by the hydrogermylation of 1-dodecene.[138] The reaction was either thermally induced (190 °C) or radically initiated with AIBN. It was found that the AIBN-induced reaction lead to monolayer coverage while the thermal reaction yielded surface oligomerization. Another functionalization towards Ge-C bonds, was conducted by the reaction of germanane with *n*-butyllithium.[139] In this reaction, lithium hydride was formed as a side product.
In addition to the functionalization through Ge-C bond formation, an alternative surface modification of germanane by the formation of a Ge-Si bond was shown.[140] This was done by the thermally induced dehydrogenative coupling of silanes, namely silicon quantum dots and organosilanes.

Recently, Ni *et al.* described the metal nanoparticle-decoration of germanane by mixing the nanosheets with aqueous solutions of metal salts (silver nitrate as well as gold, silver, copper, palladium, or platinum chloride, respectively).[141] The metal ions were reduced to metal nanoparticles and deposited onto the germanane surfaces under the evolution of hydrogen. As-prepared metal nanoparticle-decorated germanane was successfully tested as photocatalysts for the selective visible light-induced oxidation of benzyl alcohol. This work was continued and high-entropy alloy (HEA) nanoparticle-decorated germananes were prepared from aqueous solutions with mixed metal salts.[142] As-prepared HEA nanoparticles were liberated from the nanosheets by UV irradiation of an aqueous solution. The UV light induces the degradation of the germanium nanosheets into a soluble product and liberates the metal nanoparticles. HEA nanoparticle-decorated germanane was also used as precursor for high-entropy germanides, which were prepared by thermal annealing of the decorated germananes.[143]

Similar to silicane, (potential) applications of germanane are mainly in the field of (opto)electronics. For example, implementations of germanane into a transistor,[144] an electrode in a lithium-ion battery,[145] or a photodetector[146] were realized. Besides these applications, germananes were tested as photoelectrocatalysts in the hydrogen evolution reaction,[147] or in photo-triggered therapeutics and photoacoustic diagnostic imaging.[148]

2.4.2 Hydride-Terminated Mixed Germanium/Silicon Nanosheets

Similar to germanane, mixed germanium/silicon nanosheets were first prepared from epitaxially grown Zintl phase films on substrates in 2001.[149,150] In 2020, so-called *gersiloxenes* were published.[151] $Ca(Ge_{1-x}Si_x)_2$ was reacted with hydrochloric acid at −30 °C. XRD patterns were similar to germanane and siloxene, and phase separation was excluded. According to the structural analysis germanium atoms in the mixed sheets were hydride-terminated, while silicon atoms were terminated with hydrogen or hydroxyl groups depending on the silicon content in the nanosheets. With increasing silicon content the amount of hydroxyl groups increases too. UV-vis diffuse reflectance data showed that the gersiloxenes absorb light in a wide range. With increasing silicon content (decreasing germanium content), the absorption edge shifts to short wavelengths. Accordingly, the powdery gersiloxenes also differ in their colors: with high silicon content they are yellow and become brown for medium to low silicon contents and are finally dark gray for

pure germanane (see Figure 2.3). Experimental band gaps of the semiconductor materials were estimated by the Tauc analysis and were found to be in the range of 1.8 to 2.6 eV, whereas the band gap energy increases with higher silicon contents. Photocatalytic tests showed, that gersiloxenes are applicable in the photocatalytic hydrogen evolution as well as in the photocatalytic carbon dioxide reduction.

Figure 2.3: Photographs of germanane, gersiloxene with Ge/Si = 1:1, and silicane (from left to right).

As hydride-terminated mixed germanium/silicon nanosheets have only been discovered recently, not many reports on this topic exist. For example, no literature on the surface functionalization of this material can be found. However investigation of their applications has already started. In a study the same material that was previously called gersiloxene was called *siligane* and its successful implementation as anode material in lithium ion batteries was demonstrated.[152] More recently, these materials were employed as active layer in photodetectors.[153]

3

A Pathway to Oxygen-Free Hydride-Terminated Silicon Nanosheets

Hydride-terminated silicon nanosheets ($[Si_6H_6]_n$, SiNS-H) are a promising material for (opto)electronic applications, e.g. in photodetectors,[154] lithium-ion battery anodes,[111] or silicon-based field-effect transistors.[82] The state-of-the-art preparation method of this nanomaterial is the topotactic deintercalation of Ca^{2+} cations from the Zintl phase $CaSi_2$ with hydrochloric acid ($HCl_{(aq)}$). Structure analysis of as-prepared SiNS-H reveals that the material not only consists of a hydride-terminated silicon network. Vibrational spectroscopy indicates the presence of Si-OH and Si-O-Si features, thereby confirming that the nanosheets are partially oxidized. Due to this oxidation, subsequent etching with hazardous hydrofluoric acid ($HF_{(aq)}$) is needed. This etching process removes silanol groups and silicon oxides. However, this treatment is not able to quantitatively remove all oxygen from the SiNS-H, which thus remain imperfect. In general, the oxidation of SiNS-H is undesired because it complicates structure determination and hinders exfoliation of the nanosheets. Perfect SiNS-H are weakly interconnected by van der Waals forces, whereas the partially oxidized material is preferentially stacked by hydrogen bonds. This also makes the surface functionalization of the nanosheets difficult, since not all sheets are equally accessible for a reaction. In addition, the functionalization chemistry of SiNS-H is ambiguous due to lack of

knowledge of the exact structure when it is oxidized.
The objective of the project described in this chapter is to find a new way to prepare oxygen-free SiNS-H. Ideally, all silicon atoms are built into interconnected Si_6-rings that form the 2D network, and each silicon atom should be exclusively hydride-terminated. In addition to a perfect structure, this would also avoid etching with hazardous HF.
In the following, the structure of SiNS-H synthesized *via* the literature preparation method is first described. The origin of the oxidation during this process is determined and approaches to overcome this drawback of the state-of-the-art method are investigated. This includes several experiments in anhydrous reaction systems, as water is assumed to cause the oxidation by hydrolysis of SiNS-H.

3.1 State-of-the-Art Preparation of Hydride-Terminated Silicon Nanosheets

SiNS-H are currently prepared in a top-down approach using a wet-chemical method that was described by Yamanaka *et al.*[57] According to this recipe, the gray Zintl phase $CaSi_2$ is topochemically transformed into yellow SiNS-H with concentrated $HCl_{(aq)}$ under the formation of calcium chloride ($CaCl_2$) as shown in Scheme 3.1. The reaction is performed at −30 °C under an argon atmosphere. After five days, yellow SiNS-H form, which are separated from the liquid, washed with acetone to remove $CaCl_2$ and $HCl_{(aq)}$, and dried under vacuum at elevated temperatures.

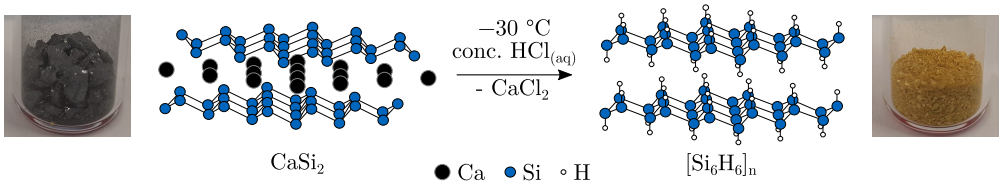

Scheme 3.1: Schematic illustration of the structure transition of $CaSi_2$ to SiNS-H and photographs of the reactants.

Fourier-transform infrared spectroscopy (FTIR) spectroscopy reveals a disadvantage of this method: The obtained product does not have the ideal structure shown in Scheme 3.1. Perfect SiNS-H would exclusively contain interconnected Si_6-rings terminated with hydrogen atoms above and below the layers. For this ideal structure, IR bands of Si-Si and Si-H vibrations should be the only ones present in the FTIR spectrum. However, spectra of SiNS-H prepared according

to the literature procedure, show a discrepancy to the expected spectrum. FTIR measurements in the range from 700 to 4000 cm^{-1} reveal additional modes as shown in Figure 3.1 and Table 3.1.

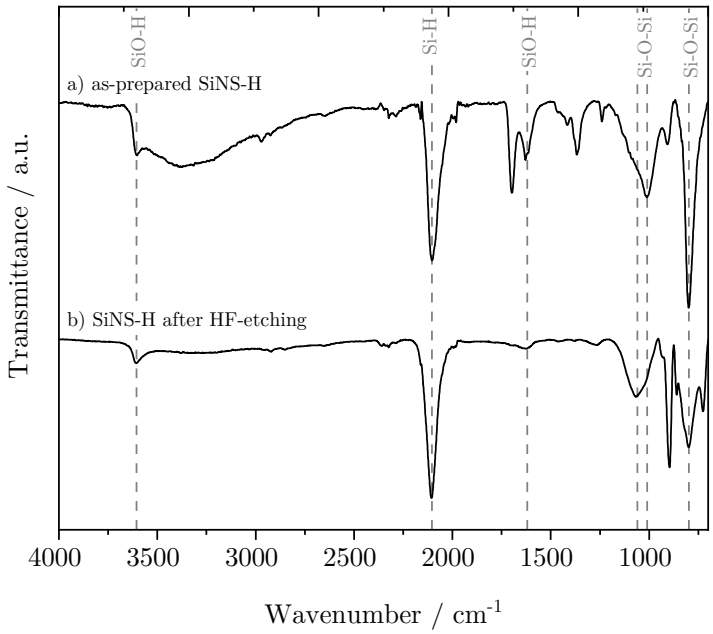

Figure 3.1: FTIR spectra of a) as-prepared and b) HF-etched SiNS-H.

Table 3.1: Assignment of IR modes observed in as-prepared and HF-etched SiNS-H. The annotations behind the experimental wavenumbers $\tilde{\nu}$ indicate whether a mode is found in the spectrum of as-prepared (A) or HF-etched SiNS-H (E).

Experimental $\tilde{\nu}$	Literature $\tilde{\nu}$	Band assignment
3606 $cm^{-1(A,\,E)}$	3600 cm^{-1} [155]	SiO-H stretch (isolated -OH groups)
3000 to 3580 $cm^{-1(A)}$	3400 cm^{-1} [156]	SiO-H stretch (H-bonds) / H_2O
2104 $cm^{-1(A,\,E)}$	2108 cm^{-1} [58]	Si_3Si-H stretch
1629 $cm^{-1(A)}$	1620 cm^{-1} [21]	O-H bend (SiO-H / H_2O)
1067 $cm^{-1(A,\,E)}$	1065 cm^{-1} [155]	Si-O-Si asymmetric stretch
1011 $cm^{-1(A,\,E)}$	1015 cm^{-1} [155]	Si-O-Si asymmetric stretch
906 $cm^{-1(A)}$	910 cm^{-1} [124]	Si-H_2 deformation
897 $cm^{-1(E)}$	895 cm^{-1} [23]	Si-H_2 bending
860 $cm^{-1(E)}$	850 cm^{-1} [17]	Si-H_2 scissor
799 $cm^{-1(A,\,E)}$	809 cm^{-1} [157]	Si-O-Si symmetric stretch
726 $cm^{-1(E)}$	706 cm^{-1} [21]	O-Si-O bend

Besides the expected Si-H stretching at approximately 2100 cm^{-1}, bands indicating partial oxidation of the nanosheets are present in the FTIR spectrum in

Figure 3.1. These vibrational modes correspond to SiO-H stretching and bending vibrations of either isolated or in hydrogen bonding involved hydroxyl groups, Si-O-Si stretching vibrations, or O-Si-O bending vibrations (see Table 3.1), respectively. Literature spectra of similarly prepared SiNS-H, resemble the spectra presented in this work and are mostly characterized by an intense Si-O-Si mode in the range from 1027 to 1100 cm^{-1} besides the Si-H peak at 2100 cm^{-1}.[57,58,76] It is therefore assumed that either oxygen inserts into Si-Si bonds in the planes or that the formation of oxygen bridges by hydrolysis of either $CaSi_2$ or ≡Si-H and subsequent condensation of two Si-OH groups occurs according to Scheme 3.2. However, there is no evidence for this type of oxygen-interconnections. The presence of Si-O-Si bonds in the 2D network of SiNS-H is unlikely, as no O_xSi-H stretching vibrations are observed, which would occur at 2200 and 2250 cm^{-1}.[21] This might be an evidence for an oxidized fraction besides the SiNS-H, which is in accordance with the reports of Yamanaka and He, who described glassy silicon oxides as impurities due to hydrolysis.[57,59] It is important to note that the relatively intense FTIR bands of the oxygen-containing species cannot be compared quantitatively with the Si-H bonds.[58]

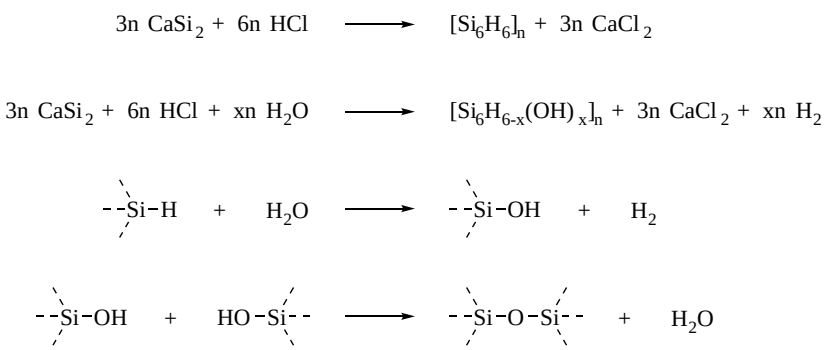

Scheme 3.2: Ideal reaction to SiNS-H and side reactions during the exposure of $CaSi_2$ to $HCl_{(aq)}$.

The observed oxidation must already take place during the preparation and not (or not only) during the FTIR measurement which is performed in ambient air. This is shown in Figure 3.2, which compares FTIR spectra of SiNS-H recorded in ambient air and inside an argon-filled glove box. Despite the poor resolution of the spectrum under argon, the oxidation bands of the measurement in air are also found in the measurement inside the glove box.

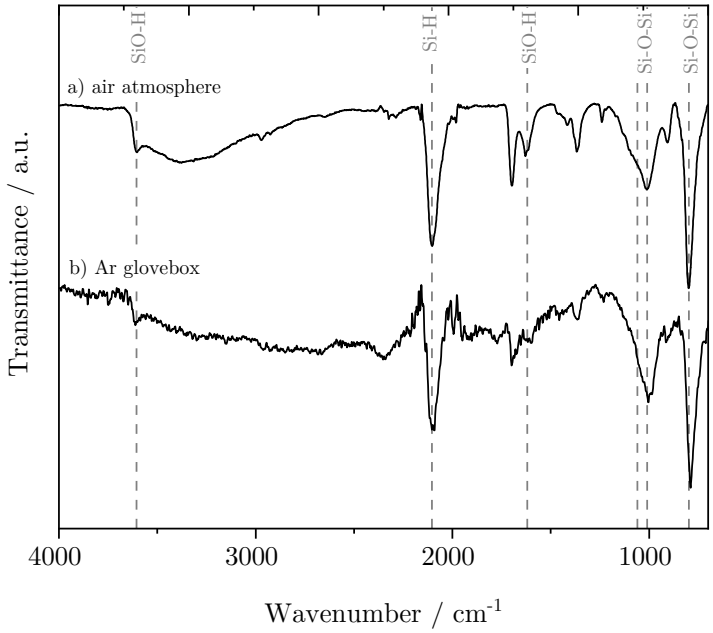

Figure 3.2: Comparison of FTIR spectra of as-prepared SiNS-H recorded a) in ambient air and b) inside an argon-filled glove box.

Although the material is inhomogeneous due to partial oxidation and thus imperfect, the nomenclature introduced earlier is still used for the as-prepared nanosheets SiNS-H. Due to the unfavorable oxidation of as-prepared SiNS-H, they are usually etched with $HF_{(aq)}$ to remove oxygen. Therefore, SiNS-H are suspended in an ethanol/water mixture and concentrated $HF_{(aq)}$ is added. The nanosheets are then extracted in an organic phase, centrifuged, washed and freeze-dried. This etching process reduces the intensity of oxidized IR bands, however it does not completely remove all oxidized species as shown in Figure 3.1 b). Following the etching process, the IR stretching modes of Si-H, SiO-H, and Si-O-Si remain. Nevertheless, the oxygen content is reduced. The intensities of the SiO-H (1629 cm^{-1}) and the Si-O-Si features decrease. The latter Si-O-Si asymmetric stretching peak shifts to a higher frequency (1011 cm^{-1}) compared to the non-etched SiNS-H. Prior to etching, the band is broad and appears to consist of two overlapping peaks at 1067 and 1011 cm^{-1}. This change indicates that HF-etching results in the partial removal of oxide species correlated with the 1011 cm^{-1} band, while the 1067 cm^{-1} band remains unaffected. Additionally, new bands appear at 897 cm^{-1} (Si-H_2 bending), 860 cm^{-1} (Si-H_2 scissor), and 726 cm^{-1} (O-Si-O bending). These spectral changes imply a structural change of the SiNS-H upon etching, but still do not show the ideal structure of the

nanosheets without oxygen. Thus, etching is either insufficient to obtain pure SiNS-H or, less likely, the etched SiNS-H oxidize rapidly under exposure to ambient air during the FTIR measurement.

3.2 Modification of the State-of-the-Art Preparation Method

To avoid the partial oxidation of SiNS-H during synthesis and avoid subsequent etching with hazardous $HF_{(aq)}$, an improved preparation pathway towards oxygen-free SiNS-H should be developed. Therefore, the origin of the partial oxidation of SiNS-H in the standard preparation pathway must first be evaluated. In the standard procedure, which is based on the method of Yamanaka *et al.*,[57] $CaSi_2$ reacts with concentrated $HCl_{(aq)}$ in an argon-filled Schlenk flask at −25 or −30 °C for five to seven days. After filtration of the product, it is washed with dry and degassed acetone in a Schlenk-frit and then dried under vacuum.[73,76,84] As described in the section above, the SiNS-H already partially oxidize during their preparation. So, the question of interest is to find the source of oxidation in this setup. To achieve this, the standard procedure is modified with respect to the three parameters, namely acid, reaction temperature, and atmosphere.

3.2.1 Influence of the Acid

As summarized in Table 3.2, different products of the reaction between $CaSi_2$ and $HCl_{(aq)}$ are known to be formed in dependence on the HCl concentration and reaction temperature.[16,57] With increasing temperature or by using a diluted acid, the oxygen content in the nanosheets increases. Thus, an approach to avoid oxidation reactions could be lowering the reaction temperature.

Table 3.2: Products of the reaction between $CaSi_2$ and $HCl_{(aq)}$ in dependence on the temperature and acid concentration. For each product, the atomic O/Si ratio is given. The data is adapted from Reference 57.

Reaction conditions	Product	O/Si ratio
conc. $HCl_{(aq)}$, −30 °C, 5 d	layered polysilane	0.16
conc. $HCl_{(aq)}$, 0 °C, 5 d	layered polysilane containing little oxygen	0.40
conc. $HCl_{(aq)}$, 30 °C, 6 h	Weiss siloxene	0.64
1 M $HCl_{(aq)}$, 30 °C, 6 h	Kautsky siloxene	1.29

In the standard procedure, concentrated $HCl_{(aq)}$ is used to convert $CaSi_2$ into

SiNS-H. This acid freezes at temperatures of about −35 °C, so the temperature range in which $HCl_{(aq)}$ can be used is limited.[158] Concentrated hydrobromic acid ($HBr_{(aq)}$) can be employed at lower temperatures than $HCl_{(aq)}$ because its melting point is about −63 °C.[159] These two aqueous solutions of hydrogen halides are not analog since they differ not only in their acidity constants ($pK_a(HCl) = -6.1$ and $pK_a(HBr) = -8.9$) but also in their redox potentials (HBr is a stronger reducing agent than HCl).[160] For this reason, it is necessary to check the applicability of concentrated $HBr_{(aq)}$ in the formation of SiNS-H under standard conditions, before using it at lower temperatures.
As a proof of concept, the reaction is conducted as usual at −25 °C, but instead of concentrated $HCl_{(aq)}$, concentrated $HBr_{(aq)}$ is used to test any affects on the reaction product. $HBr_{(aq)}$ seems to accelerate the reaction, as the starting material turns completely yellow after two days. With $HCl_{(aq)}$, however, the color change takes seven to nine days. Figure 3.3 a) and b) compares the FTIR spectra of the products obtained with $HCl_{(aq)}$ and with $HBr_{(aq)}$. Since both spectra are similar regarding the relevant SiNS-H bands, SiNS-H are formed regardless of the acid used. However, this comparison demonstrates that the bands at 1629 and 3606 cm^{-1}, which are assigned to SiO-H stretching and bending vibrations, are less intense when $HBr_{(aq)}$ is used instead of $HCl_{(aq)}$. On the other hand, the Si-O-Si vibration features at 800 and 1005 cm^{-1} are increased in comparison to the spectrum of the standard procedure. This evidence suggests that the condensation of silanols is favored in the presence of $HBr_{(aq)}$. A reduction in the pH value when using $HBr_{(aq)}$ may be a contributing factor.

3.2.2 Influence of the Temperature

The influence of the temperature on the product formation is evaluated by reacting $CaSi_2$ with $HBr_{(aq)}$ at −60 °C in a climate chamber. The FTIR spectra of the obtained product and the product of the standard procedure are compared in Figure 3.3 a) and c). Both spectra display the Si-H vibrational mode and oxidation features. As in the spectrum of the product from the reaction with $HBr_{(aq)}$ at −25 °C, the spectrum of the −60 °C sample displays the same differences to the standard method. Note, that an oxidation during the room temperature workup (filtration and acetone-wash) cannot be completely excluded, but should be negligible. With this result, it is concluded that temperatures lower than −25 °C do not prevent the nanosheets from oxidation.

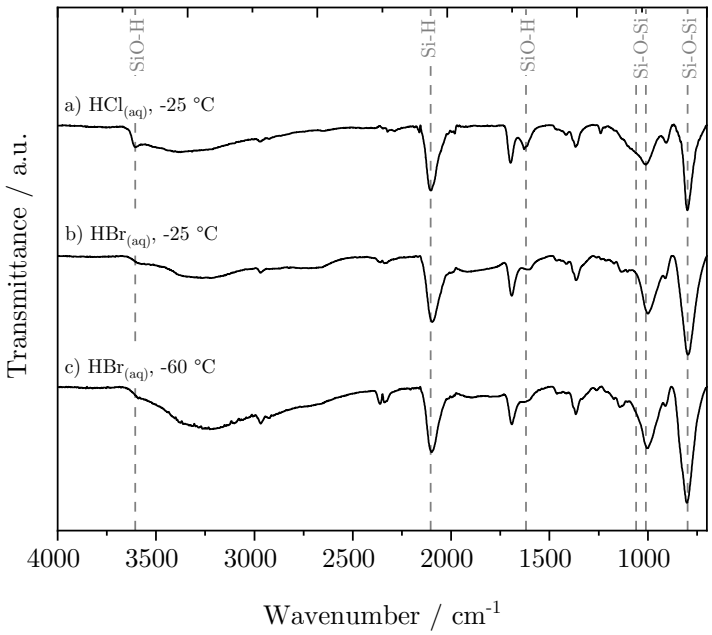

Figure 3.3: Comparison of SiNS-H prepared at −25 °C with a) concentrated $HCl_{(aq)}$ and b) concentrated $HBr_{(aq)}$ as well as c) at −60 °C with concentrated $HBr_{(aq)}$.

3.2.3 Influence of the Atmosphere

Since the reaction temperature does not affect the FTIR spectrum of SiNS-H, the influence of the atmosphere is studied. For comparison, the standard method is modified by performing the reaction in ambient air with commercially available concentrated $HCl_{(aq)}$ and under argon atmosphere with freshly prepared $HCl_{(aq)}$ by saturating degassed water with hydrogen chloride. The FTIR spectra of the yellow products obtained in these reactions are compared with the spectra of the SiNS-H prepared by the standard method in Figure 3.4.

According to these spectra, the oxidation bands do not significantly differ, which leads to the conclusion that the oxidation of SiNS-H is relatively independent of the reaction atmosphere. It is not gaseous molecular oxygen from the atmosphere that causes the partial oxidation of SiNS-H, as oxidation bands appeared in the FTIR spectra of samples prepared with and without air atmosphere. It can be reasonably deduced that the oxygen source is located in the liquid phase, which is water. Water can cause partial hydrolysis of the nanosheets as shown in Scheme 3.2. This hydrolysis is well known from siloxene preparation in which the 2D silicon sheets are terminated with -OH or -H.[16] According to Dorn *et al.*, who confirmed the presence of chlorine-terminated silicon sites,[60] an addi-

tional hydrolysis of ≡Si-Cl towards ≡Si-OH is possible. Consequently, Si-O-Si interconnected silicon sheets or glassy silicon oxides can be formed due to the condensation of ≡Si-OH groups.[15,16,57,59] Though these hydrolysis reactions are reported to take place only at temperatures above 0 °C, hydrolysis is still observed in the reactions at −25 °C.

The results of this series of experiments demonstrate that the presence of oxygen-containing air during the transformation of $CaSi_2$ with $HCl_{(aq)}$ does not significantly affect the structure of SiNS-H. Therefore, water is the source that oxidizes the nanosheets.

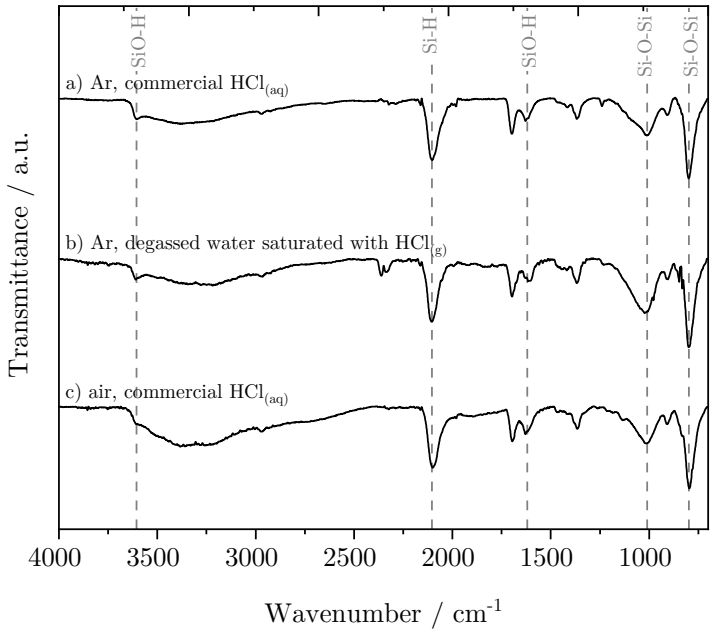

Figure 3.4: Comparison of SiNS-H prepared with a) concentrated $HCl_{(aq)}$ in argon atmosphere, b) air atmosphere, and c) with degassed water saturated with hydrogen chloride in argon atmosphere.

3.3 Solvent Effects on the Formation of Hydride-Terminated Silicon Nanosheets

After having found that water hydrolyzes SiNS-H, attempts are made to find alternative anhydrous reaction systems for the SiNS-H preparation and to investigate the role of water in the reaction. The following section describes these approaches and the corresponding results.

3.3.1 Experiments in Anhydrous Solvents

To prepare SiNS-H from $CaSi_2$, a series of experiments is conducted in which different combinations of solvents, hydrogen sources, Ca^{2+} solvation principles, and reaction temperatures are tested. The results of theses experiments are presented below.

Reactions with Hhydrogen Chloride

A similar procedure to that described above is employed to investigate the transformation of $CaSi_2$, but with organic solvents in place of water. Therefore, dry and degassed solvents are saturated with gaseous hydrogen chloride (HCl) as hydrogen source. The applied temperatures are chosen in dependence on the melting point of the solvent and are either −25 °C or −32 °C (freezer), 1 °C (refrigerator), or room temperature. The duration of the experiments is at least seven days or longer. Table 3.3 summarizes the experiments whose success is evaluated by the color and FTIR spectroscopy. The transformation into SiNS-H is only likely when the gray starting material $CaSi_2$ turns yellow.

For the first experiments (Table 3.3, entries 1 and 2), anhydrous and degassed ethanol and *N,N'*-dimethylpropyleneurea (DMPU) are used as solvents. The byproduct $CaCl_2$ is well soluble in these polar solvents. The experiment in ethanol takes place at −25 °C, and the one in DMPU is carried out at −32 and 1 °C. In these two experiments, no color change of the $CaSi_2$ from gray to yellow was observed. This indicates that no SiNS-H are formed, which is further confirmed by FTIR spectroscopy.

$CaCl_2$ has limited solubility in many organic solvents. Thus, agents which either increase its solubility or chelate the Ca^{2+} cations are employed. Tetrabutylammonium chloride (TBAC) is used in an experiment with propylene carbonate (PC) saturated with hydrogen chloride to increase the solubility of $CaCl_2$ (Table 3.3, entry 3). In the presence of TBAC, $CaCl_2$ is known to be more soluble in PC, in which it is only poorly soluble without the ammonium chloride.[161] As Ca^{2+} chelation agents, 18-crown-6 (18C6), 15-crown-5 (15C5), 4,7,13,16,21-pentaoxa-1,10-diazabicyclo[8.8.5]tricosane (Kryptofix 221), and 1,2-bis(*o*-aminophenoxy)ethane-*N,N,N',N'*-tetraacetic acid (BAPTA) are employed (Table 3.3, entries 4 to 12). These chelators are shown in Scheme 3.3. According to the hole-size cation-diameter relationship, the crown ether 15C5 (1.7 to 2.2 Å cav-

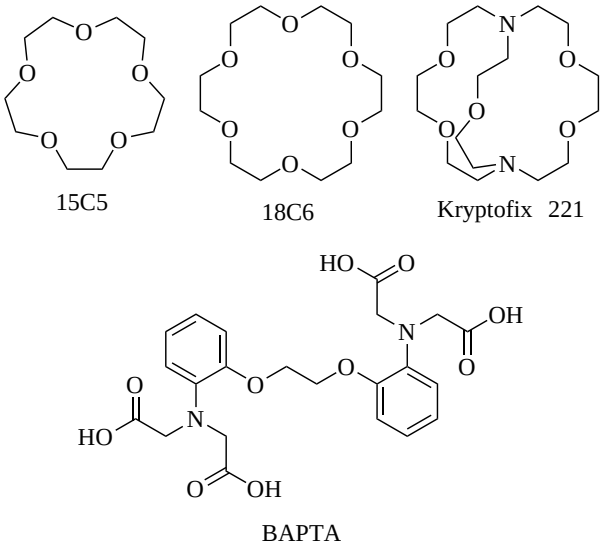

Scheme 3.3: Chemical structures of the applied chelating agents 15C5, 18C6, Kryptofix 221, and BAPTA.

ity size) shows the higher affinity for Ca^{2+} cations (1.98 Å cation radius) compared to 18C6 (2.6 to 3.2 Å hole diameter).[162] On the other hand, Gokel and coworkers observed stronger Ca^{2+} binding with 18C6 than with 15C5 in anhydrous methanol.[163] For this reason, both crown ethers are tested in the deintercalation of $CaSi_2$. These experiments are conducted in tetrahydrofuran (THF), diethyl ether (Et_2O), 1,4-dioxane, PC, and acetonitrile (MeCN). As an alternative to these, the cryptand Kryptofix 221 in PC is also tested, which is described to form a stable Ca^{2+} complex in PC.[164] The final chelating agent under investigation in potential anhydrous SiNS-H syntheses is BAPTA. It is a derivative of ethylenediaminetetraacetic acid (EDTA) that specifically binds Ca^{2+} cations and is soluble in some organic solvents like THF.[165]

For these chelating agents, the low pH value of the HCl-saturated solvents can be problematic. Protonation of the oxygen or nitrogen atoms probably interferes with the Ca^{2+} complexation. For BAPTA, instead of using the tetrasodium salt, the neutral form is used, because protonation in presence of HCl would take place anyway. Nevertheless, attempts are still being made to transform $CaSi_2$ in the described reaction systems. The solvents are selected based on the solubilities of the chelating agents. Solvents with different dielectric constants are employed (Table 3.3), ranging from 2.2 for 1,4-dioxane to 65 for PC (cf. the dielectric constant of water is 79).[166,167] Higher dielectric constants should favor the solvation

of Ca^{2+}. In none of these approaches the gray starting material $CaSi_2$ turns yellow, nor do the FTIR spectra show any characteristic bands of SiNS-H. It can be concluded that no topochemical transformation of $CaSi_2$ is possible under these conditions.

Table 3.3: Reaction conditions of non-aqueous experiments with HCl, showing the employed solvent and corresponding dielectric constant ε, the method of Ca^{2+} solvation, and the temperature.

	Solvent	ε	Ca^{2+} solvation	T / °C
1	EtOH	25 [167]	$CaCl_2$ soluble	−25
2	DMPU	36 [168]	$CaCl_2$ soluble	−32 and 1
3	PC	65 [166]	TBAC enhances $CaCl_2$ solubility	−25
4	THF	7.6 [167]	18C6 chelation	−25
5	Et_2O	4.3 [167]	18C6 chelation	1
6	THF	7.6 [167]	15C5 chelation	−25
7	Et_2O	4.3 [167]	15C5 chelation	−25
8	1,4-dioxane	2.2 [166]	15C5 chelation	−25
9	PC	65 [166]	15C5 chelation	−25
10	MeCN	38 [167]	15C5 chelation	−25
11	PC	65 [166]	Kryptofix 221 chelation	−25
12	THF	7.6 [167]	BAPTA chelation	−25

Reactions with Methanesulfonic and Triflic acid

As an alternative to HCl, methanesulfonic acid (MsOH) and triflic acid (TfOH) are evaluated as hydrogen sources for the conversion of $CaSi_2$ to SiNS-H. These acids are more acidic than HCl and in case of a successful deintercalation of Ca^{2+} cations, the calcium salts $Ca(H_3CSO_3)_2$ and $Ca(F_3CSO_3)_2$ are formed. These are soluble in the acids themselves, but also in dimethyl sulfoxide (DMSO). Both acids are tested in the SiNS-H preparation, once without solvent and once in DMSO. The experiments are performed at room temperature, except for the experiment with neat TfOH, which is performed at −32 °C.
Similar to the experiment series with HCl, these approaches are without success. No color change is observed, and consequently, no SiNS-H formed.

Reactions in the Ionic Liquid EMIM OTf

So far, no attempt to prepare SiNS-H from $CaSi_2$ with organic solvents succeeded. Another option for anhydrous reaction systems is the application of ionic liquids.

A combination of a Brønsted acid and ionic liquid is chosen for further experiments. Therefore, TfOH and trifluoroacetic acid (TFA) are combined with the ionic liquid 1-ethyl-3-methylimidazolium triflate (EMIM OTf) (see Scheme 3.4), respectively. As the solubility of Ca^{2+} cations in this ionic liquid is relatively low,[169] experiments are not only performed with $CaSi_2$ in EMIM OTf with both acids but also with additional BAPTA or 15C5 to chelate the Ca^{2+} cation, respectively. The experiments are performed at room temperature and 1 °C. Again, $CaSi_2$ remains gray in this series of experiments and no SiNS-H are formed.

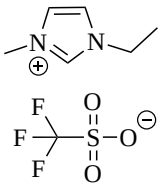

Scheme 3.4: Chemical structure of the ionic liquid EMIM OTf.

In conclusion, a variety of solvents, hydrogen sources, and Ca^{2+} solvation principles was employed in attempts to topochemically convert $CaSi_2$ to SiNS-H. In all described experiments, no conversion took place at all, $CaSi_2$ remained gray and did not change its color nor did the FTIR spectrum change. These results raise the question of whether water is required for the SiNS-H formation. This assumption is supported by several reports on the transformation of the Zintl phases $CaSi_2$ or $CaGe_2$ into silicane, siloxene, or germanane derivatives. Weiss, for example, has reported that no reaction of $CaSi_2$ is observed in anhydrous acids.[15] Gallo has stated that siloxene formation is only possible because water allows the topochemical deintercalation of Ca^{2+} from $CaSi_2$.[170] For the germanium analog, Jiang has found that water is essential for the topochemical reaction between $CaGe_2$ and iodomethane to methyl-terminated germanane in MeCN. Jiang has claimed that water is required to coordinate the Ca^{2+} cations and transport them from the Zintl phase into solution. Interestingly, he also tried replacing water with EDTA or 18C6, but $CaGe_2$ still showed no reaction.[134] However, other publications contradict this hypothesis. Ohashi or Nayad have described anhydrous methods at elevated temperatures (> 110 °C) to synthesize benzyl-, fluorobenzyl-, or tosyl-functionalized SiNS by direct exfoliation of $CaSi_2$ with benzyl bromide, 4-fluorobenzyl bromide, or tosyl chloride, respectively.[69–71] The objective of this chapter is to prepare hydride-terminated oxygen-free SiNS-H. Therefore, the application of harsh reaction conditions, which favor oxidation, is to be avoided.

It is hypothesized that under the conditions tested in the experiments described herein, water is necessary for Ca^{2+} deintercalation and solvation. This is further investigated in the next section.

The Role of Water

Having demonstrated that no SiNS-H are formed in anhydrous reaction media, it is necessary to investigate the necessity for water. Ethanolic hydrogen chloride solutions are prepared with varying concentrations of concentrated HCl. Solutions with defined water contents corresponding to x equivalents of water (x = 1, 10, 25, 50, 100) per one equivalent of $CaSi_2$ are obtained. Experiments with $CaSi_2$ and these solutions are conducted at $-32\,°C$ under argon atmosphere. In the tested range of equivalents, a color change from gray $CaSi_2$ to a yellow product occurs only in the sample with 100 equivalents of water after 12 days. This yellow product is characterized by FTIR spectroscopy (Figure 3.5). The spectrum of the sample prepared with 100 equivalents of water in ethanol shows Si-H, SiO-H and Si-O-Si vibrational features at 2104, 1628, 1040 and 800 cm^{-1}, respectively, similar to SiNS-H prepared by the state-of-the-art method. This confirms the successful formation of SiNS-H. In addition, very intense vibrational bands appear in the spectrum, indicating the presence of water (3368 and 1628 cm^{-1}). Probably the product was not sufficiently dried in this experiment.

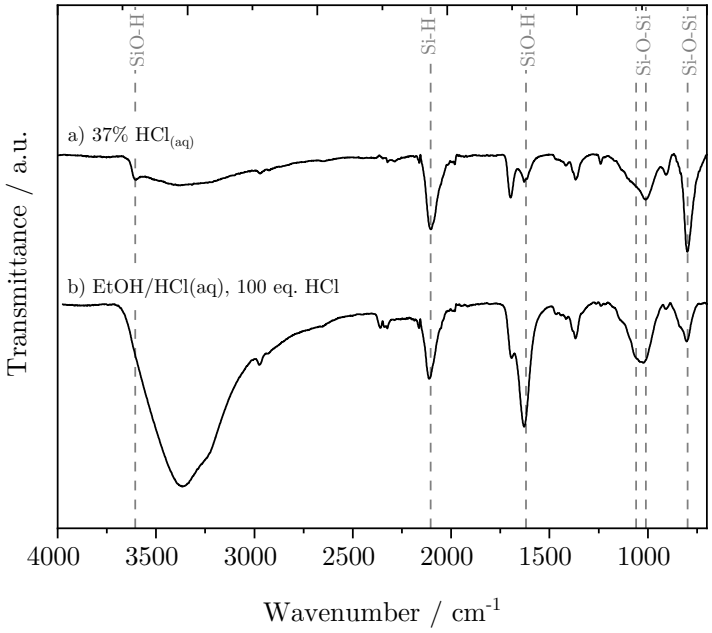

Figure 3.5: FTIR spectra of SiNS-H prepared in aqueous/ethanolic hydrogen chloride solutions.

Apparently, the experiments show that $CaSi_2$ in ethanol reacts with hydrogen chloride to form SiNS-H only in the presence of a certain minimum amount of water. It is therefore hypothesized that water is required in a key step in the formation of SiNS-H. The driving force of the reaction is assumed to be the deintercalation of Ca^{2+} from the Zintl phase $CaSi_2$ and the subsequent solvation of the cations, which is possible through coordination by water molecules. It is surprising that according to the experiments, at least 100 equivalents of water are required, since hydrated Ca^{2+} cations are already coordinated by at least six water molecules.[171]

3.4 Summary

This chapter presents a comprehensive investigation of the origin of oxygen in SiNS-H during their preparation. FTIR spectroscopy showed that oxygen-containing products are formed when $CaSi_2$ is exposed to concentrated $HCl_{(aq)}$ at $-25\,°C$. This is confirmed by the literature. There are no reports of SiNS-H that do not show Si-O vibrational features in FTIR spectra. In order to identify potential sources of SiNS-H oxidation in the state-of-the-art preparation process, the parameters acid, temperature, and atmosphere were considered individually. Lowering the reaction temperature from $-25\,°C$ to $-60\,°C$ in conjunction with replacing $HCl_{(aq)}$ with $HBr_{(aq)}$ did not avoid the presence of oxidized species as expected. A decrease in the intensity of SiO-H vibrations but an increase in the intensity of Si-O-Si vibrations was observed. Furthermore, the oxidation occurred independently of the presence of oxygen, as evidenced by the observation of IR bands corresponding to Si-O vibrations in both air and argon atmospheres. Thus, it was concluded that water is responsible for the partial oxidation of SiNS-H, or more specifically the hydrolysis with water. The first step is probably the formation of OH-terminated silicon atoms, which enables condensation reactions towards Si-O-Si.

In a next step the conversion of $CaSi_2$ towards SiNS-H was investigated in non-aqueous systems. A large variety of combinations with different anhydrous solvents, hydrogen sources, Ca^{2+} chelators or Ca^{2+} solvation methods unfortunately did not provide an alternative synthesis route to oxygen-free SiNS-H, as no conversion of $CaSi_2$ took place.

Finally, it was demonstrated that water is required for the reaction of $CaSi_2$ with hydrogen chloride by using HCl in ethanol with an increasing water content. In the range of ethanol/water ratios studied, a lower limit of 100 equivalents

of water per $CaSi_2$ was found to be necessary for a successful conversion. This finding proves hypotheses from the literature stating that no reaction is observed in anhydrous systems.[15,170]

3.5 Experimental Procedures

3.5.1 General Information

Instrument information, analytical techniques, procedures for solvent drying, the syntheses of $CaSi_2$ and SiNS-H as well as the etching procedure of SiNS-H are found in Chapter 9.
The reactants were purchased from Sigma-Aldrich, abcr, and TCI. $CaSi_2$ is either used as a commercial material or prepared from the elements. Hydrogen chloride is either prepared in situ from concentrated sulfuric acid and ammonium chloride or procured from a gas cylinder (hydrogen chloride 2.8, Praxair).
Reactions under exclusion of water and air are performed using standard Schlenk methods. All solvents are dried and degassed prior to use.

3.5.2 Modification of the Standard SiNS-H Preparation

Preparation with Hydrobromic Acid

The preparation of SiNS-H is conducted at both −25 and −60 °C. $HBr_{(aq)}$ (30 mL) is added to a Schlenk flask, which was purged with argon for 5 min. The flask and a vial containing $CaSi_2$ (300 mg, under argon) are precooled in a freezer (−25 °C) or in a climate chamber (−60 °C). In an argon counterflow, the $CaSi_2$ is added to the acid, and the flask is cooled again to −25 °C or −60 °C. The flask is occasionally stirred. Exfoliation is completed after seven days, and the resulting yellow flakes are obtained as product. The SiNS-H are filtered over a Schlenk frit, washed with acetone (3 × 20 mL), and dried in vacuum.

Preparation under Atmospheric Air

The SiNS-H are prepared following the standard procedure (see Chapter 9), with the exception that atmospheric air is used instead of argon.

Preparation in the Absence of Air

Water is degassed by passing argon gas through the solvent, followed by three freeze-pump-thaw cycles. HCl gas is then introduced into the water until the presence of gas is visible in the downstream gas bubbler behind the reaction flask. Approximately 43 mg of HCl are dissolved in 100 mL water. The as-prepared hydrogen chloride solution is employed in the standard SiNS-H preparation procedure (see Chapter 9).

3.5.3 Experiments in Anhydrous Solvents

Reactions with Hydrochloric Acid

The experiments conducted in anhydrous solvents are carried out according to the standard procedure and follow the general protocol outlined below. A heat-dried flask is filled with the organic solvent, which has been saturated with gaseous HCl, and precooled to the desired reaction temperature in a freezer or refrigerator. The precooled $CaSi_2$ is added to the acidic solution. The flask is maintained at the reaction temperature for minimum of seven days and is occasionally stirred. The solid is filtered over a Schlenk frit and washed with the pure solvent used in the corresponding experiment (3×20 mL). The resulting solid material is then dried in vacuum. Table 3.4 provides the detailed reaction conditions.

Reactions with Methanesulfonic and Triflic acid

$CaSi_2$ is dispersed in both in pure MsOH or TfOH as well as in the acids diluted with DMSO. The experiments are carried out at room temperature for several weeks, except for the experiment in pure TfOH, which is conducted at $-32\,^{\circ}C$. The amounts of the reactants used are listed in Table 3.5. As no color change is observed after several weeks, the mixtures are discarded.

Reactions with EMIM OTf

$CaSi_2$ is added to EMIM OTf in a heat-dried Schlenk flask and mixed with TfOH or TFA and BAPTA or 15C5 if necessary. All experiments are conducted at both $1\,^{\circ}C$ and room temperature for seven days. Table 3.6 gives the quantities of the reactants used in the experiments. As no color change is observed after several weeks, the mixtures are discarded.

Table 3.4: Experimental conditions for the conversion of $CaSi_2$ with HCl in anhydrous solvents.

$CaSi_2$	Ca^{2+} solvation	HCl/solvent	Reaction time and temperature
251 mg, 2.6 mmol	—	25 mL EtOH	−25 °C, 20 d
50 mg, 519 µmol	—	5 mL DMPU	−32 °C, 18 d
502 mg, 5.2 mmol, 1.0 eq.	2.9 g TBAC, 10 mmol, 2.0 eq.	35 mL PC	−25 °C, 7 d
501 mg, 5.2 mmol, 1.0 eq.	2.2 g 18C6, 8.2 mmol, 1.6 eq.	35 mL THF	−25 °C, 7 d
500 mg, 5.2 mmol, 1.0 eq.	1.6 g 18C6, 6.3 mmol 1.2 eq.	6.5 mL Et_2O	−32 °C, 30 d
501 mg, 5.2 mmol, 1.0 eq.	1.7 g 15C5, 7.9 mmol, 1.5 eq.	35 mL THF	−25 °C, 7 d
501 mg, 5.2 mmol, 1.0 eq.	1.8 g 15C5, 8.1 mmol, 1.6 eq.	35 mL Et_2O	−25 °C, 7 d
502 mg, 5.2 mmol, 1.0 eq.	1.7 g 15C5, 7.9 mmol, 1.5 eq.	35 mL 1,4-dioxane	−25 °C, 7 d
501 mg, 5.2 mmol, 1.0 eq.	1.8 g 15C5, 8.0 mmol, 1.5 eq.	35 mL PC	−25 °C, 7 d
507 mg, 5.3 mmol, 1.0 eq.	1.7 g 15C5, 7.9 mmol, 1.5 eq.	22 mL MeCN	−25 °C, 7 d
70 mg, 731 µmol, 1.0 eq.	318 mg Kryptofix 221, 956 µmol, 1.3 eq.	10 mL PC	−25 °C, 30 d
1.5 mg, 15 µmol, 1.0 eq.	3.5 mg BAPTA, 7.0 µmol, 0.46 eq.	5 mL THF	−25 °C, 20 d

Table 3.5: Experimental conditions for the conversion of $CaSi_2$ with MsOH or TfOH with or without DMSO as solvent.

$CaSi_2$	Acid/solvent
200 mg, 2.1 mmol, 1.0 eq.	20 mL MsOH (306 mmol, 145 eq.)/ —
21 mg, 0.22 mmol, 1.0 eq.	3 mL TfOH (34 mmol, 154 eq.)/ —
1.0 mg, 10 mmol, 1.0 eq.	1.7 mL TfOH (26 mmol, 2.6 eq.)/ 45 mL DMSO
1.0 g, 10 mmol, 1.0 eq.	2.3 mL TfOH (26 mmol, 2.6 eq.)/ 75 mL DMSO

Table 3.6: Experimental conditions for the conversion of $CaSi_2$ with TFA or TfOH in EMIM OTf.

$CaSi_2$	EMIM OTf	Acid	Ca^{2+} solvation
386 mg, 4.0 mmol, 1.0 eq.	7.1 mL, 38 mmol, 9.5 eq.	2.9 mL TFA, 38 mmol, 9.5 eq.	—
357 mg, 3.7 mmol, 1.0 eq.	7.1 mL, 38 mmol, 10 eq.	3.4 mL TfOH, 38 mmol, 10 eq.	—
58 mg, 0.60 mmol, 1.0 eq.	1.1 mL, 5.8 mmol, 9.6 eq.	0.51 mL TfOH, 5.8 mmol, 9.6 eq.	300 mg BAPTA, 0.63 mmol, 1.1 eq.
58 mg, 0.60 mmol, 1.0 eq.	1.1 mL, 5.8 mmol, 9.6 eq.	0.44 mL TFA, 5.8 mmol, 9.6 eq.	0.12 mL 15C5, 0.63 mmol, 1.1 eq.
58 mg, 0.60 mmol, 1.0 eq.	1.1 mL, 5.8 mmol, 9.6 eq.	0.51 mL TfOH, 5.8 mmol, 9.6 eq.	0.12 mL 15C5, 0.63 mmol, 1.1 eq.

3.5.4 Reactions with Ethanol/Water Mixtures

Ethanol is saturated with HCl gas. Per each experiment 50 mg of $CaSi_2$ (0.52 mmol, 1.0 eq.) are dispersed in the ethanolic hydrogen chloride solution (5 mL). Defined amounts of concentrated aqueous hydrochloric acid (12.5 µL, 125 µL, 312 µL, 624 µL, 1.25 mL, and 2.50 mL) are subsequently added corresponding to specific equivalents of water (1.0, 10, 25, 50, 100 and 200 eq.). The mixtures are cooled to −32 °C and maintained at this temperature for twelve days. If a yellow product is formed, it is filtered through a Schlenk frit and washed with acetone (3 × 15 mL). The resulting flakes are vacuum dried.

4

Photodegradation of Hydride-Terminated Silicon Nanosheets

Previously, yellow SiNS-H and functionalized SiNS were reported to be photosensitive as they turn white and lose their PL upon UV irradiation.[76] It was suggested that UV irradiation cleaves Si-Si bonds, which can then be easily oxidized, for example during workup. This photosensitivity is undesirable for potential applications of SiNSs. A proven method to overcome this problem is is to stabilize the material by embedding it in a polymer matrix.[76] However, the photodegradation of SiNS-H has never been investigated in detail with respect to the degradation mechanism or the composition of the white product. This chapter sheds light on this question by presenting a study of the degradation of HF-etched SiNS-H under UV light.

4.1 Preliminary Tests

4.1.1 Conditions Leading to the Degradation

In order to assess the degradation of HF-etched SiNS-H, it is necessary to identify the conditions that result in the formation of the white degradation product. First, the absorption behavior of the material is examined using UV-vis diffuse reflectance absorbance (DRA) spectroscopy to determine the region of the electro-

magnetic spectrum that interacts with the material. Figure 4.1 shows the spectrum, which demonstrates that SiNS-H absorb light in the range of approximately 530 nm and below.

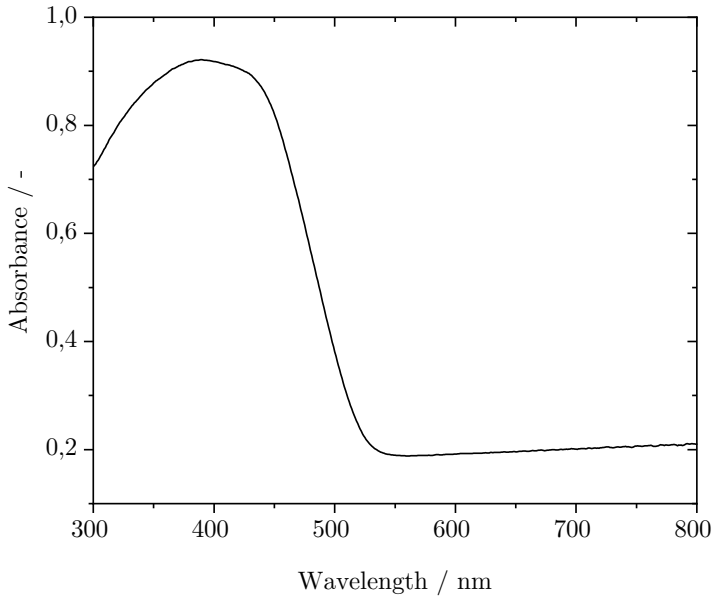

Figure 4.1: UV–vis diffuse reflectance spectrum of SiNS-H.

UV light with a wavelength of 365 nm is applied in the degradation experiments described below. In preliminary tests, low amounts of SiNS-H are dispersed in toluene under argon or air atmospheres and are exposed to UV irradiation. In both atmospheres, the visible PL of SiNS-H under UV light disappears during the irradiation. Depending on the atmosphere, the yellow dispersion of SiNS-H remains yellow in the argon atmosphere, but becomes white in air. Therefore, it is proposed that two processes take place during UV irradiation: First, independent of the atmosphere, a PL fatigue occurs, followed by the formation of a white product in the presence of air. This white product is most likely due to oxidation, since it is not observed in the experiment under argon. To make sure that the decomposition depends not only on the presence of oxygen, but also on UV irradiation, the experiment is repeated in air in the dark. This time, no white product is formed, which leads to the conclusion that the degradation of SiNS-H to the white product is a photooxidation process.
In addition to the visual evaluation of the color of the material, a gravimetric analysis of the white product obtained under exposure to 365 nm light in atmospheric air is performed. In the case of an oxidation, an increase in weight should

occur upon irradiation. Assuming the ideal structure of SiNS-H with the formula $[Si_6H_6]_n$, a theoretical weight increase of 55 % is expected if one oxygen atom is added for each silicon atom to form e.g. $[Si_6O_6H_6]_n$. A gravimetric comparison of SiNS-H before and after irradiation in air shows an increase in weight of about 53 %. This confirms the hypothesis of oxidation, since the experimental value is in good agreement with the theoretical weight increase. Observations from all these experiments are summarized in Table 4.1.

Table 4.1: Observations from the preliminary photodegradation experiments with SiNS-H.

	365 nm, air	365 nm, argon	Dark, air
PL	Fades	Fades	Remains
Color change	Yellow to white	None	None
Weight increase	53%	None	None

The FTIR spectrum of the white product shows prominent Si-O modes (Figure 4.2). After UV irradiation, the intense Si-H stretching mode at 2104 cm^{-1} and the SiO-H stretching band at 3606 cm^{-1} disappear (for more detailed band assignments see Section 3.1). The most prominent vibrational feature is the Si-O-Si stretching at 1043 cm^{-1}. New peaks which are assigned to Si-H stretching of O_3Si-H and O-Si-H arise at 833, 2243 and 2196 cm^{-1}, respectively.[21] The appearance of these new FTIR modes is due to oxygen insertion into the Si-Si bonds.

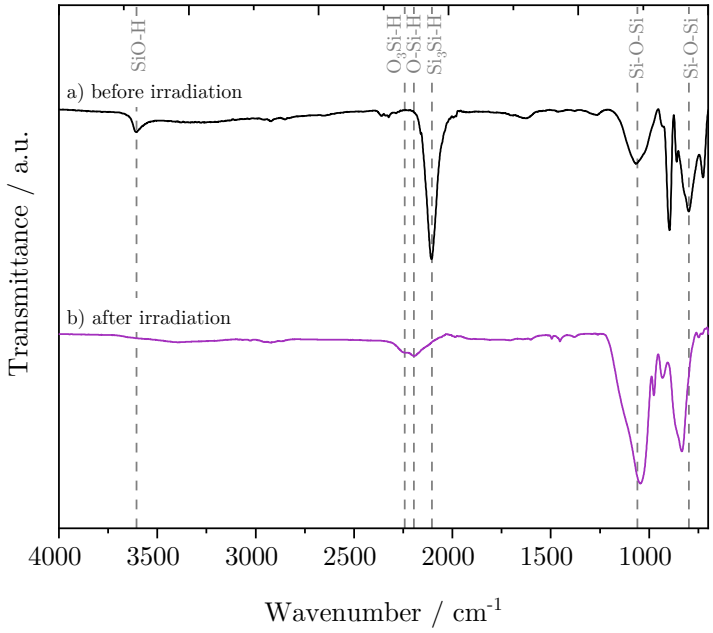

Figure 4.2: FTIR spectra of etched SiNS-H before (a) and after UV irradiation in air (b).

4.1.2 Radical Character of the Degradation

The bond energies in SiNS-H, are 210 to 250 kJ mol^{-1} (2.2 to 2.6 eV) for the Si-Si bond and 323 to 356 kJ mol^{-1} (3.3 to 3.7 eV) for the stronger Si-H bond.[172,173] Thus, UV light with a wavelength of 365 nm (3.4 eV) has sufficient energy to homolytically cleave these bonds. Knowing this, a radical nature of the degradation mechanism is possible. To prove this assumption, the irradiation of SiNS-H is used for the polymerization of methyl methacrylate (MMA), a monomer known to be radically polymerized. Polymerization of MMA is expected to occur if radicals are formed during the illumination of SiNS. Thus, polymer formation would be evidence of the presence of radicals.

To be sure that the degradation of the nanosheets is responsible for the eventual polymerization results, it is necessary to test whether the polymerization of MMA also occurs in the presence of SiNS-H in the dark and under irradiation without SiNS-H. These tests are performed twice, once in argon and once in air. No polymers precipitate in methanol in any of these tests. Therefore, experiments in which MMA and SiNS-H are irradiated with 365 nm light under both argon and air atmospheres are conducted. After exposing the samples to UV light for two hours, a colorless liquid over a small amount of white solid, which is probably degraded SiNS-H, is obtained in the air experiment. After separation of the solid from the liquid, the liquid phase is poured into methanol for precipitation. White poly(methyl methacrylate) (PMMA) precipitates, which is characterized by ^{1}H NMR spectroscopy and gel permeation chromatography (GPC). In the argon atmosphere experiment, on the other hand, a turbid phase is obtained. After centrifugation, a clear liquid is separated from a viscous phase. PMMA is precipitated from the filtered liquid phase into methanol. As with the air experiment sample, the precipitate is analyzed by ^{1}H NMR spectroscopy and GPC. The scheme in Figure 4.3 summarizes the conditions leading to the polymerization of MMA.

^{1}H NMR spectra of the precipitates in $CDCl_3$ are shown in Figure 4.4 and confirm the polymerization of MMA. Both spectra show the singlet peak at 3.60 ppm characteristic of the methoxy group, signals in the range of 0.80 to 1.25 ppm, which are assigned to methyl protons, and signals in the range of 1.75 to 2.00 ppm corresponding to the methylene protons.[94]

GPC data of DMF solutions of both dry samples (air and argon atmosphere) confirms the presence of polymers. The detection of the refractive index is

shown in Figure 4.5 and compared with the chromatogram of the monomer. Both chromatograms show an intense signal in the range of 10 to 15 min, corresponding to relative molecular weight averages (M_n by polystyrene standards) of 9.6 and 27 kg mol^{-1}, respectively, and a less intense signal at about 19 min. The molecular weight of the polymer is too high to detect the endgroup by ^{1}H NMR spectroscopy. So no insight into the initiating species is gained.

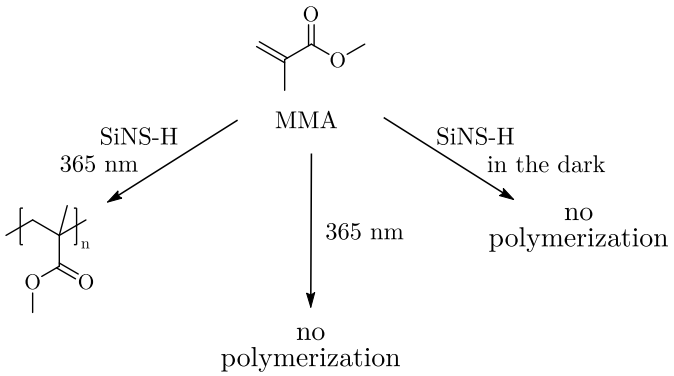

Figure 4.3: Conditions leading to MMA polymerization under argon and air atmospheres.

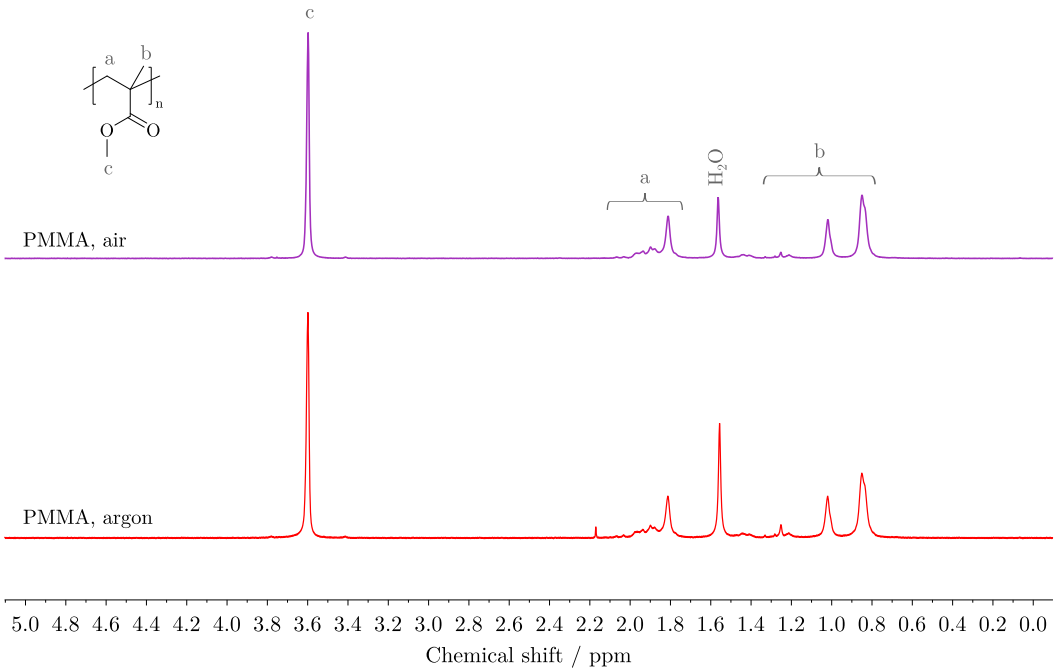

Figure 4.4: ^{1}H NMR spectra of PMMA obtained by the irradiation of MMA with SiNS-H under air and argon atmospheres. The spectra are recorded in $CDCl_3$.

In conclusion, these experiments showed that MMA polymerizes in the presence of SiNS-H under irradiation with UV light, both in argon and air atmospheres. This

unambiguously shows that a radical formation takes place during the degradation of SiNS-H by UV light.

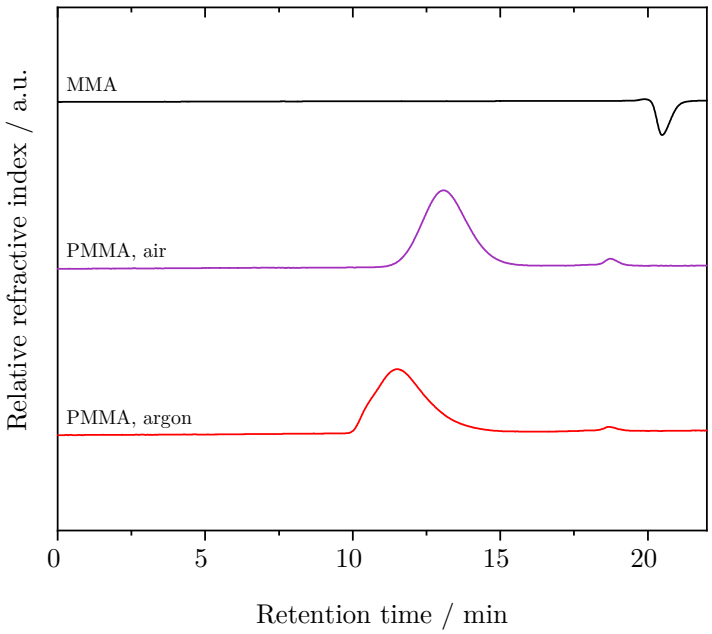

Figure 4.5: Gel permeation chromatograms of PMMA obtained by the irradiation of MMA with SiNS-H under air and argon atmospheres compared to the chromatogram of the monomer.

4.2 Investigation of the Photodegradation Product

So far, it was demonstrated that UV light induces a loss of the PL of SiNS-H under both argon and air atmospheres. A white degradation product is also formed in air. With regard to the degradation mechanism, the results with MMA indicate that radicals are involved. The present study will now investigate the degradation product and the influence of the atmosphere on the degradation in detail. For this reason, larger quantities of stirred toluene dispersions of HF-etched SiNS-H are irradiated with UV light at 365 nm as shown in Figure 4.6 c). In these irradiation experiments, three different atmospheres are employed: argon, air and oxygen. Within the first 30 min, the SiNS-H lose their visible PL (see Figure 4.6 a) and b)). A color bleaching takes place in all three experiments: The sample in oxygen turns white after seven hours of irradiation. UV irradiation of the nanosheets under air and argon atmospheres is stopped after 42 hours. At this time, both samples are still yellow, although the color of the sample in air is lighter than that of the sample in argon, which again is a little lighter than the starting material SiNS-H. The photographs in Figure 4.6 d) show the colors of the products. Toluene is removed

from all samples in vacuum immediately after the irradiation. Until characterization, the powdery samples are stored in the glove box in the dark. Analysis of the structure and composition of the three irradiated samples is performed using FTIR, Raman, XPS, and XRD. SEM images are recorded to evaluate the morphology of the materials.

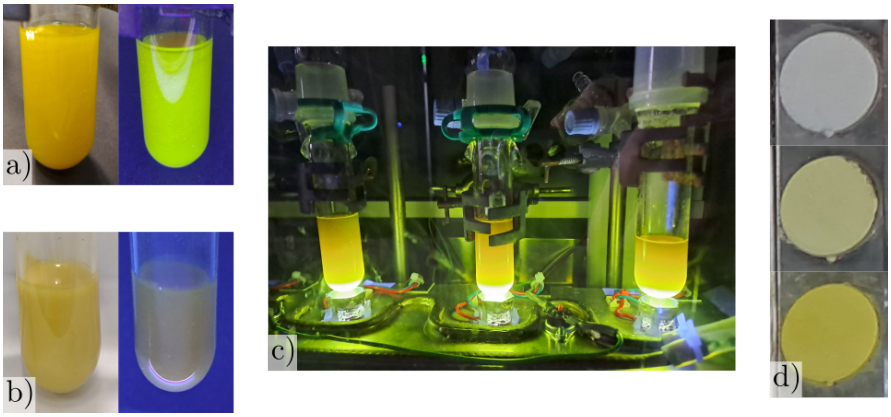

Figure 4.6: Photographs of SiNS-H dispersed in toluene under argon atmosphere before (a) and after irradiation (b) under normal light (left) and under UV light (right); irradiation setup (c); powdery products after UV irradiation under oxygen (top), air (middle), and argon atmospheres (bottom).

The FTIR spectra of the products obtained in the irradiation experiments are compared with the spectrum of the non-irradiated SiNS-H in Figure 4.7. According to these spectra, almost no structural change is observed after the irradiation in an argon atmosphere. The spectrum still exhibits an intense band correlated to the Si-H stretching vibration (2104 cm^{-1}). The SiO-H stretching vibration at 3600 cm^{-1} vanishes after UV irradiation. Minor differences are also found in the fingerprint region: The Si-O-Si vibrational feature (1077 cm^{-1}) is increased and slightly shifted to higher wavenumbers relatively to the spectrum of the non-irradiated SiNS-H. This indicates a higher oxygen content and could be due, at least in part, to condensation of ≡Si-OH groups. No oxidation should occur in an argon atmosphere, but some traces of oxygen are always present as an impurity in argon and can cause oxidation. The frequency shift results from an increased angle of the Si-O-Si bond. Thus, irradiation of SiNS-H in an inert gas leads to small changes in the FTIR spectrum. In contrast to that, the spectra of samples from the air and oxygen experiments are significantly different from the spectrum before irradiation with UV light. The spectra of the two materials irradiated in oxygen-containing atmospheres are similar. The most notable difference be-

tween the irradiated and non-irradiated samples is the disappearance of the Si-H modes at 2104 and 895 cm^{-1}. The Si-O-Si feature at 1047 cm^{-1} with a shoulder at 1145 cm^{-1} is the most prominent mode. It is accompanied by the O-Si-H bending mode at 838 cm^{-1}, which again has a shoulder at 870 cm^{-1}.[174,175] These broad bands with shoulders can be explained by different bond environments: The bands at 1047 and 838 cm^{-1} correspond to a bond environment with smaller angles than the bands at 1145 and 870 cm^{-1}.[175] At higher wavenumbers, less intense O_xSi-H stretching vibrations are observed in the range of 2150 to 2280 cm^{-1}.[21] This evidence demonstrates that in air and oxygen atmospheres, the photooxidation of SiNS-H occurs, resulting in the formation of bonds between hydride-terminated silicon atoms and oxygen atoms. On the other hand, no significant structural changes are observed after UV irradiation in argon atmosphere.

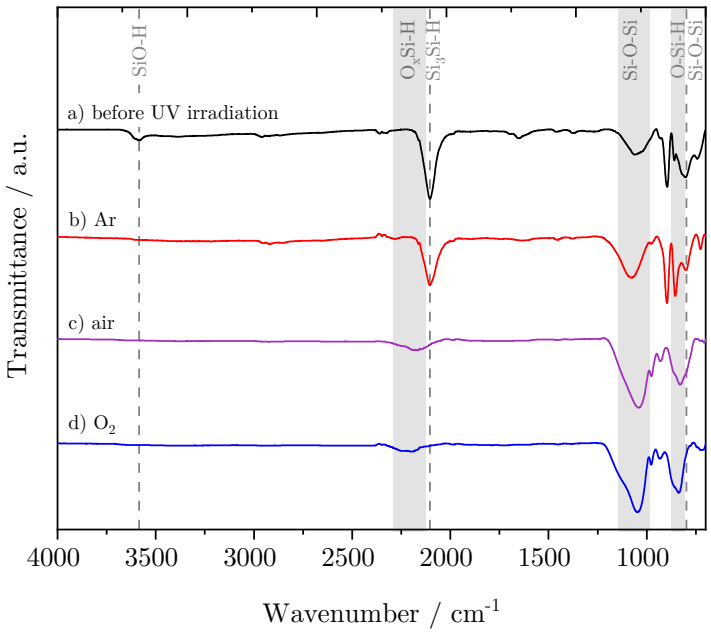

Figure 4.7: FTIR spectra of SiNS-H before (a) and after irradiation at 365 nm in argon (b), air (c), and oxygen (d) atmospheres.

Complementary information to FTIR spectroscopy is obtained by Raman scattering (Figure 4.8 I)). In the low-frequency region, the spectrum of the SiNS-H irradiated under argon atmosphere is almost identical to the spectrum of the SiNS-H before UV irradiation. In addition to the mode at 520 cm^{-1}, indicative of bulk silicon impurities, these two spectra show the characteristic SiNS-H vibrational features at 378 and 493 cm^{-1} (Si-Si) and 635 and 730 cm^{-1} (Si-H).[58] The band at 493 cm^{-1} is broadened towards lower frequencies in the sample from the argon

experiment, indicating partial amorphization of the material. In contrast, the spectrum of the sample irradiated in oxygen shows none of the bands characteristic of SiNS-H. This confirms the absence of Si-H modes corresponding to hydrogen bonded to silicon atoms within the 2D silicon network, which is also observed in the FTIR spectrum. The Raman spectrum provides new information at this point, namely that the Si-Si vibrational features disappear completely after the photooxidation. A probable explanation for this is the oxidation of the nanosheets by the insertion of oxygen into the Si-Si bonds. The inserted oxygen originates from partially hydroxyl-terminated silicon (rearrangement as known from siloxene, see Section 2.3) and oxygen from the atmosphere. The spectrum of the air experiment sample shows an intermediate pattern. Weak bands at similar Raman shifts as the unirradiated material are shown in the spectrum. Besides an intense signal assigned to bulk silicon impurities ($520\,\mathrm{cm^{-1}}$), the feature at $493\,\mathrm{cm^{-1}}$ exhibits a low-frequency tail that is more distinct than the feature observed in the argon sample. This band broadening is probably the result of an increased fraction of an amorphous phase. Since the other Raman signals are relatively weak compared to those in the spectrum before exposure to UV light, a partial degradation of the material due to photooxidation is assumed. The spectrum of this sample is intermediate between those of the samples obtained in argon or air. This is also consistent with the different colors of the irradiated products (light yellow in air, darker yellow in argon, and white in oxygen).

The high-frequency region of the Raman spectra shows different Si-H vibration modes of the irradiated samples in dependence on the atmosphere (Figure 4.8 II)). Before and after UV irradiation under argon, the spectra show the same broad band centered at $2116\,\mathrm{cm^{-1}}$. This band is assigned to the Si-H vibration in SiNS-H.[58] The Raman spectra of the samples from the air and oxygen experiments deviate from this SiNS-H spectrum. They show bands which are shifted to higher frequencies. The spectrum of the sample irradiated in air atmosphere exhibits a broad asymmetric Raman band with a maximum at $2140\,\mathrm{cm^{-1}}$ ending with a shoulder at $2255\,\mathrm{cm^{-1}}$. The spectrum of the oxygen sample is shifted even more to higher frequencies. Several bands seem to overlap in the region of 2100 to $2280\,\mathrm{cm^{-1}}$. These shifted bands observed for the nanosheet irradiated in air and oxygen atmospheres are assigned to O_xSi-H vibrations. In general, the Si-H vibrational frequency increases with the number of oxygen atoms bonded to the silicon atom.[21,174] These results confirm the earlier findings: The structure of

SiNS-H undergoes partial amorphization under UV irradiation in an argon atmosphere, whereas SiNS-H oxidize in air and oxygen atmospheres by the insertion of oxygen into the Si-Si bonds.

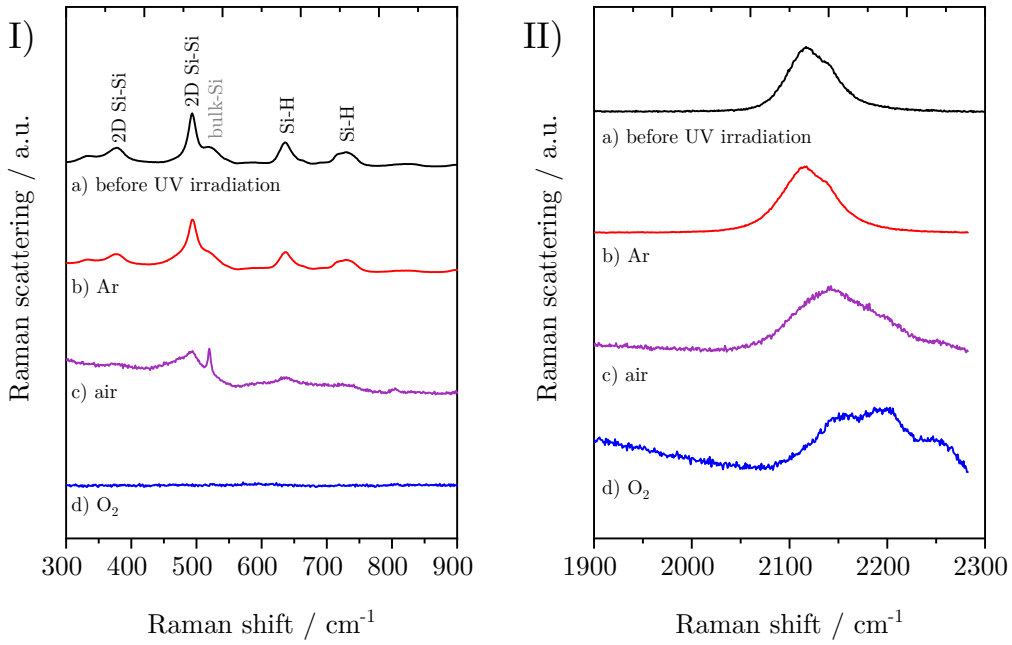

Figure 4.8: Representative Raman spectra of SiNS-H before (a) and after irradiation at 365 nm in argon (b), air (c), and oxygen (d) atmospheres. I) shows the low-frequency and II) the high-frequency range.

In addition to the vibrational spectroscopy, the samples are characterized by powder XRD analysis. The diffraction patterns of the three irradiated samples differ significantly from the XRD pattern of the SiNS-H before UV irradiation. HF-etched SiNS-H exhibit relatively sharp reflexes, consistent with literature data.[16,73] Upon exposure to UV light, these reflexes are converted to broad peaks for all samples, independent of the atmosphere. Accordingly, the materials after irradiation, exhibit poor crystallinity and are rather amorphous. In contrast to the results obtained from FTIR and Raman spectroscopy, which indicate minimal changes between the non-irradiated SiNS-H and the sample from the argon experiment, the XRD patterns of these two samples show significant discrepancies. The sample irradiated in argon atmosphere shows a broad signal centered at approximately 28° and a less intense but broad signal in the range of 42 to 60°. This pattern resembles the one of hydrogenated amorphous silicon.[21,176] The amorphization of SiNS-H under argon atmosphere could be the result of a rearrangement in the silicon framework, which is induced by the homolytic cleav-

age of Si-Si and Si-H bonds under UV light. A cleaved bond may be saturated by neighboring hydrogen or silicon atoms or by the recombination with another dangling bond. The XRD data of the samples irradiated in air and oxygen are identical. Both show a broad peak centered at approximately 23°, which is similar to the XRD pattern of (hydrogenated) amorphous silicon oxide.[177,178]

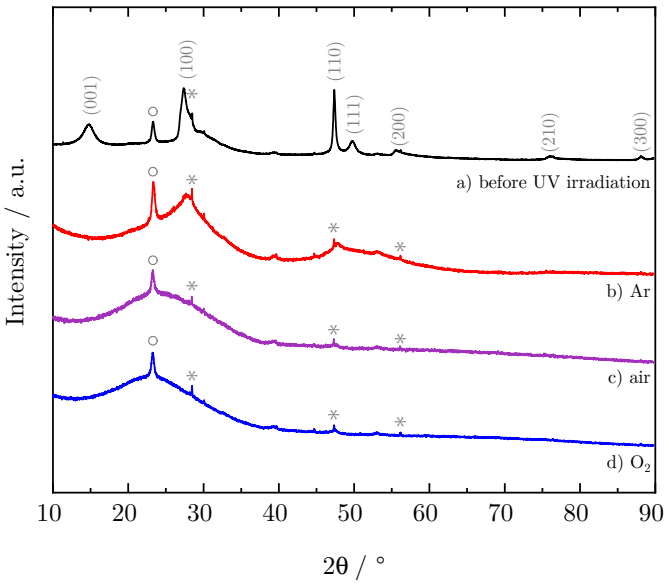

Figure 4.9: Powder XRD patterns of SiNS-H before (a) and after irradiation at 365 nm in argon (b), air (c), and oxygen (d) atmospheres. Several minor reflexes marked with an asterisk can be assigned to silicon impurities. The reflex marked with a circle is an unknown impurity.

The elemental composition and oxidation states of the surface atoms in the three irradiated SiNS-H samples are determined using XPS. Figure 4.10 compares the survey spectra and the high-resolution spectra of the O 1s and Si 2p regions. As the survey spectra show, all samples contain silicon species (Si 2p and 2s core level at binding energies of approximately 100 and 150 eV) and oxygen domains (O 1s core level at 533 eV). Significant oxygen contents are present in the samples irradiated under oxygen and air atmospheres, whereas the spectrum of the sample irradiated under argon atmosphere only shows a minor oxygen content. The found O/Si atomic ratios are 0.2, 0.7, and 0.8 for SiNS-H irradiated in argon, air, and oxygen atmospheres, respectively. In addition to the expected silicon and oxygen components, carbon, chlorine, and fluorine are also detected. The latter two impurities result from the SiNS-H preparation and etching protocols,

which include $HCl_{(aq)}$ and $HF_{(aq)}$. Some chlorine and fluorine residues (Si-Cl or Si-F bond formation) remain on the sample. The carbon impurities most likely originate from toluene residues, which were not completely removed during the drying of the samples.

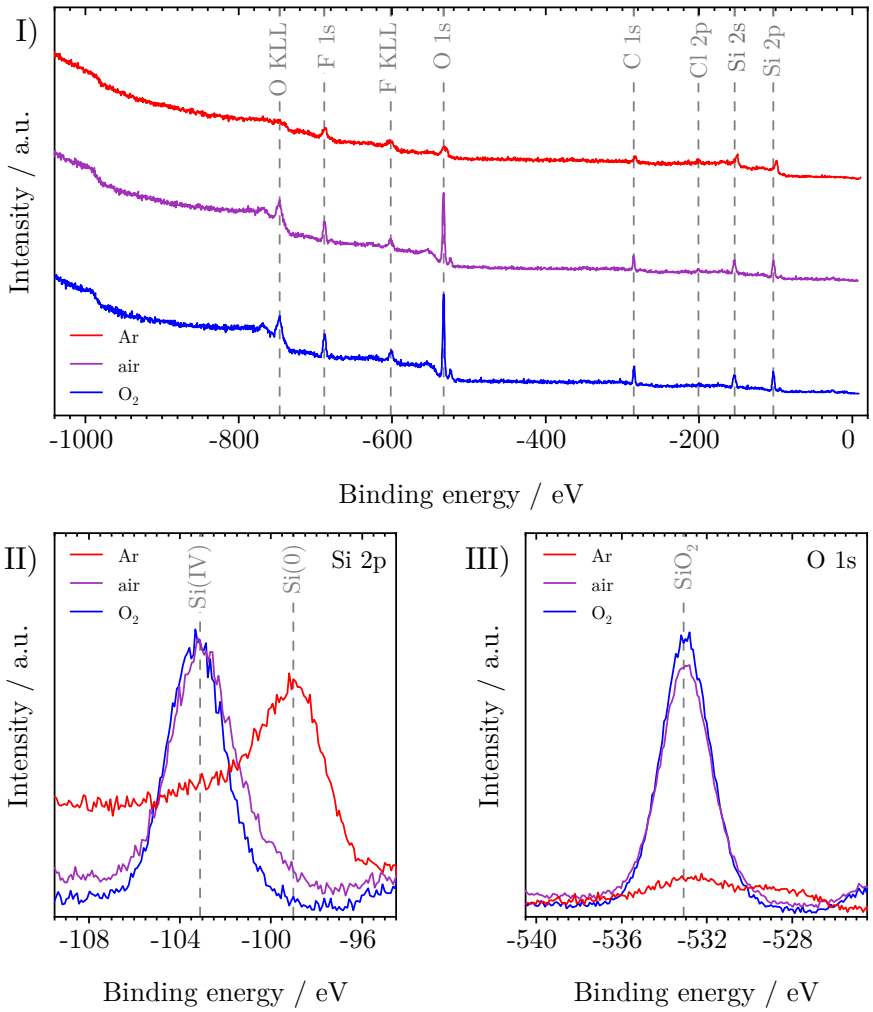

Figure 4.10: Survey (I), high-resolution Si 2p region (II), and high-resolution O 1s region (III) XPS spectra of SiNS-H irradiated under argon, air, and oxygen atmospheres.

A comparison of the high-resolution Si 2p spectra reveals differences between the three samples irradiated under different atmospheres. The Si 2p peak of SiNS-H irradiated in oxygen atmosphere exhibits a symmetric shape at a binding energy of 103.3 eV. This peak is assigned to Si(IV) in silicon oxide.[179] On the other hand, the Si 2p peak of the argon sample is centered at a binding energy of 99.0 eV, which is assigned to Si(0) and hydride-terminated silicon.[83,155] A minor contri-

bution of oxidized silicon species is indicated by a slight shift to higher binding energies. The predominant silicon species present in the sample irradiated under ambient air is Si(IV). As the Si 2p spectrum of the air sample shows an asymmetric peak with a low-energy tail, the presence of silicon suboxides becomes evident. The high-resolution O 1s spectra of SiNS-H irradiated under oxygen and air atmospheres are dominated by an intense peak at a binding energy of 533.0 eV ascribed to silicon oxide.[180] The spectrum of the sample from the argon experiment exhibits a weak feature at the same binding energy, which is attributed to minor oxidation of the material due to trace impurities of oxygen in argon. A second peak at about 528 eV probably originates from the metal oxide of the sample holder, which is visible due to the high sample charging of the argon sample.
In conclusion, the XPS results confirm that the SiNS-H undergo oxidation during irradiation in oxygen-containing atmospheres, whereas the silicon oxidation state remains essentially unchanged under argon atmosphere.

To evaluate the morphology of the irradiated samples, SEM measurements are performed. Figure 4.11 presents representative SEM images of the nanosheets before and after irradiation.

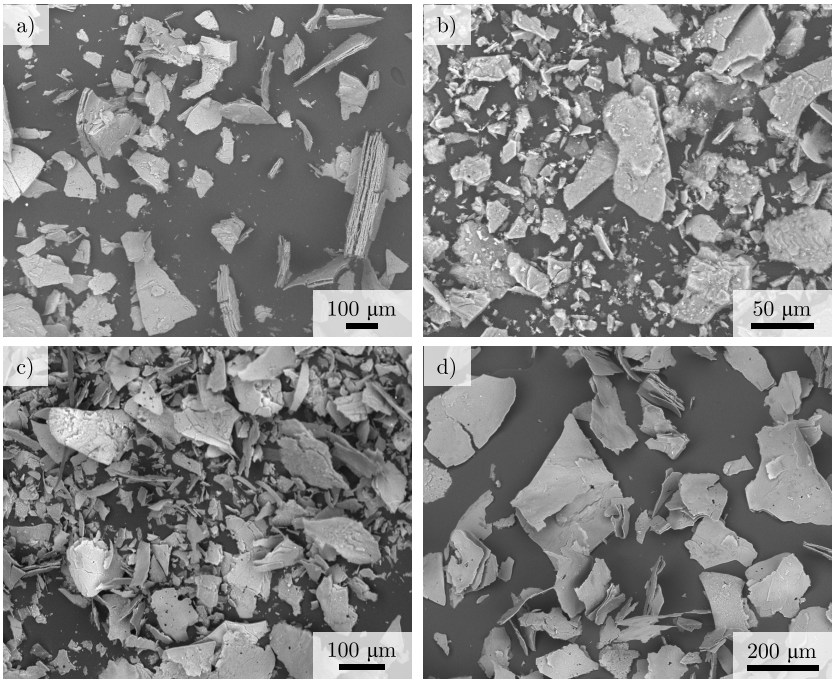

Figure 4.11: SEM images of SiNS-H before (a) and after UV irradiation in argon (b), air (c), and oxygen (d) atmospheres.

According to these images, the morphologies of the nanosheets do not change on the micrometer scale, regardless of the atmosphere. This further supports the assumption that oxygen is incorporated into the silicon network of samples irradiated under air and oxygen atmospheres.

Combining the results of FTIR and Raman spectra as well as the XRD, XPS, and SEM measurements, it is concluded that the UV irradiation of SiNS-H in argon, air, and oxygen atmospheres induces a structural change while the sheet morphology on the micrometer scale is retained. The material from the argon experiment, shows only minor changes in the vibrational spectra compared to the starting material, but a significant difference in the XRD data. This material is suggested to be a mixture of minimal oxidized SiNS-H and a hydrogenated amorphous silicon species. The material obtained by the irradiation in oxygen atmosphere, shows oxidation features and absence of Si_3Si-H bonds in the FTIR spectrum. Raman spectroscopy shows the absence of Si-Si bonds after irradiation. Thus, oxygen is inserted into the Si-Si bonds. According to the XRD measurement, the material resembles amorphous silicon oxide or hydrogenated amorphous silicon oxide, which is consistent with the results of vibrational spectroscopy. In addition, the XPS results confirm a significant amount of oxygen in the sample and Si(IV) as the main silicon species. The photodegradation product is proposed to be a mixture of several (hydrogenated) silicon oxide phases. The results of the sample irradiated in air are intermediate between those of the argon and oxygen experiments, exhibiting greater similarity to the oxygen experiment. Since the degradation is a photooxidation in the presence of oxygen, this is in agreement with the fact that the nanosheets are exposed to less oxygen in the air experiment than in the pure oxygen experiment (21 % oxygen content in air). Figure 4.12 schematically summarizes the results of this study.

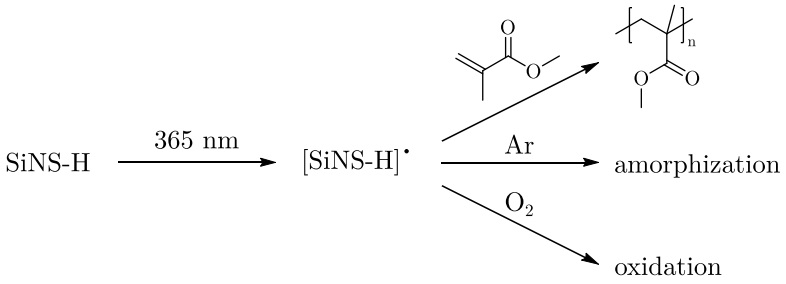

Figure 4.12: Schematic summary of the results of the photodegradation studies.

These findings are consistent with similar results reported for other silicon materials. The illumination of porous silicon and siloxene in oxygen-containing atmospheres has been demonstrated to result in the photooxidation of the materials, whereby oxygen is inserted into the Si-Si bonds.[20,21,119,124–126,129] In the literature, the photodegradation of silicon materials (e.g., silicon nanocrystals, silicon quantum dots, amorphous, and porous silicon) in inert gas has been explained by structural distortion or dangling bond formation due to the cleavage of Si-Si and Si-H bonds, which is similar to the Staebler-Wronski effect.[116,118,121]

4.3 Summary

Starting with the observation that yellow SiNS-H are photosensitive and turn white upon UV irradiation, their photodegradation was systematically investigated. Preliminary tests, in which toluene dispersions of SiNS-H are irradiated under different conditions, showed that a white degradation product is only obtained if the nanosheets are exposed to UV light and oxygen at the same time. Thus, the degradation is a photooxidation. Prior to the formation of a white solid, the visible PL of the nanomaterial disappears under UV light, regardless of the atmosphere. The origin of this PL fatigue was not investigated. For other silicon materials, such as silicon quantum dots and porous silicon, this phenomenon is explained by nonradiative recombination centers created by surface defects and/or dangling bonds due to hydrogen loss.[117,118,120,121] A similar explanation could be expected for SiNS-H. The UV light-induced disappearance of the PL in SiNS-H should be a topic of future research.

Using the radical polymerization of MMA as evidence for the formation of radicals, demonstrated that the exposure of SiNS-H to UV light leads to the formation of radicals in both argon and air atmospheres. It was concluded that a radical mechanism is involved in the first step of the photodegradation.

For a detailed investigation of the influence of the atmosphere on the degradation, irradiation experiments were performed in argon, air, and oxygen atmospheres. Under the applied conditions, light yellow products were obtained in argon and air experiments, while a white product formed in oxygen. None of the products exhibited PL under UV light. Structural analysis of the products showed that irradiation of SiNS-H in argon leads to minor structural changes accompanied by partial amorphization. The irradiation product was found to be similar to hydrogenated amorphous silicon. Characterization of the two samples from experiments

in oxygen-containing atmospheres showed evidence of oxidation and absence of Si-Si bonds. This is due to the insertion of oxygen into these bonds, which leads to amorphous partially hydrogenated silicon oxides. The degree of oxidation is higher in the sample irradiated in pure oxygen than in the air experiment sample.

4.4 Experimental Procedures

4.4.1 General Information

Instrument information, analytical techniques, procedures for solvent drying as well as the synthesis and etching of SiNS-H are found in Chapter 9.
Oxygen 3.5 was purchased from Messer. Reactions under exclusion of water and air are performed using standard Schlenk methods. Toluene is dried and degassed prior to use.

4.4.2 Preliminary Tests

Degradation Conditions

A spatula tip of HF-etched SiNS-H is dispersed in 2 mL toluene under argon in three heat-dried Schlenk tubes each. One tube remains as prepared and the mixture is stirred under irradiation with 365 nm UV light for 24 h under argon atmosphere. Air is introduced into the other two tubes by slowly bubbling air from a 20 mL syringe into the dispersion. One of these tubes is stirred under irradiation with 365 nm UV light for 24 h under air atmosphere, while the other tube is then wrapped in aluminum foil and stirred in the dark for 24 h under air atmosphere.

Weight Increase by Photooxidation

In a 50 mL glass vial with a stirring bar, 31.6 mg of etched SiNS-H (1.1 mmol) are dispersed in 4 mL toluene. 60 mL air is introduced into the dispersion *via* a syringe and the dispersion is irradiated with 365 nm UV light for 48 h. The solvent is carefully removed under vacuum and the white powder obtained is dried and weighed.

4.4.3 Methyl Methacrylate Polymerization

Experiments under argon atmosphere are carried out in heat-dried Schlenk tubes, no heat-drying is necessary for experiments in atmospheric air. In a Schlenk tube with a stirring bar, MMA and etched SiNS-H are combined in the amounts listed in Table 4.2. The mixtures are stirred for 2 h under 365 nm UV light or in the dark for control experiments. Subsequently, the liquid phase is separated from the solid (residues of SiNS-H and potentially polymer) by centrifugation and/or filtration. The liquid phase is then poured into excess methanol to precipitate a polymer if applicable. If polymer precipitates, it is filtered and washed with methanol. The polymers are dried in a vacuum oven at 60 °C prior to analysis.

Table 4.2: Reaction parameters for MMA polymerization experiments.

MMA	SiNS-H	Atmosphere	UV irradiation
4.0 mg, 40 mmol	—	Air	Yes
2.0 mg, 20 mmol	2.0 mg, 0.069 mmol	Air	No
7.0 mg, 70 mmol	6.9 mg, 0.23 mmol	Air	Yes
6.5 mg, 65 mmol	—	Ar	Yes
6.5 mg, 65 mmol	6.5 mg, 0.22 mmol	Ar	No
6.5 mg, 65 mmol	6.5 mg, 0.22 mmol	Ar	Yes

4.4.4 Irradiation of SiNS-H under Different Atmospheres

120 mg of HF-etched SiNS-H (4.1 mmol) is dispersed in 10 mL toluene under argon atmosphere in three heat-dried Schlenk tubes each. One of these tubes is left as prepared, while the other two are connected to 500 mL Schlenk flasks filled with air or oxygen, respectively. These dispersions are stirred under irradiation with 365 nm UV light for 7 h (oxygen) or 42 h (air and argon). After irradiation, the toluene is carefully removed under vacuum. The remaining degradation products are dried for several days in the dark in a 55 °C oil bath at approximately $3 \cdot 10^{-2}$ mbar. Until characterization, the powdery samples are stored in the glove box in the dark.

5

Towards Functionalized Mixed Germanium/Silicon Nanosheets

The surface functionalization of SiNS or GeNS is a well-known tool for tuning the materials' properties such as stability against external influences, dispersibility, or optical properties (see Chapter 2.2.5). Since mixed Ge/SiNS have been reported in the literature,[149,151] no functionalization of this material has been published, although it would be obvious to apply the known modification methods of the hydride-terminated monoelemental nanosheets to the mixed ones. In addition, the mixed Ge/SiNS offer the possibility to control the material properties by modification of the Ge/Si atomic ratio and subsequent functionalization. In this chapter, the applicability of the radical and thermal hydrosilylation/ hydrogermylation with 1-dodecene, known from SiNS and GeNS functionalization routes, to Ge/SiNS is demonstrated. The dodecyl-functionalized SiNS (SiNS-dodecyl), GeNS (GeNS-dodecyl), and Ge/SiNS (Ge/SiNS-dodecyl) prepared by either radical or thermal hydrometalation are compared. The ultimate goal would be the selective functionalization of Ge/SiNS-H, where the Ge atoms in the nanosheets are differently terminated than the Si atoms. Several approaches to achieve this goal are presented in this chapter.

5.1 Comparison of Dodecyl-Functionalized Group IV Nanosheets

The objective in modifying SiNS, Ge/SiNS, and GeNS with dodecyl groups is to become acquainted with the reactivity of mixed Ge/SiNS. Therefore, both the AIBN-initiated and the thermal-induced hydrometalation reactions with 1-dodecene are employed to the three different group IV nanosheets. The reaction products are compared with each other using FTIR spectroscopy and TGA. The surface coverages obtained from the TGA results provide information on the effectiveness of the functionalization reaction and, accordingly, on the reactivity of the nanosheets. No additional characterization is performed, as these reactions are only thought as an introduction into the functionalization of mixed Ge/SiNS.

5.1.1 Radical-Induced Hydrometalation

Appendix A describes the parameter optimization of the radically initiated hydrosilylation of etched SiNS-H with 1-dodecene. These optimized conditions for the AIBN-induced hydrometalation reaction according to Scheme 5.1 are applied to GeNS-H and etched mixed Ge/SiNS-H and the products obtained are compared.

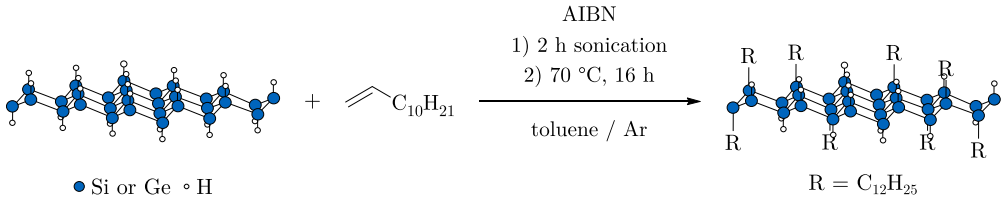

Scheme 5.1: AIBN radical-induced hydrometalation of group IV nanosheets with 1-dodecene.

The three reaction products SiNS-dodecyl, GeNS-dodecyl, and Ge/SiNS-dodecyl, are characterized *via* FTIR spectroscopy (Figure 5.1). Prominent C-H vibration features at 2850 to 2960 cm^{-1} (C-H stretching) and at about 1460 cm^{-1} (C-H deformation) as well as the absence of the C=C vibration modes (3078 and 1641 cm^{-1}) confirm a successful alkyl derivatization of the three group IV nanosheets. However, all spectra still show Si-H and Ge-H stretching bands at about 2106 and 1993 cm^{-1} respectively, indicating incomplete functionalization of the nanosheets. In addition, the FTIR spectra of SiNS-dodecyl and Ge/SiNS-dodecyl show oxidation bands (1060 cm^{-1}), although the reactions were carried out under inert conditions (argon). This may be due to oxygen impurities in the reaction system. From the intensities of the alkyl IR modes relative to the Si-H

or Ge-H modes, it is assumed that the degree of functionalization is the highest for SiNS-dodecyl and the lowest for GeNS-dodecyl.

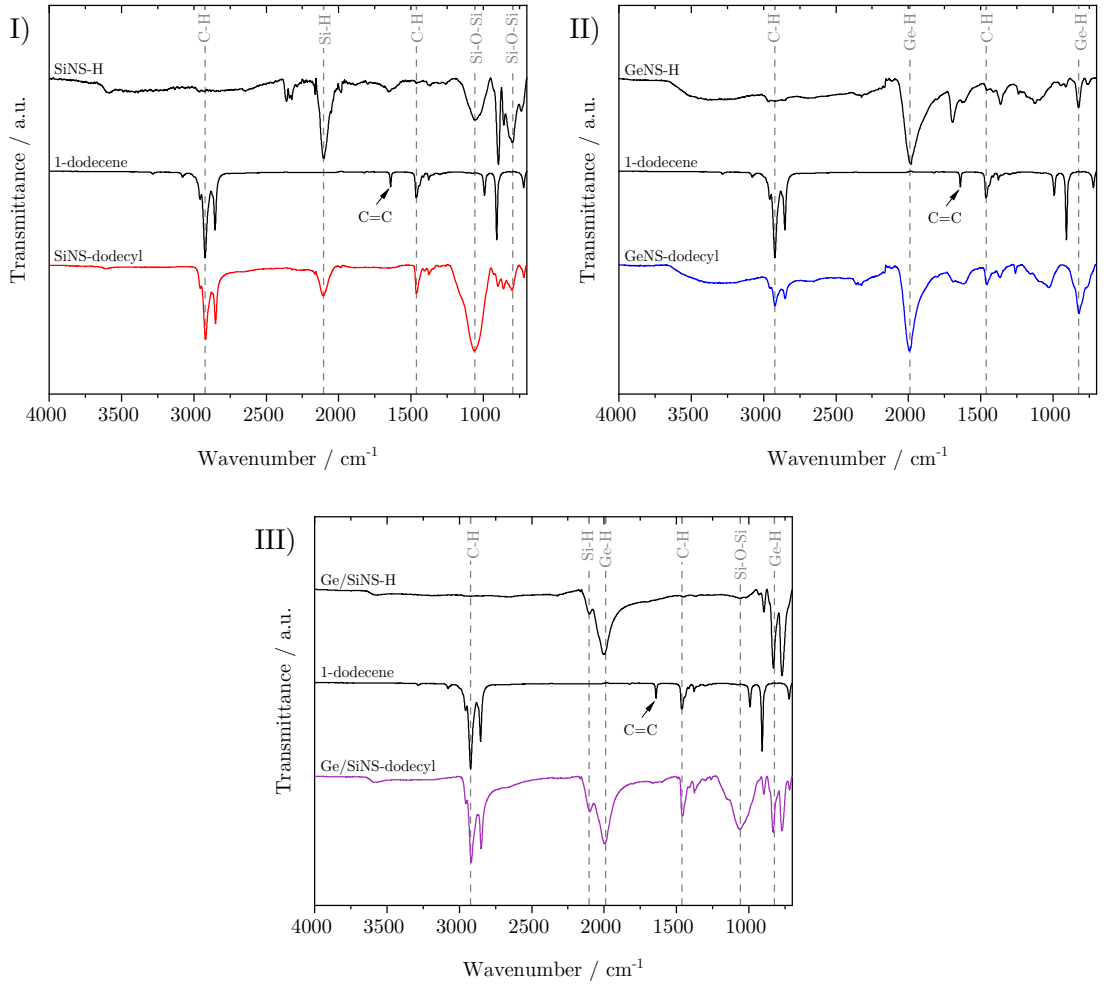

Figure 5.1: FTIR spectra of SiNS-dodecyl (I), GeNS-dodecyl (II), and Ge/SiNS-dodecyl (III) obtained in the AIBN-induced hydrometalation. The product spectra are compared to those of 1-dodecene, etched SiNS-H, GeNS-H, and etched Ge/SiNS-H, respectively.

This is further proven by the mass losses from TGA (Figure 5.2) which is used to determine the surface coverages of the functionalized nanosheets. Table 5.1 summarizes the obtained mass losses and calculated surface coverages compared to the theoretical mass loss for a surface coverage of 100 %. In the hydrometalation reactions, surface coverages of 16, 12 and 8.6 % are obtained for SiNS-dodecyl, Ge/SiNS-dodecyl, and GeNS-dodecyl, respectively. The observed surface coverage of 12 % for Ge/SiNS-dodecyl is very close to the arithmetic average of the weight losses of GeNS-dodecyl (8.6 %) and SiNS-dodecyl (16 %), which is expected from a

Ge/Si ratio of 1:1 in the mixed nanosheets. Note that the calculation of the surface coverages (see Section 9.2) is only an approximation, as ideal structures of group IV six-membered rings, terminated with hydrogen or dodecyl groups are assumed whereupon hydrogen atoms attached to silicon atoms are ignored in the calculation. This method does not consider any impurities like fluorine or chlorine termination, remaining calcium or oxidation of the nanosheets. Further for Ge/SiNS-dodecyl an exact Ge/Si ratio of 1:1 is assumed, which might slightly change after HF-etching. However, the comparison of the calculated surface coverages should still be valid. This comparison shows a trend in the reactivity of the different nanosheets: Under the investigated conditions, the radical hydrosilylation is more effective than the hydrogermylation.

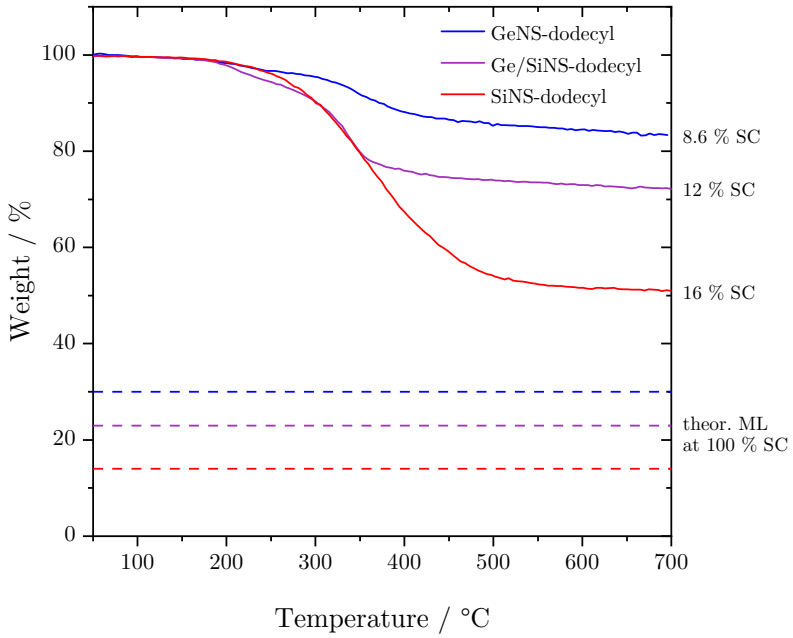

Figure 5.2: TGA measurements of dodecyl-functionalized SiNS, Ge/SiNS, and GeNS obtained by AIBN-induced hydrometalation. The dashed lines indicate the theoretical mass losses (ML) at complete surface coverage (SC).

5.1.2 Thermal-Induced Hydrometalation

As described in Section 5.1.1, the radical hydrometalation of group IV nanosheets with 1-dodecene shows a trend in the surface coverage of the products, whereas SiNS-dodecyl showed the highest degree of functionalization, while the GeNS-dodecyl exhibited the lowest. As the alkyl-functionlization of SiNS-H and GeNS-H *via* hydrometalation can be performed in different ways (cf. Chapter 2.2.5 and

2.4.1), it is studied if this trend also arises in thermal hydrometalation reactions. Accordingly, the following parameters were selected for the reaction, as depicted in Scheme 5.2. For each equivalent of hydride-terminated nanosheets, 48 equivalents of 1-dodecene is used. The mixture is ultrasonicated for 30 min and subsequently heated to 150 °C for 16 hours.

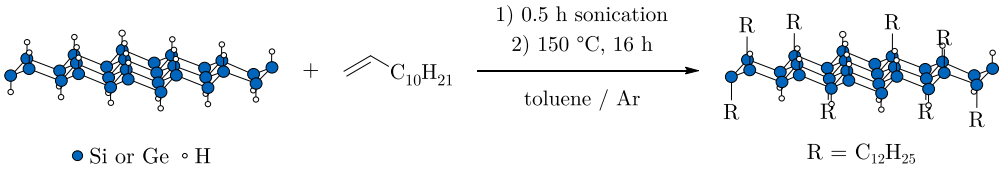

Scheme 5.2: Thermal-induced hydrometalation of group IV nanosheets with 1-dodecene.

Based upon FTIR measurements, a successful dodecyl-functionalization is proven for all kinds of nanosheets. As in the radically performed reactions, Si-H and Ge-H bands remain in the product spectra. However, this time the alkyl vibration modes are more intense relative to the remaining Si-H and Ge-H modes as shown in Figure 5.3 I). This already indicates a higher surface coverage compared to the AIBN-induced reactions which is verified by TGA (see Figure 5.3 II). For all functionalized nanosheets, the mass losses after the thermal reaction are larger than after the AIBN-induced reactions. The surface coverages are 24, 22 and 20 % for SiNS-dodecyl, Ge/SiNS-dodecyl, and GeNS-dodecyl obtained in the thermally initiated functionalization, whereas the surface coverages from the radical-induced hydrometalation are 16, 12 and 8.6 %, respectively (see Table 5.1). Again, as for the radical reaction, the Ge/SiNS-dodecyl surface coverage corresponds to the expected average value of the SiNS-dodecyl and GeNS-dodecyl surface coverages in the thermal hydrometalation reactions. The higher degree of functionalization in the thermal hydrometalation compared to the AIBN-initiated hydrometalation is consistent with results from the literature. Some years ago our group reported a TGA mass loss of 52 % for SiNS-dodecyl prepared with AIBN[76] and a mass loss of 63 % for the thermally initiated (130 °C) product.[73] Yu *et al.* compared the radically and thermally initiated hydrogermylation of GeNS-H and 1-dodecene and found a mass loss of approximately 52 % for the AIBN-induced modified GeNS, and almost a complete mass loss for the thermal-induced (190 °C) product. AFM showed a significant difference in the height profiles of these two GeNS-dodecyl samples. Thus, the authors inferred a surface oligomerization in the thermal reaction and monolayer coverage in case of the radically initiated hydrogermylation. This is also consistent with the observation of Yang *et al.* who

thermally functionalized silicon nanocrystals with 1-dodecene at temperatures between 100 and 190 °C. Using nanostructure-assisted laser desorption/ionization mass spectrometry, they investigated the nature of the surface species and proved surface oligomerization.[181] A comparison of the surface coverages of the different group IV nanosheets, shows the same trend as for the radical-induced hydrometalation: the highest surface coverage is obtained with SiNS, the lowest with GeNS. However the coverages only differ in a range of 4 % (see Table 5.1). This either means that the reactivity of the different nanosheets at high temperatures is similar, or the surface oligomerization of 1-dodecene predominates in the nanosheets containing germanium. To evaluate this in detail, the surface species would need to be characterized, e.g. using nanostructure-assisted laser desorption/ionization mass spectrometry, which is not in the scope of this project.

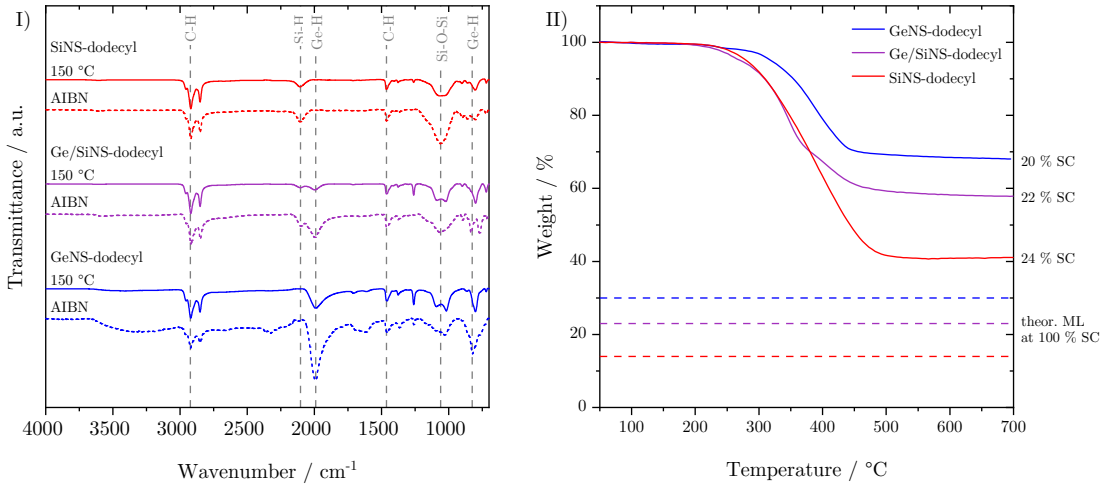

Figure 5.3: Comparison of FTIR spectra of dodecyl-functionalized group IV nanosheets (I) and TGA measurements of SiNS-dodecyl, Ge/SiNS-dodecyl, and GeNS-dodecyl obtained by thermal-induced hydrometalation (II).

Table 5.1: Comparison of the theoretical and experimental TGA mass losses and corresponding surface coverages of radically functionalized SiNS-dodecyl, GeNS-dodecyl, and Ge/SiNS-dodecyl.

	Si-dodecyl		Ge/Si-dodecyl		Ge-dodecyl	
	AIBN	150 °C	AIBN	150 °C	AIBN	150 °C
ML_{theor} / %	86	86	77	77	70	70
ML_{exp} / %	49	59	29	42	17	32
SC_{exp} / %	16	24	12	22	8.6	20

5.2 Selective Functionalization of Germanium/Silicon Nanosheets

Having shown that the literature-known hydrosilylation/hydrogermylation also works with mixed Ge/SiNS-, it is now necessary to establish a preparation pathway for the selective functionalization of Ge/SiNS- in accordance with Scheme 5.3. Introducing different functionalities (e.g. donor and acceptor groups at the same time) to the nanosheets, might enable to tune the material's properties. The question is if a functionalization reaction exists, that exclusively runs with Si or Ge. Therefore, test reactions with monoelemental nanosheets are performed, which are described in this section.

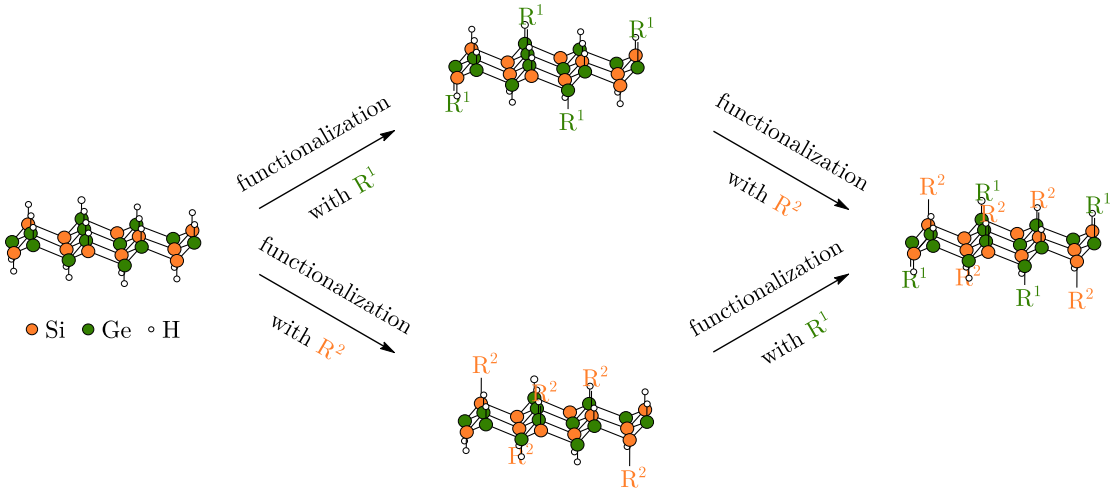

Scheme 5.3: Schematic reaction pathway for selectively functionalized mixed Ge/SiNS.

5.2.1 Hydrometalation of 1-Dodecene

Several methods of hydrometalation reactions with alkenes are known for silicon and germanium nanomaterials, as well as organosilanes or organogermanes in organic synthesis. As already mentioned in the previous section, the AIBN-initiated or thermally-induced hydrosilylation or hydrogermylation of SiNS and GeNS with alkenes yields alkyl-modified nanosheets.[73,76,138] These two initiation types are the only hydrogermylation methods reported for GeNS, whereas for SiNS, hydrosilylation was also achieved with other initiators or catalysts like diaryliodonium salts,[84] diazonium salts,[73] Lewis acids,[83] or chloroplatinic acid[79] (see Chapter 2.2.5). Whether platinum catalysts or the diaryliodonium salt BIP can also be used for the functionalization of GeNS is presented in the following.

Platinum Catalyzed Hydrometalation

Similar to the procedure described by Nakano and coworkers, who prepared hexyl-modified SiNS,[79] chloroplatinic acid hexahydrate is used in the hydrometalation of SiNS or GeNS with 1-dodecene in toluene (Scheme 5.4). The reactions are performed at room temperature. In the literature procedure, the obtained hexyl-modified SiNS is described as an oil soluble in toluene. From the previous radical and thermal hydrometalation experiments, it is known that a solid product is to be expected, which is also the case in the platinum-catalyzed reaction.

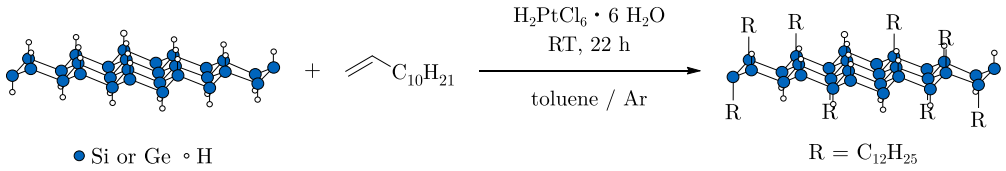

Scheme 5.4: Hydrometalation of group IV nanosheets with 1-dodecene catalyzed by chloroplatinic acid.

FTIR spectra of the two products are shown in Figure 5.4. It shows that only the reaction of SiNS-H with 1-dodecene yields a product with alkyl C-H bending and stretching vibrations at about 2920 cm^{-1} and 1460 cm^{-1}, respectively. Besides these bands, the Si-H vibration (2100 cm^{-1}) is still present after the surface modification, indicating an incompleteness of the functionalization. Further, the most intense band is the Si-O-Si vibration at 1060 cm^{-1}. No alkyl groups are present in the FTIR spectrum of the experiment with GeNS-H, and the spectrum is similar to the non-functionalized material. Consequently, chloroplatinic acid hexahydrate seems to selectively catalyze the hydrosilylation of SiNS-H but does not work in the hydrogermylation of GeNS-H. However, using this platinum salt has some drawbacks: Chloroplatinic acid hexahydrate is known to be highly hygroscopic, which is also observed while preparing the reaction mixtures. Adsorbed water due to the hygroscopy, as well as the hydrate water of the platinum salt, might cause hydrolysis of SiNS-H as described in Chapter 3. Furthermore, the chloroplatinic acid hexahydrate did not completely dissolve in toluene. A higher degree of functionalization will probably be achieved if the catalyst is completely dissolved in the reaction mixture. A complete functionalization would be desired for the selective functionalization of Ge/SiNS so that a second functionalization of Ge in the mixed nanosheets does not need to be selective. Because of these reasons, the

hydrometalation catalyzed by chloroplatinic acid hexahydrate is inconvenient for the selective functionalization of Ge/SiNS-H.

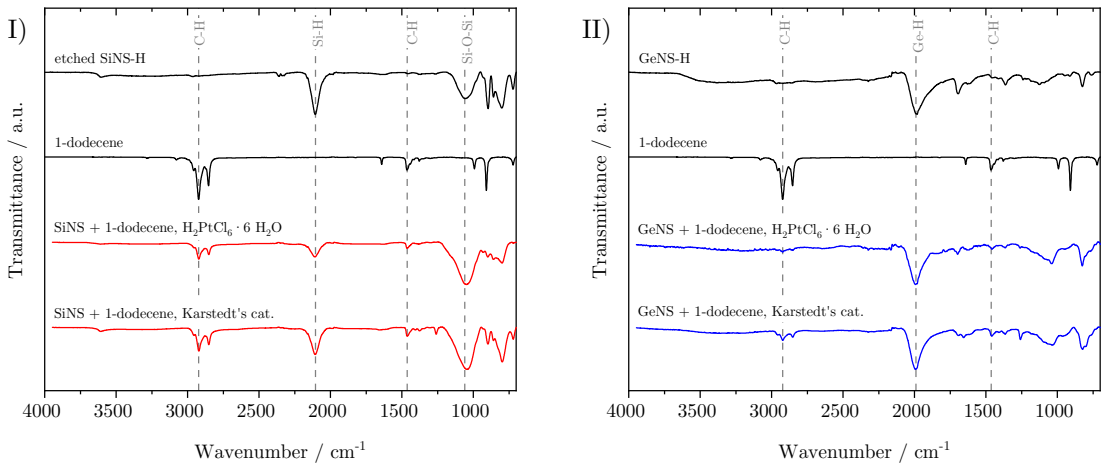

Figure 5.4: FTIR spectra of hydride-terminated nanosheets I) SiNS-H, II) GeNS-H) and 1-dodecene compared to the spectra of the products obtained in the platinum-catalyzed hydrometalation reactions between these two reactants. The used catalysts are chloroplatinic acid hexahydrate and the Karstedt's catalyst.

Alternatively, a platinum catalyst that is not hygroscopic nor contains hydrate water and, at the same time, is soluble in the reaction mixture would be ideal for the selective functionalization of Ge/SiNS. Thus, the Karstedt's catalyst platinum(0)-1,3-divinyl-1,1,3,3-tetramethyldisiloxane ($Pt_2[(Me_2SiCH{=}CH_2)_2O]_3$) is chosen, which is shown in Scheme 5.5.[182] This platinum-siloxane complex is widely employed as a hydrosilylation catalyst.

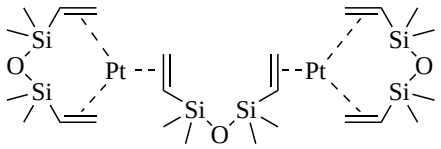

Scheme 5.5: Complex structure of the Karstedt's catalyst.

Hydrometalation reactions with 1-dodecene in toluene are carried out by adding a solution of Karstedt's catalyst in xylene before heating the mixture to 40 °C. Characterization of the products by FTIR spectroscopy (Figure 5.4) shows a similar spectrum of the alkylated SiNS compared to those obtained with chloroplatinic acid. However, the FTIR spectrum of the product obtained from GeNS-H this time shows C-H vibration modes, which were absent in the experiment with

chloroplatinic acid. Although the alkyl vibration bands are more intense with SiNS, both hydrometalation experiments yield dodecyl-functionalized nanosheets, and hence, no exclusive functionalization of SiNS using Karstedt's catalyst is possible. The surface coverages determined by TGA measurements are 7.6 and 8.2 % for SiNS-dodecyl and GeNS-dodecyl, respectively.
After testing two kinds of platinum catalysts in the hydrometalation of SiNS-H or GeNS-H, it was determined that an alternative selective functionalization method would be beneficial. Chloroplatinic acid seemed to selectively functionalize SiNS, but the hydrosilylation was not complete. Additionally, it might cause hydrolysis of the nanosheets because of hydrate water or adsorbed moisture. With Karstedt's catalyst, a surface modification with both nanosheets took place.

Diaryliodonium Salt-Initiated Hydrometalation

The successful dodecyl-functionalization of SiNS-H or hydride-terminated silicon nanocrystals by the diaryliodonium salt-initiated hydrosilylation was previously described by former members of our group.[84] This reaction is reproduced and applied to GeNS-H, with the objective of determining whether this reaction is selective towards SiNS. Therefore, the nanosheets are mixed with 1-dodecene in ethyl acetate and BIP is added as initiator. The corresponding reaction is shown in Scheme 5.6.

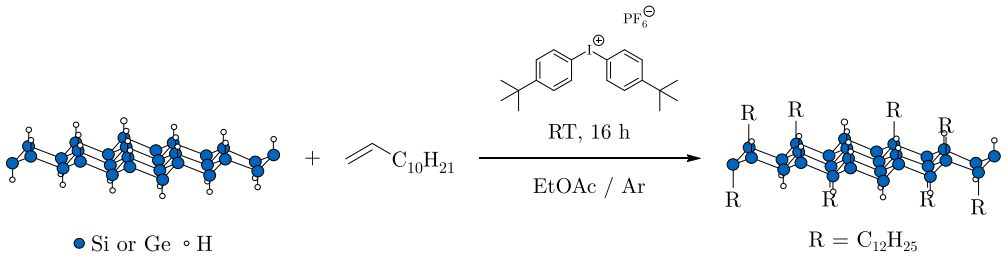

Scheme 5.6: Hydrometalation of group IV nanosheets with 1-dodecene initiated by BIP.

The FTIR spectra (Figure 5.5) of the products both show C-H stretching and bending vibrations from 2850 to 2955 cm^{-1} and at 1460 cm^{-1}, respectively, besides Ge-H (1996 cm^{-1}) or Si-H stretching vibrations (2104 cm^{-1}) and the Si-O-Si band (1040 cm^{-1}). This indicates that both nanomaterials are partially alkylated, and the surface coverages obtained from TGA measurements are 38 and 10 % for SiNS-dodecyl and GeNS-dodecyl, respectively. Thus, the diaryliodonium salt-initiated hydrometalation is not suitable for a selective functionalization of Ge/SiNS-H.

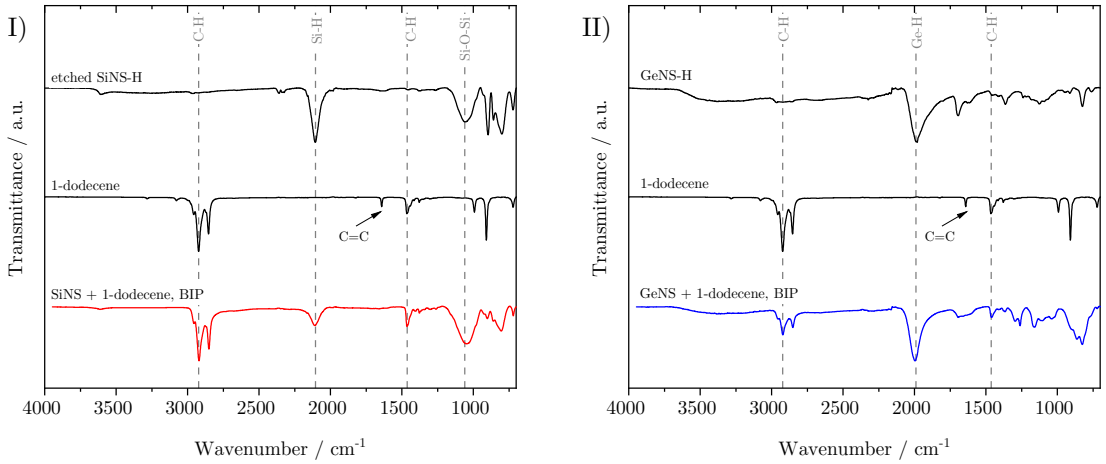

Figure 5.5: FTIR spectra of hydride-terminated nanosheets I) SiNS-H, II) GeNS-H) and 1-dodecene compared to the spectra of the products obtained in the BIP-induced hydrometalation reactions between these two reactants.

5.2.2 Amination

As previously described, attempts at selective functionalization *via* hydrometalation have been unsuccessful. Consequently, the research focus is shifting to other functionalization methods, such as the amination of the nanosheets with primary amines. Okamoto *et al.* intensively studied the amination of SiNS-H with several *n*-alkylamines or α-ω-alkyldiamines.[88,89] According to these reports, the amination takes place under the formation of hydrogen gas according to Scheme 5.7. Two binding modes between the amine and the SiNS-H occur: Si-NH-R linkages, which can further react with an adjacent Si-H group towards Si-NR-Si linkages.[88,89] The application of this or other amine modification methods to GeNS-H remains absent in literature. In order to assess the potential of the amination as a selective functionalization method, reactions with both SiNS-H and GeNS-H are conducted.

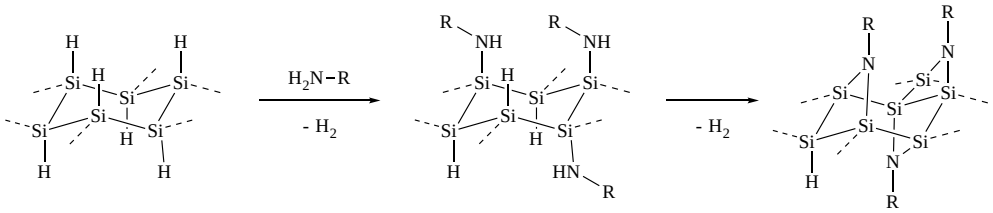

Scheme 5.7: Amination of SiNS-H with primary amines, adapted from Reference 88.

The experiments are carried out using chloroform as solvent and dodecylamine as the substrate. The mixture is stirred at 70 °C. During the reaction with

SiNS-H, the color of the sample changes from yellow to dark orange, whereas the color of the sample with GeNS remains gray. Figure 5.6 compares the FTIR spectra of the nanosheets before and after the reactions. After the reaction, strong alkyl stretching and bending vibrations at 2850 to 2950 cm^{-1}, 1468 and 1489 cm^{-1} appear in the FTIR spectrum of the SiNS containing sample. The spectrum still contains bands at approximately 2105 and 1060 cm^{-1} which belong to the Si-H stretching and the Si-O-Si stretching mode. Additionally, small bands at 930 and 1150 cm^{-1} are assigned to the asymmetric Si-N-Si stretching and the N-H bending vibration in Si-NH-C, respectively.[89] This indicates evidence of covalently bound amine ligands and, thus, a successful surface functionalization. FTIR analysis of the GeNS product shows a similar spectrum (Figure 5.6). Intense C-H vibration modes are visible beside a remaining Ge-H stretching vibration at 1999 cm^{-1}. Thus, the amination works for both SiNS and GeNS and is not eligible for selective functionalization of mixed Ge/SiNS.

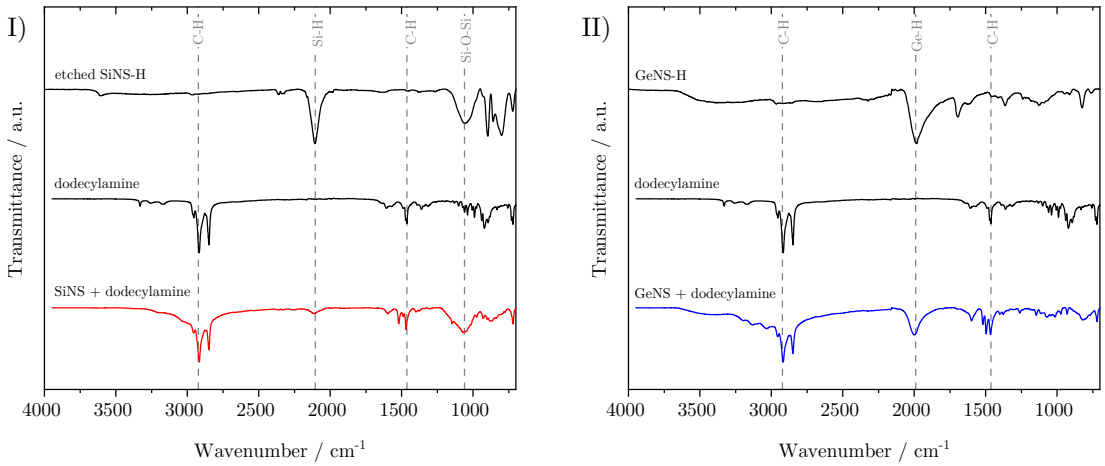

Figure 5.6: FTIR spectra of hydride-terminated nanosheets I) SiNS-H, II) GeNS-H and dodecylamine compared to the spectra of the corresponding amination products.

5.2.3 Thiolation and Subsequent Ligand Exchange

The experiments described above attempted to identify a selective reaction between an organic substrate and the Ge-H or Si-H bond. However, this approach did not yield the desired results. Therefore, a novel strategy is proposed in which both nanosheets are functionalized with a single ligand. This ligand is then selectively removed from either Si or Ge, and replaced by another substrate. This idea is inspired by a publication of the Korgel group, in which hydride-terminated silicon nanocrystals were thiolated with 1-dodecanethiol and the thiol moieties

were subsequently replaced with dodecyl groups according to Scheme 5.8.[183] The mechanism of the ligand exchange was not determined in this study.

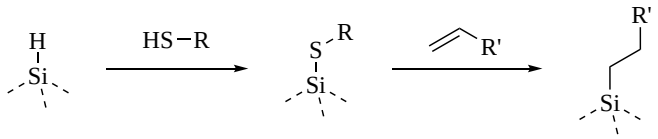

Scheme 5.8: Schematic description of the thiolation of silicon atoms in silicon nanocrystals and subsequent ligand exchange of the thiolated material by the reaction with an alkene.

Thioalkyl-modified nanosheets are attempted to be prepared through the reaction between SiNS-H or GeNS-H and 1-dodecanethiol similar to the procedure of the Korgel group. After test reactions of the thermally promoted thiolation at 185 °C, the products are characterized by FTIR spectroscopy. FTIR analysis of both products is represented in Figure 5.7 and shows a weak S-C stretching mode at 720 cm^{-1} besides C-H vibration modes (symmetric and asymmetric stretching in the range from 2850 to 2950 cm^{-1} and asymmetric bending at 1459 cm^{-1}). These bands have similar intensities as the remaining Si-H or Ge-H stretching vibrations at 2105 and 1992 cm^{-1}, respectively. This proves that the thiolation reaction under the applied conditions takes place, however is incomplete. Additionally, the spectrum of the thiolated SiNS shows evidence of oxidation because of the Si-O-Si band at 1063 cm^{-1}. Although the reaction products are only partially functionalized, an attempt is made to replace the thiododecyl groups with dodecyl groups by heating the thiol-capped nanosheets in 1-dodecene at 185 °C. Afterward, the alkyl vibration bands in the FTIR spectra (see Figure 5.7) are significantly increased compared to those after the thiolation. The spectrum of the SiNS shows a significant decrease in the intensity of the Si-H stretching band (2104 cm^{-1}). The intense Si-O-Si band, which was already present after thiolation, remains after the treatment with 1-dodecene. After exposure to 1-dodecene, the Ge-H stretching mode in the spectrum of the GeNS disappeared completely. The success of the ligand exchange is difficult to interpret from these spectra. The presence of the alkyl C-H vibrational features does not clearly confirm that the thiol groups are replaced by alkyl groups. Since the thiolation is not effective with respect to the degree of functionalization, Si-H and Ge-H bonds are still present after the thiolation. Thus, hydrometalation of the remaining Si-H or Ge-H bonds with 1-dodecene takes place in the second reaction step, leading to more intense alkyl modes in the FTIR spectra. It is not clear if this occurs simultaneously with

the ligand exchange or if only the hydrometalation occurs. Furthermore, the S-C stretching mode ($720\,cm^{-1}$) is not a valuable indicator of ligand exchange, since these bands are relatively weak in the FTIR spectra of the thiolated nanosheets. It is not clear whether these modes have disappeared in the spectra after the reaction with 1-dodecene or whether their intensity is now even lower compared to the increased alkyl bands. To further examine the reaction with 1-dodecene, energy dispersive X-ray (EDX) spectroscopy is performed before and after the conversion with the alkene. Tables 5.2 and 5.3 list the measured weight percentages of the elements detected in the samples. (Note that the EDX spectroscope cannot detect elements lighter than sodium.) Chlorine and calcium are found in all samples. The origin of these impurities is the preparation of the nanosheets from the Zintl phases $CaSi_2$ and $CaGe_2$ with $HCl_{(aq)}$. As expected, the samples contain sulfur after the thiolation reaction. The values of the S/Si and S/Ge ratios are up to 0.14 and 0.087, respectively. This confirms the FTIR results showing an incomplete functionalization of the nanosheets. If exposure to 1-dodecene results in ligand exchange, the values of the S/Si and S/Ge ratios should be zero after the reaction with the alkene. In contrast to this, the EDX analysis still confirms the presence of sulfur in both types of nanosheets. Thus, either no ligand exchange is taking place or it is insufficient.

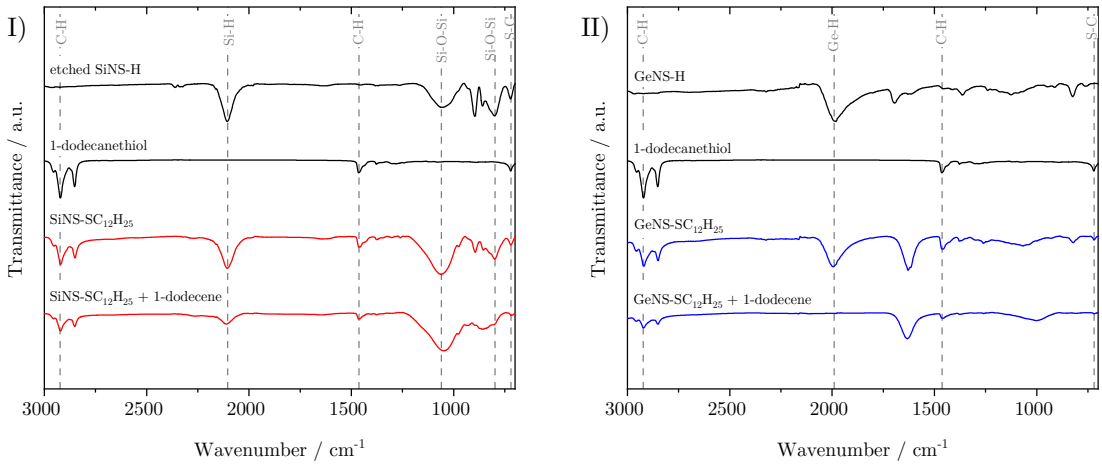

Figure 5.7: FTIR spectra of hydride-terminated nanosheets SiNS-H (I), GeNS-H (II), 1-dodecanethiol, the corresponding thiolation products and the products of their reaction with 1-dodecene.

In conclusion, thiolation is a surface modifcation method applicable to SiNS-H and GeNS-H. No high surface coverages are achieved and thus the nanosheets remain partially hydride-terminated. The experiments show that the subsequent exposure

Table 5.2: Weight percentages of the elements detected in SiNS-$SC_{12}H_{25}$ and the same materials after conversion with 1-dodecene, determined by EDX analysis. From these values the molar S/Si ratios were calculated. Each sample was measured three times at different locations.

	Si / wt%	S / wt%	Cl / wt%	Ca / wt%	S/Si
SiNS-$SC_{12}H_{25}$					
1	75	11	12	1.4	0.13
2	73	12	14	1.9	0.14
3	82	—	17	1.7	—
SiNS-$SC_{12}H_{25}$ + $C_{12}H_{25}$					
1	77	6.3	15	1.9	0.072
2	76	7.7	14	2.2	0.089
3	76	6.5	15	2.2	0.075

Table 5.3: Weight percentages of the elements detected in GeNS-$SC_{12}H_{25}$ and the same materials after conversion with 1-dodecene, determined by EDX analysis. From these values the molar S/Ge ratios were calculated. Each sample was measured three times at different locations.

	Ge / wt%	S / wt%	Cl / wt%	Ca / wt%	S/Ge
GeNS-$SC_{12}H_{25}$					
1	81	2.3	13	3.5	0.064
2	83	2.8	12	1.8	0.076
3	81	3.1	12	3.6	0.087
GeNS-$SC_{12}H_{25}$ + $C_{12}H_{25}$					
1	84	2.6	11	2.0	0.070
2	82	2.8	12	2.9	0.077
3	80	4.1	12	4.0	0.12

of the thiolated nanosheets to 1-dodecene, does not lead to the replacement of all thiol groups by alkyl groups. It cannot be excluded that some ligand exchange occurs, and if so, it occurs simultaneously with the hydrometalation between 1-dodecene and the remaining Si-H and Ge-H bonds. In conclusion, this reaction sequence is not an approach to the selective functionalization of mixed Ge/SiNS-H.

5.3 Summary

In this chapter, functionalization routes for mixed Ge/SiNS-H were investigated. The motivation for this study was the absence of functionalization methods for

mixed nanosheets in the existing literature. At the same time, various modification procedures are known for pure SiNS-H or GeNS-H. An interesting research goal is the selective functionalization of Ge/SiNS-H, where silicon and germanium atoms are modified differently.

First, functionalization experiments were conducted with the literature-known radical and thermal hydrosilylation/hydrogermylation reactions between GeNS-H, Ge/SiNS-H, and SiNS-H with 1-dodecene. Comparison of the dodecyl-terminated nanosheets showed, that thermally-induced reactions lead to higher surface coverages than radical-initiated reactions, which was already known for GeNS-H and SiNS-H. It was shown that the surface coverages increase from GeNS to Ge/SiNS to SiNS, regardless of the induction of the hydrometalation. The highest achieved surface coverage was 24 % (SiNS-H, thermal hydrometalation). The main reason for this low degree of functionalization is probably the fact that the model of an ideal nanosheet represents only a part of the real material. Most of the material exists as stacks of several nanosheets, and thus only a fraction of the surface sites is accessible to reactions. It should also be noted that the surface coverage also depends on the batch of nanosheets.

The second project described in this chapter was the search for a functionalization that runs exclusively with SiNS-H or GeNS-H. Such a reaction would be promising for a selective modification of Ge/SiNS-H. Hydrometalation reactions were conducted with 1-dodecene using either platinum catalysts or the diaryliodonium salt BIP. Subsequently, the amination of the nanosheets with dodecylamine was tested. Finally, the thiolation of the nanosheets with 1-dodecanethiol and the possible subsequent ligand exchange with 1-dodecene was investigated. It was found that all of these reactions were neither selective nor efficient in terms of surface coverage. In conclusion, none of the tested approaches proved suitable for the selective functionalization of Ge/SiNS-H.

5.4 Experimental Procedures

5.4.1 General Information

Instrument information, analytical techniques, procedures for solvent drying, the syntheses of hydride-terminated nanosheets as well as the etching procedure of SiNS-H and Ge/SiNS-H are found in Chapter 9.

The reactants were purchased from Sigma-Aldrich and abcr. 1-Dodecene is dried by passing through a column of heat-dried basic silica and degassed, before storage

over molecular sieve (4 Å) within in argon-filled glove box. AIBN is recrystallized from dry ethanol and dried in vacuum.
All reactions are performed under exclusion of water and air, using standard Schlenk methods and heat-dried glassware. All solvents are dried and degassed prior to use.

5.4.2 AIBN-Initiated Hydrometalation

The reaction mixtures are prepared inside an argon-filled glove box. Hydride-terminated nanosheets and AIBN are dispersed/dissolved in toluene in Schlenk tube. 1-dodecene is added to this mixture. Table 5.4 lists the used amounts of the reactants. Each dispersion is degassed in three freeze-pump-thaw cycles, after which they are sonicated for two hours. The mixture is then stirred at 70 °C for 16 hours. The reaction mixture is transferred into a centrifuge tube, and the mixture is centrifuged (4500 rpm, 5 min). The supernatant is discarded and the solid is redispersed in toluene (1 mL). Methanol (6 mL) is added and the mixture is centrifuged. This washing procedure is repeated three times. The remaining solid is freeze-dried from benzene.

5.4.3 Thermally induced Hydrometalation

Hydride-terminated nanosheets are dispersed in 1-dodecene in a Schlenk tube inside an argon-filled glove box. Table 5.5 lists the used amounts of the reactants. The dispersion is degassed in three freeze-pump-thaw cycles, after which the dispersion is sonicated for 30 min. The mixture is then stirred at 150 °C for 16 hours. The reaction mixture is transferred into a centrifuge tube, methanol (15 mL) is added and the mixture is centrifuged (9000 rpm, 14 min). The supernatant is discarded and the solid is redispersed in toluene (1 mL). Methanol (15 mL) is added and the mixture is centrifuged. This washing procedure is repeated twice. The remaining solid is freeze-dried from benzene.

5.4.4 Platinum Catalyzed Hydrometalation

Chloroplatinic Acid

The chloroplatinic acid catalyzed hydrometalation follows the protocol described in Reference 79. Hydride-terminated nanosheets are dispersed in toluene in a Schlenk tube in an argon-filled glove box. 1-Dodecene is added to this mixture.

The Schlenk tube is connected to a Schlenk line and chloroplatinic acid hexahydrate is added to the dispersion in an argon counterflow. The exact amounts of the reagents are listed in Table 5.6. The dispersion is degassed in three freeze-pump-thaw cycles and stirred at room temperature for 22 hours. The reaction mixture is transferred into a centrifuge tube and centrifuged (4500 rpm, 5 min). The supernatant is discarded and the solid is redispersed in toluene (0.5 mL). Methanol (5 mL) is added and the mixture is centrifuged. This washing procedure is repeated twice. To remove residues of the platinum salt, the remaining solid is washed with water (3 mL) and centrifuged. The washing/redispersion cycle with toluene and methanol is repeated three times. The remaining residue is freeze-dried from benzene.

Karstedt's Catalyst

Hydride-terminated nanosheets are dispersed in toluene in a Schlenk tube in an argon-filled glove box. 1-Dodecene and a solution of Karstedts' catalyst (2.1 to 2.4 % Pt in xylene) is added to the dispersion. The exact amounts of the reagents are listed in Table 5.7. The dispersion is degassed in three freeze-pump-thaw cycles and stirred at 40 °C for 20 hours. The reaction mixture is transferred into a centrifuge tube and centrifuged (4000 rpm, 2 min). The supernatant is discarded and the solid is redispersed in toluene (0.5 mL). Acetonitrile (5 mL) is added and the mixture is centrifuged. This washing procedure is repeated twice. The remaining residue is freeze-dried from benzene.

5.4.5 Diaryliodonium Salt-Initiated Hydrometalation

Hydride-terminated nanosheets and BIP are dispersed/dissolved in ethyl acetate in a Schlenk tube in an argon-filled glove box. 1-Dodecene is added to the dispersion. The exact amounts of the reagents are given in Table 5.8. The dispersion is degassed in three freeze-pump-thaw cycles and sonicated for two hours, after which the mixture is stirred at room temperature for 16 hours. The reaction mixture is transferred into a centrifuge tube and centrifuged (4000 rpm, 2 min). The supernatant is discarded and the solid is redispersed in toluene (0.5 mL). Acetonitrile (5 mL) is added and the mixture is centrifuged. This washing procedure is repeated twice. The remaining residue is freeze-dried from benzene.

5.4.6 Amination

The amination of hydride-terminated nanosheets follows the protocol described in Reference 89. Hydride-terminated nanosheets and dodecylamine are dispersed/dissolved in chloroform in a Schlenk tube. The exact amounts of the reagents are given in Table 5.9. The mixture is stirred at 70 °C for 18 hours. The reaction mixture is transferred into a centrifuge tube and centrifuged (4000 rpm, 2 min). The supernatant is discarded and the solid is redispersed in toluene (0.5 mL). Acetonitrile (5 mL) is added and the mixture is centrifuged. This washing procedure is repeated twice. The remaining residue is freeze-dried from benzene.

5.4.7 Thiolation and Subsequent Ligand Exchange

Hydride-terminated nanosheets are dispersed in 1-dodecanethiol in a Schlenk tube. The exact amounts of the reagents are given in Table 5.10. The mixture is stirred at 185 °C for 15 hours. The product mixture is subsequently centrifuged (4000 rpm, 2 min) and the supernatant is discarded. The solid is redispersed in toluene (0.5 mL). Acetonitrile (5 mL) is added and the mixture is centrifuged. This washing procedure is repeated twice. The remaining residue is freeze-dried from benzene.

For the ligand exchange, thiolated nanosheets are dispersed in an excess of 1-dodecene (372 mg, 2.2 mmol, 6.5 eq. for SiNS; 220 mg, 1.3 mmol, 2.4 eq. for GeNS) in a Schlenk tube. The dispersion is degassed in three freeze-pump-thaw cycles, after which the mixture is stirred at 185 °C for 16 hours. The reaction mixture is transferred into a centrifuge tube and centrifuged (4000 rpm, 2 min). The supernatant is discarded and the solid is redispersed in toluene (0.5 mL). Acetonitrile (5 mL) is added and the mixture is centrifuged. This washing procedure is repeated twice. The remaining residue is freeze-dried from benzene.

Table 5.4: Reactant compositions for the AIBN-initiated hydrometalation reactions of 1-dodecene with etched SiNS-H, etched Ge/SiNS-H, and GeNS-H.

	NS-H	AIBN	1-Dodecene	Toluene
Si	48 mg, 1.6 mmol, 1.0 eq.	238 mg, 1.5 mmol, 0.9 eq.	2.7 g, 16 mmol, 10 eq.	4.1 mL
Ge/Si	49 mg, 0.95 mmol, 1.0 eq.	138 mg, 0.84 mmol, 0.9 eq.	1.7 g, 9.8 mmol, 10 eq.	2.4 mL
Ge	50 mg, 0.67 mmol, 1.0 eq.	99.1 mg, 0.60 mmol, 0.9 eq.	1.2 g, 7.1 mmol, 10 eq.	1.7 mL

Table 5.5: Reactant compositions for the thermal hydrometalation reactions of 1-dodecene with etched SiNS-H, etched Ge/SiNS-H, and GeNS-H.

	NS-H	1-Dodecene
Si	10 mg, 0.36 mmol, 1.0 eq.	2.9 g, 17 mmol, 48 eq.
Ge/Si	11 mg, 0.15 mmol, 1.0 eq.	1.5 g, 9.1 mmol, 48 eq.
Ge	10 mg, 0.19 mmol, 1.0 eq.	1.1 g, 6.8 mmol, 46 eq.

Table 5.6: Reactant compositions for the hydrometalation reactions of 1-dodecene with etched SiNS-H and GeNS-H catalyzed by chloroplatinic acid.

	NS-H	$H_2PtCl_6 \cdot 6\ H_2O$	1-Dodecene	Toluene
Si	9.9 mg, 0.34 mmol, 1.0 eq.	37 mg, 0.07 mmol, 0.2 eq.	1.7 g, 10 mmol, 30 eq.	1.1 mL
Ge	12 mg, 0.16 mmol, 1.0 eq.	17 mg, 0.03 mmol, 0.2 eq.	830 mg, 4.9 mmol, 30 eq.	0.56 mL

Table 5.7: Reactant compositions for the hydrometalation reactions of 1-dodecene with etched SiNS-H and GeNS-H catalyzed by the Karstedt's catalyst.

	NS-H	Karstedt's catalyst	1-Dodecene	Toluene
Si	10 mg, 0.34 mmol, 1.0 eq.	50 µL	1.1 g, 5.2 mmol, 15 eq.	1.0 mL
Ge	16 mg, 0.21 mmol, 1.0 eq.	30 µL	670 mg, 3.0 mmol, 14 eq.	0.6 mL

Table 5.8: Reactant compositions for the diaryliodonium salt-initiated hydrometalation reactions of 1-dodecene with etched SiNS-H and GeNS-H.

	NS-H	BIP	1-Dodecene	Ethyl acetate
Si	10 mg, 0.34 mmol, 1.0 eq.	4.0 mg, 0.01 mmol, 0.02 eq.	259 mg, 1.5 mmol, 4 eq.	0.5 mL
Ge	10 mg, 0.14 mmol, 1.0 eq.	1.5 mg, 2.8 µmol, 0.02 eq.	106 mg, 0.63 mmol, 5 eq.	0.2 mL

Table 5.9: Reactant compositions for the amination of etched SiNS-H and GeNS-H.

	NS-H	Dodecylamine	Chloroform
Si	11 mg, 0.37 mmol, 1.0 eq.	80 mg, 0.43 mmol, 1.2 eq.	1 mL
Ge	11 mg 0.15 mmol, 1.0 eq.	33 mg 0.18 mmol, 1.2 eq.	0.4 mL

Table 5.10: Reactant compositions for the thiolation of etched SiNS-H and GeNS-H.

	NS-H	1-Dodecanethiol
Si	10 mg, 0.34 mmol, 1.0 eq.	452 mg, 2.2 mmol, 6.5 eq.
Ge	40 mg, 0.54 mmol, 1.0 eq.	723 mg, 3.6 µmol, 6.5 eq.

6

Selective Removal of Silicon from Germanium/Silicon Nanosheets

Chapter 5 describes attempts to find a functionalization procedure to selectively modify mixed Ge/SiNS. The exclusive functionalization of SiNS-H or GeNS-H with organic ligands *via* hydrometalation, amination, or thiolation and subsequent ligand exchange were tested. None of these reactions were selective towards SiNS or GeNS. A literature review provided an additional approach to selectively functionalized mixed Ge/SiNS: The reaction of hydride-terminated nanosheets with *n*-butyllithium (*n*BuLi).

In a study by Giousis *et al.*, the functionalization of GeNS-H with *n*BuLi was described, resulting in butyl-functionalized GeNS.[139] However, no comparable alkyl modification of SiNS-H can be found in the literature. Years ago, our group reported that organolithium compounds functionalize hydride-terminated silicon nanocrystals, which usually can be functionalized with the same methods as SiNS-H.[184] Apparently, the reactivities of germanium and silicon surfaces towards organolithium compounds differ from each other. Two different reaction mechanisms are described for the germanium and silicon containing nanomaterials. For GeNS, it is assumed that the nucleophilic organic moiety attaches to a germanium atom under substitution of the hydrogen atom, which forms lithium hydride (Scheme 6.1 a)).[139] In contrast, for silicon surfaces like porous silicon or

silicon nanocrystals, a cleavage of a surface Si-Si bond is supposed to happen by the addition of the organolithium reagent across the Si-Si bond. As result, one Si atom is terminated with hydrogen and the organic moiety, and the other Si atom binds to a hydrogen and a lithium atom (Scheme 6.1 b)).[184,185] Similar observations were made for molecular silicon compounds like hexamethyldisilane treated with methyllithium (Scheme 6.1 c)).[186] If this mechanism is transferred to SiNS-H, which consist of a 2D silicon network, this network is destroyed by the Si-Si bond cleavage upon reaction with an organolithium compound.

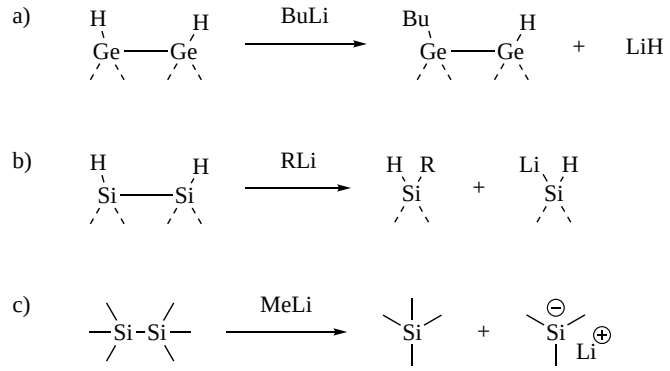

Scheme 6.1: Reactivities of germanium and silicon surfaces towards organolithium reagents: Reactions between a) GeNS-H and *n*BuLi, b) silicon surfaces and RLi, and c) hexamethyldisilane and methyllithium.

Rather than selectively functionalizing mixed Ge/SiNS, the selective decomposition of Ge/SiNS through the cleavage of Si-Si bonds with organolithium reagents is a viable option. Therefore, GeNS-H and SiNS-H are treated with *n*BuLi, which is described in the first section of this chapter. It is shown that no destruction of the Si-Si network occurs by adding *n*BuLi to SiNS-H, contrary to what was expected. Instead, it is observed that lithium methoxide (MeOLi) might induce the cleavage of Si-Si bonds and, thus, the decomposition of SiNS-H. This finding is verified in the second section of this chapter, where the reactivities of GeNS-H and Ge/SiNS-H towards MeOLi are also investigated.

6.1 Reactions with *n*-Butyllithium

6.1.1 Germanium Nanosheets

First, the butyl-functionalization of GeNS-H, following the methodology outlined by Giousis is reproduced.[139] The reaction takes place at room temperature in

hexane, and the resulting dark gray product is analyzed using FTIR spectroscopy (Figure 6.1). According to the FTIR spectra, the starting material GeNS-H, as well as the butylized GeNS, contain water as an impurity. The product spectrum displays weak C-H vibration bands of the *n*-butyl group, including symmetric and asymmetric stretching between 2850 to 2950 cm^{-1}, and bending at around 1450 cm^{-1}. The Ge-H stretching (1987 cm^{-1}) and bending (825 cm^{-1}) modes remain relatively intense after butylation. The Ge-H vibrations in the product are stronger than those reported in the literature product by Giousis.[139] This suggests that it has a lower degree of functionalization, which is reproducible low. Upon repeating the reaction, the spectrum is almost identical.

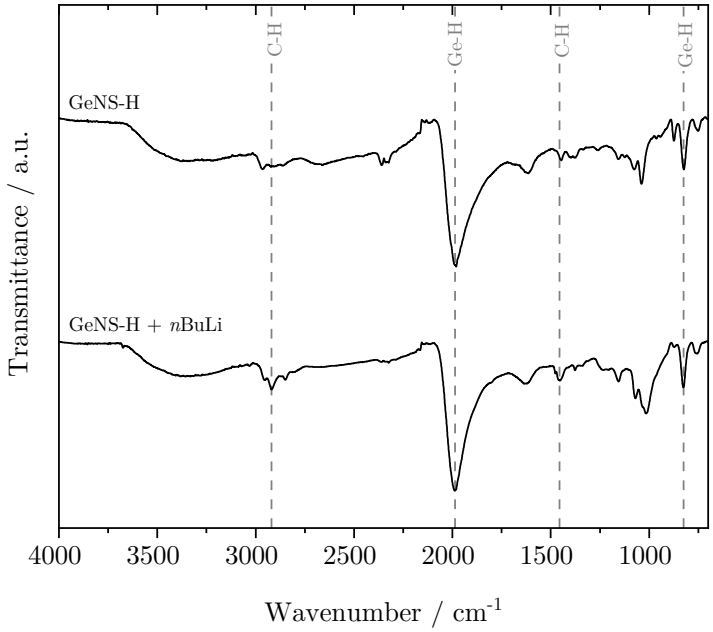

Figure 6.1: FTIR spectra of GeNS-H before and after the reaction with *n*BuLi.

6.1.2 Silicon Nanosheets

According to the literature (see above), it is anticipated that the silicon network is destroyed in SiNS-H upon the reaction with organolithium compounds.[184–186] The experimental procedure for SiNS-H is identical to that of GeNS-H. After stirring a mixture of HF-etched SiNS-H and *n*BuLi in hexane, a dispersed solid yellow product is obtained. The separated solid product is first washed with hexane and subsequently with methanol. In the initial trial, the product immediately dissolves and gas is evolved upon the addition of methanol. The disappearance of the yellow solid indicates nanosheet decomposition. However, if the nanosheets

were to decompose during the reaction with organolithium compounds, they would have already dissolved before the workup. Instead, there is no difference between the starting material and reaction product; before and after the treatment with *n*BuLi the yellow powder looks identical. Moreover, multiple repetitions of this experiment demonstrate that the first observation of the decomposition during the washing step is not reproducible, as no dissolution occurs during the workup of the repeated experiments. So, the question of how the nanosheets decomposed in the first experiment arises. An experiment is performed without the methanol washing step and the yellow powdery product is characterized by FTIR spectroscopy after the hexane wash. No significant structural change compared to SiNS-H is visible in the FTIR spectrum (Figure 6.2). Solely, some weak C-H vibrations (2850 to 2955 cm^{-1} and 1458 cm^{-1}) appear after the treatment with *n*BuLi. Therefore, either no reaction between *n*BuLi and SiNS-H takes place or a butylation of the SiNS occurs to a minor degree without destruction of the whole silicon network. Indeed, Raman spectroscopy shows that the spectra of etched SiNS-H are identical before and after the treatment with *n*BuLi as displayed in Figure 6.2. Both spectra exhibit Raman features assigned to Si-Si (378 and 493 cm^{-1}) and Si-H vibration modes (635, 730 and 2115 cm^{-1}).[58] This verifies the integrity of the silicon network after the exposure to *n*BuLi.

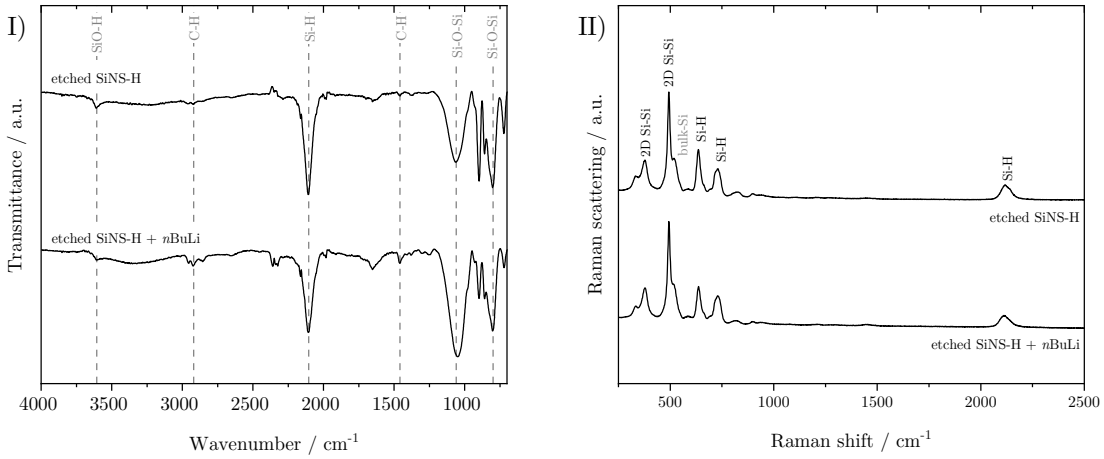

Figure 6.2: FTIR (I) and Raman spectra (II) of SiNS-H before and after treatment with *n*BuLi.

The observation of decomposition in the aforementioned experiment, in which methanol was added, suggests that the origin of the nanosheet decomposition may lie elsewhere than in the reaction with *n*BuLi. A possible explanation could

be the formation of MeOLi by the reaction of incompletely removed *n*BuLi with methanol according to Scheme 6.2. MeOLi then potentially reacts with the SiNS by cleaving the Si network. This hypothesis is proven in another experiment: After stirring the reaction mixture as usually, methanol is directly added to the reaction mixture instead of removing the *n*BuLi during the workup. A violent exothermic reaction with gas evolution takes place, which is in accordance with the formation of butane and MeOLi. At the same time, the yellow nanosheets disappear, leaving a colorless solution behind.

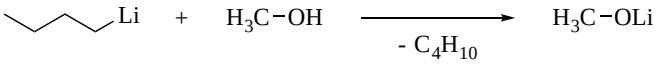

Scheme 6.2: Formation of MeOLi from *n*BuLi and methanol.

Summarizing the results of the experimental series described in this section, *n*BuLi reacts with GeNS-H yielding sparsely covered GeNS-butyl. Regarding the reaction between *n*BuLi and SiNS-H, it was anticipated that the nanosheets would decompose *via* the cleavage of Si-Si bonds, analogous to the reaction mechanism known for silicon nanocrystals or porous silicon. However, this was experimentally disproved. Instead it was found that MeOLi is able to decompose SiNS into a product which is soluble in methanol. This is further investigated in the next section.

6.2 Reactions with Lithium Methoxide

After finding that *n*BuLi does not affect the Si network structure in SiNS, the experimental results indicated that MeOLi cleaves Si-Si bonds and thus destroys the SiNS-H. This needs a detailed investigation to understand what happens in the reaction between SiNS-H and MeOLi, which is demonstrated in this section. Additionally, the reactivities of SiNS-H, GeNS-H, and Ge/SiNS-H towards MeOLi are investigated.

6.2.1 MeOLi-Induced Degradation of Silicon Nanosheets

In a first test reaction, a solution of excess MeOLi in methanol is added to SiNS-H to prove the hypothesis of MeOLi being responsible for the degradation of the nanomaterial (note that in the experiments in this section the used SiNS-H are not HF-etched). Indeed, a violent exothermic reaction with gas evolution takes

place similar to the aforementioned observation when adding methanol to the reaction mixture of the experiment with *n*BuLi. The nanosheets dissolve, and very little light gray solid remains in the colorless solution. Hence, there is a soluble and an insoluble fraction of SiNS-H decomposition products. This observation is analogous to the phenomenon observed when a solution of potassium hydroxide is added to SiNS-H.

Characterization of the Soluble Product

After separating the solution from the solid by centrifugation, the soluble product is characterized by ^{1}H NMR spectroscopy in $CDCl_3$. The spectrum of the decomposition product exhibits a singlet at 3.59 ppm, which matches the chemical shift of tetramethyl orthosilicate $Si(OMe)_4$ (TMOS), and a smaller singlet at 3.54 ppm (for a detailed analysis of the product NMR spectrum see below).
Knowing that TMOS is formed in the decomposition process, a reaction mechanism of the methanolysis is proposed, which is depicted in Scheme 6.4. Two main reactions lead to the TMOS formation. In the first step, hydride-terminated SiNS are transformed into methoxy-terminated SiNS, and in the second step, Si-Si bonds are cleaved by MeOLi and methanol. The electronegativity of hydrogen is relatively larger than that of silicon. Thus, the Si-H bond is polarized as $Si^{\delta+}$-$H^{\delta-}$ and a nucleophilic attack occurs at silicon atoms. Consequently, the nucleophilic methoxy group attaches to a silicon atom of the 2D network, and molecular hydrogen is formed by Si-H bond cleavage through the interaction with a proton of the solvent methanol. At the same time, lithium methoxide is regenerated. From the alkaline alcoholysis of organosilanes, it is known that two mechanisms are possible for this reaction.[187] Either a two-step process *via* a pentacoordinated silicon anion occurs (Scheme 6.3 a)), or a concerted mechanism takes place (Scheme 6.3 b)). It is difficult to predict which mechanism is valid for silicon surfaces like SiNS-H. Steric hindrance due to the 2D silicon network might favor the concerted mechanism, but this question cannot be answered without proof.

After the substitution of the hydrides by methoxy groups, Si-Si bond cleavage occurs, similar to the Si-H bond cleavage described before. Again, the nucleophilic attack of the methoxide either takes place through the pentavalent anionic intermediate or in a concerted way. Cleavage of the Si-Si bond through methanol results in a silicon species substituted with methoxy groups and a second one, which is hydride-terminated. This species again undergoes methanolysis under

the substitution of the hydride by a methoxy moiety. The reaction ends when all Si-Si bonds are cleaved and all hydrides are exchanged by methoxy groups. This equates to the formation of one TMOS molecule per each silicon atom in the SiNS. Overall, these reaction steps are driven by the high bond energy of the Si-O bonds formed (368 kJ mol^{-1}) compared to the lower bond energies of the Si-H (323 kJ mol^{-1}) and Si-Si bonds (210 to 250 kJ mol^{-1}).[172]

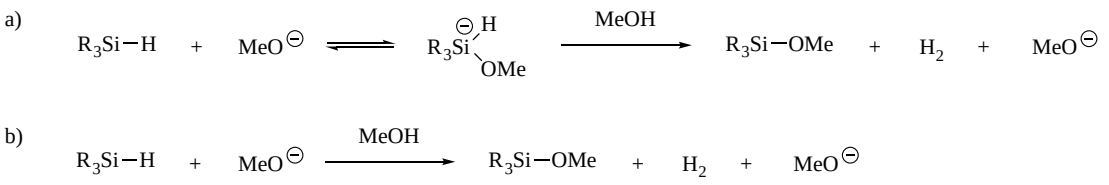

Scheme 6.3: Two possible mechanisms of the methanolysis at a hydride-terminated silicon atom. a) shows the mechanism *via* the pentacoordinated intermediate and b) depicts the concerted mechanism. Adapted from Reference 187.

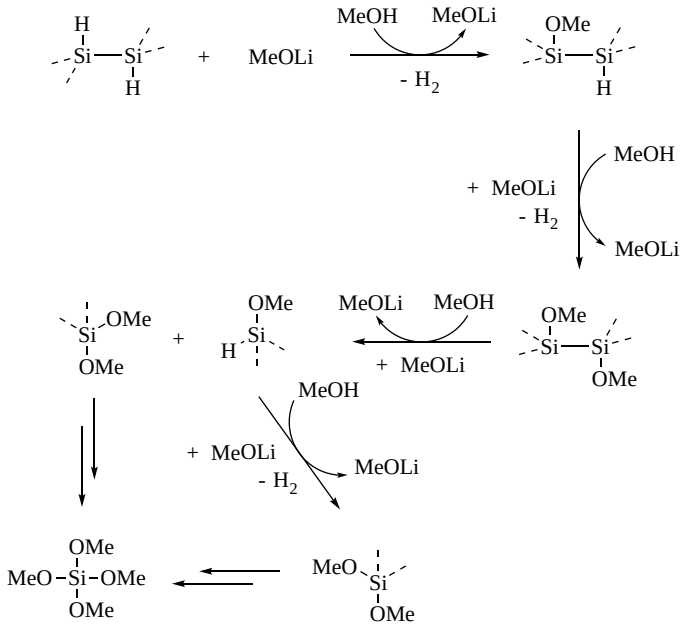

Scheme 6.4: Proposed reaction mechanism of the MeOLi-induced decomposition of SiNS-H, exemplarily represented by a Si-Si bond of the 2D silicon network. The substitution reactions either occur *via* a pentacoordinated silicon anion or in a concerted mechanism.

If this proposed mechanism was correct, MeOLi is not consumed but it is continuously recovered during the reaction, which means the reaction is autocatalytic. Thus catalytic amounts of MeOLi are expected to be sufficient for the degradation

of SiNS-H as long as there is enough methanol present. To prove this, the reaction is repeated with 0.1 and 0.5 equivalents of MeOLi.
With 0.5 equivalents of MeOLi, the decomposition of the nanosheets occurs similar to the experiment with excess MeOLi. The dissolved product is characterized by ^{1}H and ^{29}Si NMR spectroscopy in MeOD-d_4. These spectra are shown in Figure 6.3.

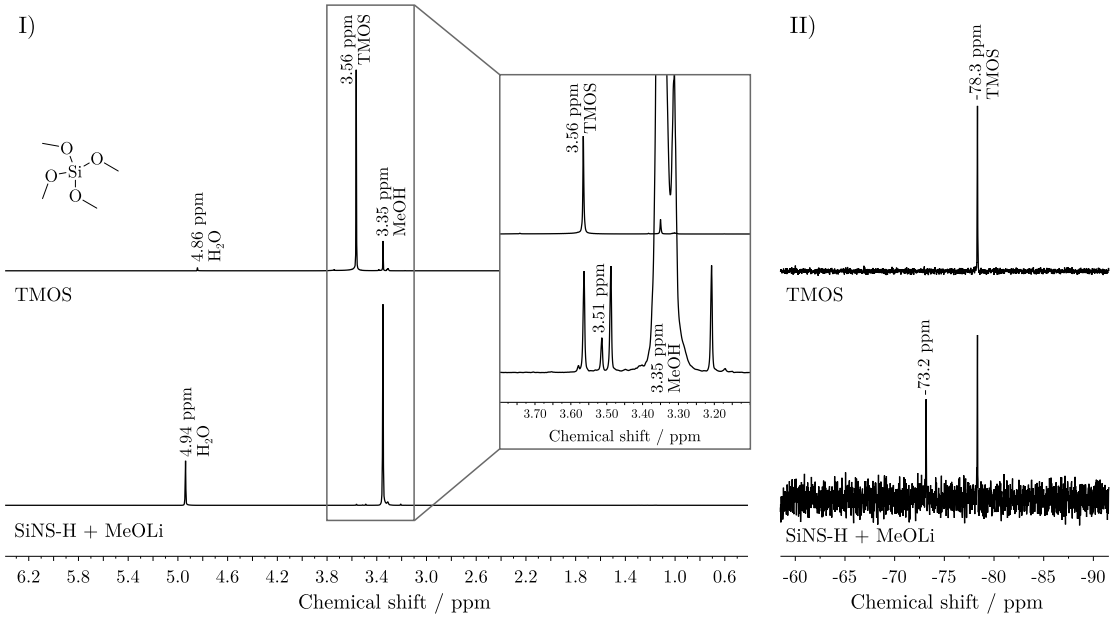

Figure 6.3: Comparison of the ^{1}H (I) and ^{29}Si NMR spectra (II) of the reaction mixture obtained from the reaction of SiNS-H with MeOLi to those of TMOS.

The ^{1}H NMR spectrum shows an intense singlet at 3.35 ppm assigned to methanol, which was not removed from the reaction mixture prior to the measurement and which forms from residual water and MeOLi. This solvent peak is framed by two spinning sidebands in a distance of 0.14 ppm. As expected, the singlet corresponding to TMOS is observed at a chemical shift of 3.56 ppm. Two further singlets appear at 3.51 and 4.94 ppm. The latter peak is assigned to water residues coordinating lithium cations (the water chemical shift in MeOD-d_4 is usually found at about 4.86 ppm). For the assignment of the peak at 3.51 ppm, it is referred to the ^{29}Si NMR spectrum, which contains the chemical shift of TMOS at -78.3 ppm and a second signal at -73.2 ppm which probably corresponds to the unknown ^{1}H NMR shift. Regarding that the used NMR solvent contains some residual water, hydrolysis and condensation of TMOS are possible. As the formation of siloxane bridges causes an upfield shift compared to TMOS, condensation reac-

tions can be excluded. According to the literature, the ^{29}Si NMR shifts of the hydrolysis products of TMOS, $Si(OCH_3)_{4-n}(OH)_n$ (n = 1 to 4), shift downfield with an increasing n value.[188] Supposing that the unknown ^{29}Si NMR peak correlates with the ^{1}H NMR signal at 3.51 ppm, at least one of the four moieties at the silicon atom should be a methoxy group. The difference in the ^{29}Si NMR chemical shifts between TMOS and the methyl orthosilicate $Si(OCH_3)(OH)_3$ is reported to be 5 ppm,[188] which is in good agreement with the observations in the ^{1}H and ^{29}Si NMR spectra of the reaction mixture.

The hypothesis of partial hydrolysis taking place with TMOS is proven by the ^{1}H NMR spectrum of the same sample measured again after three months: The spectrum of the repeated record shows no TMOS peak anymore, instead of that the peak at 3.51 ppm is the only signal besides the methanol and water peaks (Figure 6.4). Additionally, ^{1}H NMR spectra of mixtures containing TMOS and MeOLi are recorded in two separate experiments - one without any added water and the other with some added water. As anticipated, in the first experiment, the spectrum only displays the TMOS peak at 3.56 ppm. In the second experiment, the spectrum shows only the peak at 3.51 ppm. These results from NMR spectroscopy strongly indicate that $Si(OCH_3)(OH)_3$ is the second silicon-containing species in the NMR measurements of the reaction mixtures.

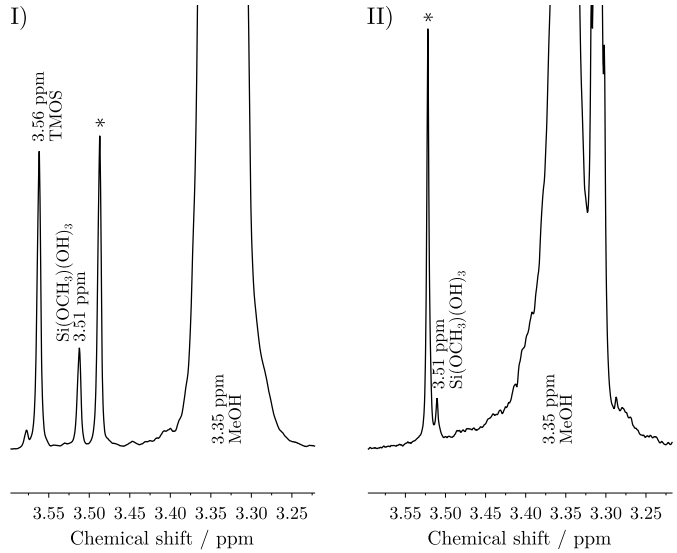

Figure 6.4: Comparison of the ^{1}H NMR spectra of the reaction mixture obtained from the reaction of SiNS-H with MeOLi directly after the reaction (I) and after three months (II). Note that the spinning sidebands (marked by the asterisk) deviate in both spectra because they were recorded on different NMR instruments.

0.1 equivalents of MeOLi yield an incomplete decomposition of the SiNS-H as some yellow nanosheets remain. The observed outcome was not anticipated based on the proposed autocatalytic mechanism for the decomposition of SiNS induced by MeOLi. This indicates that side reactions are occurring which consume MeOLi. As the starting material SiNS-H is imperfect regarding its composition, side reactions seem likely.

The FTIR spectrum of as-prepared SiNS-H (cf. Figure 6.5) shows bands indicating the presence of OH-terminated silicon atoms (3606 and 1628 cm^{-1}) besides the hydride-terminated Si atoms (2104 cm^{-1}) and Si-O-Si structures (1012 and 799 cm^{-1}). With MeOLi, silanol groups in the nanosheets will react towards the corresponding lithium silanolate (see Scheme 6.5).

EDX spectra of the starting material give further information about impurities in SiNS-H: Besides silicon, a significant amount of chlorine, and traces of calcium are detected in Cl/Si ratios from 0.2 to 0.4 and Ca/Si ratios of 0.03 as listed in Table 6.1. The calcium originates from remaining $CaSi_2$, from which SiNS-H is prepared with $HCl_{(aq)}$, which, on the other hand, is the source of the chlorine impurity. Calcium is probably present as $CaSi_2$ and chlorine as Si-Cl. This is in agreement with solid-state NMR experiments performed by Dorn *et al.*,[60] according to which 20 % of the silicon atoms in SiNS-H are covalently bonded to chlorine. Conversion of the Si-Cl group with MeOLi will lead to the substitution of chlorine with the methoxy group as shown in Scheme 6.5. In this case, lithium chloride will be formed without recovery of MeOLi. All these potential side reactions consume MeOLi and explain why higher amounts of MeOLi (but still under-stoichiometric) are needed.

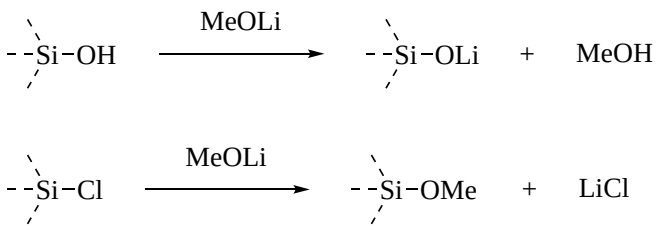

Scheme 6.5: Possible side reactions with MeOLi caused by impurities in SiNS-H.

Characterization of the Solid Residue

Raman and FTIR analysis as well as SEM coupled with EDX are used to characterize the solid, which remains after the decomposition of SiNS-H.
Raman spectroscopy reveals that the vibration modes characteristic for SiNS-H are not present in the spectrum of the solid residue after MeOLi treatment. Instead, an intense Raman band at 517 cm^{-1} is observed as can be seen in the representative spectrum in Figure 6.5. This band is assigned to bulk silicon, which is also present in SiNS-H as an impurity and which does not react with MeOLi under the applied conditions. The presence of bulk silicon - a precursor of the $CaSi_2$ synthesis - proves that this solid state reaction leads to incomplete incorporation of silicon into the Zintl phase $CaSi_2$.
The FTIR spectrum of the solid also has no similarities to SiNS, but seems to contain MeOLi or another methoxide salt: The spectrum in Figure 6.5 shows features of the C-O stretching vibration in the methoxy group (1032 cm^{-1}) and of the C-H stretching vibrations (2800 to 2940 cm^{-1}).

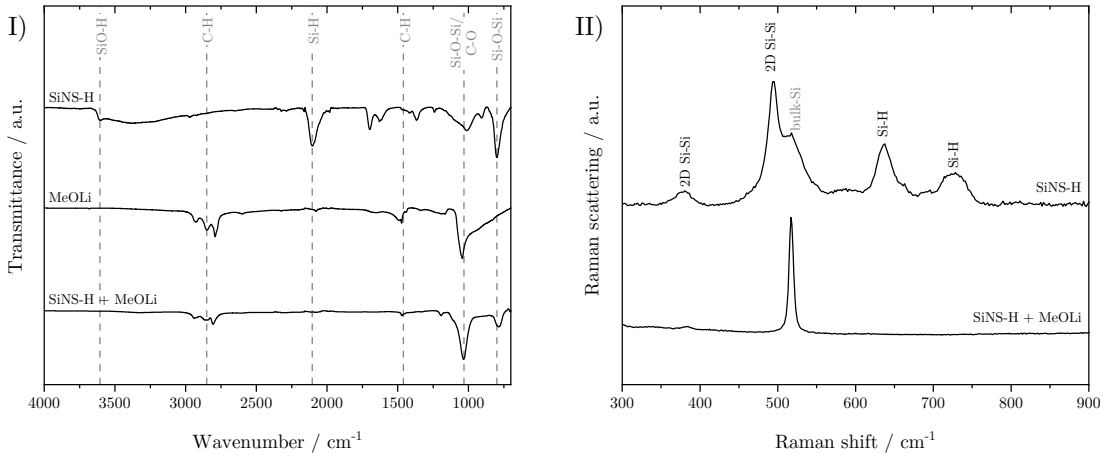

Figure 6.5: FTIR (I) and Raman spectra (II) of SiNS-H before and after treatment with MeOLi.

SEM images of the solid residue show random shapes of different sizes but no sheet structures as for SiNS-H (Figure 6.6). According to EDX, the solid contains silicon, calcium and chlorine (note that the EDX spectroscope cannot detect elements lighter than sodium). Comparison of the calculated Cl/Si and Ca/Si molar ratios in the SiNS shows an increase after the treatment with MeOLi. This is explicable by the generation of TMOS which reduces the silicon content in the solid. According to the Raman spectra, silicon is most probably present in the

form of bulk silicon, but insoluble silicon oxides possibly also exist. However, the Cl/Si and Ca/Si ratios exhibit a noticeable difference in this trend. The Cl/Si ratio experiences a 1.9-fold increase, while the Ca/Si ratio increases by 76. This is likely because of the partial transformation of Si-Cl bonds to soluble lithium chloride, as illustrated in Figure 6.5. Insoluble calcium compounds seem to be formed in side reactions, and thus, the Ca/Si ratio significantly increases. Further characterization of the solid side products of the reaction of SiNS-H with MeOLi is beyond the scope of this project.

Table 6.1: Weight percentages of the elements detected in SiNS-H and the solid product of the reaction between SiNS-H and MeOLi, determined by EDX analysis. From these values the molar ratios were calculated. Each sample was measured four times at different locations.

	Si / wt%	Cl / wt%	Ca / wt%	Cl/Si	Ca/Si
1	70	29	2.5	0.33	0.025
2	67	30	3.0	0.35	0.031
3	70	28	2.6	0.31	0.026
4	76	21	2.7	0.22	0.025
+ MeOLi					
1	53	9.2	38	0.14	0.51
2	17	16	67	0.76	2.8
3	19	16	65	0.66	2.4
4	18	17	65	0.71	2.5

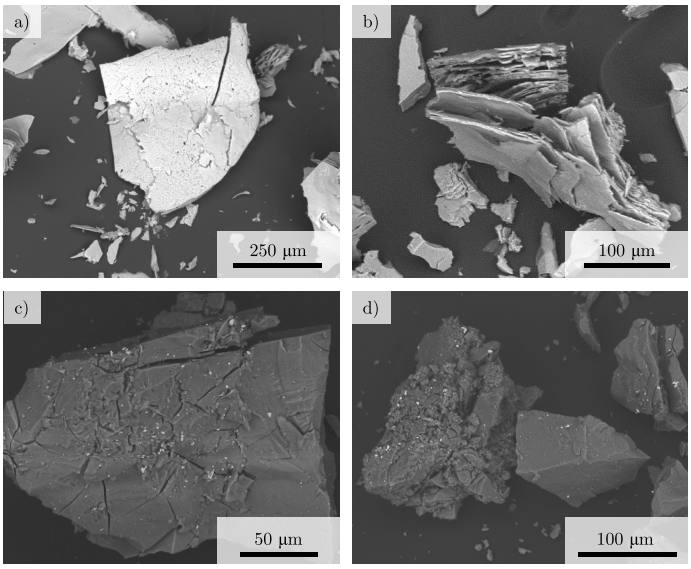

Figure 6.6: SEM images of SiNS-H (a, b) and the solid residue obtained after the reaction between SiNS-H and MeOLi (c, d).

In summary, the characterization of the gray residue obtained by treating SiNS-H with MeOLi confirms that this residue contains no SiNS-H. The appearance of this solid, which includes bulk silicon, calcium and chlorine compounds, as well as methoxide salts, originates from impurities in the SiNS-H.

6.2.2 Germanium Nanosheets

So far, it was demonstrated that SiNS-H decompose with MeOLi under the formation of TMOS, which further hydrolyzes to $Si(OCH_3)(OH)_3$. Since the modification of Ge/SiNS-H by the selective removal of silicon from the mixed nanosheets is the overall goal, the behavior of GeNS-H towards MeOLi is investigated in the next step. Similar to the experiments with SiNS-H, GeNS-H are exposed to 0.5 equivalents of MeOLi in methanol. Upon mixing the two reagents, nothing happens: A clear colorless solution above a dark gray lustrous powder is obtained which is separated by centrifugation. In a comparative experiment, the same result is obtained when a solution of potassium hydroxide is added to GeNS-H.

Characterization of the Liquid Supernatant

^{1}H NMR spectroscopy (Figure 6.10) of the separated solution only shows the solvent peak of methanol with a chemical shift of 3.35 ppm and a second peak at 5.22 ppm, corresponding to residual water, which coordinates lithium cations. Note that the spinning sidebands of methanol are closer compared to the ^{1}H NMR spectrum of the SiNS-H experiment, because the spectra were recorded on different NMR instruments. According to this NMR analysis, no soluble product forms from GeNS-H and MeOLi.

Characterization of the Solid Residue

To determine if the remaining powder differs from GeNS-H before the MeOLi treatment, FTIR and Raman spectra and SEM images are are recorded. As shown in Figure 6.7, the FTIR spectra before and after the experiment are very similar. After MeOLi treatment, additional bands appear in the range from 2800 to 2950 cm^{-1} and at about 1030 cm^{-1}. These bands most likely correspond to MeOLi, which remains in the sample if it is not completely washed out. At least, no new Ge-O vibrational modes, which would indicate a methoxy-functionalization of the nanosheets, are present in the spectrum. Figure 6.7 presents Raman spectra of GeNS-H before and after the exposure to MeOLi. Features associated with

Ge-Ge vibrations at 224 and 301 cm^{-1} are displayed in both spectra, which is characteristic of GeNS.[132] According to these vibrational spectroscopic analyses, GeNS-H are not converted to a new product with MeOLi.

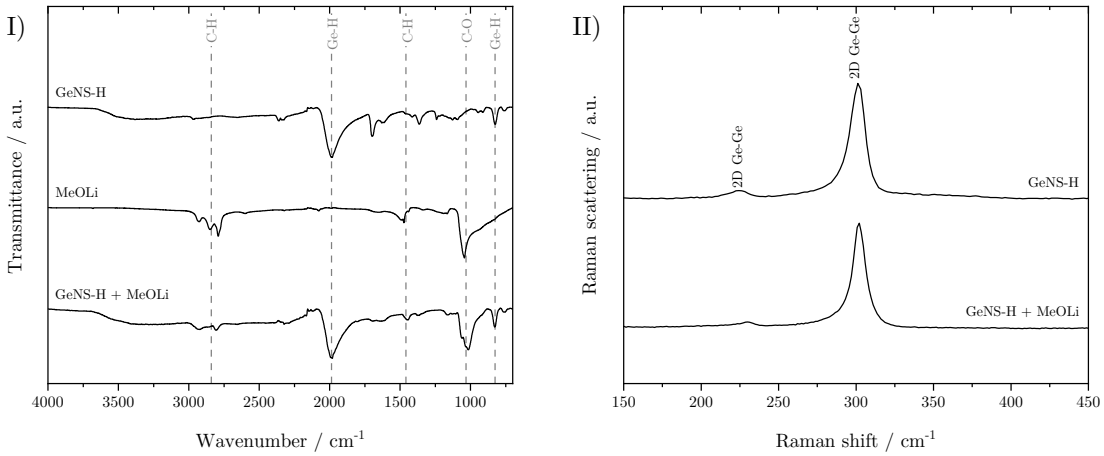

Figure 6.7: FTIR (I) and Raman spectra (II) of GeNS-H before and after treatment with MeOLi.

SEM images reveal intact sheet structures for the starting material and the product (Figure 6.8). It is therefore concluded that GeNS-H are inert towards MeOLi. These results provide a promising basis for the selective degradation of Ge/SiNS-H.

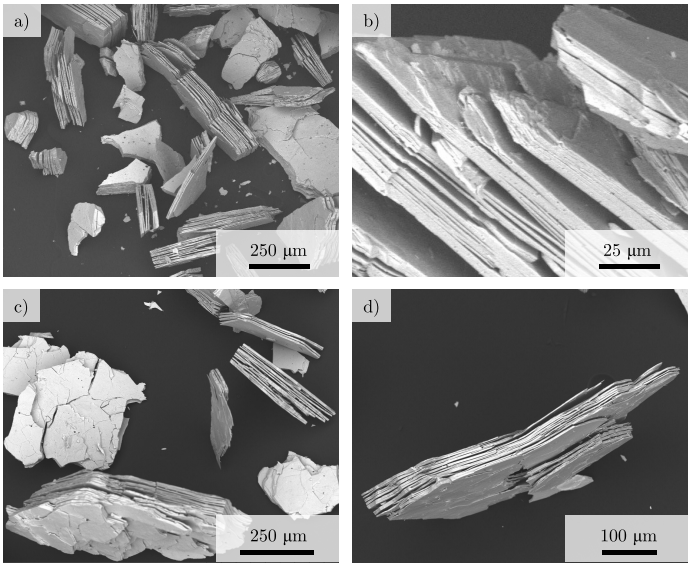

Figure 6.8: SEM images of GeNS-H before (a, b) and after (c, d) the treatment with MeOLi.

6.2.3 Selective Decomposition of Germanium/Silicon Nanosheets

In the sections above, the reactivities of SiNS-H and GeNS-H towards MeOLi are described. These reactivities significantly differ from each other. The 2D silicon network of SiNS-H completely decomposes (an insoluble fraction of impurities remains), whereas GeNS-H do not react with MeOLi. From these previous results, silicon atoms are expected to be removed from mixed Ge/SiNS-H by the cleavage of Si-Si bonds, but it is difficult to predict what will happen to Ge-Si bonds. This section, presents the reactivity of Ge/SiNS-H with MeOLi.
The behavior of Ge/SiNS-H towards MeOLi is studied by mixing 0.5 equivalents of a methanolic MeOLi solution with the nanosheets. A violent gas evolution occurs, and after the reaction has subsided, an orange-colored solution and a brown powder remain. The solid product is darker brown than the starting material as can be seen from the photograph shown in Figure 6.9. This is already an indication that silicon has been at least partially removed from the nanosheets, as pure SiNS-H are yellow and GeNS-H are dark gray. The solid is separated from the liquid phase to separately characterize them.

Figure 6.9: Photographs of Ge/SiNS-H before (left) and after (right) the reaction with MeOLi.

Characterization of the Soluble Product

The characterization of the dissolved product of Ge/SiNS-H is carried out by ^{1}H and ^{29}Si NMR spectroscopy in MeOD-d_4. The ^{1}H NMR spectrum of the soluble product is almost identical to the one of the decomposed SiNS-H (Figure 6.10). Besides the peaks of methanol (3.35 ppm) and water (5.04 ppm), the spectrum contains singlets assigned to TMOS (3.56 ppm) and its hydrolysis product $Si(OCH_3)(OH)_3$ (3.51 ppm). The corresponding ^{29}Si NMR chemical shifts appear at −78.3 ppm and −73.2 ppm, respectively. Since the NMR characterization of the dissolved products in both experiments, with SiNS-H and Ge/SiNS-H, shows the same peaks, it proves that silicon is at least partially removed from the mixed Ge/SiNS-H by MeOLi.

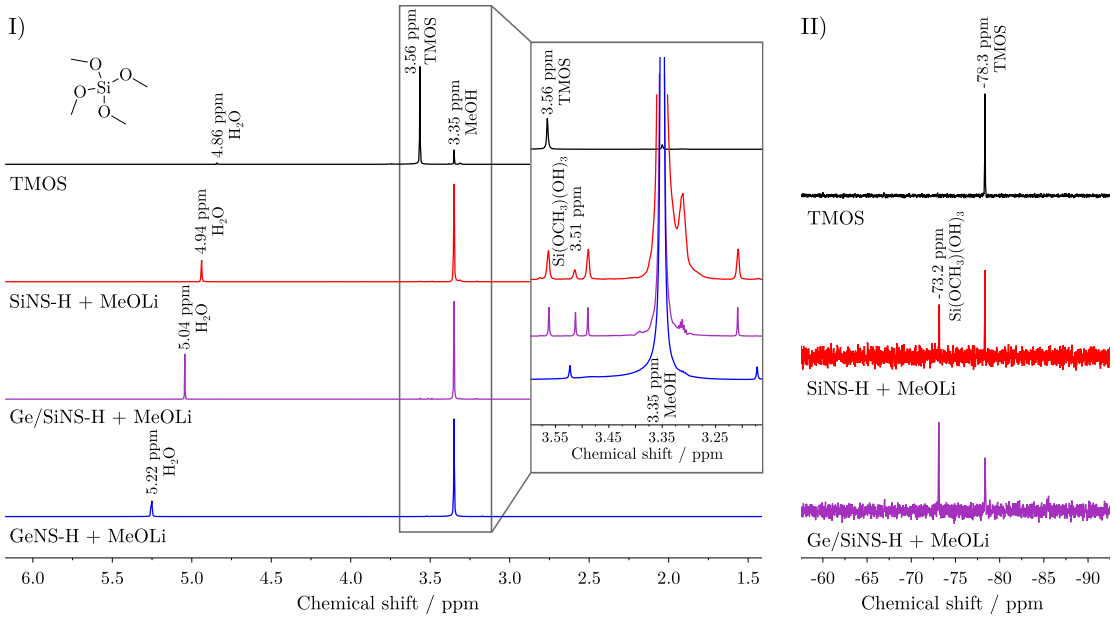

Figure 6.10: Comparison of the ^{1}H (I) and ^{29}Si NMR spectra (II) of the liquid phases obtained by adding methanolic solutions of MeOLi to SiNS-H, GeNS-H, and Ge/SiNS-H.

Characterization of the Solid Residue

It was demonstrated that MeOLi induces the formation of TMOS from silicon atoms, which are built-in to the mixed Ge/SiNS-H. In the next step, the brown solid obtained after converting Ge/SiNS-H with MeOLi is analyzed. Therefore, vibrational spectroscopy and SEM coupled with EDX are applied.

Figure 6.11 compares the FTIR spectra of neat Ge/SiNS-H and the solid product of the reaction between the nanosheets and MeOLi. In contrast to the starting material, the Si-H stretching vibration feature at about 2100 cm^{-1} vanishes in the product spectrum. This accords with the TMOS formation described above. Before the reaction with MeOLi, the Ge-H stretching vibration mode appears at 2000 cm^{-1} but is only present as a shoulder next to a band at approximately 2050 cm^{-1} after treatment with MeOLi. This band is assigned to O_2Ge-H or O_3Ge-H stretching modes.[189] Additional bands at 1038 cm^{-1} or 754 and 825 cm^{-1} represent Si-O-Si and Ge-H modes, respectively.[132,155] These results show that hydride-terminated germanium atoms are present in the solid decomposition product. These are partially oxidized and the presence of any methoxy substituted species is excluded, as no C-H vibration modes appear in the FTIR spectrum. Besides germanium some silicon remains in the solid as shown by Si-O-Si stretching vibrations.

Raman spectroscopy gives information on the binding situation of the group IV elements. Ge/SiNS-H exhibits all three possible vibrations at 293 cm^{-1} (Ge-Ge), 400 cm^{-1} (Ge-Si), and 475 cm^{-1} (Si-Si). On the other hand, the product Raman spectrum after the reaction with MeOLi displays intense Ge-Ge and Ge-Si vibration features, whereas the Si-Si vibrational mode almost disappeared (Figure 6.11). This confirms that MeOLi decomposes the Si-Si fractions in Ge/SiNS-H, whereas the Ge-Ge fractions remain intact. Also, Ge-Si bonds seem not to be cleaved by MeOLi. This is in agreement with the ^1H NMR experiment in which no soluble species other than TMOS and its hydrolysis product $Si(OCH_3)(OH)_3$ are detected.

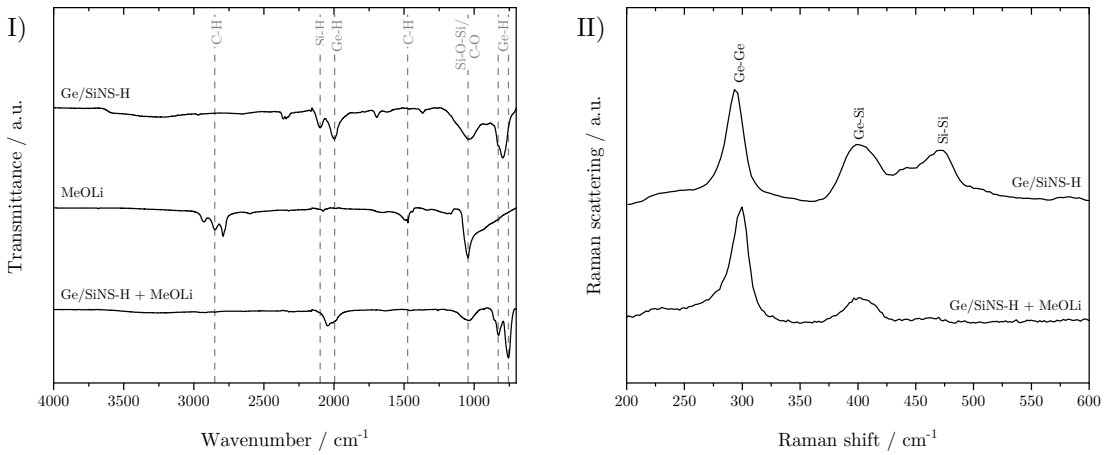

Figure 6.11: FTIR (I) and Raman spectra (II) of Ge/SiNS-H before and after the reaction with MeOLi.

SEM images provide information on the morphology of the solid product (Figure 6.12). The MeOLi-treated sample shows sheet structures similar to Ge/SiNS-H but less ordered and partially fragmented. Ge/SiNS-H exhibit a smooth surface before the reaction with MeOLi (Figure 6.12 c)). After the MeOLi treatment, the surface is rough and shows fluctuations (Figure 6.12 e) and f)). This confirms the degradation of the nanosheets and the formation of nano-sized pores due to the removal of silicon atoms.

Finally, EDX measurements at several spots in the sample are performed to determine the product's composition. The results of the EDX analysis compared to the starting material Ge/SiNS-H are listed in Table 6.2. Unsurprisingly, the silicon content decreases upon treatment with MeOLi, which confirms the previous results from FTIR and Raman spectroscopy. The Ge/Si ratio significantly increases from a range of 0.7 to 0.9 to a range of 2.5 to 5.1. Similar to the experiments with

SiNS-H, traces of calcium and chlorine are also present in Ge/SiNS-H and in the decomposition product, which derive from the nanosheet preparation.

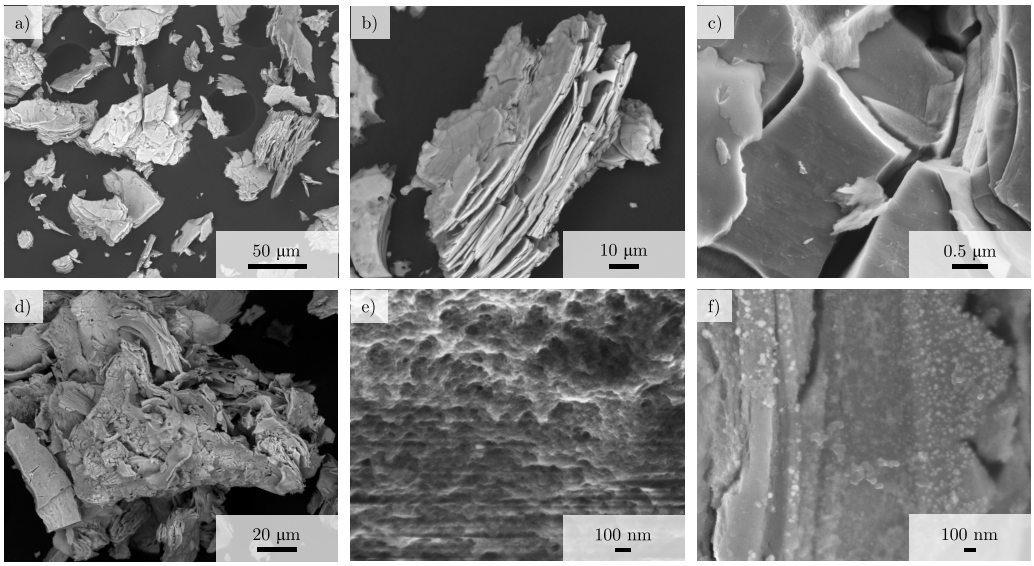

Figure 6.12: SEM images of Ge/SiNS-H before (a-c) and after (d-f) the reaction with MeOLi.

Table 6.2: Weight percentages of the elements detected in Ge/SiNS-H and the solid product of the reaction between Ge/SiNS-H and MeOLi, determined by EDX analysis. From these values the molar Ge/Si, Cl/Si, and Ca/Si ratios were calculated. Each sample was measured four times at different locations.

	Ge / wt%	Si / wt%	Cl / wt%	Ca / wt%	Ge/Si	Cl/Si	Ca/Si
1	61	25	14	—	0.94	0.43	—
2	59	27	14	—	0.86	0.43	—
3	61	26	14	—	0.91	0.42	—
4	54	29	14	3.2	0.73	0.38	0.078
+ MeOLi							
1	79	12	1.2	4.3	2.5	0.077	0.24
2	87	9.4	—	3.5	3.6	—	0.26
3	87	6.6	—	6.0	5.1	—	0.64
4	81	13	—	6.0	2.5	—	0.33

6.3 Summary

All in all, a new route in which silicon atoms are selectively removed from Ge/SiNS-H was established. This method is selective with respect to the

chemical environment of the silicon atoms. MeOLi can cleave Si-Si bonds but does not break Ge-Si and Ge-Ge bonds. This is attributed to the higher oxophilicity of silicon compared to germanium. Thus, the nanomaterial obtained by the treatment of Ge/SiNS-H with MeOLi consists mainly of germanium. This project focused on the MeOLi-induced decomposition reaction of SiNS-H and Ge/SiNS-H and the structural analysis of the products. Further investigation is required to study the properties and possible applications of the solid product obtained from Ge/SiNS-H.

6.4 Experimental Procedures

6.4.1 General Information

Instrument information, analytical techniques, procedures for solvent drying, the syntheses of hydride-terminated nanosheets as well as the etching procedure of SiNS-H are found in Chapter 9.
All chemicals were purchased from Sigma-Aldrich and are used without further purification. Experiments are performed using either Schlenk techniques or in an argon-filled glove box.

6.4.2 Reactions with *n*-Butyllithium

The reaction between hydride-terminated nanosheets and *n*BuLi is conducted in accordance with the literature-known protocol described in Reference 139.
In a heat-dried Schlenk tube, nanosheets (GeNS-H: 25 mg, 0.34 mmol, 1.0 eq.; HF-etched SiNS-H: 10 mg, 0.34 mmol, 1.0 eq.) are dispersed in hexane (6 mL). A solution of *n*BuLi (1 mL, 2.5 M in THF, 2.5 mmol, 7.4 eq.) is added dropwise, and the mixture is stirred at room temperature for three days. Workup of the reaction is performed inside an argon-filled glove box. The reaction mixture is centrifuged (6000 rpm, 4 min) to isolate the solid. The supernatant is discarded, and the residue is washed with hexane (6 mL) and centrifuged. This washing step is repeated two times before the residue is washed with methanol (6 mL). After centrifugation, the solid residue is freeze-dried from benzene.

6.4.3 Reactions with Lithium Methoxide

For the detailed investigation of the reaction between MeOLi and nanosheets, a uniform reaction protocol is used: A MeOLi solution (0.1 M in methanol,

0.5 eq, prepared from lithium and methanol) is added dropwise to the nanosheets (SiNS-H: 200 mg, 6.9 mmol, 1.0 eq.; GeNS-H: 200 mg, 2.7 mmol, 1.0 eq.; Ge/SiNS-H: 94 mg, 1.8 mmol, 1.0 eq.) in a glass centrifuge tube in an argon-filled glove box. After the addition of the MeOLi solution and completion of gas evolution (which occurs with SiNS-H and Ge/SiNS-H), the solution is separated from the solid by centrifugation (6000 rpm, 10 min). The supernatant is saved for NMR analysis and the solid residue is washed with methanol (6 mL) and then centrifuged. This washing cycle is repeated two more times. The residue is freeze-dried from benzene.

6.4.4 Reactions of Hydride-Terminated Silicon Nanosheets with Different Equivalents of Lithium Methoxide

A MeOLi solution (prepared from lithium and methanol) is added dropwise to non-etched SiNS-H in a glass centrifuge tube in an argon-filled glove box. The experiments are performed with batches of 20 mg SiNS-H. The amount of lithium is varied to test different equivalents of MeOLi. Thus, 0.1, 0.5, 1.0, 2.0, 3.0 eq. of lithium are used to prepare methanolic MeOLi solutions. A constant methanol to SiNS-H ratio of 0.07 mL mg^{-1} is therefore used. In the experiment with 0.1 eq. MeOLi, 70 mg of SiNS-H are used and the MeOLi solution is diluted with 1 mL THF. After the addition of the MeOLi solution and possible completion of gas evolution, the solution is separated from the solid residue by centrifugation (6000 rpm, 10 min). The supernatant is saved for NMR analysis and the solid residue is washed with methanol (5 mL) and subsequently centrifuged. This washing cycle is repeated two times. The residue is freeze-dried from benzene.

7

Nonlinear Optical Properties of Functionalized Silicon Nanosheets*

Many 2D materials are known to possess outstanding NLO properties.[190] Among these materials are SiNS. In recent years, the research group of Couris has been studying the third-order NLO properties of hydride-terminated and dodecyl-functionalized SiNS (see Chapter 2.2.6).[103–105] In these studies, the materials under investigation were prepared by our group through the topochemical conversion of $CaSi_2$ with $HCl_{(aq)}$ at low temperatures, and the iodonium salt-induced hydrosilylation with 1-dodecene. The NLO responses of the nanosheets dispersed in toluene were investigated using the Z-scan technique. These measurements were conducted at 532 nm and 1064 nm laser excitation in the picosecond (35 ps) and nanosecond regimes (4 ns),[103,105] as well as at 800 nm in the femtosecond regime (5 fs).[104] In these studies, dodecyl-functionalized SiNS were found to exhibit significantly enhanced NLO responses in comparison to the non-functionalized SiNS-H. Moreover, the NLO properties of these two SiNS are comparable or even superior to those of graphene or other 2D nanomaterials. These results demonstrated that the functionalization of SiNS-H is an effective method to enhance their NLO properties. Consequently, particularly function-

*This chapter is reproduced in part from Stavrou, M.; Mühlbach, A. M.; Arapakis, V.; Groß, E.; Kratky, T.; Günther, S.; Rieger, B.; Couris, S. *Nanoscale* **2023**, *15*, 16636, with permission from RSC Publishing. All coauthors have agreed to reproduce the material.

alized SiNS are promising materials for potential applications in photonics and optoelectronics.

In light of the preceding investigations, it becomes pertinent to inquire whether the NLO response of SiNS can be further enhanced through surface modification with alternative functional groups, which is elucidated in this chapter. Therefore, SiNS-H are functionalized by the iodonium salt-induced hydrosilylation with styrene and *t*BuMA. After preparation, the materials are characterized in terms of their structure, composition, morphology, and optical properties. Their NLO properties, or more precisely the NLO absorption and refraction, as well as optical limiting (OL), are investigated using Z-scan measurements at 50 fs, 400 nm and 70 fs, 800 nm laser pulses.

7.1 Preparation and Characterization of Functionalized Silicon Nanosheets

In order to investigate the influence of organic surface groups on the NLO properties of SiNS, SiNS-H are modified with styrene and *t*BuMA. In previous studies, dodecyl-functionalized SiNS were investigated, which contain a nonpolar alkyl group.[103–105] In contrast, the slightly electron-donating, nonpolar aromatic phenylethyl group, which is introduced by the hydrosilylation with styrene, and the slightly electron-withdrawing polar *tert*-butyl ester group, which is obtained by the hydrosilylation of *t*BuMA are investigated in the present study. For comparable reasons, the same hydrosilylation method is used as for the synthesis of SiNS-dodecyl, as described in References 103, 104, and 105, which is induced by the iodonium salt BIP. Scheme 7.1 schematically depicts the hydrosilylation reaction.

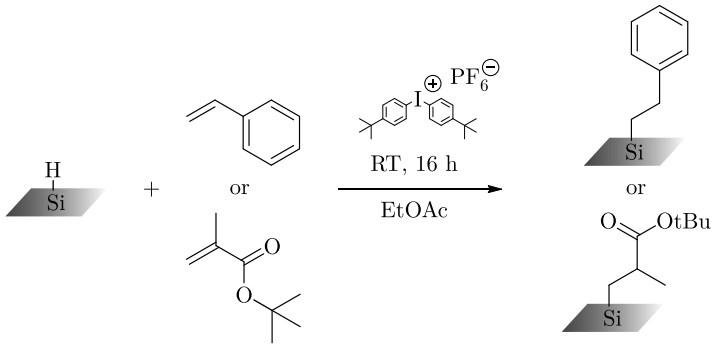

Scheme 7.1: Schematic reaction of the hydrosilylation of SiNS-H with *t*BuMA and styrene.

The successful preparation of the styrene and *t*BuMA-functionalized nanosheets, SiNS-styrene and SiNS-*t*BuMA, is proven by FTIR, Raman, and XPS. Furthermore, several microscopy techniques, as SEM, AFM and transmission electron microscopy (TEM) are employed to characterize the material's morphology.

7.1.1 Purity of the Functionalized Silicon Nanosheets

Two experiments are performed to determine whether the samples of functionalized SiNSs only consist of SiNSs covalently bonded to styrene or *t*BuMA moieties or a composite material of surface functionalized SiNSs embedded in a polymer matrix: In the first experiment, SiNS-styrene and SiNS-*t*BuMA dispersions in THF are sonicated for nine hours. The supernatant is subsequently analyzed via GPC with a refractive index detector. The chromatograms show no signals assigned to polymeric or oligomeric structures. This result is further confirmed by thin layer chromatography. Therefore, dispersions of SiNS-styrene and SiNS-*t*BuMA in DCM are sonicated for seven hours. After sedimentation of the SiNSs, small spots of the supernatants are applied to a silica plate, which is developed in THF. As no spots appear for the SiNS samples under UV light, it is concluded that the functionalized SiNSs are pure samples without any impurities (remaining initiating iodonium salt or monomers) or polymer matrix. Minor traces of polymeric structures are observed in SEM images (Figure 7.4 a), c), and e)), but as GPC experiments did not detect polymer in the samples, the low concentration of residual polymer is probably negligible.

7.1.2 Vibrational Spectroscopy

The FTIR spectra of the functionalized SiNS, presented in Figures 7.1, both exhibit the characteristic Si-H stretching vibration band at approximately 2100 cm^{-1}, indicating incomplete surface functionalization. The spectrum of SiNS-styrene further shows bands assigned to aromatic (1600 cm^{-1} and 2970 to 3110 cm^{-1}) and aliphatic signals (905, 1380 and 1510 cm^{-1} and 2805 to 2955 cm^{-1}). Absence of the C=C stretching vibration mode at 1630 cm^{-1} confirms the successful hydrosilylation reaction. The FTIR spectrum of SiNS-*t*BuMA is characterized by aliphatic signals (1340 to 1510 cm^{-1} and 2855 to 3040 cm^{-1}), and the bands of the C=O (1720 cm^{-1}) and C-O stretching vibrations (1135 cm^{-1}) besides the Si-H feature. As the spectrum does not exhibit the band of the vinylic C=C stretching vibration at 1637 cm^{-1}, the covalent bonding of the organic group to the nanosheets is

confirmed.

Complementary information to the results of the FTIR measurements is provided by Raman spectroscopy (Figure 7.2). As SiNS-H, SiNS-styrene and SiNS-*t*BuMA exhibit Raman bands at 495, 635, 730 and 2128 cm^{-1}, which are assigned to Si-Si and Si-H vibration modes, respectively. The presence of Si-H vibration features indicates partial surface coverages, which is already observed in FTIR spectra. Additional bands in the spectrum of SiNS-styrene at 1000 cm^{-1}, 1030 cm^{-1}, in the range of 1150 to 1200 cm^{-1}, 1580 and 1600 cm^{-1} represent aromatic C-H and C-C modes. As in the FTIR spectrum, no vinylic C=C vibration feature is shown in the Raman spectrum, which indicates the successful styrene functionalization and confirms the results of the FTIR data. The Raman spectrum of SiNS-*t*BuMA shows the C=O stretching band (1725 cm^{-1}) and the C-H deformation mode of the *tert*-butyl group (1455 cm^{-1}). The presence of these bands and the absence of the C=C stretching band at 1640 cm^{-1} prove the success of the functionalization with *t*BuMA.

7.1.3 Thermogravimetric Analysis

The results from FTIR and Raman spectroscopy already show that no complete surface coverage is achieved in SiNS-styrene and SiNS-*t*BuMA. This is further confirmed and quantified by TGA measurements, according to which a mass loss of 54 and 60 % is obtained for SiNS-styrene and SiNS-*t*BuMA, respectively. These mass losses are shown in Figure 7.3 and correspond to calculated surface coverages of 30 and 31 % for SiNS-*t*BuMA and SiNS-styrene, respectively.

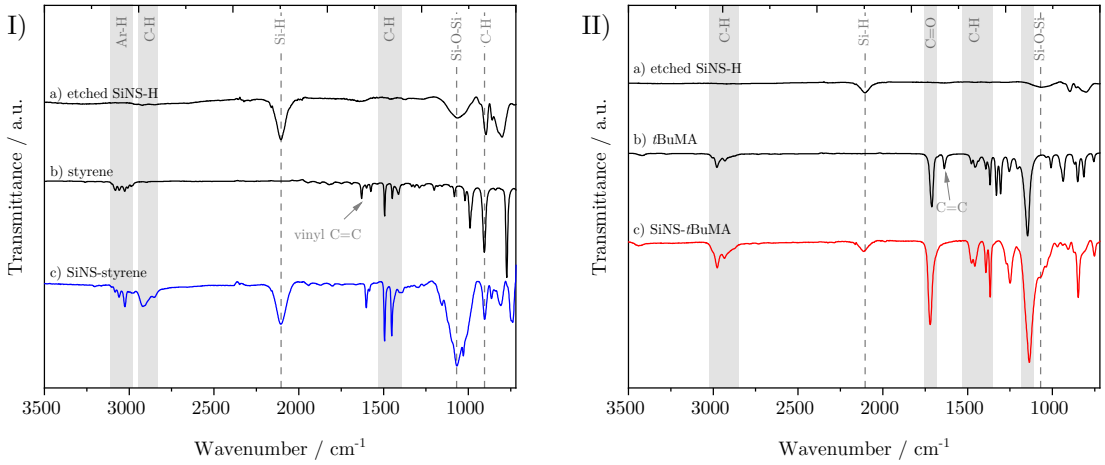

Figure 7.1: FTIR spectra of SiNS-H, SiNS-styrene, and styrene (I); and SiNS-H, SiNS-*t*BuMA, and *t*BuMA (II).

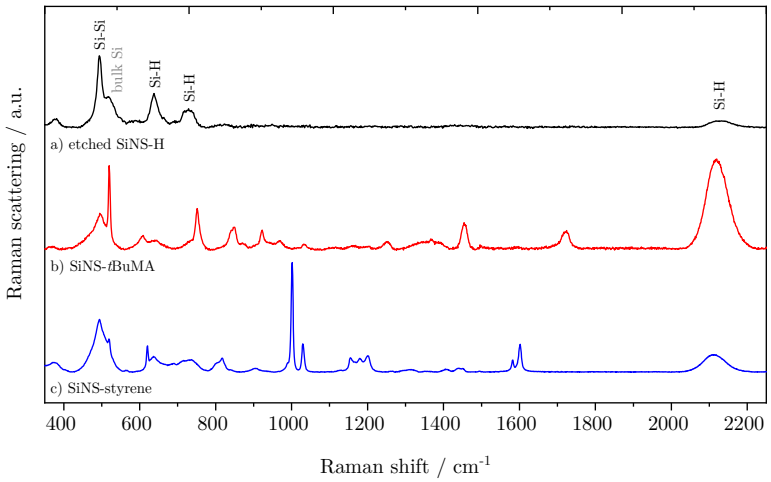

Figure 7.2: Raman spectra of SiNS-H, SiNS-*t*BuMA, and SiNS-styrene.

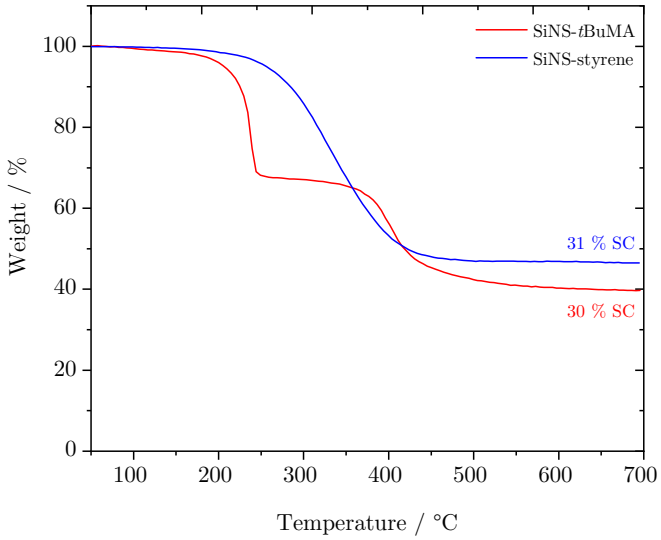

Figure 7.3: TGA data of SiNS-styrene and SiNS-*t*BuMA.

7.1.4 Electron Microscopy and Atomic Force Microscopy

In addition to the structural analysis, the morphologies of the prepared nanomaterials are investigated using microscopy techniques. Electron microscopy images obtained in SEM and TEM measurements (Figures 7.4 and 7.5), show that both materials are nanosheets with irregular shapes and inhomogeneous sizes. According to these images, the lateral nanosheet dimensions are of up to 25 and 20 µm for SiNS-styrene and SiNS-*t*BuMA, respectively. Instead of monolayers mainly

stacks of several sheets are found, indicating a tendency for agglomeration of the functionalized SiNS in the dry state.

AFM images and corresponding height profiles (Figure 7.6) reveal sheet thicknesses of 2 and 4 nm for SiNS-styrene and SiNS-*t*BuMA, respectively, which is in good agreement with literature values of other functionalized SiNSs.[79,84,88,191]

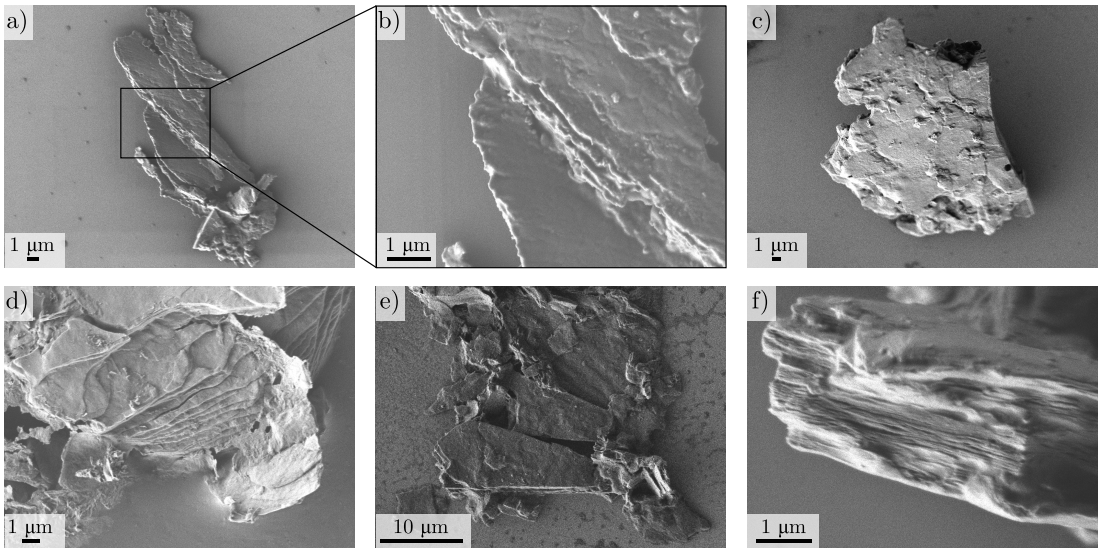

Figure 7.4: SEM images of SiNS-styrene (a-c) and SiNS-*t*BuMA (d-f). a), c), and e) show some dark spots beside the nanosheets, indicating residual polymer.

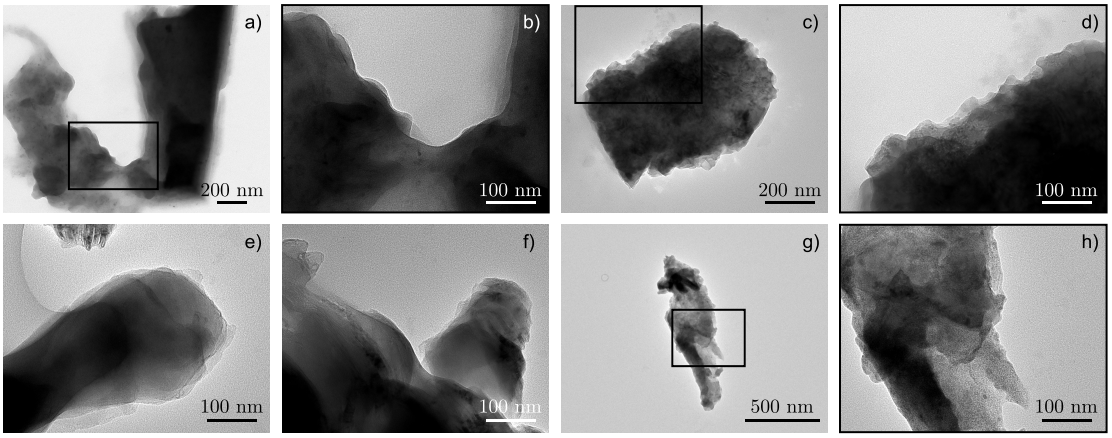

Figure 7.5: TEM images of SiNS-styrene (a-d) and SiNS-*t*BuMA (e-h). b), c), and h) show higher magnifications of a), c), and g), respectively.

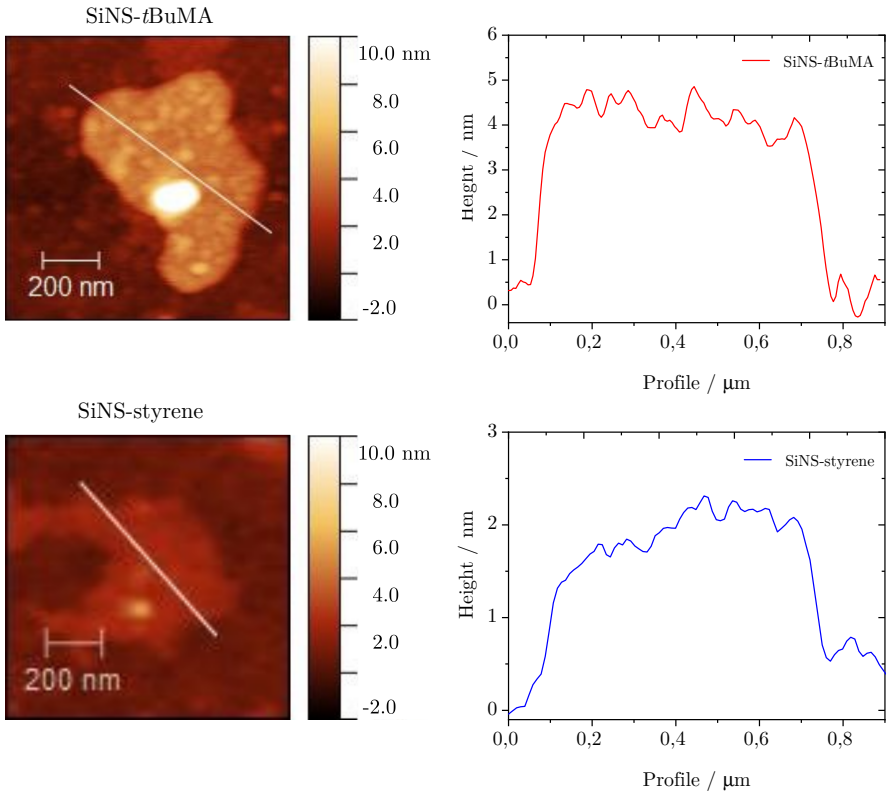

Figure 7.6: AFM images of SiNS-*t*BuMA and SiNS-styrene.

7.1.5 X-ray Photoelectron Spectroscopy

Finally both types of functionalized SiNSs are characterized by XPS. Figure 7.7 displays the fitted C 1s and Si 2p spectra scaled to the same total Si 2p peak intensity. The data prove the successful functionalization of the nanosheets.
The deconvoluted C 1s peak can be assigned to the carboxylic C and C-O-C bond present in *t*BuMA in accordance with the literature,[192] and the last species to aliphatic/aromatic carbon. The relative peak intensities of the first two species with respect to the aliphatic carbon of 0.16 match the expected ratio of 1:6 of *t*BuMA.
In the case of SiNS-styrene, essentially only the 284.5 eV species is observed as expected for the styrene functionalization. The minority species at 286.4 eV is tentatively attributed to the carbon atom through which the ligand is attached to the SiNS.
The Si 2p data underline the picture of a pristine SiNS on which the respective ligand was attached. This is indicated by the main Si(0) component between 99.5 and 99.9 eV binding energy in accordance with the literature and a slightly

shifted component at 101.6 to 101.7 eV, which is tentatively assigned to the anchoring silicon atom of the ligand.[179,193]

The AFM data proves the SiNS in a flat-lying geometry on the support with a *t*BuMA layer about twice as thick as the styrene functionalization layer around the nanosheet. The different apparent thickness of the functionalization layers is also reflected in the relative Si 2p/C 1s peak intensities, which are displayed in Figure 7.7 III). The integrated peak intensities are normalized to the photoionization cross section and the transfer function of the analyzer so that the ratio reflects the atomic ratio of the functionalized SiNSs. The value of 0.4 for the SiNS-styrene sample matches the fraction of 30 % of silicon atoms in SiNS to which eight carbon atoms of the styrene ligand are attached when neglecting any photoelectron attenuation due to the styrene layer for the emitted Si 2p photoelectrons. However, the about 1 nm thick layer (functionalization on both sides of the silicon nanosheet) will induce a signal damping of the Si 2p core level emission. With an effective attenuation length between 10 and 30 Å, an attenuation of a factor of about 2 perfectly matches the styrene coverage of about 15 % on either side of the sheet as obtained by TGA.[194] Accordingly, due to the doubling of the functionalization layer thickness in case of *t*BuMA, a further Si 2p damping by another factor of 2 is readily observed. The given error bars rather represent the uncertainties of the sample cleanliness regarding the presence of carbon sources other than the ligand species that may occur during sample preparation.

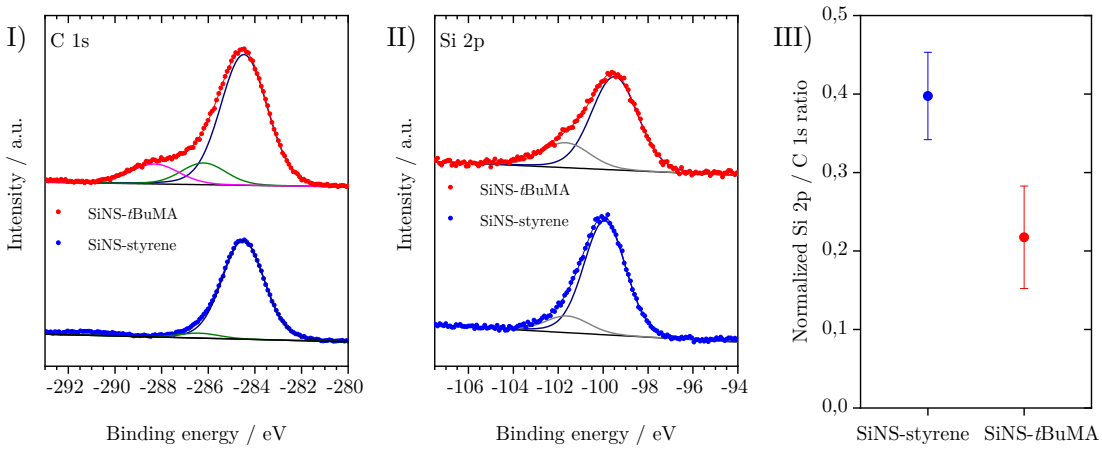

Figure 7.7: XPS spectra of the I) C 1s and II) Si 2p core levels of SiNS-*t*BuMA and SiNS-styrene. III) Normalized Si 2p / C 1s ratio reflecting the atomic surface composition.

7.1.6 Photoluminescence and Absorption Spectroscopy

Both functionalized SiNSs show a PL emission maximum at approximately 500 nm, which is in accordance with previously reported PL maxima.[73,76]

Figure 7.8 I) presents some representative UV-vis-NIR absorption spectra of SiNS-*t*BuMA and SiNS-styrene dispersions, all corresponding to the a concentration of 0.1 mg mL^{-1}. The optical absorption spectra of both SiNSs exhibit an absorption peak around 300 nm, attributed to the excitation of carriers from occupied σ to unoccupied σ^* states.[195] Transforming these data according to the Tauc plot method,[196] the optical band gap energies of SiNS-*t*BuMA and SiNS-styrene for direct interband transitions are estimated to be approximately 3.2 and 2.7 eV, respectively, as shown in Figure 7.8 II) and III). Absorption measurements performed on *t*BuMA and styrene revealed negligible absorption in the spectral region of interest.

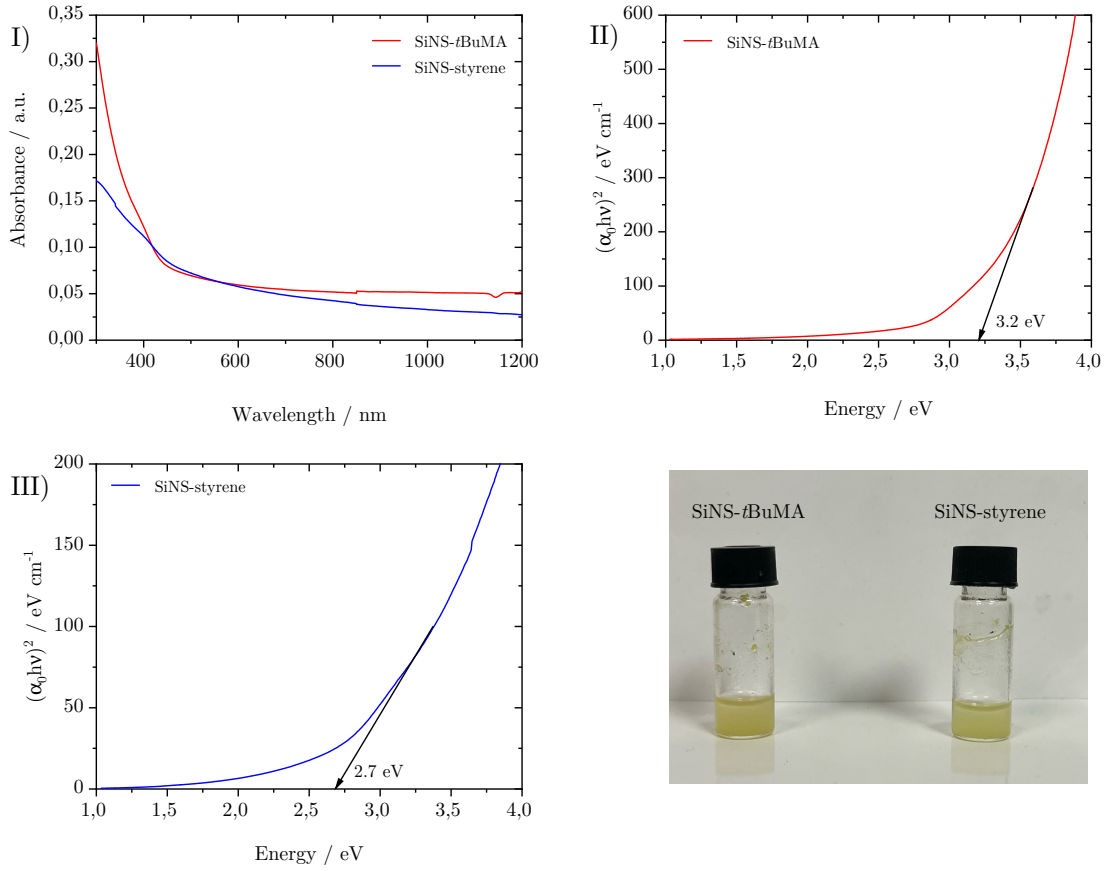

Figure 7.8: I) UV-Is-NIR absorption spectra of SiNS-*t*BuMA and SiNS-styrene dispersions in toluene. Tauc plot diagrams of SiNS-*t*BuMA (II) and SiNS-styrene (III) for direct optical transitions. IV) Photos of SiNS-tBuMA and SiNS-styrene dispersed in toluene.

7.2 Nonlinear Optical Properties of Functionalized Silicon Nanosheets

7.2.1 50 fs, 400 nm Laser Excitation

In Figure 7.9 I and II) some OA Z-scans of SiNS-*t*BuMA and SiNS-styrene toluene dispersions (0.1 mg mL^{-1}) are presented, obtained under 50 fs, 400 nm laser excitation using different laser intensities. All dispersions have a linear absorption coefficient α_0 of about 2.55 cm^{-1} at 400 nm. The solid lines correspond to the best fit of the experimental OA Z-scan data points (solid points). The fact that all OA Z-scans present a transmission maximum at the focal plane, indicates SA behavior (i.e., the nonlinear absorption coefficient $\beta < 0$), i.e. the transmittance increases with the laser intensity. The average values of the nonlinear absorption coefficient β of the SiNS-*t*BuMA and SiNS-styrene dispersions were determined to be about $(-8.3 \pm 0.8) \times 10^{-15}$ and $(-17 \pm 2) \times 10^{-15}$ m W^{-1}, respectively.

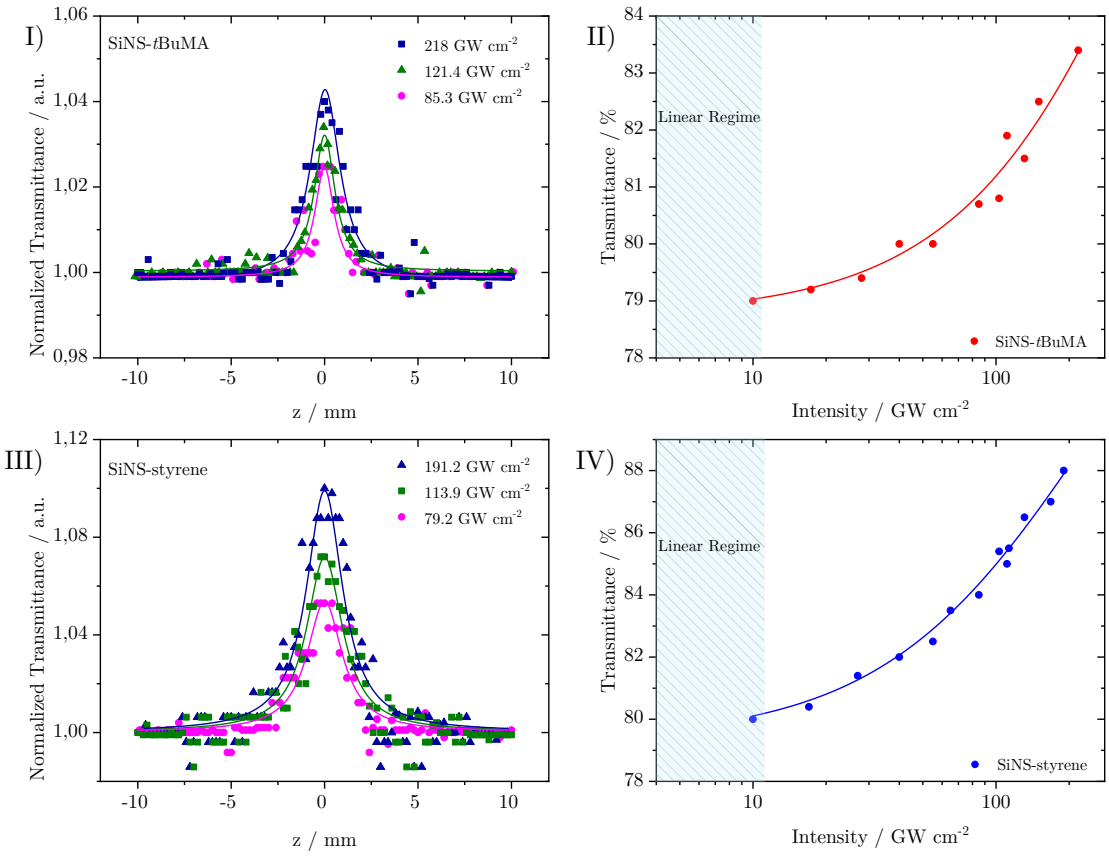

Figure 7.9: OA Z-scans (I, III) and transmittance (II, IV) of SiNS-*t*BuMA and SiNS-styrene dispersions under different laser excitation intensities at 400 nm. All dispersions have the same linear absorption coefficient α_0 of 2.55 cm^{-1}.

The variation of the transmittance at the focal plane (i.e., under maximum laser intensity) of SiNS-*t*BuMA and SiNS-styrene with the laser intensity is presented in Figure 7.9 II and IV). According to the typical model for SA for one-photon absorption (1PA),[197] the saturable intensity can be extracted from these data. The saturable intensity values are determined to be approximately 620 GW cm^{-2} for SiNS-*t*BuMA and 255 GW cm^{-2} for SiNS-styrene, respectively. The significantly lower values of the saturable intensity of SiNS-styrene compared to those of SiNS-*t*BuMA indicate that the former is a better choice for ultrafast photonic applications. Compared to other 2D materials, known to exhibit strong SA (e.g., graphene, some transition metal dichalcogenides like MoS_2, WS_2, and $MoSe_2$, black phosphorus, and MXenes),[198–202] the present SiNSs show comparable or significantly better SA properties. Therefore, they could be used as saturable absorbers in mode-locked lasers for the generation of ultrashort pulses.

In Figure 7.10 the processes contributing to the NLO absorption of the studied SiNSs are shown schematically. Since the estimated band gap energies of SiNS-styrene and SiNS-*t*BuMA are about 2.7 and 3.2 eV, respectively, 1PA-related transitions from the valence to the conduction band can readily occur under 400 nm (i.e., 3.1 eV) laser excitation (Figure 7.10 a), b)). Thus, electrons from the valence band of SiNSs can be directly promoted to higher energy states lying in the conduction band under sufficient laser intensity. From there, after an ultrashort relaxation time, the photogenerated electron-hole pairs cool down to form a Fermi-Dirac distribution.[203] As the sample approaches the focal plane, the interband transitions become more efficient due to the sufficiently higher laser intensity leading to the depletion of all the empty band states. As a result, further excitation of carriers is impeded due to the Pauli exclusion principle, giving rise to the manifestation of saturation absorbance behavior.

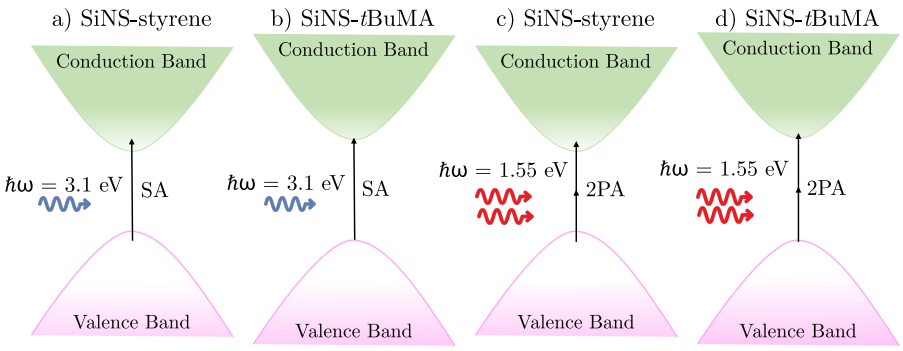

Figure 7.10: Schematic representation of the processes contributing to the NLO absorption of SiNS-styrene and SiNS-*t*BuMA under 400 nm (a, b) and 800 nm (c, d) laser excitation.

7.2.2 70 fs, 800 nm Laser Excitation

In Figure 7.11 some representative OA Z-scans of SiNS-*t*BuMA and SiNS-styrene dispersions are shown, obtained under 70 fs, 800 nm laser excitation, using different laser intensities. All dispersions have a linear absorbance α_0 of 1 cm^{-1} at 800 nm. As shown from these scans, both SiNSs exhibit a decrease in their linear transmittance close to the focal plane, indicating RSA ($\beta > 0$). This behavior is opposite to the SA behavior observed under 400 nm excitation, indicating the dependence of the NLO absorption of the SiNSs on the excitation wavelength. Since the excitation wavelength at 800 nm corresponds to a photon energy of 1.55 eV, it implies that the band gap of both SiNSs can be bridged by two photons (Figure 7.10 c), d)). Therefore, it is reasonable to assume that the observed RSA of SiNS-*t*BuMA and SiNS-styrene is due to a two-photon absorption (2PA) process. The average values of β for the 0.1 mg mL^{-1} dispersions (corresponding to a linear absorption coefficient α_0 of 1 cm^{-1}) of SiNS-*t*BuMA and SiNS-styrene are calculated to be about $(165 \pm 20) \times 10^{-15}$ and $(203 \pm 9) \times 10^{-15}$ m W^{-1}, respectively. An intensity-independent nonlinear absorption coefficient β is also observed for all other studied concentrations, suggesting that 2PA should be the dominant process contributing to the RSA behavior.[204] This can be explained by taking into account that 2PA has a lower probability, resulting in negligible ground state depletion. Thus, an intensity-independent nonlinear absorption coefficient β is expected.

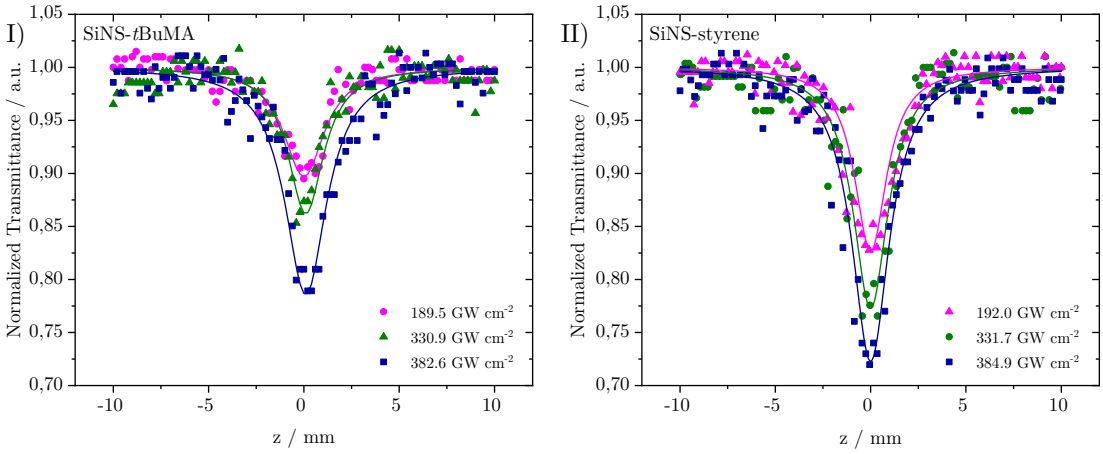

Figure 7.11: OA Z-scans of (I) SiNS-*t*BuMA and (II) SiNS-styrene dispersions under different laser intensities at 800 nm. All dispersions have a linear absorption coefficient α_0 of about 1 cm^{-1}.

Compared to other 2D nanomaterials exhibiting 2PA under similar experimental conditions,[205–209] the determined values of the nonlinear absorption coefficients β of SiNS-*t*BuMA and SiNS-styrene (0.1 mg mL^{-1}, 800 nm laser excitation) are in the upper range or even exceed their performance. Thus the large β values of both SiNS render them very promising candidates for OL devices providing protection against accidental exposure to high-power laser radiations for e.g. the human retina or sensitive optical sensors.

In general, an OL material exhibits high linear transmittance for low incident laser intensity, following the Beer-Lambert law, while its transmittance decreases at high incident laser intensity, deviating from this law. The laser intensity at which this deviation occurs is referred to as the optical limiting onset (OL_{on}) and is usually employed to characterize the efficiency of an OL material. Figure 7.12 presents the OL action of SiNS-styrene and SiNS-*t*BuMA toluene dispersions under 70 fs, 800 nm laser irradiation, with a concentration of 0.1 mg mL^{-1}. The dashed line corresponds to the linear transmittance of the samples, which is about 90 % at 800 nm, while the solid lines connecting the experimental data points guide the eye. As shown, the OL_{on} values of the SiNS-styrene and SiNS-*t*BuMA dispersions are approximately 0.0045 and 0.0065 J cm^{-2}, respectively, which are much lower than those of other 2D materials previously reported.[206,210–213]

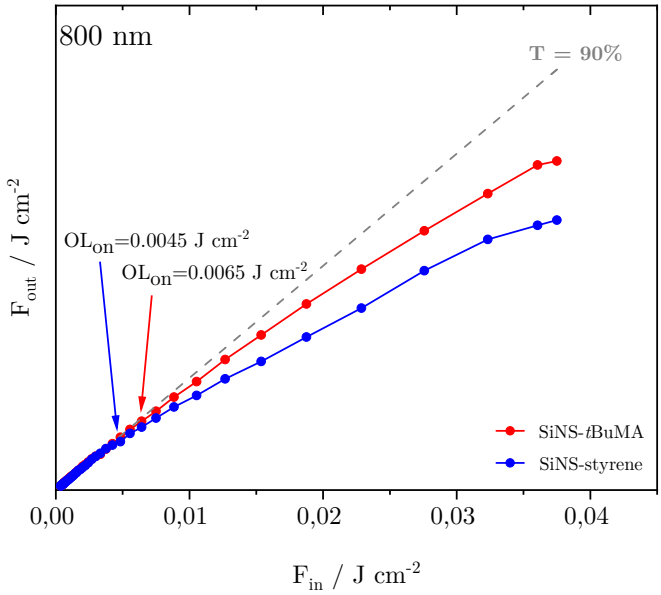

Figure 7.12: OL performance of SiNS-*t*BuMA and SiNS-styrene dispersions under 70 fs, 800 nm laser irradiation. The linear transmittance of the samples at 800 nm is approximately 90 %.

7.2.3 Comparison with Pure and Dodecyl-Functionalized Silicon Nanosheets

As can be seen from Tables 7.1 and 7.2, the functionalization of SiNS-H has a significant effect on the third-order NLO response of these SiNSs, leading to an exceptional enhancement of both the NLO absorption and refraction, opening up new possibilities for their implementation in high-performance optoelectronic and photonic devices. In more detail, the third-order susceptibilities $\chi^{(3)}$ of SiNS-*t*BuMA and SiNS-styrene obtained from the Z-scan measurements under 800 nm laser excitation, are about 35 and 50 times larger than that of SiNS-H and approximately 5 times larger than that of SiNS-dodecyl. Similarly, in the case of 800 nm laser excitation, the third-order susceptibilities $\chi^{(3)}$ of SiNS-*t*BuMA and SiNS-styrene exhibited an approximately 12 and 33 times enhancement compared to SiNS-H. At this point, it should be emphasized that since the NLO responses of neat *t*BuMA and styrene, measured under similar excitation conditions, are found to be negligible, the enhanced NLO responses of SiNS-*t*BuMA and SiNS-styrene can be undoubtedly attributed to the functionalization of the SiNSs. The above results are schematically presented in Figure 7.13. Comparing the NLO response of the two functionalized SiNSs, SiNS-styrene exhibits about 1.5 and 3 times larger third-order susceptibilities $\chi^{(3)}$ than SiNS-*t*BuMA under 800 and 400 nm laser excitation, respectively. The difference in the NLO responses of SiNS-styrene and SiNS-*t*BuMA is due to the different nature of the two functional groups, which can act as electron-donors/acceptors,[214,215] similarly to what has been reported elsewhere, e.g., for graphene.[216] So, since the NLO response of SiNS-styrene is stronger than that of SiNS-*t*BuMA, it could be reasonably assumed that the charge transfer between the styrene group and the SiNS is more efficient compared to that occurring in the case of the *t*BuMA group.

Table 7.1: NLO parameters of toluene, SiNS-H, SiNS-*t*BuMA, and SiNS-styrene determined by Z-scan techniques under 50 fs, 400 nm laser excitation. All values refer to a concentration of $1\,\mathrm{mg\,mL^{-1}}$.

Sample	β ($\times 10^{-15}$ m W^{-1})	γ' ($\times 10^{-21}$ m^2 W^{-1})	$\lvert\chi^{(3)}\rvert$ ($\times 10^{-16}$ esu)
Toluene	24.6 ± 2.0	8.0 ± 0.8	13.5 ± 1.0
SiNS-H	-5.6 ± 0.3	4.9 ± 0.9	7.2 ± 1.0
SiNS-*t*BuMA	-79.5 ± 10.0	57.7 ± 8.0	85.5 ± 11.0
SiNS-styrene	-177.0 ± 2.0	162.5 ± 18.0	237.5 ± 27.0

Table 7.2: NLO parameters of toluene, SiNS-H, SiNS-dodecyl, SiNS-*t*BuMA, and SiNS-styrene determined by Z-scan techniques under 70 fs, 800 nm laser excitation. All values refer to a concentration of 1 mg mL^{-1}. The results for SiNS-dodecyl are taken from Reference 104.

Sample	β ($\times 10^{-15}$ m W^{-1})	γ' ($\times 10^{-21}$ m^2 W^{-1})	$\lvert\chi^{(3)}\rvert$ ($\times 10^{-16}$ esu)
Toluene	53.8 ± 4.0	52.1 ± 4.0	80.4 ± 6.0
SiNS-H	—	22.0 ± 4.0	32.0 ± 6.0
SiNS-dodecyl	−400.0 ± 61.0	133.0 ± 6.0	293.0 ± 35.0
SiNS-*t*BuMA	1661.0±200.0	331.8 ± 38.0	1100.0±126.0
SiNS-styrene	1968.0 ± 90.0	728.7 ± 72.0	1530.0±114.0

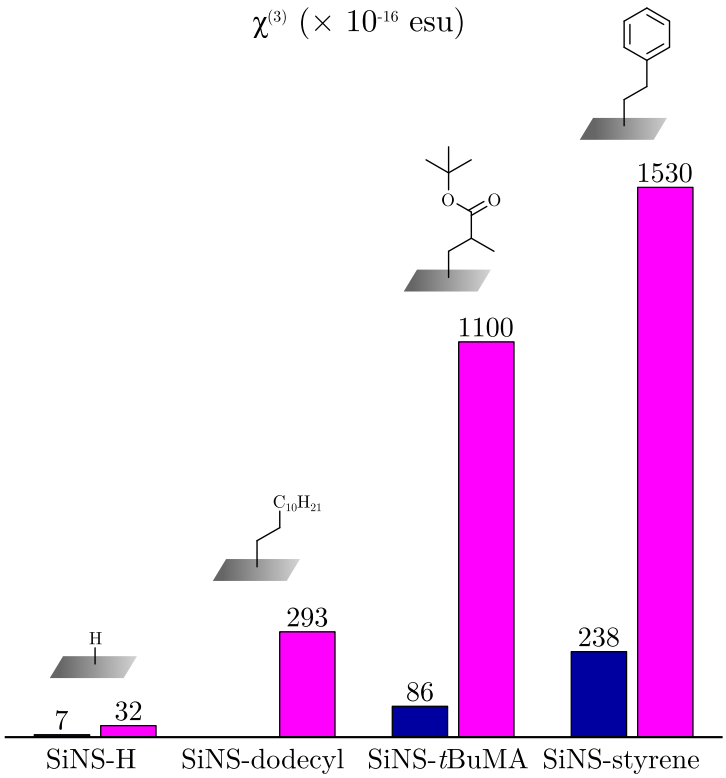

Figure 7.13: Third-order nonlinear susceptibility $\chi^{(3)}$ values of SiNS-H and SiNS-dodecyl, SiNS-*t*BuMA, and SiNS-styrene under 800 nm (magenta) and 400 nm (dark blue) laser excitation, determined by the Z-scan technique. All values refer to a concentration of 1 mg mL^{-1}.

Concerning the NLO absorptive response of the investigated SiNSs, it has to be highlighted that the chemical functionalization of SiNS-H with *t*BuMA and styrene gives rise to a very strong NLO absorption, as shown in Tables 7.1 and 7.2. So, while SiNS-H exhibit insignificant NLO absorption under 800 nm laser excitation (i.e., practically zero nonlinear absorption coefficient β, SiNS-*t*BuMA and SiNS-styrene have very large β values, i.e., $(1661 \pm 200) \times 10^{-15}$ and

$(1968 \pm 90) \times 10^{-15}$ m W^{-1}, respectively. Similar findings are observed under 400 nm laser excitation, where SiNS-*t*BuMA and SiNS-styrene possess about 15 and 32 times larger β values than SiNS-H, with the styrene functionalized SiNSs featuring the largest value. More importantly, both functionalized SiNSs show RSA (i.e., $\beta > 0$) under 800 nm excitation and SA (i.e., $\beta < 0$) under 400 nm excitation. This sign alternation of the NLO absorption is particularly interesting for photonic applications. Thus, the studied SiNSs can be employed as optical limiters or saturable absorbers by selecting the appropriate excitation wavelength.

7.3 Summary

In this study, SiNS-styrene and SiNS-*t*BuMA were prepared by the diaryliodonium salt initiated hydrosilylation between SiNS-H and the corresponding vinyl compounds. The successful functionalization was proven by vibrational spectroscopy. The functionalized SiNSs were pure samples without impurities or an embedding polymer matrix. Surface coverages of about 30 % were achieved for SiNS-styrene and SiNS-*t*BuMA as determined by TGA. XPS data further confirmed the success of the functionalization reactions and the degree of functionalization. As demonstrated in electron microscopy images, both nanomaterials are sheet structures.
These materials were investigated regarding their NLO properties under 50 fs, 400 nm and 70 fs, 800 nm laser excitations. Both SiNSs were found to exhibit very strong NLO responses significantly enhanced compared to pristine SiNS-H, demonstrating the importance of chemical functionalization for improving and tailoring the NLO response of SiNSs in view of several potential optoelectronic and photonic applications. In addition to their large optical nonlinearities, the present SiNSs were found to present wavelength-dependent NLO absorptive response, thus enlarging the range of their potential applications for optical limiting or as saturable absorbers, respectively. Concerning the NLO refraction, both SiNSs presented strong self-focusing, rendering them promising candidates for optical switching applications. Notably, the present functionalized SiNSs possessed significantly better NLO absorption and refraction than several other 2D nanostructures reported so far.

7.4 Outlook

As the aforementioned published results show, SiNS functionalized with styrene and *t*BuMA exhibit significantly enhanced NLO responses compared to SiNS-H

and SiNS-dodecyl.[102] Especially the introduction of styrene as a functional group appears to positively affect the NLO properties of the nanosheets. It would therefore be of interest to evaluate the NLO performance of SiNS functionalized with styrene derivatives. This could also provide a deeper understanding of the mechanism being responsible for the enhanced NLO properties, which was hypothesized to originate in a charge transfer between the styrene moiety and the nanosheets. Interesting styrene derivatives are e.g. phenylacetylene (C=C bond as linking unit between the phenyl ring and silicon), *N*,*N*-dimethyl-4-vinylaniline (+M effect of the dimethylamino group), or 4-cyanostyrene (−M effect of the nitrile group). Furthermore, larger conjugated π systems differently attached to the silicon network should be studied. Therefore, functionalization reactions by the BIP-induced hydrosilylation are tested. The employed substrates *N*,*N*-dimethyl-4-vinylaniline and 4-cyanostyrene as well as 1-vinylnaphthalene, 2-vinylnaphthalene, 9-vinylanthracene, 9-vinyl carbazole, and 2-vinylpyridine. All of these reactions yield functionalized SiNS-H, although the reaction protocol may require optimization with respect to the surface coverages. A complete characterization, as well as the investigation of the NLO properties of these materials, is pending. Scheme 7.2 summarizes the obtained functionalized SiNS and the corresponding surface coverages.

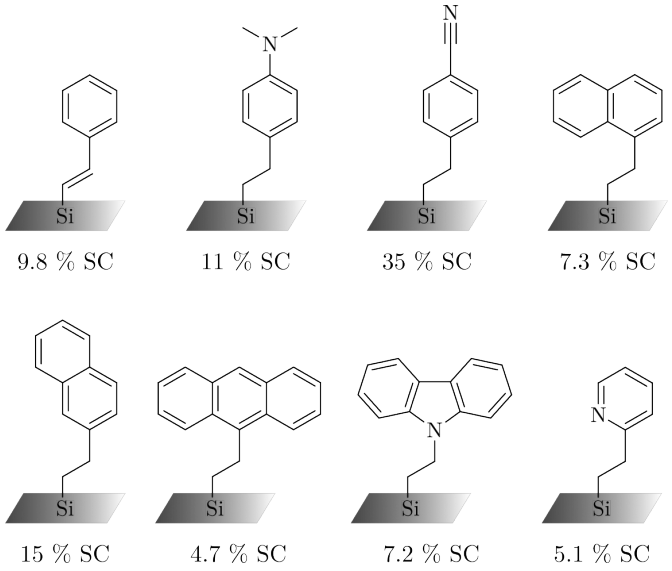

Scheme 7.2: Schematic description of SiNS-H functionalized with styrene derivatives. Applied functionalization reagents: phenylacetylene, *N*,*N*-dimethyl-4-vinylaniline, 4-cyanostyrene, 1-vinylnaphthalene, 2-vinylnaphthalene, 9-vinylanthracene, 9-vinyl carbazole, and 2-vinylpyridine (from left to right and from top to bottom).

7.5 Experimental Procedures

7.5.1 General Information

Instrument information, analytical techniques, procedures for solvent drying as well as the synthesis and etching of SiNS-H are found in Chapter 9.
The reactants were purchased from Sigma-Aldrich or TCI. The syntheses are performed under exclusion of water and air using standard Schlenk methods. All solvents are dried and degassed prior to use.

7.5.2 Functionalization with Styrene and tBuMA

HF-etched SiNS-H (45 mg, 1.5 mmol batch before etching) are dispersed in ethyl acetate (3 mL) and transferred into a heat-dried Schlenk tube for functionalization reactions. BIP (15 mg, 28 µmol) and an excess of styrene or *t*BuMA are added. The reaction mixture is degassed *via* three freeze–pump–thaw cycles. After stirring at room temperature for 16 h, toluene (6 mL) is added, and the mixture is stirred for 30 min. Workup is performed inside an argon-filled glove box: the supernatant after centrifugation (5000 rpm, 2 min) is discarded, the residue dispersed in toluene (0.5 mL), and centrifuged with methanol (6 mL). This washing cycle is repeated twice, and the residue is freeze-dried from benzene to yield SiNS-styrene or SiNS-*t*BuMA.

8

Conclusions and Outlook

This thesis describes an overview of several projects on hydride-terminated silicon and germanium nanosheets. These include the investigation of the preparation and photolysis of SiNS-H, the functionalization and selective degradation of mixed Ge/SiNS-H, as well as the modification of SiNS-H towards SiNS-styrene.

The objective of the first project was to develop a novel preparation route to obtain pure oxygen-free SiNS-H. The conventional method for synthesizing SiNS-H involves the topotactic deintercalation of calcium from the Zintl phase $CaSi_2$ through a reaction with concentrated aqueous hydrochloric acid. FTIR spectra of the as-prepared nanosheets exhibit relatively intense oxidation bands. As source of this oxidation the three parameters acid, temperature, and atmosphere were evaluated. In a series of experiments, water was identified to cause oxidation during the preparation of SiNS-H, likely occurring through hydrolysis and subsequent condensation of the silanol groups. The applicability of anhydrous reaction systems was thus investigated in the conversion of $CaSi_2$ into SiNS-H. These systems comprised a variety of solvents combined with different acids and Ca^{2+} solvation principles. $CaSi_2$ was not converted in any of these approaches, leading to the conclusion that water plays an important role in the SiNS-H formation. Indeed, a successful SiNS-H preparation was achieved with a mixture of ethanolic hydrogen chloride and aqueous hydrochloric acid with a minimum amount of 100 equivalents of water per equivalent $CaSi_2$, confirming this hypothesis.

The second project describes the investigation of the photodegradation of SiNS-H under 365 nm UV light. Previously, it has been reported that a white degradation product forms upon UV irradiation of the yellowish SiNS-H. In preliminary tests, it was demonstrated that the formation of this white product is the result of a photooxidation. The influence of the atmosphere on the photodegradation was investigated in argon, air, and oxygen atmospheres. A radical mechanism is involved in the UV light-induced degradation of SiNS-H, independent of the atmosphere. This was proven by the initiation of the polymerization of MMA upon irradiation in the presence of SiNS-H. In all atmospheres, the material lost its photoluminescence, and after irradiation, white (oxygen), light yellow (air), and yellow (argon) products were obtained. The characterization of these products revealed that irradiation of SiNS-H under argon atmosphere resulted in an amorphization of the material through rearrangement of the bonds, while photooxidation through oxygen insertion into Si-Si bonds occurred in air and oxygen atmospheres.

The functionalization of mixed Ge/SiNS-H was in the focus of the third project. Modification reactions that had already been established for both, the pure SiNS-H and GeNS-H, were applied to Ge/SiNS-H. These are the AIBN-initiated and the thermally induced hydrosilylation and hydrogermylation of alkenes. Ge/SiNS-H were successfully functionalized with 1-dodecene. The comparison of the modified nanosheets with the analogs of the pure SiNS-H and GeNS-H showed that in both reactions, SiNS-dodecyl exhibited the highest functionalization degree, while GeNS-dodecyl had a low surface coverage. The surface coverage of the mixed Ge/SiNS-dodecyl was in between the pure components. The study was continued regarding a selective functionalization of Ge/SiNS-H. In various functionalization reactions, including hydrometalation reactions, amination, and thiolation with subsequent ligand exchange, a reaction was sought that runs exclusively with either SiNS-H or GeNS-H was searched. In none of these experiments a selective reaction occurred. Instead, the tested reactions ran with both types of nanosheets.

In a follow-up study, the butyl-functionalization of SiNS-H and GeNS-H by the reaction with *n*BuLi was studied. During the workup with methanol, the SiNS-H decomposed. This decomposition was caused by MeOLi, which formed from remaining *n*BuLi and methanol. The reactivities of SiNS-H, Ge/SiNS-H, and GeNS-H towards MeOLi were compared. SiNS-H degraded by the Si-Si bond cleavage

under the formation of TMOS, while GeNS-H remained unchanged. A selective removal of silicon atoms was observed in Ge/SiNS-H. Given that silicon was not quantitatively removed, it can be concluded that the Ge-Si bonds remain intact.

Finally, SiNS-H were functionalized by the diaryliodonium salt-induced hydrosilylation of both styrene and *t*BuMA. The as-prepared modified nanosheets were characterized in detail. Vibrational spectroscopy and XPS confirmed the successful SiNS functionalization, while electron microscopy revealed sheet-like structures of the modified nanosheets. The NLO properties of SiNS-styrene and SiNS-*t*BuMA were investigated under femtosecond laser excitation at 400 and 800 nm. The functionalized materials showed exceptional NLO properties, which were strongly enhanced compared to SiNS-H and SiNS-dodecyl. A comparison of the two materials revealed a stronger NLO response for SiNS-styrene than for to SiNS-*t*BuMA. This demonstrated the importance of surface functionalization for the NLO properties of SiNS.

The methods and concepts compiled in this thesis build a basis for further research on SiNS-H and Ge/SiNS-H.
The current preparation of SiNS-H by the wet-chemical top-down approach starting with $CaSi_2$ has a significant limitation: the imperfect structure of the product. Imperfect means, that the as-prepared SiNS-H show deviations from the theoretical structure of $[Si_6H_6]_n$. Besides the oxidation of the material, chlorine, calcium, and bulk silicon impurities were found in the nanosheets. Furthermore, the IR spectra of different batches of SiNS-H showed slight variations, and the functionalization reactions yielded different surface coverages depending on the SiNS-H batch. New approaches should therefore focus on a method that a) completely converts $CaSi_2$ to SiNS-H, b) results in the formation of oxygen-free SiNS-H with a structure closer to the ideal structure, and c) is more reproducible. Another limitation of SiNS-H as well as Ge/SiNS-H regarding their surface functionalization is their stacking behavior. Although sonication of nanosheet dispersions is sometimes used in literature protocols to break up nanosheet stacks, a detailed study of the exfoliation to monolayers, e.g., *via* ultrasound treatment, should be performed. Finally, the scale-up production of SiNS-H is difficult. SiNS-H were prepared from 1 g $CaSi_2$, but HF-etching in batches larger than 60 mg was not efficient. A new method to produce larger amounts of etched SiNS-H would save time in the laboratory and allow for large scale experiments as well as series of experiments that are more comparable because only one batch is used.

The investigation of the photodegradation of SiNS-H is complete, as the structures of the decomposition products were identified. However, a detailed reaction mechanism is difficult to determine due to the imperfect structure of SiNS-H prior to UV irradiation. In situ characterization methods, such as electron paramagnetic resonance, IR, or photoluminescence spectroscopies, could provide further details on the degradation mechanism. This requires special experimental setups in which SiNS-H are exposed to defined atmospheres, and some of these techniques are not applicable to dispersions of SiNS-H.

Attempts to selectively functionalize mixed Ge/SiNS-H showed that germanium and silicon have very similar reactivities. Therefore, a selective functionalization approach appears impossible. However, the selective removal of silicon atoms from Ge/SiNS-H by MeOLi could be interesting for potential applications. It is hypothesized that holes are introduced into the nanosheets during the degradation reaction, resulting in the formation of a porous material. The porosity increases the surface area and the number of edge sites. Therefore, the properties of the porous material compared to the pristine Ge/SiNS-H should be explored with regard to applications like catalysis.

The study of the NLO properties of functionalized SiNS revealed the crucial influence of the surface group on the these properties. SiNS-styrene exhibited a better NLO performance than SiNS-*t*BuMA, which was assumed to be due to a more efficient charge transfer between styrene and SiNS. This requires further investigation using spectroscopic techniques like transient absorption spectroscopy. Additionally, SiNS functionalized with styrene derivatives such as *N*,*N*-dimethyl-4-vinylaniline (+M effect), 4-cyanostyrene (−M effect), vinylnaphthalenes or vinylanthracenes (larger conjugated π systems) could help to elucidate the enhancement of the NLO properties.

9

General Experimental Methods

9.1 Chemical and Solvent Preparations

A LABstar pro glove box by MBraun with argon 5.0 (Westfalen) as the working gas is used for storing reagents and samples, sample preparation in an inert atmosphere and general handling of solid substances that are sensitive to oxidation and moisture.

Experiments employing air or water-sensitive reagents are conducted in heat-dried glassware utilizing standard Schlenk techniques, with argon 5.0 (Westfalen) as inert gas.

All chemicals were purchased from Sigma-Aldrich, ABCR, TCI, Acros Organics, Evochem, or Wacker and are used without further purification unless otherwise stated.

Acetonitrile, toluene, benzene, dichloromethane, and diethyl ether are dried with an MBraun solvent purification system, MB SPS-800, using argon 5.0 (Westfalen). Other solvents are dried by passing through a column of heat-dried basic silica or molecular sieves. Alternatively, solvents are distilled. Activated molecular sieves (3 and 4 Å) are used to store dry solvents (except for acetone). After drying, all solvents are degassed by introducing argon for 30 min.

9.2 Instruments and Methods

Fourier-transform infrared spectroscopy (**FTIR**) measurements of the powdery nanosheet samples and liquid chemicals are conducted on a nitrogen-cooled Bruker Vertex 70A spectroscope on an attenuated total reflection module.

Raman spectra are acquired with a Renishaw inVia Raman spectrometer with a Leica DM/LM microscope and a 785 or 532 nm laser as the excitation source. A 50 × objective is used to focus the laser beam onto a spot on the surface of the sample. The powdery nanosheet samples are placed on a clean glass slide and pressed with a second glass slide to produce an even surface.

Thermogravimetric analysis (**TGA**) is performed inside an argon-filled glove box on a Netzsch TG 209 F 1 Libra instrument with a heating rate of $10\,^{\circ}\mathrm{C\,min^{-1}}$ from 20 to 700 °C under an argon flow of $20\,\mathrm{mL\,min^{-1}}$. For the sample preparation, a minimum of 2 mg of the sample is weighed into an Al_2O_3 crucible. The surface coverage (SC) of functionalized nanosheets is calculated from the measured mass loss (ML). Assuming that the mass loss obtained from TGA is due only to the cleavage of the organic groups and the remaining mass is silicon (or germanium, or a 1:1 mixture of silicon and germanium), the surface coverages are calculated by the ratio of the amount of organic groups (n_R) to the amount of the group IV element (n_M):

$$SC = \frac{n_R}{n_M} = \frac{M_M}{M_R} \cdot \frac{ML}{1 - ML} \tag{9.1}$$

where M_R is the molar mass of the organis group, and M_M is the molar mass of silicon (or germanium, or a 1:1 mixture of silicon and germanium). Protons attached to the group IV elements are neglected in this calculation.

^{1}H and ^{29}Si nuclear magnetic resonance (**NMR**) spectra are recorded on Bruker AV-400HD or AV-500C spectrometers at ambient temperature (300 K). The ^{1}H NMR spectroscopic chemical shifts δ are reported in ppm and are internally referenced to the residual resonances of the deuterated solvent. The following abbreviations are used to describe signal multiplicities: s = singlet, t = triplet, m = multiplet.

X-ray photoelectron spectra (**XPS**) are recorded on a LeyboldHeraeus LHS 10 spectrometer using a non-monochromatized Mg Kα source (1253.6 eV). Powder samples are pressed into cavities of a stainless-steel sample holder. Sample preparation and transfer into the XPS spectrometer are carried out under argon atmo-

sphere. The analyzer is operated at a constant pass energy of 100 eV leading to an energy resolution with a full width at half-maximum of approximately 1.1 eV. The energy scale of the spectra is corrected for sample charging by using the O 1s main signal of SiO_2 at 533.0 eV (for photodegraded samples). Alternatively, the energy scale is corrected by using the C 1s main signal of aliphatic/aromatic carbon at 284.5 eV (for functionalized SiNS). All spectra are recorded in an ultra-high vacuum chamber at a pressure below 5×10^{-8} mbar. Core level spectra are deconvoluted using Voigt functions after linear background subtraction.

Powder X-ray diffraction (**XRD**) measurements are recorded in transmission mode on a STOE STADI P diffractometer equipped with a Ge(111) monochromator for Cu Kα radiation (λ = 1.54056 Å) at 50 kV and 30 mA. Reflexes are detected by a Dectris MYTHEN2 R 1K detector. The samples are ground, filled into 0.3 mm glass capillaries, and then sealed prior to the measurement.

Gel permeation chromatography (**GPC**) is performed on a PL-GPC 50 Plus by Agilent with an integrated refractive index unit, two light scattering detectors and a differential pressure viscosimeter. THF (with 222 mg L^{-1} 3,5-di-*tert*-butyl-4-hydroxytoluol as stabilizer) or DMF (with 35 mmol L^{-1} LiBr) are used as eluent. Two MixedC columns (Agilent) at 40 °C are used with THF as solvent or two PolarGel M columns (Agilent) at 30 °C with DMF. Polystyrene is used as a standard for the relative molecular weight distribution.

Photoluminescence (**PL**) spectroscopy is performed with an AVA-Spec 2048 spectroradiometer (Avantes) coupled with the 365 nm light source Prizmatix (LED current controller) and an Avantes CUV-FL-UV/VIS cuvette holder. Measurements are taken from toluene dispersions in a quartz glass cuvette (40 × 10 × 1 mm) and recorded with a 90° angle between the light source and spectrometer.

Atomic force microscopy measurements (**AFM**) are recorded on a Bruker Veeco Dimension V with TAP190DLC tips in tapping mode with a scan rate of 0.5 Hz. Samples are prepared from toluene dispersions drop-casted onto polished Si/SiO_2 substrates inside an argon-filled glove box.

Scanning electron microscope (**SEM**) images are either collected on a JEOL JSM 7500F at an accelerating voltage of 1 kV or on a Hitachi TM-1000 tabletop microscope operated at 15 kV. SEM samples are prepared by depositing a droplet of diluted dispersions in toluene on a clean silicon wafer under an argon atmosphere. Alternatively, the powdered samples are placed

directly on a carbon tape.
Energy dispersive X-ray (**EDX**) spectra are collected using the a Hitachi TM-1000 tabletop microscope equipped with a SwiftED-TM EDX unit.

Transmission electron microscopy (**TEM**) is performed on a JEOL JEM 1400 plus microscope at an accelerating voltage of 120 kV. Samples are drop-casted from a toluene dispersion onto a carbon-coated 300 mesh copper grid (obtained from Quantifoil) inside an argon-filled glove box.

A homemade UV reactor system is used for the photodegradation reactions. The reactor consists of a 365 nm **UV LED** light (Osram LED Engin LuxiGen, LZ4-V4UV0R) operating at 3 W, mounted on a water-cooled metal plate which sits on a magnetic stirrer. Reaction vessels are clamped above the light source.

UV-vis-NIR absorption spectra of toluene dispersions are recorded on a JASCO V-670 double-beam spectrophotometer.

UV-vis diffuse reflectance absorbance (**DRA**) spectra are measured on a Shimadzu UV-3600 Plus with integrating sphere. The powdery samples are put between two quartz slides and barium sulfate is used as a reference.

Z-scan measurements are performed with a CPA mode-locked Ti:sapphire laser system (Trident X, Amplitude Technologies) operating at 800 nm (70 fs), and at its second harmonic at 400 nm (50 fs) at a repetition rate of 10 Hz. The laser beam is focused into the samples by a 20 cm focal length quartz lens, while its spot radius at the focus is determined by a CCD camera (approximately 20 and 25 µm for the 400 and 800 nm laser outputs, respectively). The normalized transmittance of a sample is monitored by the open-aperture (OA) and closed-aperture (CA) Z-scans. Different concentrations of the samples dispersed in toluene are measured in a 1 mm thick quartz cell at different incident laser intensities ranging from 128 to 896 GW cm^{-2}.

9.3 Experimental Information

9.3.1 Preparation of Calcium Disilicide

A pellet of stoichiometric amounts of calcium and silicon is pressed (4 t). The pellet is melted in an arc furnace within an argon-filled glove box until a homogeneous regulus is formed. The silver regulus is ground in an agate mortar and pressed

into a pellet. After a two-time repetition, $CaSi_2$ is formed, which is ground for further use.

9.3.2 Preparation of other Zintl Phases

The preparation of $CaGe_2$ and the mixed CaGeSi is analogous to that of calcium disilicide.

9.3.3 Preparation of Hydride-Terminated Silicon Nanosheets

Concentrated aqueous $HCl_{(aq)}$ (37 wt%, 100 mL) is placed in a Schlenk flask, which has been pruged with argon prior to use. The flask is precooled to a temperature of either −25 °C or −32 °C in a freezer. Precooled calcium disilicide (1 g) is added to the concentrated hydrochloric acid in an argon counterflow. The mixture is maintained at −25 °C or −32 °C for seven to nine days and the flask is occasionally stirred. The yellow flakes are filtered over a Schlenk frit and washed with acetone (3 × 50 mL). The resulting SiNS-H are dried in vacuum and stored in an argon-filled glove box.

9.3.4 Preparation of other Group IV Nanosheets

GeNS-H and mixed Ge/SiNS-H are prepared analogous to SiNS-H from the corresponding Zintl phases calcium digermanide and mixed calcium silicide germanide, respectively.

9.3.5 Etching of Silicon and Mixed Germanium/Silicon Nanosheets

SiNS-H and Ge/SiNS-H are etched in batches of 60 mg. The nanosheets are dispersed in dry and degassed ethanol (2 mL) and sonicated for 5 min to break up agglomerates. The dispersion is then transferred to a PTFE centrifuge tube, whereupon water (1 mL) and concentrated $HF_{(aq)}$ (48 wt%, 2 mL) are added. Dichloromethane is added (approximately 6 mL) and the tube is gently shaken to extract the etched nanosheets into the organic phase. The etched nanosheets are transferred into a second centrifuge tube using a polypropylene pipette. The tube is filled with toluene to facilitate subsequent centrifugation. After centrifugation (9000 rpm, 4 min), the nanosheets are washed with dry acetone (6 mL) and centrifuged again. The remaining residue is freeze-dried from benzene or dispersed in an organic solvent for subsequent reactions.

A

Optimization of the AIBN-Induced Hydrosilylation of Silicon Nanosheets

The hydrometalation of SiNS-H or GeNS-H can be induced radically, thermally, or catalytically and is a well-established route towards nanosheets functionalized with organic groups (see Chapter 2.2.5 and 2.4.1). A relevant parameter for comparing and evaluating the efficiency of functionalization reactions is the surface coverage of the nanosheets. Among other determination methods, this quantity can be calculated from the mass loss obtained in TGA. Therefore, it is assumed that the mass loss is only due to the cleavage of the organic group, and the remaining mass corresponds to the group IV element of which the nanosheet is composed.

Before attempting to functionalize Ge/SiNS-H with organic groups (see Chapter 5), the dodecyl-functionalization of SiNS-H and GeNS-H, known from the literature, is carried out. More specifically, the radical-induced hydrosilylation and hydrogermylation of SiNS-H and GeNS-H using AIBN is performed according to the literature procedures previously described by our group and the Veinot group in References 76 and 138. In these functionalization reactions, AIBN is added to the nanosheets and 1-dodecene, dispersed/dissolved in toluene. The reaction mixture is either directly heated to the reaction temperature or sonicated beforehand. As shown in Table A.1, the two dodecyl-functionalization reactions

differ in terms of the reactant equivalents, the reaction time and temperature, as well as the ultrasound pretreatment.

Attempting to reproduce the literature reaction with SiNS-H, yields a TGA mass loss of 46 %, corresponding to a surface coverage of 14 %, instead of the reported mass loss of 52 % (surface coverage of 18 %).[76] Similarly, for GeNS-H a mass loss of 15 % (surface coverage of 7.4 %) was obtained instead of 52 % (surface coverage of 47 %).[138] An explanation for these deviations from the literature values could be, that the particle size and its distribution were different and the materials had a higher specific surface area.

To compare the functionalization of all three kinds of nanosheets (Si and Ge), a provisional standard is established by rather randomly choosing the parameters listed in Table A.1, which are between those found in the literature. Using these parameters, results in low surface coverages of 11 % and 4.6 % for SiNS-dodecyl and GeNS-dodecyl, respectively, which in comparison to the literature values are not satisfying. Thus, the surface coverages should be improved by optimizing the reaction conditions before applying this new standardized method to Ge/SiNS-H. SiNS-H are therefore chosen as model nanosheet and the parameters to be systematically optimized are the equivalents of 1-dodecene and AIBN, the toluene volume, the ultrasound pretreatment, and the reaction time. The success of the functionalization is evaluated by FTIR measurements and the degree of functionalization is determined by TGA. Exemplary FTIR spectra and TGA data are shown in Figures 5.1 and 5.2.

Table A.1: Literature parameters for the AIBN-induced functionalization of SiNS-H and GeNS-H with 1-dodecene in comparison to the provisional standard parameters established in this work.

	Literature parameters		Prov. standard
	SiNS[76]	GeNS[138]	in this work
Equivalents of 1-dodecene	5.8	66	25
Equivalents of AIBN	0.06	0.9	0.5
Toluene volume / mL per mmol NS	3.9	29	5.0
Ultrasonication duration / h	—	3.0	0.5
Reaction time / h	16	12	16
Reaction temperature / °C	70	65	70
Literature surface coverage / %	18	47	—

A.1 Equivalents of 1-Dodecene

1-dodecene is the functionalization agent in the hydrosilylation of SiNS-H. Based on the provisional standard method described above, the equivalents of 1-dodecene are varied in a range of 5 to 100 equivalents, while keeping all other parameters, except for the ultrasonication period, constant. In these experiments, the reaction mixture is not sonicated prior to heating it to 70 °C. Figure A.1 I) shows the surface coverages calculated from TGA results, in dependence on the 1-dodecene equivalents. Apparently, the quantity of 1-dodecene has no influence on the surface coverage of SiNS-dodecyl in the investigated range of equivalents as the surface coverages are all similarly about 10 to 11 %. As an excess of the functionalization agent is used in all experiments, the large excess is not important. These results indicate that the number of active surface species on the nanosheets is the limiting factor. Further optimization is continued with 10 equivalents of 1-dodecene.

A.2 Equivalents of Azobisisobutyronitrile

The next parameter to be optimized is the amount of the radical initiator AIBN. A higher surface coverage of SiNS-dodecyl is expected when more AIBN is used because more radicals can be formed which induce the hydrosilylation. The amount of AIBN is modified from 0.05 to 0.9 equivalents. Indeed, the obtained surface coverages match the expected trend as can be seen from plot II) in Figure A.1. Surface coverages between 7 to 8 % are obtained for AIBN equivalents less than or equal to 0.26. On the other hand, 0.9 equivalents of radical starter lead to a surface coverage of 13 % which is 2 % higher than the surface coverage before the optimization of the amount of initiator. For this reason, 0.9 equivalents of AIBN are used in the next experiments.
Later, a reaction with 2 equivalents of AIBN also performed. This reaction yields a surface coverage of 22 %. However, this reaction is not comparable to the others, as a different batch of SiNS-H is used.

A.3 Toluene Volume

Having found optimized equivalents of 1-dodecene and AIBN, the concentrations of the reactants are changed by varying the volume of toluene. SiNS-H are not soluble in any organic solvent but can only be dispersed. Hence, a concentrated reaction mixture probably favors higher surface coverages due to reduced diffusion

limitations. Volumes in the range of 2.6 to 50 mL toluene per mmol SiNS-H are screened to find the optimum. In addition, a reaction is tested without solvent. As expected, the surface coverage inversely correlates with the toluene volume and thus the concentration of the reactants: Surface coverages of 16, 13, 10, 9.4 and 9.0 % are observed for 2.6, 5, 10, 25 and 50 mL toluene per mmol SiNS-H, respectively (see Figure A.1 III)). Interestingly, the bulk reaction without toluene does not result in a higher degree of functionalization since the surface coverage is only 14 %. This is probably due to the low volume of 1-dodecene which is hardly enough to cover the SiNS-H flakes and thus makes the reaction impracticable to perform. In this case, more equivalents of 1-dodecene would be beneficial. Because of the best performance regarding the functionalization degree, 2.6 mL toluene per mmol SiNS-H are used in the following optimization experiments.

A.4 Ultrasound Pretreatment

In the experimental procedure for the preparation of GeNS-dodecyl described by Yu *et al.*, the reaction mixture is pretreated in an ultrasonication bath for 3 hours before heating it to 65 °C.[138] This additional step compared to the method of Helbich *et al.*[76] breaks up agglomerates of nanosheets and results in their exfoliation. In consequence, a higher surface area of the nanoshseets should be accessible for the functionalization reaction. Until now, the parameter optimization did not include the ultrasonication of the reaction mixure. In a series of experiments, the influence of the ultrasonication on the reaction system is evaluated by applying sonication periods of 0, 0.5, 1, 2, 3 and 10 hours before heating and maintaining the reaction mixture to 70 °C for 16 hours. These different treatments result in surface coverages of 16, 14, 13, 17, 17 and 9.1 %, respectively, showing an optimum at 2 and 3 hours of ultrasonication (see Figure A.1 IV)). Surprisingly, the surface coverage in the sample with 10 hours of sonication has the lowest surface coverage. The FTIR spectrum of this sample also showed an intense Si-O-Si mode at 1056 cm^{-1}. Apparently, oxidation competed with hydrosilylation in this experiment.

Thus, an ultrasonication period of 2 hours is considered to be suitable for the standardized functionalization procedure and this pretreatment is employed in the following reactions. With this, the optimization is concluded and the optimum reaction conditions are listed and compared with the old standard parameters in Table A.2.

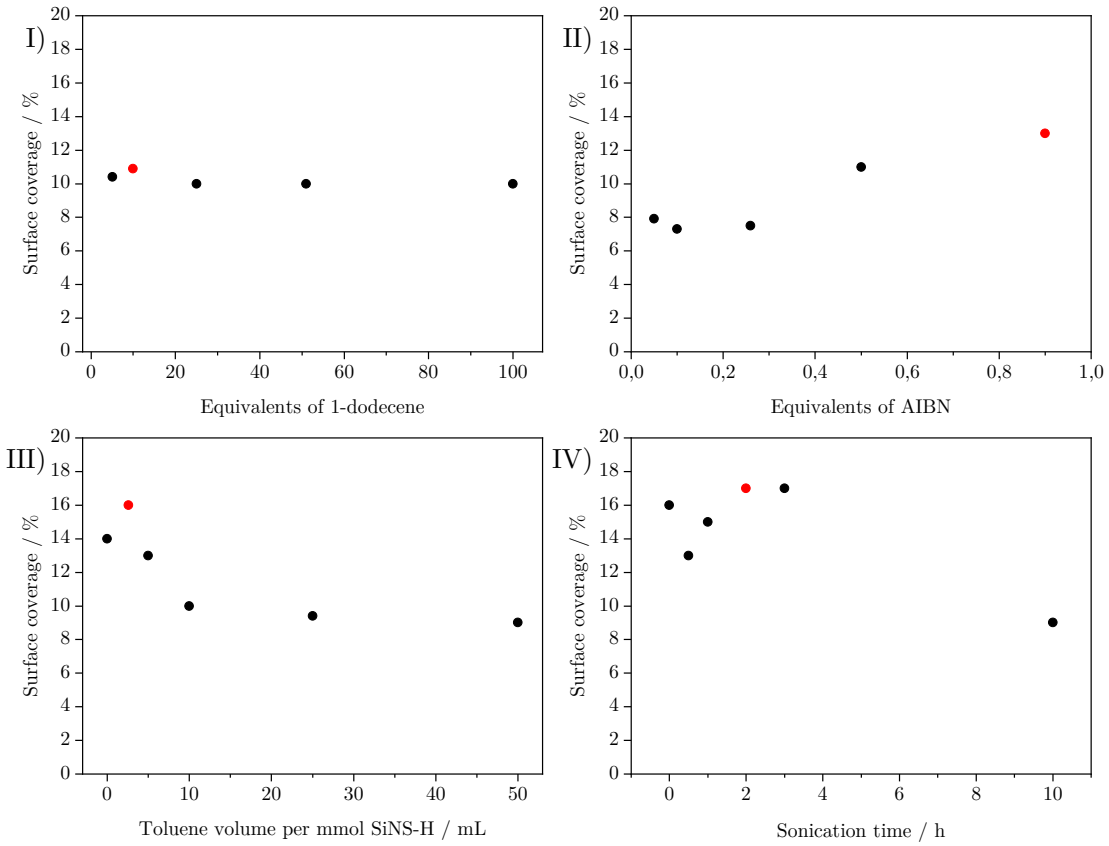

Figure A.1: Surface coverages of SiNS-dodecyl in dependence on the parameters to be optimized: Equivalents of 1-dodecene (I) and AIBN (II), toluene volume (III), and duration of sonication (IV). The red circle shows the optimum surface coverage for each parameter.

Table A.2: Optimized parameters for the AIBN-induced functionalization of SiNS-H with 1-dodecene in comparison to the previous standard parameters established in this work.

	Old standard	New standard
Equivalents of 1-dodecene	25	10
Equivalents of AIBN	0.5	0.9
Toluene volume / mL per mmol NS	5.0	2.6
Ultrasonication duration / h	0.5	2.0
Reaction time / h	16	16
Reaction temperature / °C	70	70
Surface coverage / %	11	17

A.5 Preliminary Tests: Reaction Period

Hitherto, the reactant equivalents, the concentration of toluene, and the sonication pretreatment of the hydrosilylation reaction were successfully optimized. Regarding the conversion of the reaction, it is unknown, if the reaction is completed and thus the possibly highest surface coverage is reached after the so far applied 16 hours. At least a significant amount of the AIBN has decomposed over that period (5 hours half-life time at 70 °C).[217] To find the optimal reaction time, attempts are made to track the reaction progress using the 1-dodecene/toluene ratio. With the optimized parameters (see above), the 1-dodecene/toluene molar ratio is 0.41 at the beginning of the reaction and the theoretical ratio after full conversion is 0.37. This shows, that the concentration of 1-dodecene only decreases little. In order to find a method for the accurate determination of this ratio, ^{1}H NMR spectroscopy and gas chromatography (GC) are tested.

^{1}H NMR spectra of mixtures of 1-dodecene and toluene in defined ratios are recorded in $CDCl_3$. With the integrals of the methyl groups of both chemicals (chemical shifts at 0.88 ppm (t, 3H, CH_3) for 1-dodecene and 2.36 ppm (s, 3H, CH_3) for toluene), the 1-dodecene/toluene ratios of the samples are calculated. Ratios with absolute deviations of up to 10 % from the expected values are obtained. Since this range is in the same magnitude as the difference in the reactant ratios in the beginning and after complete conversion, ^{1}H NMR spectroscopy is no suitable method to track the reaction progress.

Thus, GC is evaluated as an alternative. This time, solutions which are similar to the reaction mixture are prepared: AIBN and defined amounts of 1-dodecene and toluene are mixed. Sample preparation includes dilution of the mixtures with DCM which is performed twice to proof its reproducibility. The diluted samples are further filtered through short alox columns to remove AIBN from the mixtures. This is proven by ^{1}H NMR spectroscopy and is necessary as AIBN is not allowed to be loaded onto the GC column. The areas of the peaks in the chromatograms are used to determine the ratio of 1-dodecene and toluene. All samples are measured twice and the duplicate determinations are very precise. However, significant deviations are observed in the samples with the same reactant ratios which were twice diluted with DCM. Relative deviations of up to 40 % are found. This shows that the measurements of the samples are well reproducible, but the sample preparation is a crucial step.

After these preliminary measurements, tracking of the reaction progress of the

functionalization of SiNS-H with 1-dodecene is still tried. The used parameters are listed in Table A.2. Timed sampling of the reaction mixture is performed by taking less than 1 mL out of the reaction vessel. The solution is then diluted with DCM and filtered through an alox column to remove SiNS-H and AIBN before GC measurement. Tracking the reaction over 22 hours, did not show the expected decrease in the ratio of the reactant peak areas in the chromatograms. Instead, random ratios over the time are found and thus it can be concluded, that the sample preparation is defective and unreliable. A reason could be the vapor pressure of toluene which might evaporate during diluting the sample as the reaction mixure has a temperature of 70 °C. At this point, no more attempts are made to track the reaction progress and a reaction period of 16 hours is used as the standard reaction time.

A.6 Optimized Surface Coverages

After optimization, the new standard parameters are 10 equivalents of 1-dodecene, 0.9 equivalents of AIBN, 2.6 mL per mmol nanosheets, 2 hours sonication before 16 hours heating at 70 °C. As shown before, for SiNS-dodecyl, the surface coverage increases from 11 % with the old parameters to 17 % with the optimized ones. This corresponds to a relative increase of 55 %. The same procedure is applied to GeNS-, which yields a surface coverage of 8.6 % compared to 4.6 % before the optimization (relative increase of 87 %).
Overall, the high surface coverages from the literature[76,138] cannot be reproduced, but the surface coverages are significantly improved compared to the initial experiments described above.

A.7 Findings beyond the Scope of the Parameter Optimization

A.7.1 Ultrasonication

The dodecyl-functionalization of the SiNS-H by ultrasonication for 16 hours without subsequent heating is tried. This results in SiNS-dodecyl with a surface coverage of 18 % and shows that no radical initiator is required when using sonication treatment. The energy input into the reaction mixture by ultrasonication appears to be sufficient to generate radicals and induce the hydrosilylation reaction.

A.7.2 ABCN as Initiator

Besides AIBN, 1,1'-azobis(cyclohexanecarbonitrile) (ABCN) is tested as an alternative radical initiator. This initiator is used in the literature for the alkyl functionalization of silicon nanocrystals.[218] The optimized parameters for reactant equivalents are used, but instead of 16 hours at 70 °C with AIBN, the reaction is run at 100 °C for 18 hours with ABCN. TGA reveals a surface coverage of 24 %, which is about 7 % higher than in the functionalization with AIBN. Thus, ABCN is also a suitable initiator for the hydrosilylation of SiNS-H.

A.7.3 Batch of the Silicon Nanosheets

In the optimization experiments, an identical batch of SiNS-H was utilized. When repeating the hydrosilylation of 1-dodecene with different batches of SiNS-H, the obtained surface coverages exhibited a notable discrepancy, varying within a range of ± 13 % (absolute) or ± 82 % (relative). This indicates that the reproducibility of reactions with SiNS-H is challenging.

A.8 Experimental Procedures

A.8.1 General Information

Instrument information, analytical techniques, procedures for solvent drying, the synthesis and etching procedure of SiNS-H are found in Chapter 9.
The reactants were purchased from Sigma-Aldrich. 1-Dodecene is dried by passing through a column of heat-dried basic silica and degassed in three freeze-pump-thaw cycles, before storage over molecular sieve (4 Å) within an argon-filled glove box. AIBN is recrystallized from dry ethanol and dried in vacuum.
Reactions under exclusion of water and air are performed using standard Schlenk methods. All solvents are dried and degassed prior to use.

A.8.2 Optimization of the AIBN-Initiated Hydrosilylation

As a parameter optimization is conducted, the reaction parameters are varied in the experiments. Detailed information on the complete experimental series is provided in Table A.3.
Etched SiNS-H (10 mg batches), AIBN, and 1-dodecene are dispersed/dissolved in toluene in a heat-dried Schlenk tube inside an argon-filled glove box. The mixture is degassed in three freeze-pump-thaw cycles and sonicated upon need

before being stirred at 70 °C for 16 hours. The reaction mixture is centrifuged (4000 rpm, 2 min) and redispersed in toluene (0.5 mL). Methanol (6 mL) is added and the mixture is centrifuged. This redispersion/centrifugation cycle is repeated twice. The remaining solid is freeze-dried from benzene.

Table A.3: Varying reactant compositions and sonication periods for the hydrosilylation of 10 mg SiNS-H. The parameters highlighted in gray are the optimized values.

		Eq. $C_{12}H_{24}$	Eq. AIBN	Toluene volume / mL per mmol SiNS-H	Sonication / h
$C_{12}H_{24}$	1	5.1	0.5	5.0	—
	2	10	0.5	5.0	—
	3	25	0.5	5.0	—
	4	51	0.5	5.0	—
	5	100	0.5	5.0	—
AIBN	7	10	0.05	5.0	—
	8	10	0.1	5.0	—
	9	10	0.26	5.0	—
	10	10	0.9	5.0	—
Toluene	11	10	0.9	2.5	—
	12	10	0.9	10.0	—
	13	10	0.9	25.0	—
	14	10	0.9	50.0	—
Sonication	15	10	0.9	2.5	0.5
	16	10	0.9	2.5	1.0
	17	10	0.9	2.5	2.0
	18	10	0.9	2.5	3.0
	19	10	0.9	2.5	10.0

B

Towards Novel Silylacetylene Structures

At the beginning of my doctorate, in addition to my research on silicon nanosheets, I was also working on a second project. This second project focuses on the synthesis and characterization of novel structures built from multiple silicon/ethynyl units. Two potential structural types are considered: polyhedral cages and polymeric structures.

B.1 Theoretical Background: Silylacetylenes

In *silylacetylenes* (or *alkynylsilanes*), a silyl moiety is directly bonded to a carbon atom of a C≡C bond. Silylacetylenes are employed in organic synthesis, for instance, in silyl-protection strategies, wherein a silyl group is introduced as a protection group of the ≡C-H bond. Additionally, silylacetylenes improve and dictate the regioselectivity of reactions at the triple bond. Following the reaction of silylacetylenes, silyl groups can be converted into other functionalities.[219]
Silylacetylenes can be synthesized through a variety of coupling reactions involving terminal alkynes. Among these, the coupling with chlorosilanes or the dehydrogenative coupling with hydrosilanes are the most commonly employed reactions. In these reactions, bases such as organometallic reagents (diethylzinc,[220] *n*BuLi,[221] or Grignard reagents[222]), metal hydrides,[223] metal hydroxides,[224] or alkoxides and amides of alkali metals or barium[221] are used. Alternatively, metal and metal salt catalysts can be utilized.[225–229] Other coupling reactions of

alkynes occur, for example, with vinylsilanes,[230] aminosilanes,[231] or trimethylsilyl triflate.[232]

In the literature, molecules containing alternating silicon-acetylene units have been demonstrated: Cyclic molecules with four to 25 repeating units,[233–235] dendrimers,[236,237] and linear polymers have been reported. Scheme B.1 shows some examples of the literature known structures consisting of multiple silicon-acetylene units.

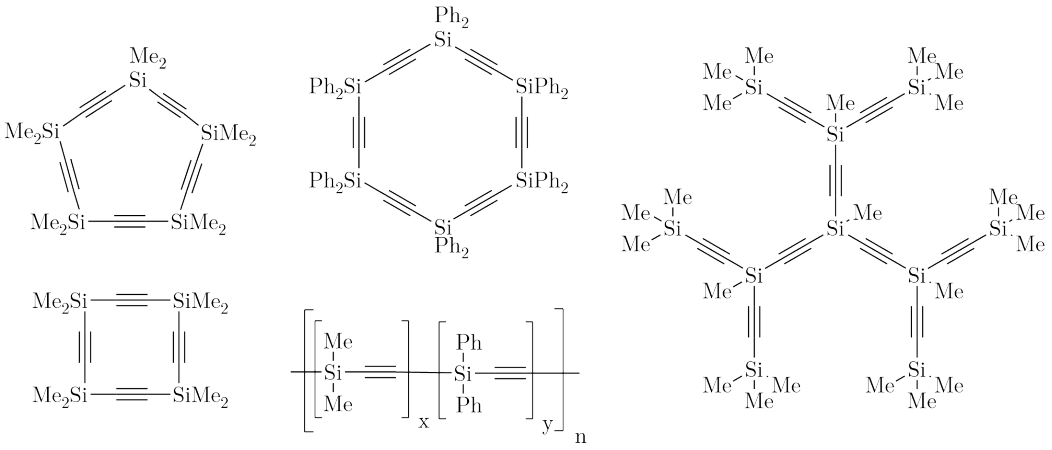

Scheme B.1: Literature examples of molecules comprising repeating silicon-acetylene units.[233–237]

With regard to the polymers, the nomenclature of this type of organosilicon polymers is not uniform in the literature. For example, the terms polysilethynes,[238] poly(silacetylenes),[239] and poly(silapropynylenes)[240,241] can be found. Polymerization is achieved in different approaches, which all are polycondensation reactions. The reaction of the di-Grignard reagent $R^1R^2i(C{\equiv}CMgX)_2$ with dichlorosilanes R_2SiCl_2 results in low yields of polymers with low molecular weights.[242,243] Higher yields and molecular weights, are achieved by the reaction of disodium acetylide or dilithium acetylide with dichlorosilanes R_2SiCl_2.[241,243] Polymers of the structure $[SiR^1R^2C{\equiv}C]_n$ are moldable insulators.[241–243] Furthermore, they can be used as ceramic precursors as they form silicon carbide under pyrolysis at high temperatures.[241–244]

B.2 Silicon-Acetylene Polyhedral Cages

To find novel silylacetylene compounds, polyhedral structures consisting of silicon-acetylene units, where silicon atoms are the corners and C≡C units are the edges,

are the target molecules. For example, a cube similar to cubic silsesquioxanes, where the oxygen atoms are formally replaced by a C≡C moiety, a tetrahedron, or a dodecahedron are possible structures. Synthesis plans were drafted, which are shown in Scheme B.2 for a cubic structure as an example.

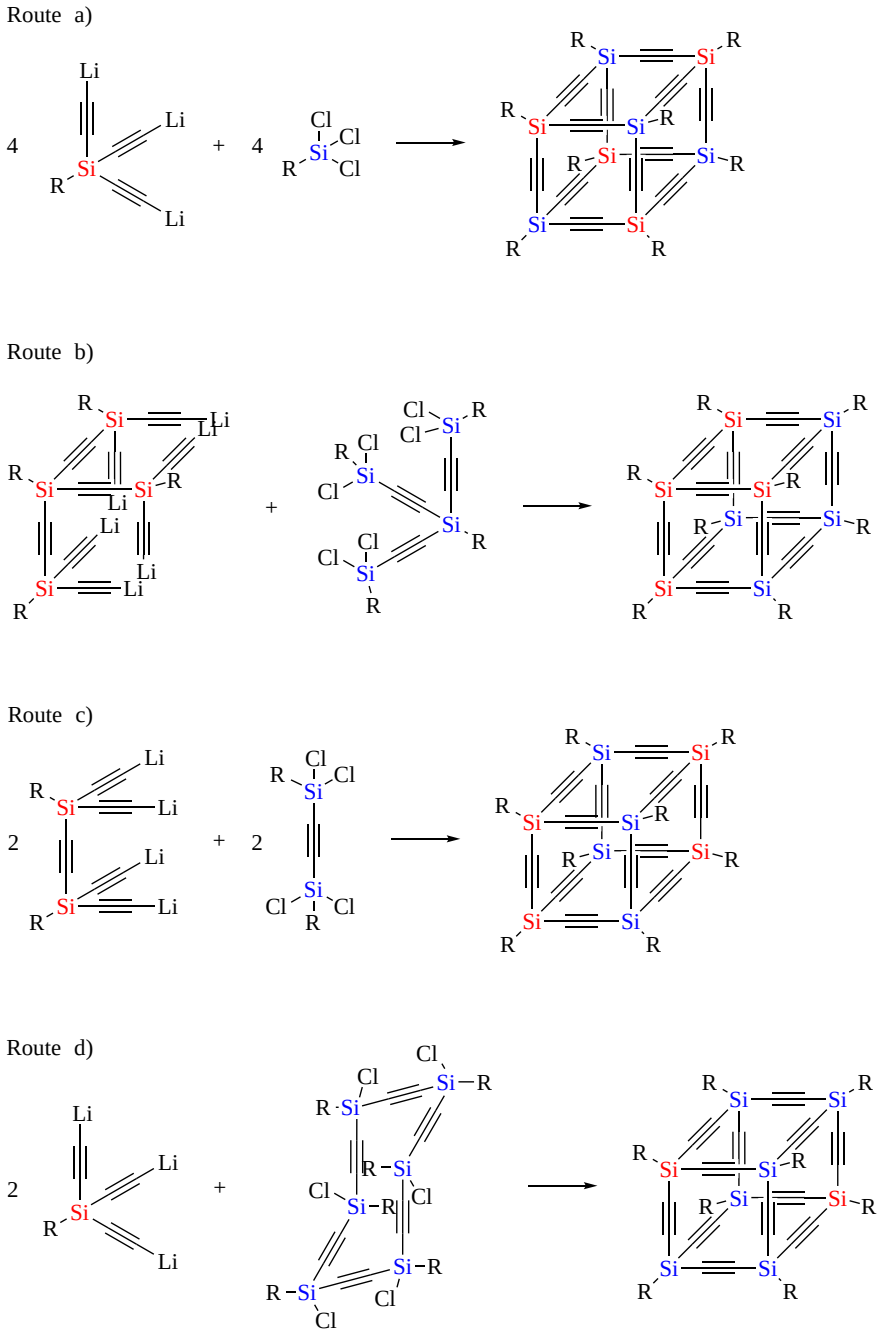

Scheme B.2: Proposed reaction pathways to a cubic structure consisting of silicon-acetylene units.

These synthesis plans are based on self-organized reactions between metalated silylacetylenes and chlorosilanes. Methyl or phenyl groups are defined as the fourth substituent on the silicon atoms.
The synthesis of a cube or other polyhedra presents several challenges:

1. The formation of a cage with a regular structure competes with the formation of a polymeric random network. Therefore, many byproducts and low yields of the target molecule are expected.
2. Exact stoichiometries are required to assemble the building blocks into a polyhedron.
3. The angles in the geometries of the polyhedra deviate from the tetrahedral bond angle expected from four-valent silicon atoms. This could be adjusted to some extent by the choice of the fourth substituent on the silicon atom.
4. A controlled stereochemistry at the silicon atoms is required.

B.2.1 Results

The formation of a polyhedral cage structure according to route a) presented in Scheme B.2 with R = Ph is investigated. Therefore, triethynylphenylsilane is first prepared. This structure is synthesized similar to the procedure described in Reference 245 by reacting ethynylmagnesium bromide with trichlorophenylsilane (Scheme B.3). The analog reaction with sodium acetylide was not successful.

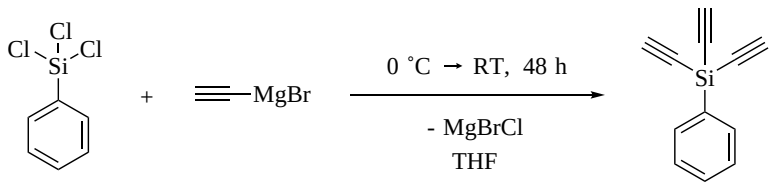

Scheme B.3: Formation of triethynylphenylsilane by the reaction of trichlorophenylsilane and ethynylmagnesium bromide.

Before the following reaction of the triethynylphenylsilane with silyl electrophiles, the terminal alkyne is deprotonated by a strong base to form the corresponding metal-acetylide (Scheme B.4). For this purpose, potassium *tert*-butoxide (KO*t*Bu), ethylmagnesium bromide (EtMgBr), and *n*BuLi are tested. The conversion with KO*t*Bu leads to the formation of phenyltri(*tert*-butoxy)silane. An incomplete metalation occurs with EtMgBr. Only attempts with *n*BuLi result in

the complete metalation of triethynylphenylsilane as proven by the entrapment of the lithiated compound with trimethylsilyl chloride and subsequent ^{1}H NMR analysis.

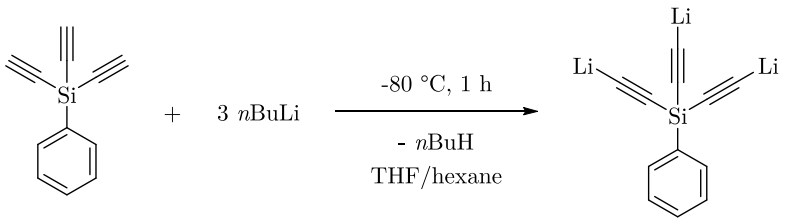

Scheme B.4: Metalation of triethynylphenylsilane with *n*BuLi.

For the reaction according to route a) in Scheme B.2, trilitihium phenylsilyltriacetylide is prepared to which equimolar amounts of trichlorophenylsilane are added. According to the Ziegler-Ruggli dilution principle, intramolecular reactions should be preferred in dilute solutions. Thus, different concentrations are screened. Furthermore, the reaction temperature and reaction time are varied, and different workup procedures are used (see experimental procedures in Section B.5). THF and dimethoxyethane are compared as solvents, as the solvent probably affects the reactivity of the lithium reagents. The solid crude products are analyzed by ^{1}H NMR spectroscopy and GPC. In the ^{1}H NMR spectrum of a polyhedral structure, only aromatic signals should be present. The experimental spectra show signals in the aromatic region, but also peaks appearing in the upfield region. Thus, NMR spectroscopy indicates that a product mixture was obtained as expected. However, NMR spectroscopy is not an appropriate method to get more information about the possible presence of a polyhedron molecule. GPC is performed to determine the molecular weight distribution in the crude products. The chromatograms show broad peaks assigned to a wide range of molecular weights, confirming the presence of multiple products. Overall, the results are inconclusive and do not provide evidence for the formation of any polyhedral molecules. Attempts to separate the crude product by column chromatography with different solvents and stationary phases still gave fractions with multiple components as shown by ^{1}H MNR. Further purification was not done as the focus of the research shifted towards the nanosheet projects, rather than continuing the investigation of the preparation of polyhedral silylacetylene structures.

B.3 Poly(silacetylenes)

The preparation of novel poly(silacetylenes) is investigated in addition to the preparation of defined three-dimensional silacetylenes. Since several polymers with repeating silylacetylene units are already literature-known, the motivation of this project is the synthesis of new structures in which silicon atoms are partially substituted with boron or phosphorus by the copolymerization of the dilithiated diethynyldiphenylsilane with dichlorophenylborane and dichlorophenylphosphine, respectively (see Scheme B.5). The introduction of boron or phosphorus could potentially change the properties of poly(silacetylenes). The realization of both kinds of polymers (one containing borane groups, the other containing phosphine groups) would result in polymeric Lewis acids or bases, which together could form supramolecular networks due to Lewis adduct formation. Such materials could be interesting for functional polymers.

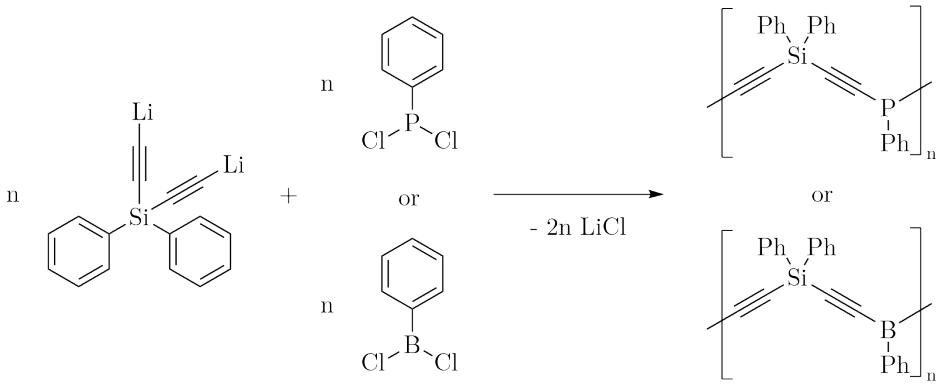

Scheme B.5: Polymerization of the lithiated derivative of diethynyldiphenylsilane with dichlorophenylborane and dichlorophenylphosphine, respectively.

Bortolin *et al.* described the polycondensation between lithium salts of diethynylsilanes $SiR^1_2(C{\equiv}CLi)_2$ and dichlorosilanes $R^2_2SiCl_2$ towards copolymers.[240,246] According to those reaction protocols, a statistical distribution of the silylethynl units in the copolymer is obtained when the dichlorosilane is added to the lithium salt. The random distribution of the silyl units is the result of a redistribution reaction. Addition of the reactants in the reverse order yields an alternating copolymer as expected from a polycondensation reaction. Bortolin *et al.* only achieved low number average molecular weights of up to $3600\,g\,mol^{-1}$ for copolymers containing both $SiPh_2$ and $SiMe_2$ units, which corresponds to 26 repeating units.
In the project described in this section, the reproduction of these literature results

as well as the optimization of the molecular weights is the first goal. With an optimized experimental procedure, it is planned to carry out the copolymerization of diethynylsilanes with both dichloroboranes and dichlorophosphines.

B.3.1 Results

Diethynyldiphenylsilane is synthesized similar to triethynylphenylsilane and *n*BuLi is used for the metalation. In several attempts with different reaction conditions (addition order, concentration) the copolymerization of the lithiated diethynyldiphenylsilane with dichloromethylsilane is tested. ^{1}H NMR spectra of the obtained products show an incomplete conversion because the peak corresponding to ≡C-H is still present. A maximum conversion of 94 % is determined by comparison with the integrals of the aromatic signals. GPC experiments confirm this, as the chromatograms exhibit the monomer peak of diethynyldiphenylsilane. In addition, the chromatograms show only a second peak corresponding to a molecular weight about twice that of the monomer. Thus, no polymers were formed. No further characterization of the products is performed, and since the copolymerization from the literature cannot be reproduced, this project is terminated.

B.4 Summary

This project was abandoned at a very early stage in order to concentrate on the nanosheet projects, which are now the main part of this thesis. So only very first results were obtained.
Synthesis strategies for the preparation of polyhedral silylacetylene structures were developed. First experiments towards a cage structure by the reaction between lithiated triethynylphenylsilane and trichlorophenylsilane demonstrated the complexity of the synthesis of the target molecules. A broad array of products was formed and separation proved to be a major obstacle. Challenges include unselective reactions, likely unfavorable bond angles, and, most importantly, difficult analysis of the product mixture. The parameter variations in testing this response covered only a limited space. A more systematic approach would be required for future experiments.
In a second approach, linear polymer structures were the target molecules. Attempts to reproduce the copolymerization of lithiated diethynylphenylsilane with dichloromethylsilane, as described in the literature, did not succeed. No polymers

were obtained. These reactions were not subjected to further investigation, and the plans to prepare novel poly(silacetylenes) doped with boron or phosphorus were abandoned.

B.5 Experimental Procedures

B.5.1 General Information

Instrument information, analytical techniques, and procedures for solvent drying are found in Chapter 9.
The reactants were purchased from Sigma-Aldrich, Acros Organics and are used without further purification, except for the chlorosilanes which are distilled prior to use.
The reactions are conducted under exclusion of water and air using standard Schlenk methods. All solvents are dried and degassed prior to use.

B.5.2 Synthesis of Triethynylphenylsilane

The synthesis of triethynylphenylsilane follows a literature procedure described in Reference 245.
An ethynylmagnesium bromide solution (600 mL, 0.5 M in THF, 0.30 mol, 3.1 eq.) is diluted with THF (175 mL) and cooled in an ice bath. Trichlorophenylsilane (20.3 g, 0.096 mol, 1.0 eq.) is added dropwise to the cold solution of the Grignard reagent. The mixture is warmed to room temperature and stirred for 48 h. The solvent is removed with a rotary evaporator and a beige solid is obtained. The crude product is washed with diethyl ether and the solvent is removed from the organic filtrate under vacuum. The brownish solid is purified by vacuum distillation (0.17 mbar, 80 to 85 °C) to yield a white crystalline product (50 % yield).
^{1}H NMR (400 MHz, $CDCl_3$, 300 K): δ (ppm) = 7.83 – 7.81 (m, 2H, H_{Ar}), 7.53 – 7.42 (m, 3H, H_{Ar}), 2.69 (s, 1H, ≡CH).

B.5.3 Lithiation of Triethynylphenylsilane

An *n*BuLi solution (2.1 mL, 1.6 M in hexane, 3.38 mmol, 3.0 eq.) is added dropwise to a solution of triethynylphenylsilane (203 mg, 1.13 mmol, 1.0 eq.) in THF (20 mL) at −80 °C. The mixture is stirred at −80 °C for 1 h.

B.5.4 Reactions Towards Cage Structures

These experiments are performed with varying parameters, which are listed in Table B.1.
Solutions of the trilithiated derivative of triethynylphenylsilane in THF/hexane are prepared as described above in different concentrations. Trichlorophenylsilane is added in equimolar amounts either in the pure form or diluted with THF at −80 °C or room temperature. The reaction is carried out either at room temperature, 90 °C, or 100 °C. The reactions are terminated either by the addition of an aqueous saturated ammonium chloride solution followed by extraction with diethyl ether, or by removal of the volatile compounds followed by extraction with chloroform. After removal of the solvents, oily products are obtained in each experiment.

Table B.1: Parameters of the reactions between equimolar amounts of lithiated triethynylphenylsilane and trichlorophenylsilane. The concentrations are given with respect to the separate solutions before the addition of trichlorophenylsilane.

c(PhSi(C≡CLi)$_3$) / mM	Addition of $PhSiCl_3$	Reaction conditions
66	pure $PhSiCl_3$ at −80 °C	15 min at RT
170	pure $PhSiCl_3$ at −80 °C	45 min at RT
11	11 M $PhSiCl_3$ in THF at −80 °C	45 min at RT
11	11 M $PhSiCl_3$ in THF at RT	17 h at RT, 1 h at 90 °C
11	11 M $PhSiCl_3$ in THF at RT	1 h at 100 °C

B.5.5 Synthesis of Diethynyldiphenylsilane

Diphenyldichlorosilane (16.0 g, 63.1 mmol, 1.0 eq.) is added dropwise to a solution of ethynlmagnesium bromide (265 mL, 0.5 M in THF, 132 mol, 2.1 eq.) diluted with THF (150 mL), which is cooled in an ice bath. The mixture is warmed to room temperature and stirred for 48 h. The solvent is removed with a rotary evaporator and a brown solid is obtained. The solid is dissolved in a mixture of diethyl ether (50 mL) and washed with water (50 mL). After extraction of the aqueous phase with diethyl ether, the combined organic phases are dried with sodium sulfate and

the solvent is removed from the organic filtrate. The crude product is a brown oil, which is purified by column chromatography (silica pentane/ethyl acetate = 9:1). The product is obtained as a colorless to pinkish oil (38 % yield).
^{1}H NMR (400 MHz, $CDCl_3$, 300 K): δ (ppm) = 7.77 – 7.75 (m, 4H, H_{Ar}), 7.48 – 7.39 (m, 6H, H_{Ar}), 2.75 (s, 2H, ≡CH).

B.5.6 Copolymerization Reactions

The experimental protocols described in References 240 and 246 are used as guidance. The lithiation of diethynyldiphenylsilane is performed analogously to the metalation of triethynylphenylsilane (see above). For the polycondensation reactions different concentrations and addition orders of the reactants are tested, which are listed in Table B.2. The solution of a monomer is slowly added to the solution of the comonomer at room temperature. An equimolar amount of both monomers is used. The mixture is stirred overnight and the reaction is terminated by adding an aqueous saturated ammonium chloride solution followed by extraction with diethyl ether. The organic phases are washed with brine, dried over sodium sulfate, and the solvent is removed from the filtrate under vacuum to give an oily product.

Table B.2: Parameters of the reactions between equimolar amounts of lithiated diethynyldiphenylsilane and dichlorodimethylsilane. The concentrations are given with respect to the individual solutions prior to their combination.

c($Ph_2Si(C{\equiv}CLi)_2$) / mM	c(Me_2SiCl_2) / mM	Added monomer
0.18	0.43	Me_2SiCl_2
0.52	0.67	Me_2SiCl_2
0.43	0.89	$Ph_2Si(C{\equiv}CLi)_2$
0.51	0.87	$Ph_2Si(C{\equiv}CLi)_2$
0.51	0.86	$Ph_2Si(C{\equiv}CLi)_2$

References

[1] Feynman, R. P. There is Plenty of Room at the Bottom. *Eng. Sci.* **1960**, *22*, 22–36.

[2] Bhushan, B. Governance, policy, and legislation of nanotechnology: a perspective. *Microsyst. Technol.* **2015**, *21*, 1137–1155.

[3] NobelPrize.org, The Nobel Prize in Chemistry 2023. `https://www.nobelprize.org/prizes/chemistry/2023/summary/`, Accessed: 15 May 2024.

[4] Novoselov, K. S.; Geim, A. K.; Morozov, S. V.; Jiang, D.; Zhang, Y.; Dubonos, S. V.; Grigorieva, I. V.; Firsov, A. A. Electric Field Effect in Atomically Thin Carbon Films. *Science* **2004**, *306*, 666–669.

[5] Gogotsi, Y.; Anasori, B. The Rise of MXenes. *ACS Nano* **2019**, *13*, 8491–8494.

[6] Manzeli, S.; Ovchinnikov, D.; Pasquier, D.; Yazyev, O. V.; Kis, A. 2D transition metal dichalcogenides. *Nat. Rev. Mater.* **2017**, *2*, 17033.

[7] Zhang, K.; Feng, Y.; Wang, F.; Yang, Z.; Wang, J. Two dimensional hexagonal boron nitride (2D-hBN): synthesis, properties and applications. *J. Mater. Chem. C* **2017**, *5*, 11992–12022.

[8] Wiberg, N. In *Lehrbuch der Anorganischen Chemie*; Holleman, A. F., Ed.; De Gruyter: Berlin, Boston, 2008; pp 861–1041.

[9] Wöhler, F. Ueber Verbindungen des Siliciums mit Sauerstoff und Wasserstoff. *Justus Liebigs Ann. Chem.* **1863**, *127*, 257–274.

[10] Hönigschmid, O. Über das Silicon. *Monatsh. Chem.* **1909**, *30*, 509–525.

[11] Kautsky, H. Über einige ungesättigte Siliciumverbindungen. *Z. Anorg. Allg. Chem.* **1921**, *117*, 209–242.

[12] Kautsky, H.; Herzberg, G. Über das Siloxen und seine Derivate. *Z. Anorg. Allg. Chem.* **1924**, *139*, 135–160.

[13] Kautsky, H.; Blinoff, G. Siloxen als Adsorbens. *Z. Phys. Chem.* **1928**, *139A*, 497–515.

[14] Kautsky, H. Probleme der Siliciumchemie - Zweidimensionale Kristallstrukturen. *Z. Naturforsch., B* **1952**, *7*, 174–183.

[15] Weiss, A.; Beil, G.; Meyer, H. The topochemical reaction of $CaSi_2$ to a two-dimensional subsiliceous acid $Si_6H_3(OH)_3$ (= Kautskys' Siloxene). *Z. Naturforsch.* **1979**, *34b*, 25–30.

[16] Dahn, J. R.; Way, B. M.; Fuller, E.; Tse, J. S. Structure of siloxene and layered polysilane (Si_6H_6). *Phys. Rev. B* **1993**, *48*, 17872–17877.

[17] Dettlaff-Weglikowska, U.; Hönle, W.; Molassioti-Dohms, A.; Finkbeiner, S.; Weber, J. Structure and optical properties of the planar silicon compounds polysilane and Wöhler siloxene. *Phys. Rev. B* **1997**, *56*, 13132–13140.

[18] Kurmaev, E. Z.; Shamin, S. N.; Ederer, D. L.; Dettlaff-Weglikowska, U.; Weber, J. Local and Electronic Structure of Siloxene. *J. Mater. Res.* **1999**, *14*, 1235–1237.

[19] Brandt, M. S.; Fuchs, H. D.; Stutzmann, M.; Weber, J.; Cardona, M. The origin of visible luminescencefrom "porous silicon": A new interpretation. *Solid State Commun.* **1992**, *81*, 307–312.

[20] Fuchs, H. D.; Stutzmann, M.; Brandt, M. S.; Rosenbauer, M.; Weber, J.; Cardona, M. Visible luminescence from porous silicon and siloxene. *Phys. Scr.* **1992**, *1992*, 309.

[21] Fuchs, H. D.; Stutzmann, M.; Brandt, M. S.; Rosenbauer, M.; Weber, J.; Breitschwerdt, A.; Deák, P.; Cardona, M. Porous silicon and siloxene: Vibrational and structural properties. *Phys. Rev. B* **1993**, *48*, 8172–8189.

[22] Deák, P.; Stutzmann, M.; Brandt, M. S.; Rosenbauer, M.; Finkbeiner, S.; Fuchs, H. D.; Weber, J. Theoretical and experimental studies on siloxene. *Mod. Phys. Lett. B* **1993**, *7*, 1343–1364.

[23] Zamanzadeh-Hanebuth, N.; Brandt, M. S.; Stutzmann, M. Vibrational properties of siloxene: isotope substitution studies. *J. Non-Cryst. Solids* **1998**, *227–230*, 503–506.

[24] Vogg, G.; Zamanzadeh-Hanebuth, N.; Brandt, M. S.; Stutzmann, M.; Albrecht, M. Preparation and Characterization of Epitaxial $CaSi_2$ and Siloxene Layers on Silicon. *Monatsh. Chem.* **1999**, *130*, 79–87.

[25] Brandt, M. S.; Ready, S. E.; Boyce, J. B. ^{29}Si nuclear magnetic resonance of luminescent silicon. *Appl. Phys. Lett.* **1997**, *70*, 188–190.

[26] Kautsky, H.; Keck, H.; Kunze, H. Notizen: Die Reduktion von Aldehyden und Ketonen durch Siloxen. *Z. Naturforsch., B* **1954**, *9*, 165–166.

[27] Kautsky, H.; Thiele, H. Umsetzungen des Siloxens mit Halogenverbindungen und ihre Auslösung durch Licht und chemische Reaktionen. *Z. Anorg. Allg. Chem.* **1925**, *144*, 197–217.

[28] Kautsky, H.; Zocher, H. Über die Beziehung zwischen Chemi- und Photolumineszenz bei ungesättigten Siliziumverbindungen. *Z. Physik* **1922**, *9*, 267–284.

[29] Canham, L. T.; Houlton, M. R.; Leong, W. Y.; Pickering, C.; Keen, J. M. Atmospheric impregnation of porous silicon at room temperature. *J. Appl. Phys.* **1991**, *70*, 422–431.

[30] Brandt, M. S.; Rosenbauer, M.; Stutzmann, M. Two-Dimensional Excitons in Siloxene. *MRS Online Proc. Libr.* **1993**, *298*, 301–306.

[31] Stutzmann, M.; Brandt, M. S.; Rosenbauer, M.; Fuchs, H. D.; Finkbeiner, S.; Weber, J.; Deak, P. Luminescence and optical properties of siloxene. *J. Lumin.* **1993**, *57*, 321–330.

[32] Deák, P.; Rosenbauer, M.; Stutzmann, M.; Weber, J.; Brandt, M. S. Siloxene: Chemical quantum confinement due to oxygen in a silicon matrix. *Phys. Rev. Lett.* **1992**, *69*, 2531–2534.

[33] Brandt, M. S.; Stutzmann, M. Triplet excitons in porous silicon and siloxene. *Solid State Commun.* **1995**, *93*, 473–477.

[34] Stutzmann, M.; Brandt, M. S.; Rosenbauer, M.; Weber, J.; Fuchs, H. D. Photoluminescence excitation spectroscopy of porous silicon and siloxene. *Phys. Rev. B* **1993**, *47*, 4806–4809.

[35] Brandt, M. S.; Puchert, T.; Stutzmann, M. Electronic transport in crystalline siloxene. *Solid State Commun.* **1997**, *102*, 365–368.

[36] Hirabayashi, I.; Morigaki, K.; Yamanaka, S. Optical properties of disordered silicide layer compound: Siloxene ($Si_6(OH)_3H_3$) — Time resolved luminescence. *J. Non-Cryst. Solids* **1983**, *59-60*, 645–648.

[37] Ares, P.; Novoselov, K. S. Recent advances in graphene and other 2D materials. *Nano Mater. Sci.* **2022**, *4*, 3–9.

[38] Takeda, K.; Shiraishi, K. Theoretical possibility of stage corrugation in Si and Ge analogs of graphite. *Phys. Rev. B* **1994**, *50*, 14916–14922.

[39] Cahangirov, S.; Topsakal, M.; Aktürk, E.; Şahin, H.; Ciraci, S. Two- and One-Dimensional Honeycomb Structures of Silicon and Germanium. *Phys. Rev. Lett.* **2009**, *102*, 236804.

[40] Vogt, P.; De Padova, P.; Quaresima, C.; Avila, J.; Frantzeskakis, E.; Asensio, M. C.; Resta, A.; Ealet, B.; Le Lay, G. Silicene: Compelling Experimental Evidence for Graphenelike Two-Dimensional Silicon. *Phys. Rev. Lett.* **2012**, *108*, 155501.

[41] Houssa, M.; Dimoulas, A.; Molle, A. Silicene: a review of recent experimental and theoretical investigations. *J. Phys.: Condens. Matter* **2015**, *27*, 253002.

[42] Oughaddou, H.; Enriquez, H.; Tchalala, M. R.; Yildirim, H.; Mayne, A. J.; Bendounan, A.; Dujardin, G.; Ait Ali, M.; Kara, A. Silicene, a promising new 2D material. *Prog. Surf. Sci.* **2015**, *90*, 46–83.

[43] Molle, A.; Grazianetti, C.; Tao, L.; Taneja, D.; Alam, M. H.; Akinwande, D. Silicene, silicene derivatives, and their device applications. *Chem. Soc. Rev.* **2018**, *47*, 6370–6387.

[44] Solonenko, D.; Selyshchev, O.; Zahn, D. R. T.; Vogt, P. Oxidation of Epitaxial Silicene on Ag(111). *Phys. Status Solidi B* **2019**, *256*, 1800432.

[45] Ritter, V.; Genser, J.; Nazzari, D.; Bethge, O.; Bertagnolli, E.; Lugstein, A. Silicene Passivation by Few-Layer Graphene. *ACS Appl. Mater. Interfaces* **2019**, *11*, 12745–12751.

[46] Nazzari, D.; Genser, J.; Ritter, V.; Bethge, O.; Bertagnolli, E.; Ramer, G.; Lendl, B.; Watanabe, K.; Taniguchi, T.; Rurali, R.; Kolíbal, M.; Lugstein, A. Highly Biaxially Strained Silicene on Au(111). *J. Phys. Chem. C* **2021**, *125*, 9973–9980.

[47] Molle, A.; Grazianetti, C.; Chiappe, D.; Cinquanta, E.; Cianci, E.; Tallarida, G.; Fanciulli, M. Hindering the Oxidation of Silicene with Non-Reactive Encapsulation. *Adv. Funct. Mater.* **2013**, *23*, 4340–4344.

[48] Schäfer, H.; Eisenmann, B.; Müller, W. Zintl Phases: Transitions between Metallic and Ionic Bonding. *Angew. Chem., Int. Ed. Engl.* **1973**, *12*, 694–712.

[49] Böhm, J.; Hassel, O. Die Kristallstruktur des Calciumsilicids $CaSi_2$. *Z. Anorg. Allg. Chem.* **1927**, *160*, 152–164.

[50] Janzon, K. H.; Schäfer, H.; Weiss, A. Notizen: Zur Struktur der Phase $CaSi_2$. *Z. Naturforsch., B* **1968**, *23*, 1544–1544.

[51] Evers, J. Transformation of three-connected silicon nets in $CaSi_2$. *J. Solid State Chem.* **1979**, *28*, 369–377.

[52] Vogg, G.; Brandt, M. S.; Stutzmann, M.; Albrecht, M. From $CaSi_2$ to siloxene: epitaxial silicide and sheet polymer films on silicon. *J. Cryst. Growth* **1999**, *203*, 570–581.

[53] Yaokawa, R.; Nakano, H.; Ohashi, M. Growth of $CaSi_2$ single-phase polycrystalline ingots using the phase relationship between $CaSi_2$ and associated phases. *Acta Mater.* **2014**, *81*, 41–49.

[54] Nedumkandathil, R.; Benson, D. E.; Grins, J.; Spektor, K.; Häussermann, U. The 3R polymorph of $CaSi_2$. *J. Solid State Chem.* **2015**, *222*, 18–24.

[55] Okamoto, H.; Sugiyama, Y.; Nakano, H. Synthesis and Modification of Silicon Nanosheets and Other Silicon Nanomaterials. *Chem. - Eur. J.* **2011**, *17*, 9864–9887.

[56] Sheka, E. F. Why sp^2-like nanosilicons should not form: Insight from quantum chemistry. *Int. J. Quantum Chem.* **2013**, *113*, 612–618.

[57] Yamanaka, S.; Matsu-ura, H.; Ishikawa, M. New deintercalation reaction of calcium from calcium disilicide. Synthesis of layered polysilane. *Mater. Res. Bull.* **1996**, *31*, 307–316.

[58] Ryan, B. J.; Hanrahan, M. P.; Wang, Y.; Ramesh, U.; Nyamekye, C. K. A.; Nelson, R. D.; Liu, Z.; Huang, C.; Whitehead, B.; Wang, J.; Roling, L. T.; Smith, E. A.; Rossini, A. J.; Panthani, M. G. Silicene, Siloxene, or Silicane? Revealing the Structure and Optical Properties of Silicon Nanosheets Derived from Calcium Disilicide. *Chem. Mater.* **2020**, *32*, 795–804.

[59] He, J.; S. Tse, J.; D. Klug, D.; F. Preston, K. Layered polysilane: thermolysis and photoluminescence. *J. Mater. Chem.* **1998**, *8*, 705–710.

[60] Dorn, R. W.; Ryan, B. J.; Lamahewage, S. N. S.; Dodson, M. V.; Essner, J. B.; Biswas, R.; Panthani, M. G.; Rossini, A. J. Chlorination of Hydrogenated Silicon Nanosheets Revealed by Solid-State Nuclear Magnetic Resonance Spectroscopy. *Chem. Mater.* **2023**, *35*, 539–548.

[61] Nakano, H.; Mitsuoka, T.; Harada, M.; Horibuchi, K.; Nozaki, H.; Takahashi, N.; Nonaka, T.; Seno, Y.; Nakamura, H. Soft Synthesis of Single-Crystal Silicon Monolayer Sheets. *Angew. Chem., Int. Ed.* **2006**, *45*, 6303–6306.

[62] Tchalala, M. R.; Ali, M. A.; Enriquez, H.; Kara, A.; Lachgar, A.; Yagoubi, S.; Foy, E.; Vega, E.; Bendounan, A.; Silly, M. G.; Sirotti, F.; Nitshe, S.; Chaudanson, D.; Jamgotchian, H.; Aufray, B.; Mayne, A. J.; Dujardin, G.; Oughaddou, H. Silicon sheets by redox assisted chemical exfoliation. *J. Phys.: Condens. Matter* **2013**, *25*, 442001.

[63] Schott, G.; Naumann, D. Über Polysilane. Die Umsetzung von $CaSi_2$ mit Halogenwasserstoff in $AlBr_3$-Schmelzen. *Z. Anorg. Allg. Chem.* **1957**, *291*, 112–116.

[64] Bonitz, E. Lepidoide, VI: Ein neuer Weg zur Herstellung von aktivem Silicium oder Siliciummonochlorid. *Chem. Ber.* **1961**, *94*, 220–225.

[65] Hengge, E.; Scheffler, G. Zur Kenntnis schichtförmiger Si-Verbindungen des Typs $(SiX)_n$. *Monatsh. Chem.* **1964**, *95*, 1450–1460.

[66] Schott, G.; Naumann, D. Über Polysilane. Die Umsetzung von $CaSi_2$ mit Halogenwasserstoff in wasserfreiem Äthanol. *Z. Anorg. Allg. Chem.* **1957**, *291*, 103–111.

[67] Sugiyama, Y.; Okamoto, H.; Nakano, H. Synthesis of Siloxene Derivatives with Organic Groups. *Chem. Lett.* **2010**, *39*, 938–939.

[68] Liu, C.-w.; Lau, V.; Tsui, L.-y.; Loo, B. Q.; Hsu, H.-p.; Lan, C.-w. Exfoliability of two-dimensional silicon nanosheets from calcium disilicide and its enhanced performance as lithium-ion battery anode material. *J. Energy Storage* **2023**, *72*, 108399.

[69] Ohashi, M.; Shirai, S.; Nakano, H. Direct Chemical Synthesis of Benzyl-Modified Silicane from Calcium Disilicide. *Chem. Mater.* **2019**, *31*, 4720–4725.

[70] Nayad, A.; Hasnaoui, A.; Fkhar, L.; Hnawi kaotar, S. K.; Mehdi, A.; El Firdoussi, L.; Ait Ali, M. New two-dimensional functionalised silicon nanosheets prepared by direct exfoliation of calcium disilicide with tosyl chloride. *Adv. Mater. Process. Technol.* **2022**, *8*, 3402–3412.

[71] Nayad, A.; Hasnaoui, A.; Hadouch, Y.; Fkhar, L.; Idouhli, R.; Abdessalam, A.; Mehdi, A.; Dikici, B.; Mezzane, D.; Firdoussi, L. E.; Ait Ali, M. Chemical Synthesis of Organo-siloxene 2D Materials from Calcium Di-Silicide: Characterization, Dielectric and Electrochemical Studies. *Silicon* **2023**, *15*, 321–335.

[72] Nakano, H.; Ikuno, T. Soft chemical synthesis of silicon nanosheets and their applications. *Appl. Phys. Rev.* **2016**, *3*, 040803.

[73] Helbich, T.; Lyuleeva, A.; Höhlein, I. M. D.; Marx, P.; Scherf, L. M.; Kehrle, J.; Fässler, T. F.; Lugli, P.; Rieger, B. Radical-Induced Hydrosilylation Reactions for the Functionalization of Two-Dimensional Hydride Terminated Silicon Nanosheets. *Chem. - Eur. J.* **2016**, *22*, 6194–6198.

[74] Ohshita, J.; Yamamoto, K.; Tanaka, D.; Nakashima, M.; Kunugi, Y.; Ohashi, M.; Nakano, H. Preparation and Photocurrent Generation of Silicon Nanosheets with Aromatic Substituents on the Surface. *J. Phys. Chem. C* **2016**, *120*, 10991–10996.

[75] Sugiyama, Y.; Okamoto, H.; Mitsuoka, T.; Morikawa, T.; Nakanishi, K.; Ohta, T.; Nakano, H. Synthesis and Optical Properties of Monolayer Organosilicon Nanosheets. *J. Am. Chem. Soc.* **2010**, *132*, 5946–5947.

[76] Helbich, T.; Lyuleeva, A.; Ludwig, T.; Scherf, L. M.; Fässler, T. F.; Lugli, P.; Rieger, B. One-Step Synthesis of Photoluminescent Covalent Polymeric Nanocomposites from 2D Silicon Nanosheets. *Adv. Funct. Mater.* **2016**, *26*, 6711–6718.

[77] Bansal, A.; Li, X.; Yi, S. I.; Weinberg, W. H.; Lewis, N. S. Spectroscopic Studies of the Modification of Crystalline Si(111) Surfaces with Covalently-Attached Alkyl Chains Using a Chlorination/Alkylation Method. *J. Phys. Chem. B* **2001**, *105*, 10266–10277.

[78] Buriak, J. M. Organometallic chemistry on silicon surfaces: formation of functional monolayers bound through Si–C bonds. *Chem. Commun.* **1999**, 1051–1060.

[79] Nakano, H.; Nakano, M.; Nakanishi, K.; Tanaka, D.; Sugiyama, Y.; Ikuno, T.; Okamoto, H.; Ohta, T. Preparation of Alkyl-Modified Silicon Nanosheets by Hydrosilylation of Layered Polysilane (Si_6H_6). *J. Am. Chem. Soc.* **2012**, *134*, 5452–5455.

[80] Holland, J. M.; Stewart, M. P.; Allen, M. J.; Buriak, J. M. Metal Mediated Reactions on Porous Silicon Surfaces. *J. Solid State Chem.* **1999**, *147*, 251–258.

[81] Andsager, D.; Hilliard, J.; Hetrick, J. M.; AbuHassan, L. H.; Plisch, M.; Nayfeh, M. H. Quenching of porous silicon photoluminescence by deposition of metal adsorbates. *J. Appl. Phys.* **1993**, *74*, 4783–4785.

[82] Lyuleeva, A.; Holzmüller, P.; Helbich, T.; Stutzmann, M.; Brandt, M. S.; Becherer, M.; Lugli, P.; Rieger, B. Charge transfer doping in functionalized silicon nanosheets/P3HT hybrid material for applications in electrolyte-gated field-effect transistors. *J. Mater. Chem. C* **2018**, *6*, 7343–7352.

[83] Helbich, T.; Lyuleeva, A.; Marx, P.; Scherf, L. M.; Purkait, T. K.; Fässler, T. F.; Lugli, P.; Veinot, J. G. C.; Rieger, B. Lewis Acid Induced Functionalization of Photoluminescent 2D Silicon Nanosheets for the Fabrication of Functional Hybrid Films. *Adv. Funct. Mater.* **2017**, *27*, 1606764.

[84] Helbich, T.; Kloberg, M. J.; Sinelnikov, R.; Lyuleeva, A.; Veinot, J. G. C.; Rieger, B. Diaryliodonium salts as hydrosilylation initiators for the surface functionalization of silicon nanomaterials and their collaborative effect as ring opening polymerization initiators. *Nanoscale* **2017**, *9*, 7739–7744.

[85] Kampmeier, J. A.; Nalli, T. W. Initiation of cationic polymerization of cyclic ethers by redox radical-chain reactions of onium salts. *J. Org. Chem.* **1994**, *59*, 1381–1388.

[86] Crivello, J. V.; Lam, J. Diaryliodonium salts. A new class of photoinitiators for cationic polymerization. *Macromolecules* **1977**, *10*, 1307–1315.

[87] Kloberg, M. J.; Helbich, T.; Rieger, B. Silicon nanosheets as co-initiators for diaryliodonium induced radical and cationic polymerization. *Nanotechnology* **2018**, *30*, 075602.

[88] Okamoto, H.; Kumai, Y.; Sugiyama, Y.; Mitsuoka, T.; Nakanishi, K.; Ohta, T.; Nozaki, H.; Yamaguchi, S.; Shirai, S.; Nakano, H. Silicon Nanosheets and Their Self-Assembled Regular Stacking Structure. *J. Am. Chem. Soc.* **2010**, *132*, 2710–2718.

[89] Okamoto, H.; Sugiyama, Y.; Nakanishi, K.; Ohta, T.; Mitsuoka, T.; Nakano, H. Surface Modification of Layered Polysilane with n-Alkylamines, α,ω-Diaminoalkanes, and ω-Aminocarboxylic Acids. *Chem. Mater.* **2015**, *27*, 1292–1298.

[90] Lew Yan Voon, L. C.; Sandberg, E.; Aga, R. S.; Farajian, A. A. Hydrogen compounds of group-IV nanosheets. *Appl. Phys. Lett.* **2010**, *97*, 163114.

[91] Ding, Y.; Wang, Y. Electronic structures of silicene fluoride and hydride. *Appl. Phys. Lett.* **2012**, *100*, 083102.

[92] Guzmán-Verri, G. G.; Lew Yan Voon, L. C. Band structure of hydrogenated Si nanosheets and nanotubes. *J. Phys.: Condens. Matter* **2011**, *23*, 145502.

[93] Houssa, M.; Scalise, E.; Sankaran, K.; Pourtois, G.; Afanas'ev, V. V.; Stesmans, A. Electronic properties of hydrogenated silicene and germanene. *Appl. Phys. Lett.* **2011**, *98*, 223107.

[94] Li, F.; Lu, R.; Yao, Q.; Kan, E.; Liu, Y.; Wu, H.; Yuan, Y.; Xiao, C.; Deng, K. Geometric and Electronic Structures as well as Thermodynamic Stability of Hexyl-Modified Silicon Nanosheet. *J. Phys. Chem. C* **2013**, *117*, 13283–13288.

[95] Restrepo, O. D.; Mishra, R.; Goldberger, J. E.; Windl, W. Tunable gaps and enhanced mobilities in strain-engineered silicane. *J. Appl. Phys.* **2014**, *115*, 033711.

[96] Shu, H.; Wang, S.; Li, Y.; Yip, J.; Wang, J. Tunable electronic and optical properties of monolayer silicane under tensile strain: A many-body study. *J. Chem. Phys.* **2014**, *141*.

[97] Jamdagni, P.; Kumar, A.; Sharma, M.; Thakur, A.; Ahluwalia, P. K. Electronic, mechanical and dielectric properties of silicane under tensile strain. *AIP Conf. Proc.* **2015**, *1661*, 080007.

[98] Liu, Y.; Shu, H.; Liang, P.; Cao, D.; Chen, X.; Lu, W. Structural, electronic, and optical properties of hydrogenated few-layer silicene: Size and stacking effects. *J. Appl. Phys.* **2013**, *114*, 094308.

[99] Spencer, M. J.; Bassett, M. R.; Morishita, T.; Snook, I. K.; Nakano, H. Interactions between stacked layers of phenyl-modified silicene. *New J. Phys.* **2013**, *15*, 125018.

[100] Gao, N.; Zheng, W. T.; Jiang, Q. Density functional theory calculations for two-dimensional silicene with halogen functionalization. *Phys. Chem. Chem. Phys.* **2012**, *14*, 257–261.

[101] Boyd, R. W. *Nonlinear Optics*; Elsevier Science & Technology: San Diego, 2020.

[102] Stavrou, M.; Mühlbach, A. M.; Arapakis, V.; Groß, E.; Kratky, T.; Günther, S.; Rieger, B.; Couris, S. Exceptional ultrafast nonlinear optical response of functionalized silicon nanosheets. *Nanoscale* **2023**, *15*, 16636–16649.

[103] Stavrou, M.; Papadakis, I.; Stathis, A.; Kloberg, M. J.; Mock, J.; Kratky, T.; Günther, S.; Rieger, B.; Becherer, M.; Lyuleeva-Husemann, A.; Couris, S. Silicon Nanosheets versus Graphene Nanosheets: A Comparison of Their Nonlinear Optical Response. *J. Phys. Chem. Lett.* **2021**, *12*, 815–821.

[104] Stathis, A.; Stavrou, M.; Papadakis, I.; Mock, J.; Kloberg, M. J.; Becherer, M.; Lyuleeva-Husemann, A.; Couris, S. Silicon Nanosheets: A Promising 2D Material with Strong Ultrafast Nonlinear Optical Response. *J. Phys. Chem. C* **2021**, *125*, 18510–18516.

[105] Stavrou, M.; Stathis, A.; Papadakis, I.; Lyuleeva-Husemann, A.; Koudoumas, E.; Couris, S. Silicon Nanosheets: An Emerging 2D Photonic Material with a Large Transient Nonlinear Optical Response beyond Graphene. *Nanomaterials* **2022**, *12*.

[106] Kloberg, M. J.; Yu, H.; Groß, E.; Eckmann, F.; Restle, T. M. F.; Fässler, T. F.; Veinot, J. G. C.; Rieger, B. Surface-Anisotropic Janus Silicon Quantum Dots via Masking on 2D Silicon Nanosheets. *Adv. Mater.* **2021**, *33*, 2100288.

[107] Qian, C.; Sun, W.; Hung, D. L. H.; Qiu, C.; Makaremi, M.; Hari Kumar, S. G.; Wan, L.; Ghoussoub, M.; Wood, T. E.; Xia, M.; Tountas, A. A.; Li, Y. F.; Wang, L.; Dong, Y.; Gourevich, I.; Singh, C. V.; Ozin, G. A. Catalytic CO_2 reduction by palladium-decorated silicon–hydride nanosheets. *Nat. Catal.* **2019**, *2*, 46–54.

[108] You, Y.; Zhu, Y.-X.; Jiang, J.; Wang, M.; Chen, Z.; Wu, C.; Wang, J.; Qiu, W.; Xu, D.; Lin, H.; Shi, J. Water-Enabled H_2 Generation from Hydrogenated Silicon Nanosheets for Efficient Anti-Inflammation. *J. Am. Chem. Soc.* **2022**, *144*, 14195–14206.

[109] Li, H.; Wang, Y.; Dai, X.; Gao, Y.; Lu, G.; Fang, Z.; He, H.; Huang, J.; Ye, Z. Tailoring the lateral size of two-dimensional silicon nanomaterials to produce highly stable and efficient deep-blue emissive silicene-like quantum dots. *J. Mater. Chem. C* **2021**, *9*, 10065–10072.

[110] Deng, X.; Zheng, X.; Yuan, T.; Sui, W.; Xie, Y.; Voznyy, O.; Wang, Y.; Yang, Z. Ligand Impact of Silicanes as Anode Materials for Lithium-Ion Batteries. *Chem. Mater.* **2021**, *33*, 9357–9365.

[111] Kumai, Y.; Shirai, S.; Sudo, E.; Seki, J.; Okamoto, H.; Sugiyama, Y.; Nakano, H. Characteristics and structural change of layered polysilane (Si_6H_6) anode for lithium ion batteries. *J. Power Sources* **2011**, *196*, 1503–1507.

[112] Kumai, Y.; Kadoura, H.; Sudo, E.; Iwaki, M.; Okamoto, H.; Sugiyama, Y.; Nakano, H. Si–C composite anode of layered polysilane (Si_6H_6) and sucrose for lithium ion rechargeable batteries. *J. Mater. Chem.* **2011**, *21*, 11941–11946.

[113] Staebler, D. L.; Wronski, C. R. Reversible conductivity changes in discharge-produced amorphous Si. *Appl. Phys. Lett.* **1977**, *31*, 292–294.

[114] Dersch, H.; Stuke, J.; Beichler, J. Light-induced dangling bonds in hydrogenated amorphous silicon. *Appl. Phys. Lett.* **1981**, *38*, 456–458.

[115] Pfanner, G.; Freysoldt, C.; Neugebauer, J.; Inam, F.; Drabold, D.; Jarolimek, K.; Zeman, M. Dangling-bond defect in a-Si:H: Characterization of network and strain effects by first-principles calculation of the EPR parameters. *Phys. Rev. B* **2013**, *87*, 125308.

[116] Yang, J.; Liptak, R.; Rowe, D.; Wu, J.; Casey, J.; Witker, D.; Campbell, S. A.; Kortshagen, U. UV and air stability of high-efficiency photoluminescent silicon nanocrystals. *Appl. Surf. Sci.* **2014**, *323*, 54–58.

[117] Cheong, I. T.; Yang Szepesvari, L.; Ni, C.; Butler, C.; O'Connor, K. M.; Hooper, R.; Meldrum, A.; Veinot, J. G. C. Not all silicon quantum dots are equal: photostability of silicon quantum dots with and without a thick amorphous shell. *Nanoscale* **2024**, *16*, 592–603.

[118] Wu, J. J.; Kortshagen, U. R. Photostability of thermally-hydrosilylated silicon quantum dots. *RSC Adv.* **2015**, *5*, 103822–103828.

[119] Aouida, S.; Saadoun, M.; Ben Saad, K.; Bessaïs, B. UV photooxidation induced structural and photoluminescence behaviors in vapor-etching based porous silicon. *Materials Science and Engineering: C* **2006**, *26*, 495–499.

[120] Tischler, M. A.; Collins, R. T.; Stathis, J. H.; Tsang, J. C. Luminescence degradation in porous silicon. *Appl. Phys. Lett.* **1992**, *60*, 639–641.

[121] Collins, R. T.; Tischler, M. A.; Stathis, J. H. Photoinduced hydrogen loss from porous silicon. *Appl. Phys. Lett.* **1992**, *61*, 1649–1651.

[122] Choi, S.-H.; Chung, H.; Shin, G.-S. Conditions of luminescence degradation or enhancement in porous silicon. *Solid State Commun.* **1995**, *95*, 341–345.

[123] Mauckner, G.; Thonke, K.; Sauer, R. Dynamics of the degradation by photo-oxidation of porous silicon: FTPL and FTIR absorption study. *J. Phys.: Condens. Matter* **1993**, *5*, L9.

[124] Harper, J.; Sailor, M. J. Photoluminescence Quenching and the Photochemical Oxidation of Porous Silicon by Molecular Oxygen. *Langmuir* **1997**, *13*, 4652–4658.

[125] Koropecki, R. R.; Arce, R. D.; Schmidt, J. A. Photo-oxidation effects in porous silicon luminescence. *Phys. Rev. B* **2004**, *69*, 205317.

[126] Kovalev, D.; Gross, E.; Diener, J.; Timoshenko, V. Y.; Fujii, M. Photodegradation of porous silicon induced by photogenerated singlet oxygen molecules. *Appl. Phys. Lett.* **2004**, *85*.

[127] Hirabayashi, I.; Morigaki, K.; Yamanaka, S. Fatigue Effect and Temperature Dependence in Luminescence of Disordered Silicide Layer Compound: Siloxene ($Si_6H_3(OH)_3$). *J. Phys. Soc. Jpn.* **1983**, *52*, 671–676, PL fatigue.

[128] Hengge, E. Siloxen und schichtförmig gebaute Siliciumsubverbindungen. Silicium-Chemie. 1967; pp 145–164.

[129] Rosenbauer, M.; Stutzmann, M. Transport properties and electroluminescence of siloxene. *J. Appl. Phys.* **1997**, *82*, 4520–4524.

[130] Wang, W.; Chen, H. C.; Zheng, X. L. Photoluminescence and laser-irradiation effect of siloxene compound. *Mater. Lett.* **1992**, *14*, 343–346.

[131] Vogg, G.; Brandt, M. S.; Stutzmann, M. Polygermyne—A Prototype System for Layered Germanium Polymers. *Adv. Mater.* **2000**, *12*, 1278–1281.

[132] Bianco, E.; Butler, S.; Jiang, S.; Restrepo, O. D.; Windl, W.; Goldberger, J. E. Stability and Exfoliation of Germanane: A Germanium Graphane Analogue. *ACS Nano* **2013**, *7*, 4414–4421.

[133] Jiang, S.; Butler, S.; Bianco, E.; Restrepo, O. D.; Windl, W.; Goldberger, J. E. Improving the stability and optical properties of germanane via one-step covalent methyl-termination. *Nat. Commun.* **2014**, *5*, 3389.

[134] Jiang, S.; Arguilla, M. Q.; Cultrara, N. D.; Goldberger, J. E. Improved Topotactic Reactions for Maximizing Organic Coverage of Methyl Germanane. *Chem. Mater.* **2016**, *28*, 4735–4740.

[135] Jiang, S.; Krymowski, K.; Asel, T.; Arguilla, M. Q.; Cultrara, N. D.; Yanchenko, E.; Yang, X.; Brillson, L. J.; Windl, W.; Goldberger, J. E. Tailoring the Electronic Structure of Covalently Functionalized Germanane via the Interplay of Ligand Strain and Electronegativity. *Chem. Mater.* **2016**, *28*, 8071–8077.

[136] Sturala, J.; Luxa, J.; Matějková, S.; Plutnar, J.; Hartman, T.; Pumera, M.; Sofer, Z. Exfoliation of Calcium Germanide by Alkyl Halides. *Chem. Mater.* **2019**, *31*, 10126–10134.

[137] Sturala, J.; Luxa, J.; Matějková, S.; Sofer, Z.; Pumera, M. Germanane synthesis with simultaneous covalent functionalization: towards highly functionalized fluorescent germananes. *Nanoscale* **2019**, *11*, 19327–19333.

[138] Yu, H.; Helbich, T.; Scherf, L. M.; Chen, J.; Cui, K.; Fässler, T. F.; Rieger, B.; Veinot, J. G. C. Radical-Initiated and Thermally Induced Hydrogermylation of Alkenes on the Surfaces of Germanium Nanosheets. *Chem. Mater.* **2018**, *30*, 2274–2280.

[139] Giousis, T.; Fang, S.; Miola, M.; Li, S.; Lazanas, A.; Prodromidis, M.; Tekelenburg, E. K.; Moschovas, D.; Loi, M. A.; Rudolf, P.; Gournis, D.; Pescarmona, P. P. Germanane and butyl-functionalized germanane as visible-light photocatalysts for the degradation of water pollutants. *J. Environ. Chem. Eng.* **2023**, *11*, 109784.

[140] Yu, H.; Thiessen, A. N.; Hossain, M. A.; Kloberg, M. J.; Rieger, B.; Veinot, J. G. C. Thermally Induced Dehydrogenative Coupling of Organosilanes and H-Terminated Silicon Quantum Dots onto Germanane Surfaces. *Chem. Mater.* **2020**, *32*, 4536–4543.

[141] Ni, C.; Chevalier, M.; Veinot, J. G. C. Metal nanoparticle-decorated germanane for selective photocatalytic aerobic oxidation of benzyl alcohol. *Nanoscale Adv.* **2023**, *5*, 228–236.

[142] Ni, C.; O'Connor, K. M.; Trach, J.; Butler, C.; Rieger, B.; Veinot, J. G. C. Facile synthesis of high-entropy alloy nanoparticles on germanane, Ge nanoparticles and wafers. *Nanoscale Horiz.* **2023**, *8*, 1217–1225.

[143] Ni, C.; O'Connor, K. M.; Butler, C.; Veinot, J. G. C. Synthesis of high-entropy germanides and investigation of their formation process. *Nanoscale Horiz.* **2024**, *9*, 580–588.

[144] Madhushankar, B. N.; Kaverzin, A.; Giousis, T.; Potsi, G.; Gournis, D.; Rudolf, P.; Blake, G. R.; van der Wal, C. H.; van Wees, B. J. Electronic properties of germanane field-effect transistors. *2D Mater.* **2017**, *4*, 021009.

[145] Serino, A. C.; Ko, J. S.; Yeung, M. T.; Schwartz, J. J.; Kang, C. B.; Tolbert, S. H.; Kaner, R. B.; Dunn, B. S.; Weiss, P. S. Lithium-Ion Insertion Properties of Solution-Exfoliated Germanane. *ACS Nano* **2017**, *11*, 7995–8001.

[146] Liu, N.; Qiao, H.; Xu, K.; Xi, Y.; Ren, L.; Cheng, N.; Cui, D.; Qi, X.; Xu, X.; Hao, W.; Dou, S. X.; Du, Y. Hydrogen Terminated Germanene for

a Robust Self-Powered Flexible Photoelectrochemical Photodetector. *Small* **2020**, *16*, 2000283.

[147] Ng, S.; Sturala, J.; Vyskocil, J.; Lazar, P.; Martincova, J.; Plutnar, J.; Pumera, M. Two-Dimensional Functionalized Germananes as Photoelectrocatalysts. *ACS Nano* **2021**, *15*, 11681–11693.

[148] Ge, M.; Zong, M.; Xu, D.; Chen, Z.; Yang, J.; Yao, H.; Wei, C.; Chen, Y.; Lin, H.; Shi, J. Freestanding germanene nanosheets for rapid degradation and photothermal conversion. *Mater. Today Nano* **2021**, *15*, 100119.

[149] Vogg, G.; Meyer, A. J.-P.; Miesner, C.; Brandt, M. S.; Stutzmann, M. Efficient tunable luminescence of SiGe alloy sheet polymers. *Appl. Phys. Lett.* **2001**, *78*, 3956–3958.

[150] Vogg, G.; Meyer, L. J. P.; Miesner, C.; Brandt, M. S.; Stutzmann, M. Polygermanosilyne Calcium Hydroxide Intercalation Compounds Formed by Topotactic Transformation of $Ca(Si_{1-x}Ge_x)_2$ Alloy Zintl Phases in Ambient Atmosphere. *Monatsh. Chem.* **2001**, *132*, 1125–1135.

[151] Zhao, F.; Feng, Y.; Wang, Y.; Zhang, X.; Liang, X.; Li, Z.; Zhang, F.; Wang, T.; Gong, J.; Feng, W. Two-dimensional gersiloxenes with tunable bandgap for photocatalytic H_2 evolution and CO_2 photoreduction to CO. *Nat. Commun.* **2020**, *11*, 1443.

[152] Chen, X.; Loaiza, L. C.; Monconduit, L.; Seznec, V. 2D Silicon–Germanium-Layered Materials as Anodes for Li-Ion Batteries. *ACS Appl. Energy Mater.* **2021**, *4*, 12552–12561.

[153] Roy, P. K.; Hartman, T.; Šturala, J.; Luxa, J.; Melle-Franco, M.; Sofer, Z. Hydrogen-Terminated Two-Dimensional Germanane/Silicane Alloys as Self-Powered Photodetectors and Sensors. *ACS Appl. Mater. Interfaces* **2023**, *15*, 25693—25703.

[154] Gonzalez-Rodriguez, R.; del Castillo, R. M.; Hathaway, E.; Lin, Y.; Coffer, J. L.; Cui, J. Silicene/Silicene Oxide Nanosheets for Broadband Photodetectors. *ACS Appl. Nano Mater.* **2022**, *5*, 4325–4335.

[155] Ryan, B. J.; Roling, L. T.; Panthani, M. G. Anisotropic Disorder and Thermal Stability of Silicane. *ACS Nano* **2021**, *15*, 14557–14569.

[156] Brandt, M. S.; Vogg, G.; Stutzmann, M. In *Silicon Chemistry*; Jutzi, P., Schubert, U., Eds.; 2007; pp 194–213.

[157] Loaiza, L. C.; Monconduit, L.; Seznec, V. Siloxene: A potential layered silicon intercalation anode for Na, Li and K ion batteries. *J. of Power Sources* **2019**, *417*, 99–107.

[158] Thermo Fisher Scientific, Sicherheitsdatenblatt Salzsäure ∼37%. https://www.fishersci.de/chemicalProductData_uk/wercs?itemCode=10316380&lang=DE, Accessed: 30 April 2024.

[159] Lanxess, Product Safety Assessment: Hydrobromic Acid. https://lanxess.com/-/media/Project/Lanxess/Corporate-Internet/07_US-Media/Product-Safety-Assessments/Hydrobromic-Acid.pdf, Accessed: 30 April 2024.

[160] Janiak, C. *Nichtmetallchemie*; Berichte aus der Chemie; Shaker Verlag: Aachen, 2012.

[161] Kossev, K.; Koseva, N.; Troev, K. Calcium chloride as co-catalyst of onium halides in the cycloaddition of carbon dioxide to oxiranes. *J. Mol. Catal. A: Chem.* **2003**, *194*, 29–37.

[162] Dietrich, B. Coordination chemistry of alkali and alkaline-earth cations with macrocyclic ligands. *J. Chem. Educ.* **1985**, *62*, 954.

[163] Gokel, G. W.; Goli, D. M.; Minganti, C.; Echegoyen, L. Clarification of the hole-size cation-diameter relationship in crown ethers and a new method for determining calcium cation homogeneous equilibrium binding constants. *J. Am. Chem. Soc.* **1983**, *105*, 6786–6788.

[164] Cox, B. G.; Garcia-Rosas, J.; Schneider, H. Solvent dependence of the stability of cryptate complexes. *J. Am. Chem. Soc.* **1981**, *103*, 1384–1389.

[165] Tsien, R. Y. New calcium indicators and buffers with high selectivity against magnesium and protons: design, synthesis, and properties of prototype structures. *Biochemistry* **1980**, *19*, 2396–2404.

[166] Schwetlick, K. *Organikum*, 23rd ed.; Wiley: Weinheim, 2009.

[167] Bruice, P. Y. *Organische Chemie: Studieren Kompakt*, 5th ed.; Pearson Studium - Chemie Series; Pearson Education Deutschland GmbH, 2011.

[168] Rosenfarb, J.; Huffman, J., Hugh L.; Caruso, J. A. Dielectric constants, viscosities, and related physical properties of several substituted liquid ureas at various temperatures. *J. Chem. Eng. Data* **1976**, *21*, 150–153.

[169] Pereiro, A. B.; Araújo, J. M. M.; Oliveira, F. S.; Esperança, J. M. S. S.; Canongia Lopes, J. N.; Marrucho, I. M.; Rebelo, L. P. N. Solubility of inorganic salts in pure ionic liquids. *J. Chem. Thermodyn.* **2012**, *55*, 29–36.

[170] Gallo, M. P. Zur Chemie von Siloxenen und zur Darstellung von Polysilinen und nanodimensionierten Siliciumteilchen. Dissertation, Universität Bielefeld, Bielefeld, 2004.

[171] Kaufman Katz, A.; Glusker, J. P.; Beebe, S. A.; Bock, C. W. Calcium Ion Coordination: A Comparison with That of Beryllium, Magnesium, and Zinc. *J. Am. Chem. Soc.* **1996**, *18*, 5752–5763.

[172] Buriak, J. M. Organometallic Chemistry on Silicon and Germanium Surfaces. *Chem. Rev.* **2002**, *102*, 1271–1308.

[173] Gupta, P.; Colvin, V. L.; George, S. M. Hydrogen desorption kinetics from monohydride and dihydride species on silicon surfaces. *Phys. Rev. B* **1988**, *37*, 8234–8243.

[174] Wang, Z.-H.; Urisu, T.; Watanabe, H.; Ooi, K.; Ranga Rao, G.; Nanbu, S.; Maki, J.; Aoyagi, M. Assignment of surface IR absorption spectra observed in the oxidation reactions: 2H+H_2O/Si(100) and H_2O+H/Si(100). *Surf. Sci.* **2005**, *575*, 330–342.

[175] Loboda, M. J.; Grove, C. M.; Schneider, R. F. Properties of a-SiO_x : H Thin Films Deposited from Hydrogen Silsesquioxane Resins. *J. Electrochem. Soc.* **1998**, *145*, 2861.

[176] Guha, S.; Yang, J.; Williamson, D. L.; Lubianiker, Y.; Cohen, J. D.; Mahan, A. H. Structural, defect, and device behavior of hydrogenated amorphous Si near and above the onset of microcrystallinity. *Appl. Phys. Lett.* **1999**, *74*.

[177] Dahn, J. R.; Way, B. M.; Fuller, E. W.; Weydanz, W. J.; Tse, J. S.; Klug, D. D.; Van Buuren, T.; Tiedje, T. X-ray diffraction and X-ray absorption studies of porous silicon, siloxene, heat-treated siloxene, and layered polysilane. *J. Appl. Phys.* **1994**, *75*, 1946–1951.

[178] Rana, M.; Banerjee, C.; Chowdhury, P. Studies on optical signal due to oxygen effect on hydrogenated amorphous/crystalline silicon thin films. *Appl. Phys. A* **2021**, *127*, 192.

[179] Dasog, M.; Yang, Z.; Regli, S.; Atkins, T. M.; Faramus, A.; Singh, M. P.; Muthuswamy, E.; Kauzlarich, S. M.; Tilley, R. D.; Veinot, J. G. C. Chemical Insight into the Origin of Red and Blue Photoluminescence Arising from Freestanding Silicon Nanocrystals. *ACS Nano* **2013**, *7*, 2676–2685.

[180] Lehner, A.; Steinhoff, G.; Brandt, M. S.; Eickhoff, M.; Stutzmann, M. Hydrosilylation of crystalline silicon (111) and hydrogenated amorphous silicon surfaces: A comparative X-ray photoelectron spectroscopy study. *J. Appl. Phys.* **2003**, *94*, 2289–2294.

[181] Yang, Z.; Iqbal, M.; Dobbie, A. R.; Veinot, J. G. C. Surface-Induced Alkene Oligomerization: Does Thermal Hydrosilylation Really Lead to Monolayer Protected Silicon Nanocrystals? *J. Am. Chem. Soc.* **2013**, *135*, 17595–17601.

[182] Karstedt, B. Platinum complexes of unsaturated siloxanes and platinum containing organopolysiloxanes (US3775452A), **1973**.

[183] Yu, Y.; Rowland, C. E.; Schaller, R. D.; Korgel, B. A. Synthesis and Ligand Exchange of Thiol-Capped Silicon Nanocrystals. *Langmuir* **2015**, *31*, 6886–6893.

[184] Höhlein, I. M. D.; Angı, A.; Sinelnikov, R.; Veinot, J. G. C.; Rieger, B. Functionalization of Hydride-Terminated Photoluminescent Silicon Nanocrystals with Organolithium Reagents. *Chem. - Eur. J.* **2015**, *21*, 2755–2758.

[185] Song, J. H.; Sailor, M. J. Functionalization of Nanocrystalline Porous Silicon Surfaces with Aryllithium Reagents: Formation of Silicon−Carbon Bonds by Cleavage of Silicon−Silicon Bonds. *J. Am. Chem. Soc.* **1998**, *120*, 2376–2381.

[186] Nadler, E. B.; Rappoport, Z. Hexamethyldisilane as a source of both trimethylsilyl and pentamethyldisilyl anions. Formation of a substituted pentamethyldisilyl stable enol. *Tetrahedron Lett.* **1990**, *31*, 555–558.

[187] Eaborn, C.; Jenkins, I. D. The mechanism of the base-catalysed alcoholysis of triorganosilanes. *J. Organomet. Chem.* **1974**, *69*, 185–192.

[188] Bernards, T. N. M.; van Bommel, M. J.; Boonstra, A. H. Hydrolysis-condensation processes of the tetra-alkoxysilanes TPOS, TEOS and TMOS in some alcoholic solvents. *J. Non-Cryst. Solids* **1991**, *134*, 1–13.

[189] Chou, Y.-P.; Lee, S.-C. Evidence for the void size related IR absorption frequency shifts in hydrogenated amorphous germanium films. *Solid State Commun.* **1999**, *113*, 73–75.

[190] You, J.; Bongu, S.; Bao, Q.; Panoiu, N. Nonlinear optical properties and applications of 2D materials: theoretical and experimental aspects. *Nanophotonics* **2019**, *8*, 63–97.

[191] Lyuleeva, A.; Helbich, T.; Rieger, B.; Lugli, P. Polymer-silicon nanosheet composites: bridging the way to optoelectronic applications. *J. Phys. D: Appl. Phys.* **2017**, *50*, 135106.

[192] Qaiser, A. A.; Hyland, M. M. X-Ray Photoelectron Spectroscopy Characterization of Polyaniline-Cellulose Ester Composite Membranes. *Mater. Sci. Forum* **2010**, *657*, 35–45.

[193] Galuska, A. A.; Uht, J. C.; Marquez, N. Reactive and nonreactive ion mixing of Ti films on carbon substrates. *J. Vac. Sci. Technol., A* **1988**, *6*, 110–122.

[194] Gries, W. H. A Universal Predictive Equation for the Inelastic Mean Free Pathlengths of X-ray Photoelectrons and Auger Electrons. *Surf. Interface Anal.* **1996**, *24*, 38–50.

[195] Chowdhury, S.; Jana, D. A theoretical review on electronic, magnetic and optical properties of silicene. *Rep. Prog. Phys.* **2016**, *79*, 126501.

[196] Tauc, J. *Mater. Res.* **1968**, *1*, 37–46.

[197] Garmire, E. Resonant optical nonlinearities in semiconductors. *IEEE J. Sel. Top. Quantum Electron.* **2000**, *6*, 1094–1110.

[198] Wang, K.; Feng, Y.; Chang, C.; Zhan, J.; Wang, C.; Zhao, Q.; Coleman, J. N.; Zhang, L.; Blau, W. J.; Wang, J. Broadband ultrafast nonlinear absorption and nonlinear refraction of layered molybdenum dichalcogenide semiconductors. *Nanoscale* **2014**, *6*, 10530–10535.

[199] Lu, C.; Quan, C.; Si, K.; Xu, X.; He, C.; Zhao, Q.; Zhan, Y.; Xu, X. Charge transfer in graphene/WS_2 enhancing the saturable absorption in mixed heterostructure films. *Appl. Surf. Sci.* **2019**, *479*, 1161–1168.

[200] Wang, K.; Wang, J.; Fan, J.; Lotya, M.; O'Neill, A.; Fox, D.; Feng, Y.; Zhang, X.; Jiang, B.; Zhao, Q.; Zhang, H.; Coleman, J. N.; Zhang, L.; Blau, W. J. Ultrafast Saturable Absorption of Two-Dimensional MoS_2 Nanosheets. *ACS Nano* **2013**, *7*, 9260–9267.

[201] Lu, S. B.; Miao, L. L.; Guo, Z. N.; Qi, X.; Zhao, C. J.; Zhang, H.; Wen, S. C.; Tang, D. Y.; Fan, D. Y. Broadband nonlinear optical response in multi-layer black phosphorus: an emerging infrared and mid-infrared optical material. *Opt. Express* **2015**, *23*, 11183–11194.

[202] Jiang, X.; Liu, S.; Liang, W.; Luo, S.; He, Z.; Ge, Y.; Wang, H.; Cao, R.; Zhang, F.; Wen, Q.; Li, J.; Bao, Q.; Fan, D.; Zhang, H. Broadband Nonlinear Photonics in Few-Layer MXene $Ti_3C_2T_x$ (T = F, O, or OH). *Laser Photonics Rev.* **2018**, *12*, 1700229.

[203] Cinquanta, E.; Fratesi, G.; dal Conte, S.; Grazianetti, C.; Scotognella, F.; Stagira, S.; Vozzi, C.; Onida, G.; Molle, A. Optical response and ultrafast carrier dynamics of the silicene-silver interface. *Phys. Rev. B* **2015**, *92*, 165427.

[204] Rumi, M.; Perry, J. W. Two-photon absorption: an overview of measurements and principles. *Adv. Opt. Photonics* **2010**, *2*, 451–518.

[205] Ran, L.; Chai, Z.; Gao, Y.; Wu, W.; Chang, Q.; Kong, D. The nonlinear absorption of graphene oxide water solution in femtosecond regime. *Curr. Appl. Phys.* **2016**, *16*, 985–988.

[206] Jiang, X.-F.; Polavarapu, L.; Neo, S. T.; Venkatesan, T.; Xu, Q.-H. Graphene Oxides as Tunable Broadband Nonlinear Optical Materials for Femtosecond Laser Pulses. *J. Phys. Chem. Lett.* **2012**, *3*, 785–790.

[207] Wang, G.; Bennett, D.; Zhang, C.; Ó Coileáin, C.; Liang, M.; McEvoy, N.; Wang, J. J.; Wang, J.; Wang, K.; Nicolosi, V.; Blau, W. J. Two-Photon Absorption in Monolayer MXenes. *Adv. Opt. Mater.* **2020**, *8*, 1902021.

[208] Maldonado, M.; da Silva Neto, M. L.; Vianna, P. G.; Ribeiro, H. B.; Gordo, V. O.; Carvalho, I. C. S.; de S. Menezes, L.; de Araújo, C. B.; de Matos, C. J. S.; Seixas, L.; Jawaid, A. M.; Busch, R.; Ritter, A. J.; Vaia, R. A.; Gomes, A. S. L. Femtosecond Nonlinear Optical Properties of 2D Metallic NbS_2 in the Near Infrared. *J. Phys. Chem. C* **2020**, *124*, 15425–15433.

[209] Lu, C.; Luo, M.; Ge, Y.; Huang, Y.; Zhao, Q.; Zhou, Y.; Xu, X. Layer-Dependent Nonlinear Optical Properties of WS_2, MoS_2, and Bi_2S_3 Films Synthesized by Chemical Vapor Deposition. *ACS Appl. Mater. Interfaces* **2022**, *14*, 2390–2400.

[210] Wang, J.; Hernandez, Y.; Lotya, M.; Coleman, J. N.; Blau, W. J. Broadband Nonlinear Optical Response of Graphene Dispersions. *Adv. Mater.* **2009**, *21*, 2430–2435.

[211] Dong, N.; Li, Y.; Feng, Y.; Zhang, S.; Zhang, X.; Chang, C.; Fan, J.; Zhang, L.; Wang, J. Optical Limiting and Theoretical Modelling of Layered Transition Metal Dichalcogenide Nanosheets. *Sci. Rep.* **2015**, *5*, 14646.

[212] Huang, J.; Dong, N.; Zhang, S.; Sun, Z.; Zhang, W.; Wang, J. Nonlinear Absorption Induced Transparency and Optical Limiting of Black Phosphorus Nanosheets. *ACS Photonics* **2017**, *4*, 3063–3070.

[213] Shen, W.; Hu, J.; Ma, T.; Wang, J.; Wei, Y.; Zhang, Y.; Wu, J.; Chen, J. Antimonene Prepared by Laser Irradiation Applied for Nonlinear Optical Limiting. *Electron. Mater. Lett.* **2021**, *17*, 521–531.

[214] Srichan, S.; Chan-Seng, D.; Lutz, J.-F. Influence of Strong Electron-Donor Monomers in Sequence-Controlled Polymerizations. *ACS Macro Lett.* **2012**, *1*, 589–592.

[215] Goseki, R.; Matsuo, Y.; Hirao, A. Precise syntheses of structurally possible all tetrablock quaterpolymers by a methodology combining living anionic polymerization with linking chemistry using 1 : 1 addition reaction. *Polym. Chem.* **2018**, *9*, 834–844.

[216] Das, B.; Voggu, R.; Rout, C. S.; Rao, C. N. R. Changes in the electronic structure and properties of graphene induced by molecular charge-transfer. *Chem. Commun.* **2008**, 5155–5157.

[217] Odian, G. *Principles of Polymerization*; John Wiley & Sons, Inc, 2004.

[218] Wheeler, L. M.; Anderson, N. C.; Palomaki, P. K. B.; Blackburn, J. L.; Johnson, J. C.; Neale, N. R. Silyl Radical Abstraction in the Functionalization of Plasma-Synthesized Silicon Nanocrystals. *Chem. Mater.* **2015**, *27*, 6869–6878.

[219] Larson, G. L. Some Aspects of the Chemistry of Alkynylsilanes. *Synthesis* **2018**, *50*, 2433–2462.

[220] Huang, P.; Xu, D.; Reich, R. M.; Kaiser, F.; Liu, B.; Kühn, F. E. Et_2Zn-mediated stoichiometric C(sp)-H silylation of 1-alkynes and chlorosilanes. *Tetrahedron Lett.* **2019**, *60*, 1574–1577.

[221] Ishikawa, J.-I.; Itoh, M. Dehydrogenative Coupling between Hydrosilanes and Alkynes Catalyzed by Alkoxides, Alkylmetals, and Metalamides. *J. Catal.* **1999**, *185*, 454–461.

[222] Wrackmeyer, B.; Bayer, S.; Tok, O. L.; Klimkina, E. V.; Milius, W.; Kempe, R.; Khan, E. Alkynylsilanes and Alkynyl(vinyl)silanes. Synthesis,Molecular Structures and Multinuclear Magnetic Resonance Study. *Z. Naturforsch., B* **2010**, *65*, 725–744.

[223] Ishikawa, J.-I.; Inoue, K.; Itoh, M. Dehydrogenative cross-coupling reactions between phenylsilane and ethynylbenzene in the presence of metal hydrides. *J. Organomet. Chem.* **1998**, *552*, 303–311.

[224] Toutov, A. A.; Betz, K. N.; Schuman, D. P.; Liu, W.-B.; Fedorov, A.; Stoltz, B. M.; Grubbs, R. H. Alkali Metal-Hydroxide-Catalyzed C(sp)–H Bond silylation. *J. Am. Chem. Soc.* **2017**, *139*, 1668–1674.

[225] Kavthe, R. D.; Ishikawa, Y.; Kusuma, I.; Asao, N. Chemoselective Aerobic Cross-Dehydrogenative Coupling of Terminal Alkynes with Hydrosilanes by a Nanoporous Gold Catalyst. *Chem. - Eur. J.* **2018**, *24*, 15777–15780.

[226] Yamaguchi, K.; Wang, Y.; Oishi, T.; Kuroda, Y.; Mizuno, N. Heterogeneously Catalyzed Aerobic Cross-Dehydrogenative Coupling of Terminal Alkynes and Monohydrosilanes by Gold Supported on OMS-2. *Angew. Chem., Int. Ed.* **2013**, *52*, 5627–5630.

[227] Voronkov, M. G.; Ushakova, N. I.; Tsykhanskaya, I. I.; Pukhnarevich, V. B. Dehydrocondensation of trialkylsilanes with acetylene and monosubstituted acetylenes. *J. Organomet. Chem.* **1984**, *264*, 39–48.

[228] Kownacki, I.; Marciniec, B.; Dudziec, B.; Kubicki, M. Silylative Coupling of Terminal Alkynes with Iodosilanes: New Catalytic Activation of sp-Hybridized Carbon−Hydrogen Bonds. *Organometallics* **2011**, *30*, 2539–2545.

[229] Sugita, H.; Hatanaka, Y.; Hiyama, T. Silylation of 1-alkynes with chlorosilanes promoted by zinc: Preparation of alkynylsilanes in a single step. *Tetrahedron Lett.* **1995**, *36*, 2769–2772.

[230] Marciniec, B.; Dudziec, B.; Kownacki, I. A New Catalytic Route for the Activation of sp-Hybridized Carbon–Hydrogen Bonds. *Angew. Chem., Int. Ed.* **2006**, *45*, 8180–8184.

[231] Andreev, A. A.; Konshin, V. V.; Komarov, N. V.; Rubin, M.; Brouwer, C.; Gevorgyan, V. Direct Electrophilic Silylation of Terminal Alkynes. *Org. Lett.* **2004**, *6*, 421–424.

[232] Rahaim, R. J.; Shaw, J. T. Zinc-Catalyzed Silylation of Terminal Alkynes. *J. Org. Chem.* **2008**, *73*, 2912–2915.

[233] Hengge, E.; Baumegger, A. Synthese und Eigenschaften einiger Ethinylsilane. *J. Organomet. Chem.* **1989**, *369*, C39–C42.

[234] Unno, M.; Saito, T.; Matsumoto, H. Silapericyclyne, $(Ph_2SiC{\equiv}C)_6$: Spontaneous Conformational Resolution of Boat- and Chair-'Exploded' Cyclohexane. *Chem. Lett.* **1999**, *28*, 1235–1236.

[235] Bortolin, R.; Parbhoo, B.; Brown, S. S. D. Pericyclynosilanes: synthesis of a new class of cyclic organosilicon compounds. *J. Chem. Soc., Chem. Commun.* **1988**, 1079–1081.

[236] Zhilitskaya, L. V.; Istomina, E. E.; Yarosh, N. O.; Voronkov, M. G.; Albanov, A. I.; Yarosh, O. G. Spherical polyunsaturated organosilicon and organogermanium first generation dendrimers of regular structure. *Russ. J. Gen. Chem.* **2006**, *76*, 1864–1869.

[237] Matsuo, T.; Uchida, K.; Sekiguchi, A. Silylacetylene dendrimers: synthesis and characterization. *Chem. Commun.* **1999**, 1799–1800.

[238] Yarosh, O. G.; Voronkov, M. G.; Brodskaya, E. I. Macromolecular and macrocyclic polyunsaturated silicohydrocarbons. *Russ. Chem. Rev.* **1995**, *64*, 839–855.

[239] Kong, L.; Zuo, X.; Zhu, S.; Li, Z.; Shi, J.; Li, L.; Feng, Z.; Zhang, D.; Deng, D.; Yu, J. Novel carbon-poly(silacetylene) composites as advanced thermal protection material in aerospace applications. *Compos. Sci. Technol.* **2018**, *162*, 163–169.

[240] Bortolin, R.; Brown, S. S. D.; Parbhoo, B. Microstructural analysis of polysilapropynylene copolymers by ^{13}C and ^{29}Si nuclear magnetic resonance. *Macromolecules* **1990**, *23*, 2465–2469.

[241] Jo, S.-M.; Lee, W.-S.; Lyu, H.-S. The efficient synthesis of poly(silapropynylenes) via condensation of NaC≡CNa with $R_1R_2SiCl_2$ activated by pyridine. *Polym. Bull.* **1993**, *30*, 621–627.

[242] Chen, M.; Xiong, P.; Zhou, Q.; Ni, L.; Wang, G. Synthesis, curing behavior and thermal properties of silicon-containing hybrid polymers with Si—C≡C units. *Polym. Int.* **2014**, *63*, 1531–1536.

[243] Ijadi-Maghsoodi, S.; Pang, Y.; Barton, T. J. Efficient, "one-pot" synthesis of silylene–acetylene and disilylene–acetylene preceramic polymers from trichloroethylene. *J. Polym. Sci., Part A: Polym. Chem.* **1990**, *28*, 955–965.

[244] Baklanova, N. I.; Kulyukin, V. N.; Kostrovsky, V. G.; Lyakhov, N. Z.; Terskikh, V. V.; Turkina, G. Y.; Zhilitskaya, L. V.; Yarosh, O. G.; Voronkov, M. G. High-Temperature Evolution of SiC/C Products Derived from Preceramic Polymers. *J. Mater. Synth. Process.* **1999**, *7*, 289–296.

[245] Horstmann, J.; Lamm, J.-H.; Strothmann, T.; Neumann, B.; Stammler, H.-G.; Mitzel, N. W. Bi- and tridentate silicon-based acceptor molecules. *Z. Naturforsch., B* **2017**, *72*, 383.

[246] Bortolin, R.; Brown, S.; Selby, D.; Parbhoo, B. Verfahren zur Herstellung von Silethinylpolymeren (DE4100257A1), **1991**.

Publications

The following publication is included in parts in this thesis:

- Stavrou, M.[‡]; Mühlbach, A. M.[‡]; Arapakis, V.; Groß, E.; Kratky, T.; Günther, S.; Rieger, B.; Couris, S. Exceptional ultrafast nonlinear optical response of functionalized silicon nanosheets. *Nanoscale* **2023**, *15*, 16636. [‡]These authors contributed equally.

The following publication is beyond the scope of this thesis:

- Kränzlein, M.; Pehl, T. M.; Halama, K.; Großmann, P. F.; Kratky, T.; Mühlbach, A. M.; Rieger, B. Azide-modified poly(diethyl vinylphosphonate) for straightforward graft-to carbon nanotube functionalization. *Macromol. Mater. Eng.* **2022**, *308*, 2200635.